

SYNTHESIS, CHARACTERIZATION, AND PHOTOTHERMAL  
PROPERTIES OF PLASMONIC METAL NITRIDE NANOPARTICLES

By

Reem Ahmed Karaballi

Submitted in partial fulfilment of the requirements  
for the degree of Doctor of Philosophy.

Dalhousie University

Halifax, Nova Scotia

July 2022

© Copyright by Reem A. Karaballi, 2022

## Dedication

بِسْمِ اللَّهِ الرَّحْمَنِ الرَّحِيمِ

I would like to dedicate this body of work to God, as none of it would be possible without the strength and patience he has given me to persevere my studies.

Also, I would like to dedicate this work to my parents: Ahmed Karaballi and Nafissa Faidalla, my brothers: Mohammed, Omar, Khalid, and Tariq, and my husband Mohammad Elkawifi. It would be unfathomable for me to even start this work without the many blessings like that of my family who has stood with me from day one, believing in me when no one else would. The love and support that my family provided me over the past years is tremendous and it helped bring out the best me. I'm grateful to have you all by my side throughout my academic journey, even though sometimes you made it a little bit tough, I still appreciate and love you all.

## Table of Contents

List of Tables .....	viii
List of Figures .....	ix
Abstract .....	xviii
List of Abbreviations and Units Used.....	xix
Acknowledgements.....	xxvii
Chapter 1: Introduction .....	1
1.1 Nanomaterials .....	1
<i>1.1.1 Classification of Nanomaterials</i> .....	3
<i>1.1.2 Synthesis of Nanomaterials</i> .....	6
1.2 Plasmonic Materials.....	7
1.3 Factors that Influence the LSPR .....	12
<i>1.3.1 The Effect of Nanostructure Composition</i> .....	12
<i>1.3.2 The Effect of Nanostructure Size</i> .....	13
<i>1.3.3 The Effect of Nanostructure Shape</i> .....	15
<i>1.3.4 The Effect of Surrounding Refractive Index</i> .....	17
1.4 Plasmonic Nanomaterials.....	18
<i>1.4.1 Metallic Nanostructures</i> .....	19
<i>1.4.2 Semiconductors and Transparent Conducting Oxides</i> .....	23

1.4.3 <i>Transition Metal Nitrides</i> .....	26
1.5 Synthesis of Plasmonic Transition Metal Nitrides Nanomaterials .....	29
1.6 Scope of Thesis .....	38
Chapter 2: Experimental Methods and Techniques .....	39
2.1 Introduction.....	39
2.2 Transmission Electron Microscopy .....	40
2.3 Scanning Electron Microscopy .....	44
2.4 X-ray Powder Diffraction .....	46
2.5 X-ray Photoelectron Spectroscopy .....	49
2.6 Absorbance Spectroscopy .....	54
2.7 Dynamic Light Scattering and Zeta Potential.....	56
2.8 Synthesis of Transition Metal Nitride Nanoparticles.....	59
2.8.1 <i>Preparation of Transition Metal Nitride Nanoparticles</i> .....	60
2.9 Photothermal Measurements.....	61
2.10 Computational Studies .....	65
Chapter 3: Synthesis of Group IVB Plasmonic Metal Nitrides .....	67
3.1 Introduction.....	68
3.1 Experimental .....	69
3.1.1 <i>Materials</i> .....	69



3.1.2 Preparation of Transition Metal Nitride Nanoparticles .....	69
3.1.3 Characterization Techniques .....	69
3.1.4 Computational Studies .....	71
3.2 Results and Discussion .....	71
3.3 Conclusion .....	86
Chapter 4: Photothermal Properties of Group IVB Nitrides in NIR Region .....	87
4.1 Introduction .....	88
4.2 Experimental .....	92
4.2.1 Materials .....	92
4.2.2 Preparation of Transition Metal Nitride Nanoparticles .....	92
4.2.3 Characterization Techniques .....	92
4.2.4 Photothermal Measurements .....	92
4.2.5 Computational Studies .....	92
4.3 Results and Discussion .....	93
4.4 Conclusion .....	103
Chapter 5: Oxidative and Colloidal Stability of Plasmonic Group IVB Nitrides .....	104
5.1 Introduction .....	105
5.2 Experimental .....	108
5.2.1 Materials .....	108

5.2.2 Preparation of Transition Metal Nitride Nanoparticles .....	108
5.2.3 Characterization Techniques .....	108
5.2.4 Stability Measurements .....	108
5.3 Results and Discussion .....	109
5.4 Conclusions.....	119
Chapter 6: Solid-State Synthesis of UV-Plasmonic Cr <sub>2</sub> N Nanoparticles .....	120
6.1 Introduction.....	121
6.2 Experimental .....	122
6.2.1 Materials .....	122
6.2.2 Synthesis of Cr <sub>2</sub> N Nanoparticles .....	122
6.2.3 Photothermal Measurements .....	122
6.2.4 Computational Studies .....	123
6.2.5 Characterization techniques .....	123
6.3 Results and Discussion .....	124
6.4 Conclusion .....	140
Chapter 7: Synthesis of Plasmonic Group IVB Nitrides using Solid-Gas Method .....	141
7.1 Introduction.....	142
7.2 Experimental .....	143
7.2.1 Material.....	143

<i>7.2.2 Synthesis of Transition Metal Nitride Nanoparticles</i> .....	143
<i>7.2.3 Characterization Techniques</i> .....	143
7.3 Results and Discussion .....	143
7.4 Conclusion .....	150
Chapter 8: Conclusions .....	151
References:.....	161
Appendix.....	186

## List of Tables

<b>Table 1:</b> Photothermal efficiencies of plasmonic nanostructures reported in the literature. ....	90
<b>Table 2:</b> Summary of photothermal parameters for TMNs and Au NRs. ....	98
<b>Table 3:</b> Comparison of TMN NPs prepared using solid-state metathesis ( $\text{MO}_2+\text{Mg}_3\text{N}_2$ ), and solid-gas route ( $\text{Mg} +\text{N}_2$ ).....	150

## List of Figures

- Figure 1:** Illustration of carbon-based nanomaterial classification based on their dimension ranging from 0D to 3D. Adapted from reference [28]. Images reproduced with permission from reference [29] under the terms of the Creative Commons Attribution 4.0 International License (<http://creativecommons.org/licenses/by/4.0/>). .....5
- Figure 2:** Illustration of top-down and bottom-up approaches for nanoparticles synthesis. Adapted from reference [33]. .....7
- Figure 3:** Schematic representation of the two SPR modes. Adapted from reference [46]. .....9
- Figure 4:** Calculated spectra of the efficiency of absorption  $\sigma_{\text{abs}}$  (dashed line), scattering  $\sigma_{\text{sca}}$  (dotted line), and extinction  $\sigma_{\text{ext}}$  (solid line) for gold nanospheres (A)  $D = 20$  nm, (B)  $D = 40$  nm, (C)  $D = 80$  nm. Reproduced with permission from reference [73]. Copyright 2006, American Chemical Society. ....15
- Figure 5:** Schematic representation of longitudinal and transverse electron oscillation on nanorods. Adapted from reference [76]. .....16
- Figure 6:** Comparison of (A) real component, (B) imaginary component of the dielectric function of metals (Ag, Au), TCOs (AZO, GZO, ITO), and nitrides (TiN, ZrN). The arrows show the ranges over which TCOs, and nitrides are metallic. Reproduced with permission from reference [80]. Copyright 2011, Optica Publishing Group. ....25
- Figure 7:** Comparison of calculated (A) real, (B) imaginary parts of the dielectric function, and (C) LSPR Q factor of selected refractory materials with Au and Ag as

shown in dashed black and red lines, respectively. Reproduced with permission from reference <sup>[68]</sup>. Copyright 2016, American Chemical Society.....29

**Figure 8:** (A) TEM image of TiN particles obtained from laser ablation of pressed TiN powder target. Reproduced with permission from reference <sup>[147]</sup>. Copyright 2004, Springer. (B) TEM image of ZrN NPs obtained from laser ablation of ZrN target. Reproduced with permission from reference <sup>[148]</sup>. Copyright 2003, Springer. (C) Particle size distribution and TEM image, and (D) extinction spectra of TiN NPs. Reproduced with permission from reference <sup>[149]</sup>.....31

**Figure 9:** (A) TEM image and (B) extinction spectrum of TiN NPs prepared via the arc plasma method. Reproduced with permission from reference <sup>[152]</sup>. Copyright 2018, the Royal Society of Chemistry. ....33

**Figure 10:** (A) TEM image and SAED pattern and (B) extinction spectra of TiN NPs prepared using the nonthermal plasma method with TiCl<sub>4</sub> and NH<sub>3</sub> as precursors. Reproduced with permission from reference <sup>[154]</sup>. Copyright 2017, American Chemical Society. (C) Absorbance spectrum of TiN NPs prepared by using the nonthermal plasma method with TDMAT and NH<sub>3</sub> as precursors. Reproduced with permission from reference <sup>[155]</sup>. Copyright 2018, American Chemical Society. (D) TEM image of bare ZrN NPs prepared by the nonthermal plasma method, (E) experimental and (F) calculated extinction spectra of bare and silicon oxynitride coated ZrN NPs, and (G) electron microscopy-energy-dispersive X-ray mapping of silicon oxynitride coated ZrN NPs, showing elemental composition. Reproduced with permission from reference <sup>[156]</sup>. Copyright 2019, American Chemical Society.....35

<b>Figure 11:</b> TEM images of core–shell TiO <sub>2</sub> –SiO <sub>2</sub> NPs (A) before and (B) after nitridation with NH <sub>3</sub> . (C) Extinction spectra of bare and SiO <sub>2</sub> -coated TiN NPs. Reproduced with permission from reference <sup>[166]</sup> . Copyright 2019, American Chemical Society.....	37
<b>Figure 12:</b> Schematic illustration of the interaction of an electron beam with atoms of a sample and the consequent processes. Adapted from reference <sup>[170]</sup> .....	40
<b>Figure 13:</b> Schematic diagram of transmission electron microscopy system. Adapted from reference <sup>[172]</sup> .....	43
<b>Figure 14:</b> Schematic diagram of scanning electron microscopy system. Adapted from reference <sup>[183]</sup> .....	45
<b>Figure 15:</b> Schematic configuration of an X-ray diffractometer. Adapted from reference <sup>[185]</sup> .....	47
<b>Figure 16:</b> Schematic depicting the interaction of X-ray with the sample to satisfy Bragg’s equation. Adapted from reference <sup>[186]</sup> .....	48
<b>Figure 17:</b> Schematic illustration of X-ray photoelectron spectroscopy set-up. Adapted from reference <sup>[188]</sup> .....	50
<b>Figure 18:</b> Emission of a core electron in XPS technique. Adapted from reference <sup>[192]</sup> . .....	51
<b>Figure 19:</b> Energy level diagram of the sample and the spectrometer in a core-level photoemission experiment of a metallic sample. Adapted from reference <sup>[192]</sup> .....	53
<b>Figure 20:</b> Schematic diagram of Ultraviolet-visible spectroscopy. Adapted from reference <sup>[194]</sup> .....	56

<b>Figure 21:</b> Schematic illustration of the electric double layer around the NPs. Adapted from reference <sup>[198]</sup> .....	58
<b>Figure 22:</b> Representation of solid-state synthesis set-up.....	59
<b>Figure 23:</b> Representation of data obtained from photothermic experiment. ....	62
<b>Figure 24:</b> Illustration of the photothermal experimental set-up. ....	65
<b>Figure 25:</b> (A) Powder XRD pattern and (B) TEM image of anatase phase TiO <sub>2</sub> NPs. ....	72
<b>Figure 26:</b> (A) Powder XRD pattern and (B) TEM image of monoclinic phase ZrO <sub>2</sub> NPs.....	72
<b>Figure 27:</b> (A) Powder XRD pattern and (B) TEM image of monoclinic phase HfO <sub>2</sub> NPs.....	73
<b>Figure 28:</b> Schematic illustration of solid-state metathesis route and the resulting dispersible and sintered NPs. ....	74
<b>Figure 29:</b> Powder XRD patterns of (A) TiN, ZrN, and HfN powder, and (B) dispersed TiN, ZrN, and HfN prepared via solid-state metathesis reaction.....	75
<b>Figure 30:</b> TEM images of water dispersed (A, B) TiN, (C, D) ZrN, and (E, F) HfN NPs.....	76
<b>Figure 31:</b> TEM images of non-dispersible (A) TiN, (B) ZrN, and (C) HfN powders. ...	77
<b>Figure 32:</b> High-resolution X-ray photoelectron spectra of Ti 2p and N 1s region of TiN NPs. Experimental data represented as open circles, and the overall fitted data represented as a black line. ....	78



<b>Figure 33:</b> High-resolution X-ray photoelectron spectra of Zr 3d and N 1s region of ZrN NPs. Experimental data represented as open circles, and the overall fitted data represented as a black line. ....	79
<b>Figure 34:</b> High-resolution X-ray photoelectron spectra of Hf 4f and N 1s region of HfN NPs. Experimental data represented as open circles, and the overall fitted data represented as a black line. ....	79
<b>Figure 35:</b> (A) Calculated absorption spectra of TiN, ZrN, and HfN NPs. (B) Absorption spectra of aqueous dispersions of TiN, ZrN, and HfN NPs. (Inset: photograph of NPs dispersed in water under white light).....	80
<b>Figure 36:</b> Refractive index dependent absorption maxima for (A) TiN, (B) ZrN, and (C) HfN NPs. ....	83
<b>Figure 37:</b> SEM images of TiN, ZrN, and HfN NPs before (A, B, and C) and after annealing at 1000 °C (D, E, and F).....	85
<b>Figure 38:</b> Illustration of the photothermal light to heat conversion of plasmonic NPs. Adapted from reference <sup>[242]</sup> .....	88
<b>Figure 39:</b> TEM image commercially purchased citrate stabilized Au NRs. ....	93
<b>Figure 40:</b> TEM images of HfN NPs showing varying thickness of oxide shell around the particles. ....	94
<b>Figure 41:</b> (A) Extinction spectra of TMN NPs and citrate functionalized Au NRs in water. (B) Mass extinction coefficients of TiN, ZrN, HfN NPs and Au NRs dispersed in water.....	95

<b>Figure 42:</b> Representative temperature change plots as a function of time during heating (first 30 minutes) and cooling (last 30 minutes) for 10.0 nM TMN and Au NR solutions. ....	97
<b>Figure 43:</b> Plots of cooling time vs. negative natural log of the temperature change during the cooling stage for TMN NPs and Au NRs. ....	98
<b>Figure 44:</b> (A) Photothermal transduction efficiencies of TMN NPs and Au NRs under 1.0 W cm <sup>-2</sup> illumination at 850 nm. (B) FEM simulations of effective scattering cross-sections of TMN NPs and Au NRs on a log scale at 850 nm. ....	100
<b>Figure 45:</b> Photothermal stability of 10.0 nM (A) TiN, (B) ZrN, and (C) HfN NP solutions over 5 cycles at 850 nm under 1 W cm <sup>-2</sup> illumination. ....	101
<b>Figure 46:</b> Representative temperature change plots as a function of time of TMN NPs at 1.0, 0.75, 0.50, and 0.25 W cm <sup>-2</sup> illumination intensities at 850 nm. ....	102
<b>Figure 47:</b> Schematic Illustration of surface charge of TMN NPs at different pH. ....	109
<b>Figure 48:</b> (A) Images of TiN, ZrN, and HfN NP dispersions in water at different pH. (B) Zeta potential of TiN, ZrN, and HfN NPs at different pH ranging between 1 and 10. ....	110
<b>Figure 49:</b> Demonstration of reversible colloidal stability of ZrN NPs. ....	111
<b>Figure 50:</b> Colloidal suspension of TiN at pH 0 (A) before and (B) after the addition of H <sub>2</sub> O <sub>2</sub> . ....	112
<b>Figure 51:</b> The change in LSPR (A) maxima and (intensity) over time for TiN, ZrN, and HfN. (Inset: photograph of TiN NPs dispersed in water under white light on day 1 vs. day 60). ....	113

<b>Figure 52:</b> Comparison of absorption spectra of ZrN and HfN after four years. (Inset: photograph of NPs dispersed in water under white light).....	114
<b>Figure 53:</b> High-resolution X-ray photoelectron spectra of Ti 2p and N 1s region of TiN NPs on day 1 and day 30. Experimental data represented as open circles, and the overall fitted data represented as a black line. ....	116
<b>Figure 54:</b> High-resolution X-ray photoelectron spectra of Zr 3d and N 1s region of ZrN NPs on day 1 and day 30. Experimental data represented as open circles, and the overall fitted data represented as a black line. ....	117
<b>Figure 55:</b> High-resolution X-ray photoelectron spectra of Hf 4f and N 1s region of HfN NPs on day 1 and day 30. Experimental data represented as open circles, and the overall fitted data represented as a black line. ....	118
<b>Figure 56:</b> (A) and (B) transmission electron microscopy images, (C) particle size distribution, and (D) aspect ratio distribution of Cr <sub>2</sub> O <sub>3</sub> NPs. ....	125
<b>Figure 57:</b> Powder XRD pattern of chromium nitride synthesized using the solid-state metathesis reaction at (A) 1000 °C, (B) 800 °C, (C) 750 °C, (D) 700 °C, and (E) 650 °C for 12 hours.....	127
<b>Figure 58:</b> (A) Powder X-ray diffraction pattern of Cr <sub>2</sub> O <sub>3</sub> and Cr <sub>2</sub> N NPs. (B) TEM image of Cr <sub>2</sub> N NPs. Inset: Higher magnification TEM image of a single Cr <sub>2</sub> N NP showing the oxide shell. (C) Cr <sub>2</sub> N particle size distribution. (D) HAADF-STEM image and EELS map of (E) chromium (F) nitrogen and (G) oxygen content of Cr <sub>2</sub> N NPs. ....	129
<b>Figure 59:</b> TEM images of Cr <sub>2</sub> N NPs from multiple synthesis. ....	129
<b>Figure 60:</b> High resolution XP spectra of Cr 2p and N 1s regions of Cr <sub>2</sub> O <sub>3</sub> nanopowder and Cr <sub>2</sub> N NPs.....	131

<b>Figure 61:</b> High magnification TEM images of Cr <sub>2</sub> N NPs showing the oxide shell around the particles. ....	131
<b>Figure 62:</b> (A) Real and imaginary components of the dielectric function of Cr <sub>2</sub> N. (B) Calculated absorption cross-section and measured absorbance of Cr <sub>2</sub> N NPs. Inset: Photograph of Cr <sub>2</sub> N NP suspension in water. Calculated (C) absorption and (D) scattering coefficients of Cr <sub>2</sub> N NPs between 10-100 nm. ....	133
<b>Figure 63:</b> (A) Low-loss EELS spectra and (B) aloof EELS spectra of Cr <sub>2</sub> N NPs. Inset: STEM-HAADF images indicating spots where the spectra were collected (scale bar = 20 nm). ....	135
<b>Figure 64:</b> (A) STEM-HAADF image and EELS loss probability maps images in the energy range of (B) 0.91–2.13 eV, (C) 3.06–4.90 eV, (D) 6.96–8.6 eV, (E) 9.44–10.95 eV, and (F) 11.86–13.85 eV of Cr <sub>2</sub> N NPs. ....	136
<b>Figure 65:</b> Images of Cr <sub>2</sub> N NPs suspension at different pH and the corresponding zeta potential.....	137
<b>Figure 66:</b> (A) Representative temperature change plots as a function of time of Cr <sub>2</sub> N NPs at 1.0, 0.75, 0.50, and 0.25 W cm <sup>-2</sup> illumination intensities at 365 nm. (B) Representative plot of temperature change at different illumination density. (C) Photothermal stability of 10.0 nM Cr <sub>2</sub> N NP solutions over 5 cycles at 365 nm under 1 W cm <sup>-2</sup> illumination.....	139
<b>Figure 67:</b> Powder XRD patterns of TiN, ZrN, and HfN NPs prepared by reacting metal oxides with Mg metal under N <sub>2</sub> flow. ....	144
<b>Figure 68:</b> TEM images of (A, B) TiN, (C, D) ZrN, and (E, F) HfN NPs. ....	145

<b>Figure 69:</b> High-resolution X-ray photoelectron spectra of Ti 2p and N 1s region of TiN NPs. Experimental data represented as open circles, and the overall fitted data represented as a black line. ....	147
<b>Figure 70:</b> High-resolution X-ray photoelectron spectra of Zr 3d and N 1s region of ZrN NPs. Experimental data represented as open circles, and the overall fitted data represented as a black line. ....	148
<b>Figure 71:</b> High-resolution X-ray photoelectron spectra of Hf 4f and N 1s region of HfN NPs. Experimental data represented as open circles, and the overall fitted data represented as a black line. ....	148
<b>Figure 72:</b> Normalized absorbance spectra of water dispersed TiN, ZrN, and HfN NPs. (Inset: photograph of NPs dispersed in water under white light). ....	149
<b>Figure 73:</b> A photograph of TiN, ZrN, HfN, and Cr <sub>2</sub> N solution lined up from left to right. ....	152
<b>Figure 74:</b> Spectral regions of LSPR for TiN, ZrN, HfN, and Cr <sub>2</sub> N NPs.....	153

## Abstract

Plasmonic materials have been widely used for applications such as photothermal therapy, chemical and biological sensing, energy generation and conversion devices. Most common plasmonic nanomaterials are composed of noble metals, Au and Ag. However, these materials are expensive and hinder applications that require large-scale synthesis. The nanostructures of Au and Ag are susceptible to sintering when used as solar concentrators and Ag can oxidize under ambient conditions, further limiting the practical use of these metals. As an alternative to noble metals, theoretical investigations have shown transition metal nitrides to be promising alternatives. Transition metal nitrides (TMNs) are relatively inexpensive, have high melting points and therefore can possess thermal stability, and their refractory nature can render chemical stability and mechanical hardness. However, these TMNs have not been thoroughly investigated experimentally.

The focus of this doctoral work is to synthesize plasmonic TMN nanostructures, examine their properties, and compare them to well-established noble metal plasmonic materials. Free-standing and water-dispersible group IVB (Ti, Zr, and Hf) nitrides were synthesized using a solid-state metathesis reaction between the respective transition metal oxides and magnesium nitride. The nanoparticles were characterized using XRD, SEM, TEM, DLS, and XPS. Additionally, the optical properties were investigated using absorbance spectroscopy. The photothermal properties of group IVB TMNs were investigated using an 850 nm LED source and their performance was compared to Au nanorods. The long-term oxidative and chemical stability of group IVB TMNs were also investigated. Furthermore, the group IVB TMNs were successfully synthesized using a solid-gas approach by reacting the respective transition metal oxides with Mg under the flow of N<sub>2</sub> gas.

The solid-state metathesis reaction was used to synthesize plasmonic Cr<sub>2</sub>N successfully, and the resulting nanoparticles were characterized using various techniques. The LSPR peak of plasmonic Cr<sub>2</sub>N is in the deep UV region, therefore EELS loss probability maps were used to probe the plasmonic responses. Additionally, the chemical stability of Cr<sub>2</sub>N colloidal suspension at different pH was also investigated. Moreover, the photothermal properties of Cr<sub>2</sub>N using a 365 nm LED source were investigated. These studies suggest the possibility of using Cr<sub>2</sub>N for water treatment and disinfection applications.

## List of Abbreviations and Units Used

AAO	Anodic Aluminum Oxide
BE	Binding Energy
BSE	Back-Scattered Electrons
CCD	Charge-Coupled Diode
CMOS	Complementary Metal Oxide Semiconductor
CTAB	Cetyltrimethylammonium Bromide
DI	Deionized
DLS	Dynamic Light Scattering
EELS	Electron Energy Loss Spectroscopy
FEM	Finite Element Method
FE	Fermi Level
FWHM	Full Width at Half Maximum
HRTEM	High Resolution-TEM
IR	Infrared
KE	Kinetic Energy
LED	Light Emitting Diode
LSPR	Localized Surface Plasmon Resonance
MOFs	Metal Organic Frameworks
$m_{\text{total}}$	Mass of all the Nanoparticles

$m_{\text{particle}}$	Mass of Individual Nanoparticles
NPs	Nanoparticles
Nd:YAG	Neodymium-doped Yttrium Aluminum Garnet
NIR	Near-Infrared
N	Number of Nanoparticles
$N_A$	Avogadro's constant
PML	Perfectly Matched Layers
PSS	Polystyrene Sulfonate
PDDA	Poly(Diallyldimethylammonium Chloride)
PZC	Point of Zero Charge
SAED	Selected Area Electron Diffraction
Sccm	Standard Cubic Centimeters per Minutes
SE	Secondary Electrons
SEM	Scanning Electron Microscopy
STEM	Scanning Transmission Electron Microscopy
SERS	Surface Enhanced Raman Spectroscopy
SPP	Surface Plasmon Polariton
SPR	Surface Plasmon Resonance
TDMAT	Tetrakis(Dimethylamino) Titanium
TEM	Transmission Electron Microscopy



TMN	Transition Metal Nitride
UV-vis	Ultraviolet-visible Spectroscopy
XRD	X-ray Diffraction
XPS	X-ray Photoelectron Spectroscopy
Yb:KGW	Ytterbium-doped Potassium Gadolinium Tungstate
A	Absorbance
A	Ampere
$A_{\lambda}$	Optical Density
cm	Centimeter
C	Concentration
$C_{\text{abs}}$	Absorption Cross-Section
$C_{\text{sca}}$	Scattering Cross-Section
$C_p$	Heat Capacity
$C_{\text{ext}}$	Extinction Cross-Section
D	Speed of the Particles
d	Diameter of the Nanoparticles
eV	Electronvolts
E	Energy
f(ka)	Henry Function
fs	Femtoseconds

g	Grams
$\hbar$	Reduced Planck's Constant
h	Heat Transfer Coefficient
h	Planck's Constant
h	hour
h $\nu$	Photon Energy
I	Incident Light Intensity
J	Joules
K	Kelvin
KeV	Kiloelectronvolt
kV	Kilovolts
K	Shape Factor
k <sub>B</sub>	Boltzmann Constant
kg	Kilogram
l	Path Length
L	Crystallite Size
L	Liter
m	Mass
m	Meter
mbar	Millibar

mL	Milliliter
meV	Millielectronvolts
mV	Millivolts
mg	Milligrams
mm	Millimeter
mrad	Milliradians
M	Molar
nm	Nanometer
nM	Nanomolar
$n_m$	Refractive Index of the Surrounding Medium
N	Number of Nanoparticles in the Solution
p	Momentum
$P_0$	Incident Radiant Power
Pa	Pascal
ps	Picoseconds
P	Transmitted Radiant Power
Q	Quality Factor
$Q_{abs}$	Absorption Coefficients
$Q_{sca}$	Scattering Coefficients
$Q_I$	Energy Input

$Q_0$	Baseline Energy Input
$Q_{\text{ext}}$	Outgoing Energy
R	Radius
rpm	Revolutions Per Minutes
$R_H$	Hydrodynamic Radius
T	Temperature
$T_{\text{amb}}$	Ambient Temperature
$T_{\text{max}}$	Maximum Temperature
T	Transmittance
s	Seconds
S	Surface Area
S	Refractive Index Sensitivity
$S_A$	Surface Scattering Constant
$U_e$	Electrophoretic Mobility
v	Velocity
V	Volume
$V_F$	Fermi Velocity
W	Watts
z	Zeta Potential
wt%	Weight Percentage

$\mu\text{m}$	Micrometer
$\mu\text{J}$	Microjoule
$\varepsilon$	Molar Absorptivity
$\varepsilon$	Dielectric Function
$\varepsilon_r$	Real Component of Dielectric Function
$\varepsilon_i$	Imaginary Component of Dielectric Function
$\varepsilon_m$	Dielectric Constant of the Surrounding Medium
$\lambda$	Wavelength
$\omega$	Frequency of the External Electric Field
$\omega_p$	Plasmon Frequency
$\omega_{\text{max}}$	LSPR Peak Frequency
$\gamma$	Damping Frequency
$\rho$	Bulk Density
$\beta$	Full Width at Half Maximum
$\sigma_{\text{Ext}}$	Optical Extinction Spectrum
$\sigma_{\text{Abs}}$	Absorbed Photons
$\sigma_{\text{Sca}}$	Scattered Photons
$\theta$	Bragg Angle
$\phi$	Work Function
$\tau$	Time Constant

$\eta$	Absolute Zero-Shear Medium Viscosity
$\eta_T$	Photothermal Transduction Efficiency
Å	Angstrom
0D	Zero-Dimensional
1D	One-Dimensional
2D	Two-Dimensional
3D	Three-Dimensional

## Acknowledgements

As I conclude my graduate studies, it is important to extend my gratitude to those who contributed to my educational and professional development. Over the past years, I have been in contact with many professors, colleagues, staff, technicians, and students that without their help and support this thesis would not have been complete.

First and foremost, I would like to thank my supervisor Dr. Mita Dasog for giving me the opportunity to do research in her group and perform my PhD studies. Mita has been a remarkable supervisor and mentor who always ensures the laboratory environment is suitable and inclusive for everyone. She has always been very enthusiastic about research and very proud of the work that we have done in the laboratory. I cannot believe I'm writing this after four years, but these past years have been exciting (despite having lived half of that period in a global pandemic) as I gained a tremendous amount of knowledge and was able to grow as a scientist and a researcher. Thank you for guiding me throughout these projects, through which I have both achieved my goals and learned many useful life lessons along the way. I cannot thank Mita enough for hosting me in her laboratory during the past years and continuously pushing me to be the best version of myself.

I would like to thank Dr. Heather Andreas for always generously dedicating her time toward helping me throughout the past four years. I have learned so much from you during our meetings, and I'm so grateful for the "grilling sessions" we used to have even though they were tough, and I struggled badly but you were so humble and non-judgmental which made me feel very comfortable. Thank you for always being there for me, always smiling and making me feel safe to discuss anything. Dr. Andreas has been an outstanding

professor and mentor, and I'm so grateful to have had her as an external examiner for my Master's degree and now as a committee member for my PhD studies.

I would like to thank my other supervisory committee members: Dr. Norman Schepp, and Dr. Peng Zhang for agreeing to be part of my committee and guiding me throughout my PhD studies. I appreciate all the guidance and support that they have provided me with throughout the past years. I would like to thank Dr. Erika Merschrod for serving as an external examiner and for providing me with valuable inputs.

I would like to thank all the past and present Dasog group members for being there for me and supporting me. I had the opportunity to work with many great students in the Dasog group who made this journey a little easier and a lot more fun. Especially, I would like to thank Sarah, Izzy, and Dreenan for creating our own snapchat group to talk about the issues we are facing, help each other feel better, sharing pet videos to keep our sanity, and always finding a way to share funny memes or videos. I want to thank Adrienne Allison for being the best Co-President of the WIC chapter, without all her help we wouldn't have been able to do all the amazing work we did. Thank you for proof-reading my documents and always providing me with feedback and suggestions.

I would like to thank Ping Li and Mary Ann Trevors for training me on the TEM. I would like to thank Dr. Craig Bennett for the TEM measurements on some of my samples. I would like to thank Andrew George for training me on the XRD and performing some of the XPS measurements. I would like to thank Dr. Rob Coridan for performing some of the XPS measurements. I would like to thank Benjamin Trueman for training me on the DLS,



Dr. Graham Gagnon for DLS access, and Heather Daurie for always accommodating me and letting me use the DLS at any time. I would like to thank Hoayang Yu for the HRTEM, and Nanofab at the University of Alberta for the XPS measurements. I would like to thank Dr. Carmen Andrei and Dr. Isobel Bicket for the TEM/ HRTEM and EELS measurements, respectively. Patricia Scallion and CTRI are thanked for their assistance with SEM measurements. Andreas group is thanked for access to spectrometer for absorbance studies. CMC Microsystems is thanked for Lumerical software that was used for computational studies.

I would like to thank all the Faculty in the Department of Chemistry and especially Dr. Angela Crane-Garnier, and Dr. Jennifer Macdonald for welcoming me in the first-year team and nourishing me with all the support and opportunities they provided me to become a better teacher. I have learned so much from them and I'm grateful for all the teaching opportunities and awards I received. Additionally, thanks to all the staff especially Lea Gawne for making sure that I complete all the forms needed on time, and always answering my emails. Thanks to NSERC and the Sumner fellowships for providing me with the financial support.

I would like to thank my family for their endless love and support and always believing in me when I had doubt. No words can express the amount of love I have for all of them and I'm infinitely grateful for having them in my life. Especial thanks to my husband Mohammed Elkawifi, who made the last year more enjoyable and did everything to make me less stressed and happier. I appreciate all the work he did for me, and all the times he went on work trips so I can focus on writing my thesis.

I would like to thank my best friends (Gladness, Zeina, Ayesha, Wafaa, and Ines) who always believed in me and cheered me up when I was feeling down. Specifically, I would like to thank Ines for helping me through the “Experimental Techniques” course and performing photothermal fitting calculations. Additionally, I would like to thank my best friend and cancer buddy Osai Clarke for always pushing me to pursue research in chemistry. He has been there throughout my whole academic life, and I couldn’t ask for a better friend to share these memorable moments with. Thank you for always believing in me, sending me positive thoughts, and pushing me to do better. Finally, I would like to thank Dr. Christa Brosseau for always believing in me and supporting throughout my journey. Thank you for always being so proud of me and encouraging me to do better.

At the end I would like to acknowledge myself for not giving up when things got too difficult, life has been very stressful and sometimes unbearable but somehow, I was able to pull through. I’m saddened to have this chapter end but I’m excited to start a new life journey and hopeful for a better future.

“It always seems impossible until it is done”-*Nelson Mandela*

## Chapter 1: Introduction

### 1.1 Nanomaterials

Nanotechnology involves manipulation of materials on the nanoscale to fabricate structures and devices with tunable chemical and physical properties. As the size of matter is reduced from bulk to the nanometer (nm) scale, new optical, magnetic, electronic, and structural properties arise thus making these nanomaterials very promising for many new avenues.<sup>[1,2]</sup> Over the past several decades, nanomaterials have been widely used in various applications such as energy conversion,<sup>[3,4]</sup> catalysis,<sup>[5,6]</sup> sensing,<sup>[7,8]</sup> and biomedicine<sup>[9,10]</sup>. The prefix “nano” is a Greek word meaning “dwarf” or very small, and it represents one billionth of a unit, and in the case of distance it represents  $10^{-9}$  m.<sup>[11]</sup> A nanomaterial is defined as a substance that is on the nanoscale and has at least one dimension between 1 and 100 nm. To put the size of these materials into perspective, the thickness of a strand of a human hair is 60,000 nm, the diameter of red blood cells is 10,000 nm, and the radius of the DNA double helix is 2 nm.<sup>[12]</sup>

The concept of nanomaterials was first introduced by Nobel laureate Richard Feynman in 1959 while providing a lecture titled, “*There’s Plenty of Room at the Bottom*” where he discussed the possibility of manipulating and arranging individual atoms and molecules by using tiny machines. During this lecture, Feynman asked, “why can’t we write the entire 24 volumes of the Encyclopedia Britannica on the head of a pin?”<sup>[13]</sup> Based on his analysis, this should be achievable, however, the limitation lies in the lack of appropriate equipment and techniques. After this discussion, many scientists were intrigued to explore the concepts presented by Feynman, and thus the field of

nanotechnology emerged. In 1974, Norio Taniguchi was the first person to use the term nanotechnology and defined it as the processing of separation, consolidation, and deformation of materials by one atom or one molecule.<sup>[14]</sup> It was not until the early 1980s, where interest in nanoscience and nanotechnology began to rise with the invention of scanning tunneling microscopy and atomic force microscopy.<sup>[15]</sup> Over the years, there have been many revolutionary developments in various fields that supported Feynman's ideas of modifying matter at the atomic scale.<sup>[16]</sup> Nowadays, nanoscience is known as a convergence of physics, materials science, and biology which deals with the manipulation of materials at the atomic and molecular scale, while nanotechnology is the ability to observe, measure, manipulate, assemble, control, and manufacture matter on the nanoscale.<sup>[11]</sup>

Due to the advancement in state-of-art technologies and the development of analytical instrumentations, the use of nanomaterials was traced to several millennia ago where they were used as colorants for glass and ceramics due to their optical properties.<sup>[17]</sup> The Lycurgus cup from the 4<sup>th</sup> Century is the oldest example of dichroic glass where the color changes in certain lighting conditions.<sup>[17]</sup> It appears red by reflection and green by transmission, and detailed scanning electron microscopy (SEM) analysis in 1990 has indicated the presence of nanosized (up to 100 nm) particles of Ag (66.2%), Au (31.2%), and Cu (2.6%) embedded in the glass.<sup>[18]</sup> The gold nanoparticles (Au NPs) are responsible for producing the red color as a result of light absorption whereas the green color is attributed to the light scattering by the silver nanoparticles (Ag NPs). Different sizes and shapes of Au and Ag provide different colors such as yellow, green, red, and orange which

allowed these metals to be widely used in pottery and stained glasses.<sup>[18]</sup> Additionally, during the 13-18<sup>th</sup> centuries “Damascus blades” were made to be very strong, sharp, resilient, and flexible.<sup>[19]</sup> These blades proved to contain cementite nanowires and carbon nanotubes which were responsible for the material’s unique properties.<sup>[11,20]</sup> Nanomaterials such as carbon black, fumed silica, titania, and their industrial applications have been dated to the 1900s.<sup>[18]</sup> These are just a few examples that highlight the use of nanomaterials since ancient history; even though at the time the concept of synthesizing materials at the nanoscale was not established. In 1857, Michael Faraday accidentally prepared a “ruby” solution while mounting pieces of Au leaf onto microscope slides.<sup>[21,22]</sup> Further investigation of this solution indicated the synthesis of a Au colloidal solution by reducing gold chloride with a phosphorous reducing agent. This discovery has paved the way for nanoscience which now plays a crucial role in our daily lives.

### ***1.1.1 Classification of Nanomaterials***

In the past decades, nanomaterials have been playing a tremendous role in the rapid progress of science and technology in medicine, imaging, electronics, catalysis, and many other fields.<sup>[23,24]</sup> The term nanomaterial is very broad, and it includes all types of materials that are on the nanoscale. However, scientists have classified nanomaterials based on different parameters such as their origin, chemical composition, and dimensionality.<sup>[18]</sup> Nanomaterials can be classified into two categories based on their origin—either natural or synthetic. Natural and unintentionally prepared nanomaterials refer to nano-sized particles that occur naturally in the environment such as proteins, viruses, minerals (i.e., oxides and carbonates), carbon particles resulting from human activity (i.e., diesel

combustion), or volcanic eruptions that form Al and SiO<sub>2</sub> particles.<sup>[18]</sup> On the contrary, synthetic, or intentionally made nanomaterials, include nanomaterials that were produced deliberately through a defined fabrication process. These will be discussed in more detail throughout this thesis.

Nanomaterials can be classified into four categories based on their chemical composition including carbon-based, inorganic-based, organic-based, and composite-based nanomaterials.<sup>[25]</sup> Carbon-based nanomaterials include carbon nanotubes, carbon fibers, fullerenes, carbon black, and graphene. Inorganic-based nanomaterials include metal and metal oxide nanoparticles such as Ag, Au, titanium dioxide (TiO<sub>2</sub>), zinc oxide (ZnO) NPs, and semiconductors such as Si and ceramics.<sup>[25]</sup> Organic-based nanomaterials are organic matter such as dendrimers, micelles, liposomes, and polymer NPs. Composite-based nanomaterials are any combination of metal-based, metal oxide-based, carbon-based, and/or organic-based nanomaterials which can have complicated structures similar to metal organic frameworks (MOFs) but can exhibit unique combination properties.<sup>[25]</sup> In this thesis, the focus will be on the synthesis of inorganic-based nanomaterials.

Furthermore, nanomaterials can be classified into four categories based on their number of dimensions which are outside the nanoscale range, as shown in **Figure 1**. Zero-dimensional (0D) nanomaterials have all their dimensions within the nanoscale (<100 nm). Examples of 0D nanomaterials include nanoparticles, clusters, fullerenes, and quantum dots.<sup>[26]</sup> One-dimensional (1D) nanomaterials have only one dimension outside of the nanoscale, and this can include nanotubes, nanowires, nanofibers, and nanorods.<sup>[27]</sup>

Two-dimensional (2D) nanomaterials have two dimensions outside of the nanoscale, and this can include plate-like shapes, graphene, nanosheets, and nanolayers. Three-dimensional (3D) nanomaterials have all their dimensions outside of the nanoscale and these tend to include bulk powders, dispersions of nanoparticles, bundles of nanowires, and multi-nanolayers.<sup>[18,27]</sup> In this thesis, 0D nanomaterials and more specifically nanoparticles will be studied.

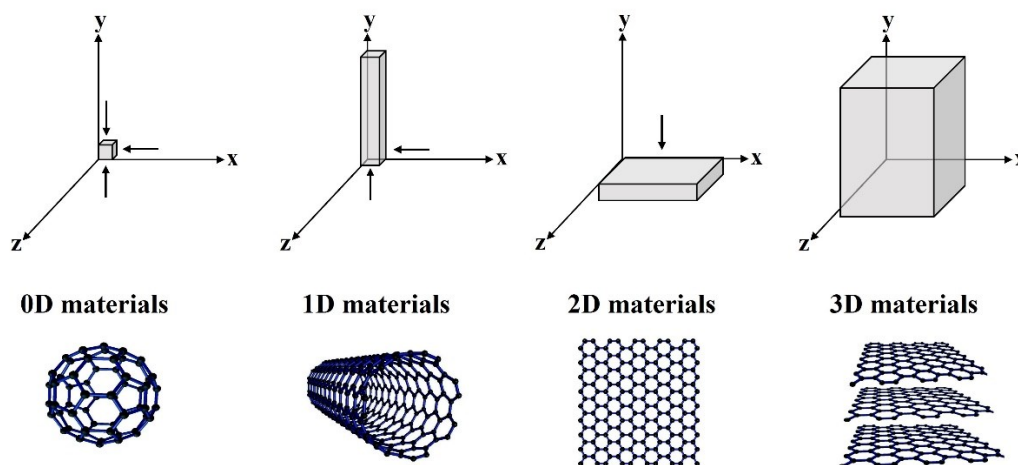


**Figure 1:** Illustration of carbon-based nanomaterial classification based on their dimension ranging from 0D to 3D. Adapted from reference <sup>[28]</sup>. Images reproduced with permission from reference <sup>[29]</sup> under the terms of the Creative Commons Attribution 4.0 International License (<http://creativecommons.org/licenses/by/4.0/>).

### ***1.1.2 Synthesis of Nanomaterials***

The first discovered nanomaterial was prepared by vacuum evaporation of Fe in inert gas and condensed on to a cooled substrate.<sup>[30]</sup> Since then, there have been many methods used to synthesize nanomaterials. Mainly, two approaches are used to generate nanomaterials which are top-down or bottom-up methods, as shown in **Figure 2**. In top-down methods, the material is broken from the bulk material to make the desired nanostructures. This can be done by mechanical strategies such as milling or grinding, or chemical strategies such as evaporation, sputtering, and etching techniques.<sup>[25]</sup> There are a couple of physical methods used for a top-down approach such as thermolysis, laser ablation, lithography, sputtering, atomization, and pyrolysis.<sup>[25]</sup>

In bottom-up methods, atoms or molecules are assembled to generate nanostructures via the reduction of metal salt or precipitation.<sup>[31-34]</sup> In this method, the nanomaterials are commonly synthesized via salt reduction using various reducing agents such as sodium citrate, phosphor, or sodium borohydride because it allows better control over the size, shape, composition, and structure.<sup>[32,34]</sup> However, there are other methods as well such as hydrothermal, chemical vapor deposition, solvothermal, sol-gel, and template-assisted.<sup>[25]</sup>



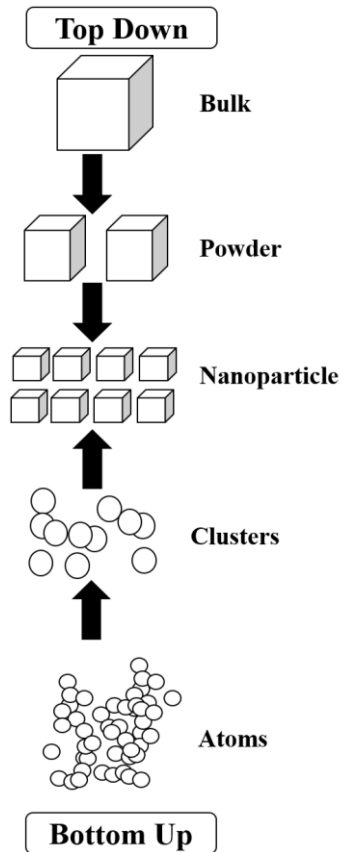


**Figure 2:** Illustration of top-down and bottom-up approaches for nanoparticles synthesis. Adapted from reference <sup>[33]</sup>.

## 1.2 Plasmonic Materials

For many decades after Faraday synthesized the Au colloids, scientists were eager to find an explanation for the unexpected color of Au NPs compared to their bulk counterpart. In the 1900s, Gustav Mie provided an optical response simulation of spherical metal colloids by solving Maxwell's electromagnetic theory.<sup>[35]</sup> This method explained the scattering and absorption of the electromagnetic radiation by nanospheres (<20 nm), which was then identified as surface plasmon resonance (SPR). SPR was first observed by Woods

who discovered that bulk metal materials provide a pattern of unusual dark and light bands that appear in the reflected light when polarized light is shone onto a metal-backed diffraction grating.<sup>[36,37]</sup> In the 1950s, Rayleigh addressed this anomaly for the first time using a theoretical approach.<sup>[38]</sup> Later, Pines and Bohm suggested that the energy losses observed are due to the excitation of conducting electrons which results in plasma oscillation.<sup>[39]</sup> In the 1960s, the term surface plasmon was first proposed by Pines as a quantum of elementary excitation associated with high-frequency collective motion. Since then the term SPR has been widely used in the field of plasmonics.<sup>[40–42]</sup>

In the past decades, SPR phenomena have shown to be prominent for metal particles with dimensions much smaller than the wavelength of the incident light.<sup>[43]</sup> Generally, SPR are optical modes occurring at the interface between a dielectric and a metal nano-object, which originate from the resonant coupling between a surface-charge oscillation and the electromagnetic field.<sup>[44]</sup> As a result, two modes are formed by surface oscillation as shown in **Figure 3**. The first is the surface plasmon polariton (SPP) mode which are surface waves traveling along with the metal and dielectric interfaces. The second is the localized surface plasmon resonance (LSPR) mode which is confined in a very small volume around an isolated nanostructure.<sup>[1,45]</sup>

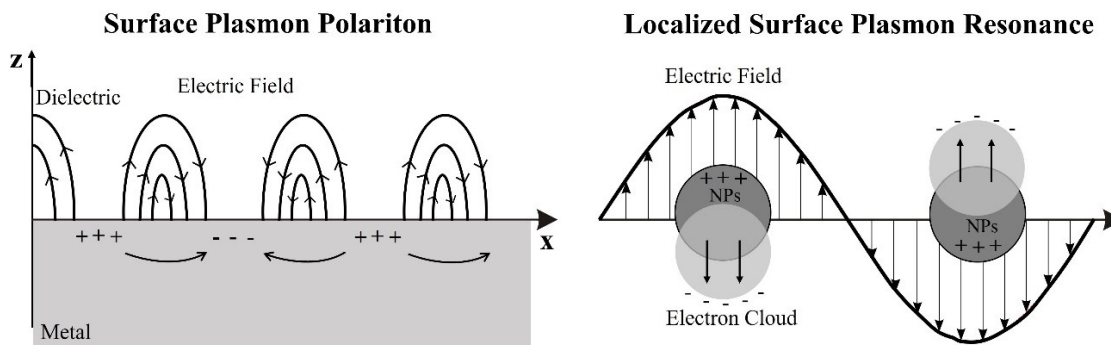


**Figure 3:** Schematic representation of the two SPR modes. Adapted from reference [46].

The LSPR mode is the most relevant to this thesis and will be discussed in more detail. As shown in **Figure 3**, an electromagnetic wave simulates a collective motion of the confined free electrons of a NP, which creates a surface charge. This can be thought of as a mass-spring harmonic oscillator driven by the energy resonant light wave, where the nuclei act as a restoring force that induces the electrons to return toward the core of the NP.<sup>[47-49]</sup> Only light with frequency in resonance with the oscillation can excite the surface plasmons.<sup>[48]</sup> Nanomaterials that have free conduction electrons and the appropriate dielectric function can strongly couple with the light and support a surface plasmon. These are referred to as plasmonic nanomaterials, and they have been explored for many groundbreaking applications such as surface-enhanced Raman spectroscopy (SERS),<sup>[50,51]</sup> sensing,<sup>[32,52-54]</sup> solar energy harvesting,<sup>[6,55-57]</sup> and photothermal therapy<sup>[58-60]</sup> as a consequence of their light-material interactions.

Metallic nanostructures were among the first materials chosen for plasmonic applications because they contain a large number of conduction band electrons which can

contribute to the LSPR.<sup>[61]</sup> The current theories on plasmonic properties are constructed around metals and will be briefly discussed here. The electron cloud oscillation is strongly dependent on the dielectric constant of the metal NP ( $\epsilon$ ) and the external environment ( $\epsilon_m$ ). Furthermore, the dielectric function can be expressed in terms of the real component of the dielectric function of the metal ( $\epsilon_r$ ), and the imaginary component of the dielectric function of the metal ( $\epsilon_i$ ), as shown in **equation (1)**:

$$\epsilon(\lambda) = \epsilon_r(\lambda) + i\epsilon_i(\lambda) \quad (1)$$

The  $\epsilon_i$  and  $\epsilon_r$  components of the dielectric constants of the metal can roughly determine the dephasing and position of the LSPR peak, respectively.<sup>[61]</sup> The  $\epsilon_r$  describes the strength of the polarization induced by the external electric field. The  $\epsilon_i$  is associated with losses encountered in polarizing the material, and thus smaller  $\epsilon_i$  indicates a low loss material.<sup>[62]</sup> The losses depicted by the  $\epsilon_i$  can be attributed to intraband and interband transitions and additional scattering losses due to defects in the sample.<sup>[63]</sup> The intraband losses occur when electrons are being excited within the same band, this can be observed at the longer wavelengths (typically near-IR (NIR) region). The interband electronic transition occurs due to transitions from the Fermi level ( $F_E$ ) to the next higher empty conduction band or transition from a lower filled valence band to the  $F_E$  or higher levels, and these can be observed at shorter wavelengths.<sup>[63]</sup>

The LSPR induces a strong absorption of the incident light which can be typically measured using absorbance spectroscopy. The LSPR absorption band intensity and wavelength depend on various factors such as the metal type, particle size, shape,

composition, and the dielectric constant of the surrounding medium.<sup>[2,17]</sup> Some of these factors have been theoretically described by the Mie theory and expressed by **equation (2)**:

$$C_{\text{ext}} = \frac{24\pi^2 R^3 \epsilon_m^{3/2}}{\lambda} \frac{\epsilon_i}{(\epsilon_r + 2\epsilon_m)^2 + \epsilon_i^2} \quad (2)$$

where  $C_{\text{ext}}$  is the extinction cross-section which is a measure of the nanomaterials ability to absorb or scatter the incident light,  $\lambda$  is the wavelength of the incident light,  $R$  is the radius of the particles,  $\epsilon_r$  and  $\epsilon_i$  are the real and imaginary components of the dielectric constant of the plasmonic material, and  $\epsilon_m$  is the dielectric constant of the surrounding medium.<sup>[1,17,47,64]</sup> A strong LSPR peak can only occur when the condition of  $\epsilon_r = -2\epsilon_m$  is satisfied, therefore, not all materials can satisfy this condition and thus cannot exhibit plasmonic properties.<sup>[1,17,64]</sup> Because the strength of the LSPR and the performance of the materials are highly dependent on the  $\epsilon_r$  and  $\epsilon_i$ , a quality factor ( $Q$ ) is used to quantify the overall material quality.<sup>[62,65,66]</sup> The  $Q$  of LSPR systems describes how many optical periods of the plasmon oscillation can occur before the field decays, and how many times the local optical field at the surface of the plasmonic NP exceeds the external field.<sup>[65]</sup> The  $Q$  of the LSPR is only dependent on the dielectric function of the nanomaterial ( $\epsilon_r$  and  $\epsilon_i$ ) at the given plasmon frequency ( $\omega_p$ ) and not on the geometric form and shape of the nanomaterial,<sup>[67,68]</sup> as shown in **equation (3)**:

$$Q = \frac{\omega_p \left( \frac{d\epsilon_r}{d\omega} \right)}{2(\epsilon_i)} \quad (3)$$

Generally, for a material to be considered for plasmonic applications, the value of  $Q$  should be 10 or higher.<sup>[66]</sup> Larger values of  $Q$  indicate strong plasmons whereas, a smaller value of  $Q$  indicate weak surface plasmons and hence, a small  $C_{\text{ext}}$ .<sup>[66]</sup> Although the  $Q$  factor determines the performance of plasmonic materials, other factors such as synthesis and fabrication, the feasibility of integration, cost, and elemental abundance play a major role in choosing a suitable plasmonic material.<sup>[62]</sup> Despite being widely used, these metrics do not take into account the surrounding medium, and therefore quantitative comparisons and accurate efficiencies are not possible. Additionally, the losses considered in the  $Q$  factor are the losses occurring only in the metal part of the nanostructure, however, losses from radiation and surface imperfection are neglected. It is however worth noting that these losses effectively increase the loss coefficient ( $\epsilon_i$ ) and may reduce the  $Q$  factor.<sup>[67]</sup> Therefore, an attempt to obtain a metric to estimate the relative efficiency of plasmonic materials for different applications needs to be established.<sup>[69]</sup>

### **1.3 Factors that Influence the LSPR**

As mentioned earlier, the LSPR can be greatly influenced by many factors such as the refractive index of the surrounding medium, size, shape, and composition of the nanomaterial.<sup>[17]</sup> In the next sections, each of these factors will be discussed in more detail.

#### ***1.3.1 The Effect of Nanostructure Composition***

The plasmonic properties of any material, such as its  $Q$  factor and LSPR width, intensity, and position are all based on the material's dielectric function.<sup>[48]</sup> Therefore, depending on the chemical composition of the nanostructure, the LSPR properties can vary.

For example, the LSPR of Ag and Au NPs with the same size are completely different. The LSPR of Ag NPs (25 nm) is narrow and centered at ~420 nm whereas the LSPR of Au NPs (25 nm) is comparatively broad and centered around ~550 nm.<sup>[61]</sup> Therefore, depending on the intended application and desired LSPR response, different nanomaterials can be explored. Most nanostructures consist of one element; however, alloying with different metals can help tune the optical properties and has been shown to be very useful toward overcoming issues with scalability, synthesis, biocompatibility, physical and chemical stability.<sup>[48,70,71]</sup> Additionally, it can improve the LSPR response and allow for better catalytic activity.<sup>[48]</sup> However, the effect of the chemical composition of the nanostructures on the LSPR has not been addressed in Mie theory which complicates the evaluation of these materials.<sup>[17]</sup> Surface chemistry can influence plasmonic properties as well and studies have been done to investigate the effect of coating NPs with a silica shell. While this improves the stability of the NPs, increasing the thickness of a silica shell can redshift and dampens the LSPR response and thus decreases the sensitivity.<sup>[64]</sup> Therefore, tuning the composition of the nanomaterials and surface chemistry can play a major role in the plasmonic responses.

### ***1.3.2 The Effect of Nanostructure Size***

The optical properties of the LSPR are highly dependent on the size of the nanostructures. The LSPR peak position is predicted to shift to a longer wavelength when the size of the NPs increases.<sup>[24]</sup> The plasmon linewidth also varies with particle size due to the combination of interband transitions, which contribute to increased linewidth for small nanostructures, and higher-order plasmon modes, which contribute to increased

linewidth for larger nanostructures.<sup>[72]</sup> Not only the position and linewidth of the plasmon peaks can be influenced by the size of the NPs, but also the properties of the optical extinction spectrum. **Figure 4** illustrates that the measured optical extinction spectrum ( $\sigma_{\text{Ext}}$ ) of a metallic NP is the sum of absorbed ( $\sigma_{\text{Abs}}$ ) and scattered photons ( $\sigma_{\text{Sca}}$ ), this can be mathematically presented as shown in **equation (4)**:

$$\sigma_{\text{Ext}} = \sigma_{\text{Abs}} + \sigma_{\text{Sca}} \quad (4)$$

When the NPs are much smaller than the wavelength of the light, the optical extinction spectrum arises mostly from the absorption cross-section and not the scattering cross-section, as shown in **Figure 4A**.<sup>[73]</sup> However, as the particle's size increases, multipolar plasmon oscillation occurs and therefore both absorption and scattering occur (**Figure 4B**).<sup>[45]</sup> As the particle size increases further, the optical extinction spectrum will be dominated by scattering, as shown in **Figure 4C**.<sup>[73]</sup> Therefore, for applications requiring higher scattering efficiency such as imaging, larger NPs are preferred, and applications requiring higher absorption efficiency such as photothermal therapy, smaller NPs are preferred.<sup>[1,31]</sup> It is important to note that the size dispersion in the sample solution also affects the LSPR peak and induces broadening. The full width at half maximum (FWHM) of the LSPR is dependent on the average size of the NPs and the size distribution. Thus, optimizing the reaction conditions to make monodisperse NPs is more desirable.<sup>[74]</sup>



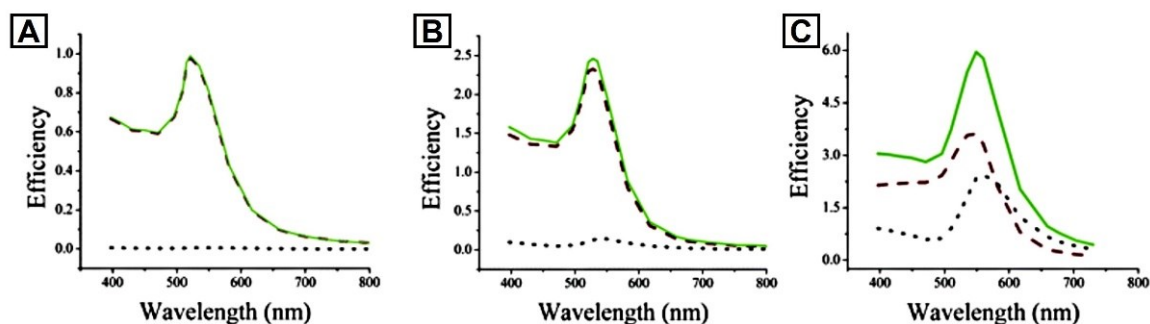


**Figure 4:** Calculated spectra of the efficiency of absorption  $\sigma_{\text{abs}}$  (dashed line), scattering  $\sigma_{\text{sca}}$  (dotted line), and extinction  $\sigma_{\text{ext}}$  (solid line) for gold nanospheres (A)  $D = 20$  nm, (B)  $D = 40$  nm, (C)  $D = 80$  nm. Reproduced with permission from reference <sup>[73]</sup>. Copyright 2006, American Chemical Society.

### 1.3.3 The Effect of Nanostructure Shape

The position, width, and number of LSPR peaks are also highly dependent on the shape of the nanostructures. It has been shown that the LSPR for nanostructures with sharp vertices and edges can be more sensitive to changes in the refractive index of the surrounding medium compared to rounded NPs.<sup>[75]</sup> This can be attributed to the large charge separation occurring on sharp edges which reduces the restoring forces for the dipole oscillation, and hence a reduction in resonance frequency or red-shift in wavelength is expected.<sup>[66]</sup> There have been various shapes of nanomaterials synthesized such as spheres, triangles, stars, rods, and disks to tune the LSPR peak position.<sup>[27,76]</sup> By changing the geometrical shape of the nanostructure, the particle-particle interaction in the solution can change which results in a shift of the LSPR peak to higher wavelengths and a broadening of the peak. For this reason, modification of the surface of the nanostructure might be required to prevent aggregation.<sup>[77]</sup>

Changing the shape of the nanostructure not only shifts the LSPR peak but can also result in the appearance of more than one LSPR peak, as predicted by Gan theory.<sup>[1,76]</sup> For a nanorod shape, two LSPR peaks are observed due to the longitudinal and transverse electron oscillation as shown in **Figure 5**. The two LSPR peaks arise because of the lower symmetry which makes it possible to polarize the electrons in more than one way.<sup>[66]</sup> The excitation along the major axis (longitudinal) is more intense than the excitation along the minor axis (transverse).<sup>[48]</sup> The longitudinal LSPR peak occurs at a higher wavelength due to the lower charge accumulation, which results in smaller restoring forces, and consequently, smaller resonance frequencies.<sup>[74]</sup>

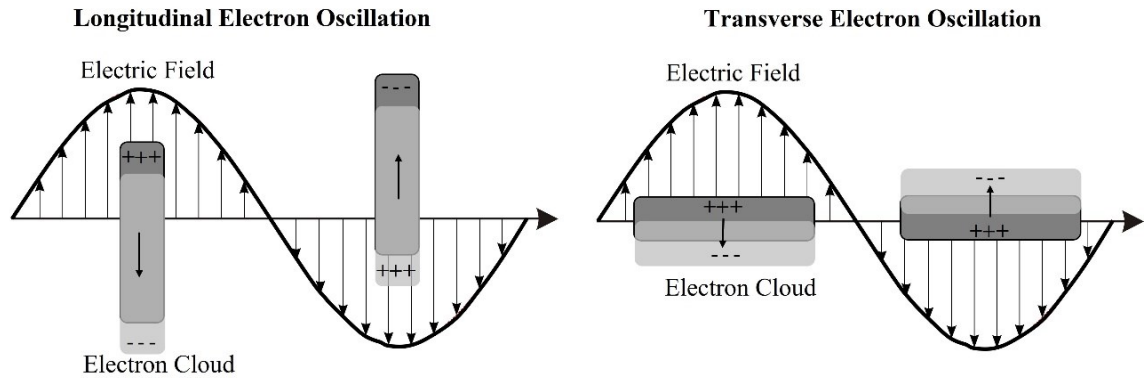


**Figure 5:** Schematic representation of longitudinal and transverse electron oscillation on nanorods. Adapted from reference <sup>[76]</sup>.

The optical properties of a rod-shaped nanostructure are highly dependent on the ratio of length to width; this is known as the aspect ratio.<sup>[76]</sup> As the aspect ratio increases, the LSPR modes shift to longer wavelengths. Also, the magnitude of wavelength shift of the longitudinal LSPR is much higher than that of the transverse.<sup>[76]</sup> The longitudinal LSPR

position can be tuned from visible to NIR regions by simply varying the aspect ratio, which makes it very attractive for many biological and sensing applications.<sup>[78]</sup>

#### ***1.3.4 The Effect of Surrounding Refractive Index***

The relationship between the LSPR and the dielectric function of the medium can be explained by the Drude model for the frequency-dependent expression of  $\epsilon_r$ , as shown in **equation (5)**:<sup>[72,79]</sup>

$$\epsilon_r = 1 - \frac{\omega_p^2}{\omega^2 + \gamma^2} \quad (5)$$

where  $\omega$  is the frequency of the external electric field,  $\omega_p$  and  $\gamma$  are the plasmon frequency and damping frequency of the bulk metal, respectively. The  $\gamma$  represents the optical losses in the material and therefore to obtain low losses,  $\gamma$  should be minimized.<sup>[80]</sup> For visible and NIR frequencies, it can be assumed that  $\gamma \ll \omega_p$  which simplifies **equation (5)** into **equation (6)**:

$$\epsilon_r = 1 - \frac{\omega_p^2}{\omega^2} \quad (6)$$

For LSPR to occur, the resonance condition ( $\epsilon_r \approx -2\epsilon_m$ ) needs to be satisfied, and therefore **equation (6)** becomes **equation (7)**:

$$\omega_{\max} = \frac{\omega_p}{\sqrt{2\epsilon_m + 1}} \quad (7)$$

where  $\omega_{\max}$  is the LSPR peak frequency. By converting the frequency to wavelength using  $\lambda = 2\pi c/\omega$ , and the dielectric constant to index of refraction via  $\epsilon_m = n^2$ , **equation (7)** becomes **equation (8)**:

$$\lambda_{\max} = \lambda_p \sqrt{2n_m^2 + 1} \quad (8)$$

Therefore, based on **equation (8)**, it is clear that the position of the LSPR peak is dependent on the refractive index of the surrounding medium ( $n_m$ ). It has been shown that the LSPR peak wavelength increases nearly linearly as the refractive index of the surrounding medium increases.<sup>[72]</sup> Therefore, the refractive index sensitivity  $S$  of a nanostructure is reported in nm of peak shift ( $d\lambda_p$ ) per refractive index unit ( $dn$ ) as shown in **equation (9)**:

$$S = \frac{d\lambda_p}{dn} \quad (9)$$

Using such nanostructures for LSPR sensing applications, demands careful selection of the nanostructure size, shape, and composition. In addition, the stability of the nanostructures in surrounding medium with different refractive indices need to be considered.

#### 1.4 Plasmonic Nanomaterials

As mentioned earlier, coinage metals such as Au, Ag, and Cu have been used in ancient cultures to add color to glass and ceramic artifacts.<sup>[17,66]</sup> This combined with theories developed for the metals, has spurred research to focus on these materials for plasmonic applications, and as a result in the past decades, there has been a tremendous advancement in the synthesis and characterization of these plasmonic noble metals nanomaterials. However, with the push for commercial plasmonic devices, such metals

might not be completely suitable and hence other plasmonic nanomaterials have also been explored. In the following sections, different classes/materials of plasmonic nanostructures will be discussed.

#### ***1.4.1 Metallic Nanostructures***

Au and Ag nanostructures have been widely explored for many applications since their LSPR responses lie within the visible range of the electromagnetic spectrum. By changing the size and shape of these nanostructures, the observed optical properties can vary significantly. For example, Au NPs have a characteristic red color, whereas Ag NPs have a characteristic yellow color.<sup>[81]</sup> Many synthetic strategies have been explored to tune their plasmonic responses to allow them to be used for various applications.<sup>[31,81-84]</sup>

Even though Au NPs remain the most studied nanomaterial for plasmonic applications, Ag NPs have been shown to offer better sensing sensitivity. Studies have shown that Ag NPs have higher refractive index sensitivity compared to Au NPs, which makes them a better option for refractive sensing applications.<sup>[85]</sup> Ag NPs provide a sharper LSPR peak compared to Au NPs because the imaginary component ( $\epsilon_i$ ) of their dielectric function is lower which results in less damping, higher scattering efficiency, and a narrower plasmon band.<sup>[72]</sup> In other words, the interband transition for Ag occurs at higher energies ( $\sim 3.8$  eV) whereas the interband transition for Au occurs at  $\sim 2.5$  eV.<sup>[86]</sup> Ag is considered to have the largest Q factor between 300-1200 nm, whereas the Q factor of Au is limited to wavelength longer than 500 nm.<sup>[66]</sup>

After many years of studying Au nanostructures, it has been shown that Au NPs are oxidatively stable and have high biocompatibility, which is critical for biomedical applications.<sup>[23,33,77,87,88]</sup> Recently, Au NPs have taken a critical role in the development of point-of-care testing for the detection of SARS-COV-2 based on a simple colorimetric change that can be easily seen visually without the requirement of expensive instrumentation.<sup>[89,90]</sup> This has shown that plasmonic Au nanostructures are still continually being used for a wide range of urgently relevant applications. On the other hand, Ag NPs are being commonly used as well, as it is estimated that ~320 tons of Ag NPs are manufactured every year and used in nanomedical imaging, biosensing, and food products.<sup>[91]</sup>

Despite their desired plasmonic properties, there are some disadvantages that can limit their use including cost, stability, and toxicity. Not only can the cost of Au and Ag limit large-scale synthesis, but also the cost associated with the synthetic routes and the materials used in the process. Additionally, since Au and Ag NPs colloidal suspension suffer from instability, capping or stabilizing agents such as surfactants, organic ligands, biomolecular ligands, and shell coating are required.<sup>[84]</sup> All of these factors can lead to higher cost systems with limited uses. Another issue is toxicity, as recent studies have shown that Ag NPs produce reactive oxygen species and free radicals which can lead to cell death in biological applications.<sup>[91]</sup> The toxicity of Ag NPs is dependent on the particle size (small NPs are more toxic), concentration, pH of the medium, synthesis route (green vs. non-green method), and cell exposure time.<sup>[91]</sup> Also, the large real component ( $\epsilon_r$ ) of their dielectric function limits their use in metamaterials manufacturing and transformation

optics devices.<sup>[92,93]</sup> Furthermore, Au and Ag NPs can soften at temperatures lower than their bulk melting points, leading to sintering and loss of plasmonic properties.

Although Ag and Au are the most used plasmonic nanomaterials, the LSPR is theoretically possible in any metal, alloy, or semiconductor with a negative  $\epsilon_r$  and a small  $\epsilon_i$  components of the dielectric constant. Researchers have been focusing on finding new plasmonic nanomaterials that are cost-effective, chemically stable with high melting points, and easy to fabricate.

Cu NPs have been investigated as an alternative to Au and Ag since Cu is more abundant and cost-effective. Cu NPs exhibit plasmonic properties in the visible and NIR range, more specifically between 500-900 nm, based on its Q factor.<sup>[66]</sup> The optical response is weaker compared to Au and Ag since the resonance occurs very close to the interband transition ( $\sim 2.1$  eV).<sup>[86]</sup> The position of the LSPR peak suggests that Cu NPs should be ideal for photovoltaics, photocatalysis, biosensing, and waveguide applications.<sup>[94]</sup> However, Cu NPs are highly susceptible to oxidation under ambient conditions and suffer from chemical instability which can hinder their potential use in LSPR applications. There have been efforts made to increase the stability of Cu NPs by removing the oxide layer using glacial acetic acid treatment or coating them with a polymer, carbon, or SiO<sub>2</sub>.<sup>[95-97]</sup> It has been shown that the removal of the copper oxides, results in a narrower and more intense LSPR peak.<sup>[95]</sup> These recent results could create new opportunities for using Cu NPs in solar enhancing applications, and nanoelectronics components.

Al NPs have also emerged as a potential alternative to noble metals due to the high natural abundance, low cost, and high bulk plasmon frequency ( $\sim 13$  eV) resulting in a LSPR response in the UV region.<sup>[98,99]</sup> The interband transition occurs at much lower energies ( $\sim 1.5$  eV) which means that Al NPs are a great candidate for UV applications compared to Ag, Au, and Cu.<sup>[62]</sup> Additionally, Al NPs have broad wavelength tunability, which allows the plasmon peak to be tuned from the UV to IR region by varying the NP size and shape.<sup>[100,101]</sup> Despite that, their utility has been restricted due to rapid surface oxidation, which can strongly affect the LSPR response and result in inconsistencies between calculated and experimental plasmon resonance energies.<sup>[102,103]</sup> Overcoming surface oxidation is a challenging feat; many efforts have focused on using organic surface passivation agents or metal coatings to protect the particles from rapid oxidation under ambient conditions.<sup>[103,104,104,105]</sup> Recently, it was shown that Al nanostructures can be stabilized by incorporating a Cu shell, which can also significantly enhance the plasmonic properties.<sup>[106]</sup> Regardless of their potential, the synthesis of Al nanostructures, especially in the size regimes of a few nanometers, can be difficult and, therefore, more detailed experimental exploration needs to be conducted.<sup>[103]</sup>

Furthermore, other materials such as Mg,<sup>[107,108]</sup> In,<sup>[109,110]</sup> Ga,<sup>[111,112]</sup> Pt,<sup>[113,114]</sup> Pd,<sup>[115,116]</sup> Sn,<sup>[117,118]</sup> Tl,<sup>[117]</sup> Sb,<sup>[118,119]</sup> Pb,<sup>[117]</sup> Bi,<sup>[119,120]</sup> and Rh<sup>[121,122]</sup> can support plasmon resonances in the UV spectral region but there has been far less experimental work with these materials. Alkali metals such as Na, K, and Li have been shown to have low losses that are lesser than or comparable to those of Ag.<sup>[62,123]</sup> However, their plasmonic potential has not been explored experimentally due to their extreme reactivity in air and water.<sup>[62,123]</sup>



Nonetheless, metallic nanostructures are constantly being explored and their utilization in different applications has been growing drastically.

#### ***1.4.2 Semiconductors and Transparent Conducting Oxides***

In recent years, it was discovered that plasmon resonances are not fundamentally limited to metals and in fact semiconductors and transparent conducting oxides (TCOs) with sufficient number of free conduction electrons could sustain the LSPR.<sup>[63,124–126]</sup> Due to their low-cost and abundancy compared to noble metals, these materials have attracted considerable attention in many applications such as photocatalysis, SERS, optical detection, and photothermal applications.<sup>[127]</sup>

In order to qualify as a low-loss plasmonic material, the bandgap and plasma frequency of the semiconductor must be larger than the frequency spectrum range of interest.<sup>[62,63]</sup> This is because the bandgap corresponds to the onset of the interband transition which can increase optical losses.<sup>[63,125]</sup> The tunability of the bandgap of semiconductors requires heavy doping and the plasma frequencies observed are much lower than those of metals.<sup>[62,63,125]</sup> The heavy doping increases the carrier concentration of semiconductors which allows their optical properties to become metallic in the desired wavelength range.<sup>[63]</sup> Semiconductors such as tungsten oxides, molybdenum oxides, and copper chalcogenides have free carrier density of  $10^{21}$  to  $10^{22}$   $\text{cm}^{-3}$  resulting in LSPR in vis-NIR.<sup>[126–129]</sup> Although, these materials display favorable advantages, the heavy doping can raise concerns about the solid solubility limit, the fraction of active dopant, and doping compensation effects. In general, doping mechanism is complicated and not all dopant

atoms succeed in contributing free charge carriers. Additionally, high doping levels can significantly degrade carrier mobility due to an increase in impurity scattering and as a result losses will increase.<sup>[63]</sup>

Transparent conductive oxides (TCOs) have also been explored due to their optical transparency and high IR conductivity and reflectivity. TCOs exhibit no interband transitions in the IR-visible regions and their large bandgap results in fewer free carriers.<sup>[63,80]</sup> The majority of losses arise from intraband transitions, however due to the lower carrier concentration and available states for scattering to occur, these losses are lower in the IR region compared to metals.<sup>[80]</sup> Indium-tin-oxide (ITO) a transparent conducting oxide that has been widely studied in the field of optoelectronics have shown to be a potential plasmonic material in the NIR region.<sup>[80]</sup> Since ITO is a non-stoichiometric compound, its optical properties are largely dependent on the growth and deposition processes and annealing conditions. Therefore, achieving high quality films with low losses can be challenging and the deposition temperature, oxygen partial pressure, and dopant concentration must be optimized. This also applies to other conductive oxides that have been explored such as aluminum-zinc-oxide (AZO) and gallium-zinc-oxide (GZO). Naik *et al.* have compared the  $\epsilon_r$  and  $\epsilon_i$  components of the dielectric function of different TCOs to Ag and Au as shown in **Figure 6A, B**. This has shown that TCOs have low carrier concentrations that allows them to exhibit losses nearly five times smaller than Ag in the near-IR (as shown in **Figure 6B**).<sup>[63]</sup> Aside from oxide semiconductors, III-V semiconductors (i.e., GaAs, GaN, InP) have also been explored as potential plasmonic candidates in the NIR and optical spectral ranges.<sup>[62]</sup> These materials exhibit wide

tunability in the optical bandgap which can be controlled by varying the composition of their ternary and quaternary compounds.<sup>[80]</sup> However, heavy doping is still a problem that needs to be addressed when considering these materials as alternative options to noble metals.<sup>[62]</sup> Nonetheless, TCOs have shown to be good alternatives to noble metals in the near to mid-IR region which can be suitable for biological applications, metamaterial devices, and photonic devices.<sup>[62,130]</sup>

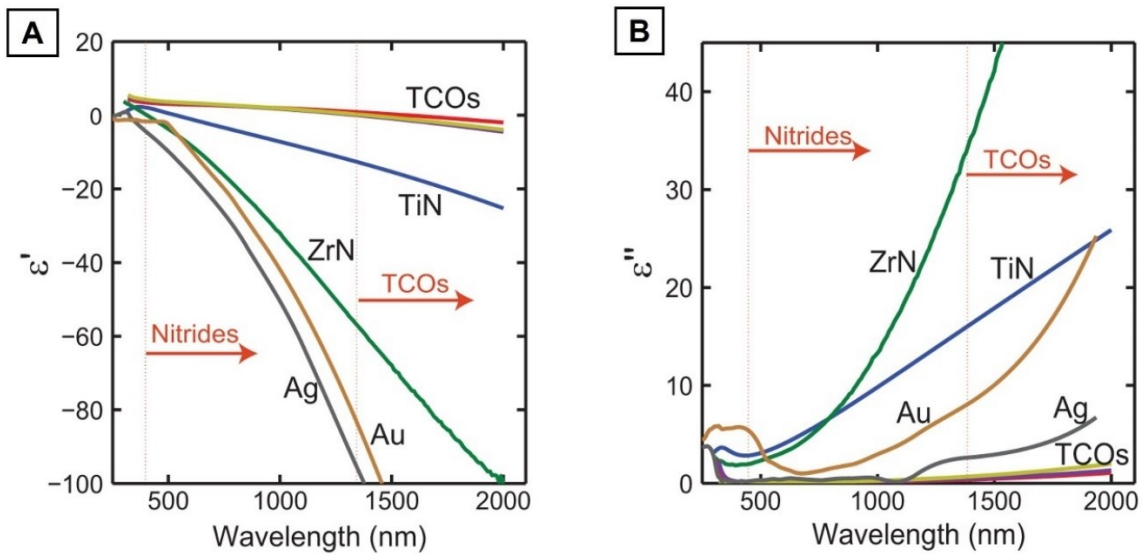


**Figure 6:** Comparison of (A) real component, (B) imaginary component of the dielectric function of metals (Ag, Au), TCOs (AZO, GZO, ITO), and nitrides (TiN, ZrN). The arrows show the ranges over which TCOs, and nitrides are metallic. Reproduced with permission from reference <sup>[80]</sup>. Copyright 2011, Optica Publishing Group.

### 1.4.3 Transition Metal Nitrides

Refractory materials have high chemical and thermal stability allowing them to be used in applications requiring high temperatures.<sup>[63]</sup> Refractory materials such as transition metal nitrides (TMNs) are predicted to have a plasmonic responses in the visible/NIR region owing to their high carrier concentration ( $10^{22}$ - $10^{23}$  cm<sup>-2</sup>), along with low interband losses.<sup>[68,131]</sup> The losses observed for TMNs are higher than metallic NPs due to larger  $\epsilon_i$  values as shown in **Figure 6B**, however, in the regions where interband losses are absent, the losses are mainly due to Drude damping (losses arising from free carriers).<sup>[80]</sup> Metallic nanostructures tend to experience high Drude damping due to structural imperfections and surface roughness, which can be minimized in crystalline TMNs.<sup>[132]</sup> Thus, in the regions where interband losses are absent, TMNs can be a great alternative to metallic nanostructures.<sup>[80]</sup> TMNs show a combination of metallic and covalent properties which make them useful for many applications. Like metals they have high electrical conductivity, their covalent properties include hardness and high melting point.<sup>[133]</sup> In the last decade, it has also been proposed that the properties of TMNs can be tuned by varying the material's composition, size, and shape.<sup>[134]</sup> Additionally, they can sustain high temperatures without succumbing to sintering and exhibit exceptional chemical stability.<sup>[69,134-136]</sup> However, many of the plasmonic behavior reported for TMNs were predominantly based on computational studies.<sup>[68,69,134-136]</sup>

Many of the initial computational and experimental studies focused primarily on thin films of titanium nitride (TiN). Hibbins *et al.* reported the first study of the optical dielectric function of thin TiN<sub>x</sub> films and indicated that the stoichiometric ratio of Ti to N

should be close to 1 for the films to be metallic in nature.<sup>[137]</sup> Years later, Cortie *et al.* showed that the dielectric properties of  $\text{TiN}_{1-x}$  films depend upon stoichiometry and are favorable for plasmon resonance phenomena in the mid-visible to NIR range of the spectrum when  $x \sim 0$ .<sup>[138]</sup> The optical extinction peaks of isolated TiN cubes ranging between 10-50 nm were predicted to be between 500-600 nm, where the peak intensity increases and red-shifts as the size of the cubes increased.<sup>[138]</sup> Chen *et al.* investigated the excitation of surface plasmon waves of various thickness of TiN films prepared by sputtering and compared the responses with numerical simulations.<sup>[139]</sup> It was found that TiN films performed better than Au films and were found to be a plausible solution for surface plasmon wave applications in the red and IR spectral ranges.<sup>[139]</sup> Comparison studies between TiN and Au have been conducted by Guler *et al.* to prove that TiN has field enhancement and enhanced local heating in the biological transparency window (where absorption of light by biological tissues is minimal) comparable to Au.<sup>[140,141]</sup> These studies reveal the promising aspect of using TiN not only in biological applications but in several applications ranging from catalysis to heat-assisted magnetic recording.<sup>[141]</sup>

Additional studies have investigated the structure and electronic properties of other mononitride films such as ZrN and HfN.<sup>[80]</sup> Theoretical calculations have predicted that ZrN provides resonance responses very similar to Au with slightly higher near-field intensities and better small-particle performance which suggests that ZrN is an ideal alternative to Au.<sup>[140]</sup> Meng *et al.*, have shown that the optical properties of ZrN can be tuned by tailoring its nitrogen content ( $\text{ZrN}_x$ ).<sup>[142]</sup> It was reported that the optical properties of  $\text{ZrN}_x$  films with  $x$  ranging from 0.98 to 1.35 will evolve from metallic behavior to

dielectric behavior.<sup>[142]</sup> This change in behavior reveals the importance of controlling the Zr to N ratio, as the addition of N will result in the depletion of free electrons.<sup>[142]</sup> HfN is less frequently studied compared to TiN and ZrN, nonetheless, there were a few studies that investigated the electrical, mechanical, and metallic properties of HfN films.<sup>[143–145]</sup>

The electronic structure calculations performed on TiN, ZrN, and HfN have shown that the  $E_F$  is located within the metal d-band which contributes to their pseudo-metallic properties.<sup>[68]</sup> The  $\epsilon_i$  and  $\epsilon_r$  components of the dielectric functions of these TMNs are similar to those of noble metals, making them promising candidates for plasmonic applications, as shown in **Figure 7A, B**. To assess the performance of certain TMNs compared to Au and Ag, the Q factor was calculated, as shown in **Figure 7C**. Based on the Q factor, it showed that Ag outperforms all the other materials, however, ZrN and HfN perform better than Au in the visible region in addition to their advantages in terms of chemical stability and cost, making TMNs the more ideal choice.<sup>[68]</sup> Even though ZrN and HfN exhibit higher Q factor than TiN, they have received far less attention than TiN. Overall, the TMNs have shown promise in overcoming many issues associated with metallic NPs such as better chemical and thermal stability, lowering-cost, and most importantly, greater compatibility with standard silicon manufacturing processes which could allow easy integration of silicon electronics with plasmonics.<sup>[132]</sup> While the dielectric properties of the thin films of TMNs have been explored to some extent, experimental investigations of the plasmonic behavior of free-standing TMN NPs are even more scarce. Therefore, our group was interested in exploring methods to synthesize free-standing

plasmonic TMNs NPs, starting with an intensive literature search to determine the different methods reported to date.

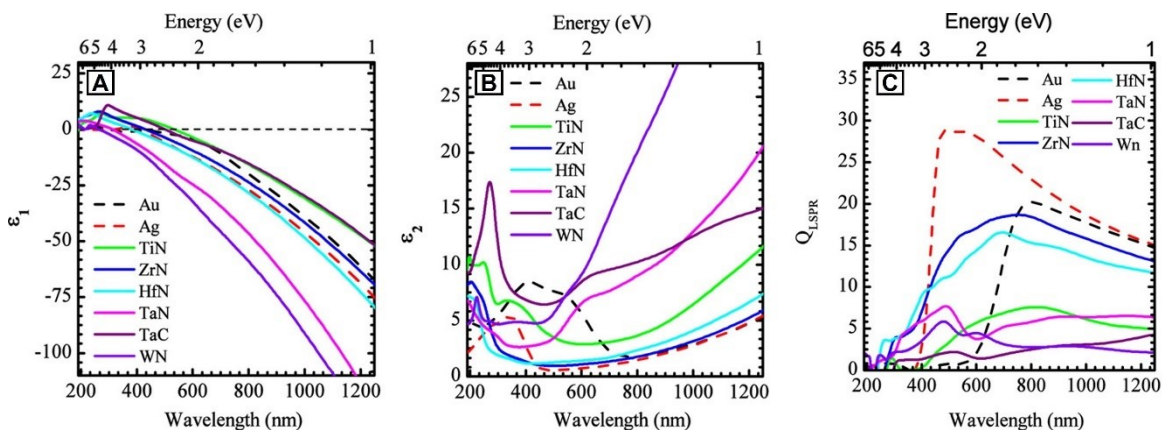


**Figure 7:** Comparison of calculated (A) real, (B) imaginary parts of the dielectric function, and (C) LSPR Q factor of selected refractory materials with Au and Ag as shown in dashed black and red lines, respectively. Reproduced with permission from reference [68]. Copyright 2016, American Chemical Society.

### 1.5 Synthesis of Plasmonic Transition Metal Nitrides Nanomaterials

*This author wishes to clarify her contribution to the research described in Section 1.5 of this thesis document.* This section discusses the synthetic methods to prepare plasmonic free-standing TMN NPs. Part of this section was published in Chemistry-A European Journal. Dr. Yashar E. Monfared and I were co-first authors in this minireview. I wrote the sections highlighting the different synthetic routes for the synthesis of TMNs, while Dr. Yashar E. Monfared wrote the introductory section of the review. **(Reference:** R. A. Karaballi\*, Y. E. Monfared\*, M. Dasog, Overview of Synthetic Methods to Prepare Plasmonic Transition-Metal Nitride Nanoparticles. *Chemistry-A European Journal*, **2020**, 26 (39), 8499-8505. Reprinted by permission of John Wiley & Sons, Inc.)

The first theoretical analysis of the LSPR of TiN NPs was conducted by Quinten where the optical spectra was calculated using the Mie theory for monodispersed spherical particles.<sup>[146]</sup> Based on these studies, it was predicted that TiN colloidal solution would have a blue color, and the extinction band would be broad compared to that of Ag and Au.<sup>[146]</sup> A few years later, Reinholdt *et al.* showed that irradiating a pressed TiN powder target with a Neodymium-doped Yttrium Aluminum Garnet (Nd:YAG) laser formed cuboid-shaped particles by using transmission electron microscopy (TEM) as shown in **Figure 8A**.<sup>[147]</sup> The particles were crystalline and below 10 nm in size, with a relatively broad size distribution. The composition of TiN NPs was analyzed by using secondary ion mass spectrometry and Electron Energy Loss Spectroscopy (EELS) which indicated mostly the presence of Ti and N with partial oxidation occurring upon exposure to ambient atmosphere. The LSPR maximum was found to vary between 1.65 (751 nm) and 1.79 eV (693 nm).<sup>[147]</sup> The results obtained contradicted the predictions made by Cortie *et al.* where the plasmon peak was more blue-shifted.<sup>[138]</sup> This discrepancy could be due to the combined effects of the dielectric function of the surrounding matrix and/or agglomeration of the individual NPs.<sup>[138]</sup> A similar method was used to prepare, for the first time, plasmonic ZrN NPs by irradiating ZrN target with a Nd:YAG laser, while N<sub>2</sub> was fed as a seed gas to prevent oxidation.<sup>[148]</sup> Pseudospherical particles with an average diameter of about 6 nm were obtained, as shown in **Figure 8B**. The NPs were determined to be crystalline from Selected Area Electron Diffraction (SAED) analysis of the TEM data. The LSPR maximum was found to be around 1.9 eV (653 nm).<sup>[148]</sup> The calculated LSPR values were different from the experimental data; this was hypothesized to be due to surface oxidation of the ZrN NPs.



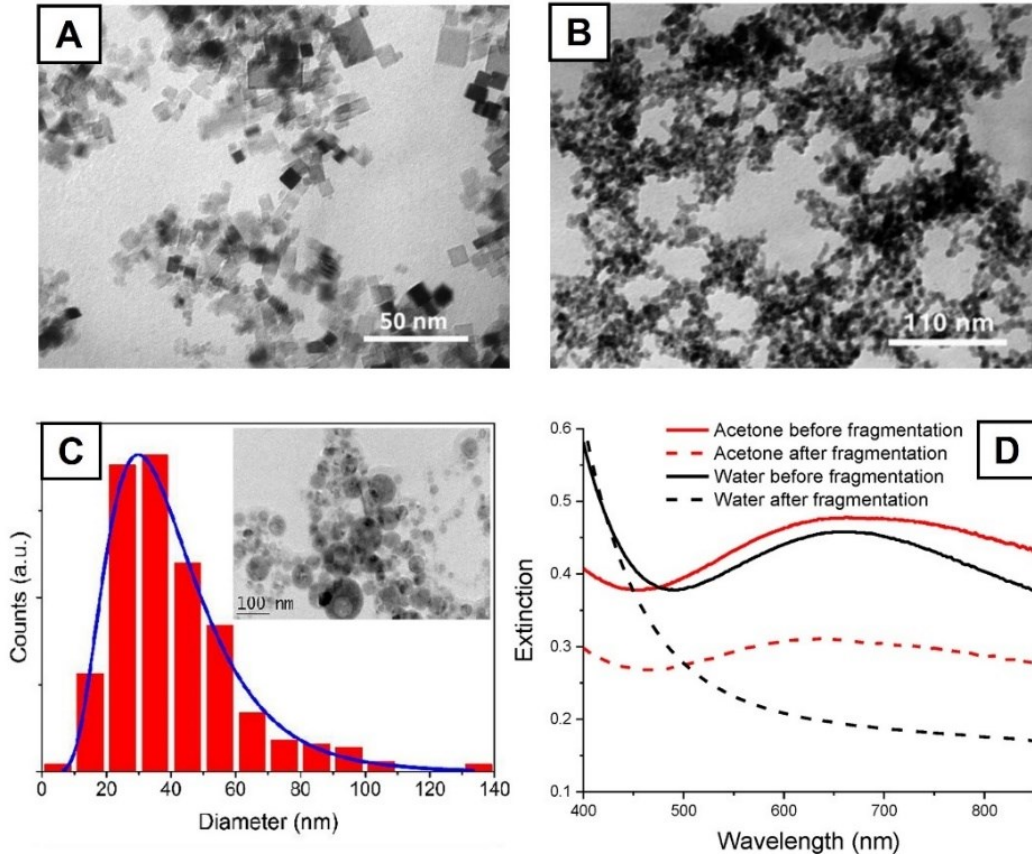


**Figure 8:** (A) TEM image of TiN particles obtained from laser ablation of pressed TiN powder target. Reproduced with permission from reference <sup>[147]</sup>. Copyright 2004, Springer. (B) TEM image of ZrN NPs obtained from laser ablation of ZrN target. Reproduced with permission from reference <sup>[148]</sup>. Copyright 2003, Springer. (C) Particle size distribution and TEM image, and (D) extinction spectra of TiN NPs. Reproduced with permission from reference <sup>[149]</sup>.

More recently, the synthesis of plasmonic TiN where a hot-pressed TiN target was irradiated with a Ytterbium-doped Potassium Gadolinium Tungstate (Yb:KGW) laser (1025 nm) has been reported.<sup>[149]</sup> This resulted in spherically shaped (**Figure 8C**) polycrystalline TiN NPs with a mean diameter of 25 and 40 nm if laser pulse energy of 10

and 100  $\mu\text{J}$ , respectively, were used.<sup>[149]</sup> The colloidal suspensions of TiN NPs had a surface potential of -30 mV and were found to be stable for months in water and acetone. A broad LSPR with a maximum near 700 nm was observed for TiN NPs in both water and acetone, as shown in **Figure 8D**.<sup>[149]</sup> To further reduce the particle size, a colloidal solution of TiN NPs was irradiated with the laser in the absence of the Ti target. To eliminate surface oxidation, argon (Ar) gas was used to remove dissolved oxygen. The fragmentation in water resulted in the disappearance of the LSPR due to oxidation and formation of  $\text{TiO}_x$ , whereas a blueshift in the LSPR position to 640 nm was observed in acetone, which was attributed to the reduction of particle size (**Figure 8C**).<sup>[149]</sup> The biocompatibility of TiN NPs was also assessed by performing *in vitro* studies where TiN NPs were incorporated into human microvascular endothelial cells and human cancer cells. The assay showed that TiN had low toxicity and no accumulation in lysosomes, or nuclei, and no other intracellular structure was observed.<sup>[149]</sup>

Direct current arc plasma allows the synthesis of nanopowders, including those composed of refractory materials.<sup>[150]</sup> The high temperature of the plasma enables rapid evaporation of the target material and increases chemical reactivity. As the vapor travels away from the hot regions of the plasma, rapid cooling results in a supersaturated state, which leads to nucleation and growth of NPs.<sup>[151]</sup> Arc plasma was used to synthesize TiN NPs by striking Ti metal with a tungsten tip, which resulted in evaporation of the metal to further react with  $\text{N}_2$  in the reaction chamber.<sup>[152]</sup> The NPs are deposited onto the chamber wall and physically collected and suspended in water to generate the solution of NPs. TEM images showed the formation of cubic-shaped NPs with an average diameter of 10 nm, as

shown in **Figure 9A**.<sup>[152]</sup> Powder X-ray diffraction (XRD) analysis showed the product to be crystalline. The X-ray photoelectron spectroscopy (XPS) data indicated that the arc plasma resulted in carbon contamination and the presence of oxides and oxynitrides on the surface of the TiN NPs.<sup>[152]</sup> The extinction spectrum showed broad absorbance with a LSPR maximum at 726 nm (**Figure 9B**).<sup>[152]</sup> The authors also demonstrated that varying the arc current could significantly influence the properties of the TiN NPs. Increasing the arc current from 100 to 210 A, increased the particle size from 6.3 to 15 nm. The cubic nature of the NPs also increased with increasing current.<sup>[152]</sup>

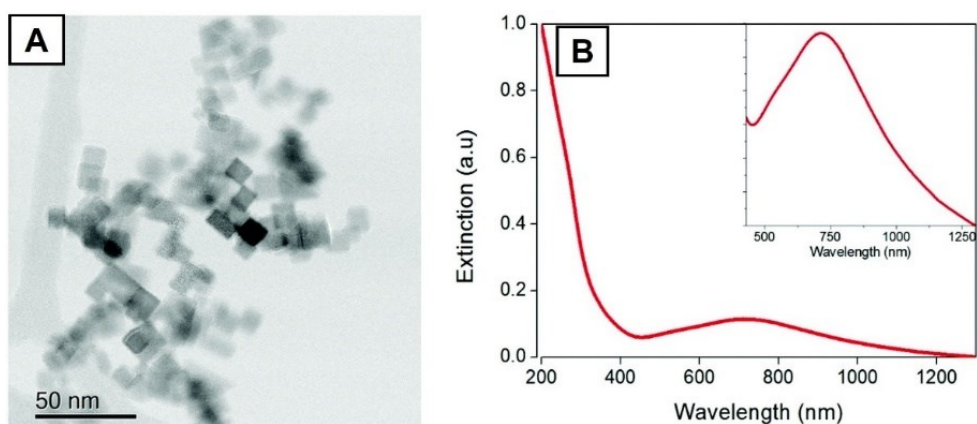


**Figure 9:** (A) TEM image and (B) extinction spectrum of TiN NPs prepared via the arc plasma method. Reproduced with permission from reference <sup>[152]</sup>. Copyright 2018, the Royal Society of Chemistry.

Non-thermal plasma synthesis allows the fabrication of high-purity NPs with a narrower size distribution.<sup>[153]</sup> The exact mechanism of nucleation and the growth process of NPs in the nonthermal plasma method depends upon the precursor and the synthesis conditions.<sup>[153]</sup> Plasmonic TiN NPs were prepared by reacting titanium tetrachloride (TiCl<sub>4</sub>) and ammonia (NH<sub>3</sub>) in a continuous-flow nonthermal plasma reactor.<sup>[154]</sup> The

particle size and composition were controlled by changing the amount of  $\text{NH}_3$  supplied. Using this method, crystalline TiN NPs with a cubic shape were produced at a rate of about 50 mg/h (**Figure 10A**).<sup>[154]</sup> The crystallite size increased from 4 to 8 nm as the flow rate of  $\text{NH}_3$  changed from 6 to 1.5 sccm. Furthermore, TiN NPs prepared at a higher flow rate (6 sccm) exhibited a broad extinction spectrum, and the LSPR maximum blue-shifted with decreasing flow rate (**Figure 10B**).<sup>[154]</sup> XPS analysis showed that the NPs prepared at higher flow rates (smaller crystallites) mostly consisted of Ti oxynitrides, whereas at slower flow rates (bigger crystallites) the NPs were composed of TiN with small amounts of oxide, leading to a narrower extinction spectrum. TiN NPs were found to be susceptible to oxidation if annealed in air, which caused a redshift in the LSPR position.<sup>[154]</sup> Replacing  $\text{TiCl}_4$  precursor with tetrakis(dimethylamino) titanium (TDMAT) yielded TiN NPs exhibiting a narrower extinction band (**Figure 10C**).<sup>[155]</sup> The NPs were uniform and ranged from 6 to 8 nm in size. XPS analysis showed the presence of oxide and oxynitride on the NP surface; however, the LSPR peak position did not change upon storing solutions of TiN NPs in air for several days.

Nonthermal plasma synthesis was used to prepare free-standing plasmonic ZrN NPs.<sup>[156]</sup> Zirconium tetrachloride ( $\text{ZrCl}_4$ ) was reacted with  $\text{NH}_3$  to yield a crystalline product at a rate of about 20 mg/h. TEM analysis showed the particles to be spherically shaped, with an average size of 8.2 nm, as shown in **Figure 10D**.<sup>[156]</sup> The extinction spectrum of ZrN NPs showed the LSPR maximum at 585 nm (**Figure 10E**). Simulations showed that the LSPR position is reflective of the presence of an oxide shell. To prevent surface oxidation, ZrN NPs were coated with about a 2 nm amorphous silicon oxynitride shell through the plasma method (**Figure 10G**).<sup>[156]</sup> The LSPR maximum blue-shifted to

527 nm after the coating (**Figure 10E**) and had better agreement with the calculated extinction spectrum as shown in **Figure 10F**. Silicon oxynitride coated ZrN were also found to be stable under air annealing up to 400 °C.<sup>[156]</sup>

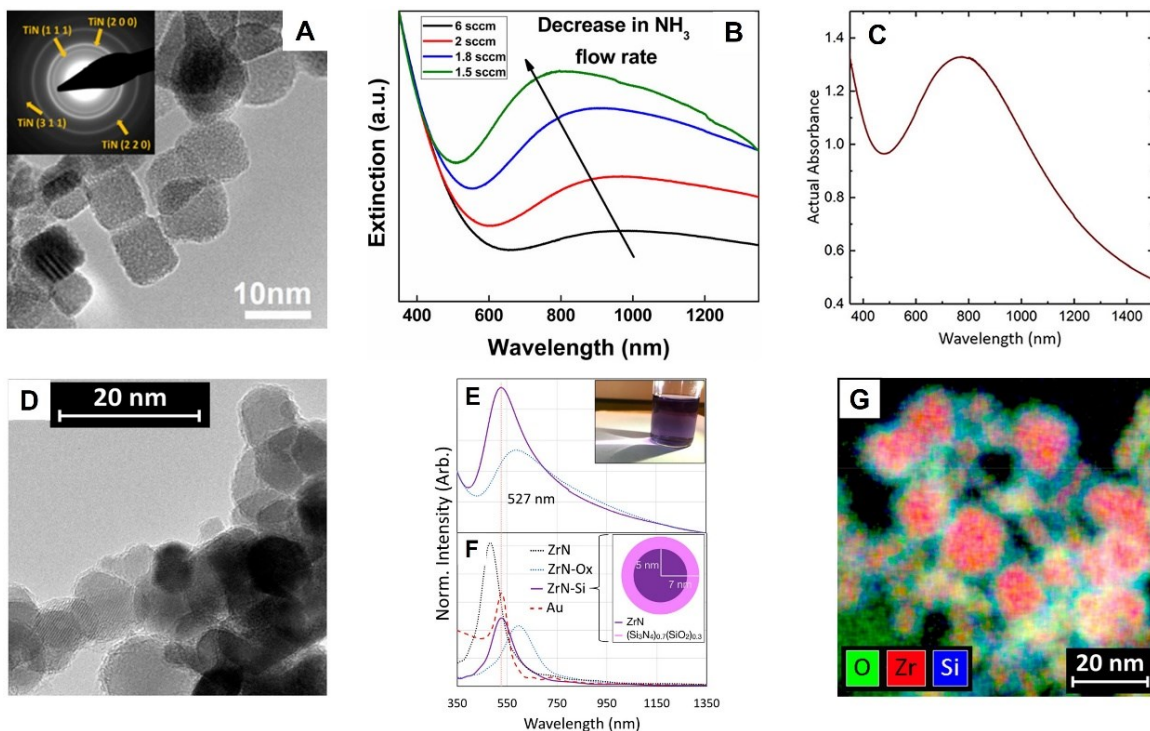


**Figure 10:** (A) TEM image and SAED pattern and (B) extinction spectra of TiN NPs prepared using the nonthermal plasma method with  $\text{TiCl}_4$  and  $\text{NH}_3$  as precursors. Reproduced with permission from reference <sup>[154]</sup>. Copyright 2017, American Chemical Society. (C) Absorbance spectrum of TiN NPs prepared by using the nonthermal plasma method with TDMAT and  $\text{NH}_3$  as precursors. Reproduced with permission from reference <sup>[155]</sup>. Copyright 2018, American Chemical Society. (D) TEM image of bare ZrN NPs prepared by the nonthermal plasma method, (E) experimental and (F) calculated extinction spectra of bare and silicon oxynitride coated ZrN NPs, and (G) electron microscopy-energy-dispersive X-ray mapping of silicon oxynitride coated ZrN NPs, showing elemental composition. Reproduced with permission from reference <sup>[156]</sup>. Copyright 2019, American Chemical Society.

Even though non-thermal plasma synthesis has been successfully used to prepare TiN and ZrN NPs, these syntheses require the use of corrosive precursors and specialized equipment that can be cost and infrastructure intensive. Many TMNs have been synthesized by reacting metal oxide or halides with a N source such as  $\text{Li}_3\text{N}$ ,  $\text{Ca}_3\text{N}_2$ ,  $\text{NaN}_3$ ,  $\text{N}_2$ , or  $\text{NH}_3$  at high temperatures.<sup>[157–165]</sup> However, those studies have not investigated the plasmonic properties of the synthesized material. Recently, TiN NPs have been generated through nitridation of  $\text{TiO}_2$  with  $\text{NH}_3$ .<sup>[166]</sup> The crystallite size (as determined by XRD) of TiN increased from 15 to 35 nm when the reaction temperature was changed from 650 to 1000 °C.<sup>[166]</sup> An extinction peak between 700 and 1300 nm, corresponding to the LSPR, was observed (**Figure 11C**).<sup>[166]</sup> Nitriding for longer times and temperatures between 650 and 750 °C resulted in an optimum extinction peak. Coating the  $\text{TiO}_2$  precursor with  $\text{SiO}_2$  was shown to potentially prevent aggregation during the nitridation process.<sup>[166]</sup> Retention of the  $\text{SiO}_2$  shell and particle morphology during high-temperature nitridation was shown through TEM analysis (**Figure 11A, B**). The LSPR was found to be more intense and spectrally narrower in the presence of the  $\text{SiO}_2$  shell (**Figure 11C**). Bare TiN NPs in close proximity of each other can couple, leading to the extinction peak broadening and shifting to longer wavelengths. The  $\text{SiO}_2$  shell acts as a spacer and prevents such plasmonic coupling. Later, it was demonstrated that  $\text{NH}_3$  nitridation led to the formation of smaller TiN crystallites than those of the parent  $\text{TiO}_2$ .<sup>[167]</sup> The best photothermal performance and biocompatibility were obtained with 10 wt %  $\text{SiO}_2$ -coated TiN NPs.

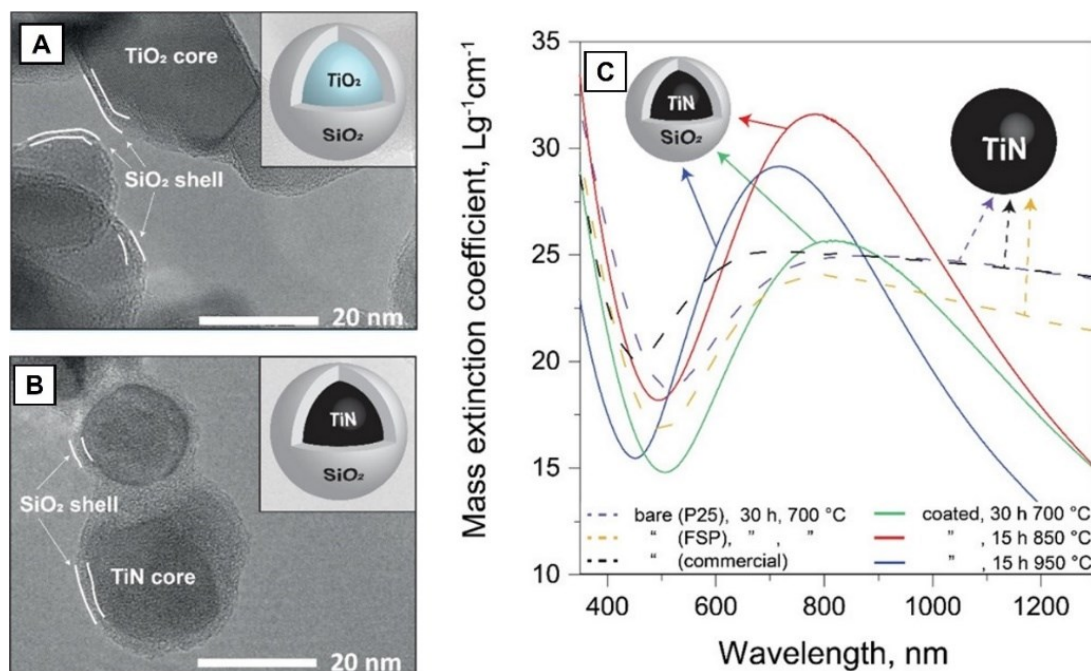


**Figure 11:** TEM images of core-shell TiO<sub>2</sub>-SiO<sub>2</sub> NPs (A) before and (B) after nitridation with NH<sub>3</sub>. (C) Extinction spectra of bare and SiO<sub>2</sub>-coated TiN NPs. Reproduced with permission from reference <sup>[166]</sup>. Copyright 2019, American Chemical Society.

Our group was interested in synthesizing free-standing TMNs using solid-state metathesis reaction and investigating the plasmonic properties of the TMNs obtained. Overall, solid-state metathesis reactions are straightforward, complex infrastructure is not required, precursors used are readily available, good atom economy is obtained, and crystalline products are formed.<sup>[168]</sup> However, some of the disadvantages include the need for high temperature, long reaction time, formation of undesirable phases, inability to monitor the reaction progress in-situ, and difficulty in sample purification. Therefore, solid-state metathesis reactions require a lot of optimizations to overcome their drawbacks.

## 1.6 Scope of Thesis

This thesis consists of eight chapters. In this Chapter (Chapter 1), a detailed literature review of the important concepts relevant to this project including nanomaterials, plasmonic materials, theory of plasmonic properties, and parameters affecting the plasmonic response is provided. Chapter 2 provides a detailed description of the theory which underlines the major experimental techniques used in this work including TEM, SEM, EELS, XRD, XPS, UV-vis spectroscopy, and DLS. A detailed description of the experimental conditions and procedures, the photothermal transduction efficiency calculations, and details regarding the simulations and computational work theory are also described. Chapter 3 discusses the synthesis and characterization of group IVB TMN NPs. This chapter was published in *Angewandte Chemie*. Chapter 4 discusses the photothermal properties by studying the influence of LED power density on the photothermal properties of group IVB TMN NPs dispersed in water and its comparison to Au NRs. This chapter was recently published in *Langmuir*. Chapter 5 discusses the long-term stability and oxidative stability of group IVB TMN NPs. Chapter 6 discusses the synthesis and characterization of plasmonic dichromium nitride ( $\text{Cr}_2\text{N}$ ), and its photothermal properties. Chapter 7 discusses the preparation of group IVB TMN NPs using solid-gas route by reacting the metal oxide precursors with Mg metal under the flow of  $\text{N}_2$  gas. Chapter 8 summarizes the most important results obtained from this work and discusses future work for this project.



## Chapter 2: Experimental Methods and Techniques

### 2.1 Introduction

Since transition metal nitride (TMN) NPs are a new class of plasmonic materials, extensive characterization of these nanomaterials is required to establish their properties. Different characterization methods have been utilized to study the structure, composition, surface charge, and optical properties of these plasmonic materials. In this chapter, powder X-ray diffraction (XRD), X-ray photoelectron spectroscopy (XPS), transmission electron microscopy (TEM), scanning electron microscopy (SEM), electron energy loss spectroscopy (EELS), Ultraviolet and visible (UV-vis) absorbance spectroscopy, and dynamic light scattering (DLS) are discussed in detail.

Many of the techniques used to characterize the NPs are based on elastic and inelastic interaction of electrons with the sample which can provide useful information about the material at the atomic level. In 1925, the first theory stating that electrons had wave-like characteristics with a wavelength substantially less than the visible light was developed by Louis de Broglie.<sup>[169]</sup> This can be represented by **equation (10)**:

$$\lambda = \frac{h}{p} = \frac{h}{mv} \quad (10)$$

where  $\lambda$  is the wavelength of the particle,  $h$  is Planck's constant ( $6.626 \times 10^{-34} \text{ m}^2 \text{ kg s}^{-1}$ ),  $p$  is momentum,  $m$  is mass, and  $v$  is the velocity of the moving particle. This equation indicates that the resolution power of electron microscopes, which is related to the electrons' wavelength, can be controlled by changing the accelerating voltage which is related to the electron velocity. **Figure 12** shows the many types of electron-sample

interactions and from these interactions, sample information such as composition, morphology, and crystallinity can be gathered.

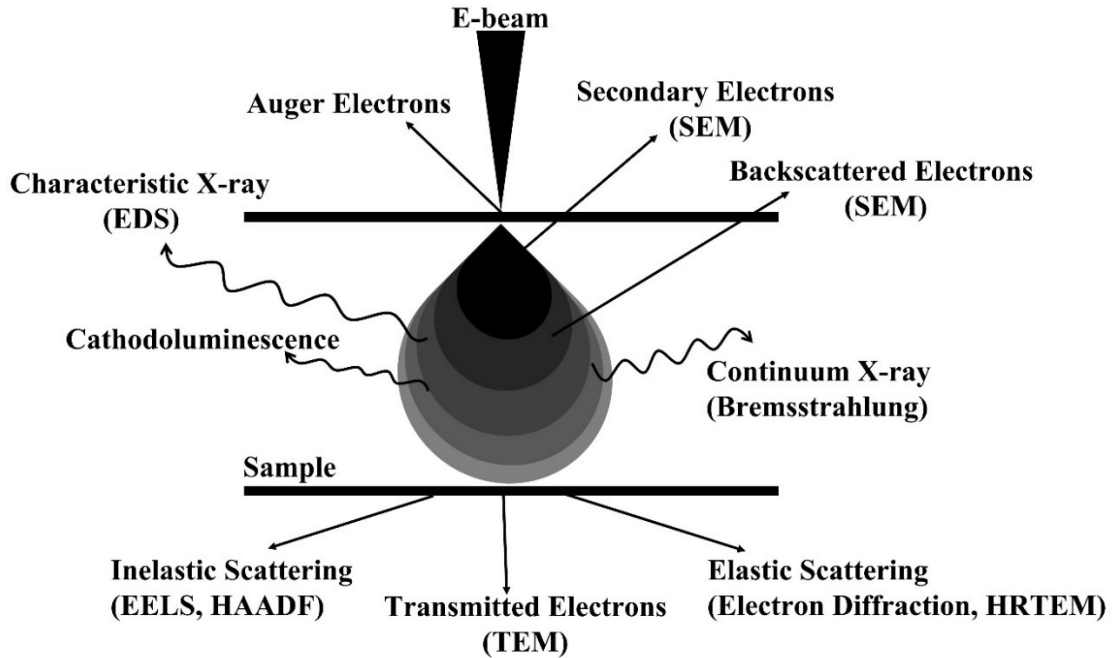


**Figure 12:** Schematic illustration of the interaction of an electron beam with atoms of a sample and the consequent processes. Adapted from reference <sup>[170]</sup>.

## 2.2 Transmission Electron Microscopy

Electron microscopes were developed to overcome the limited image resolution of light microscopes, which is imposed by the wavelength of the visible light. One of the widely used electron microscopy techniques is TEM which involves the use of an electron gun to produce an electron beam via thermionic emission.<sup>[171–173]</sup> The electron beam is focused using a series of lenses before reaching the sample, all operating in vacuum.<sup>[169]</sup> Condenser lenses are present along the column and their role is demagnification of the

electron beam.<sup>[171–173]</sup> The sample stage is where the sample can be held and inserted or withdrawn from the microscope.

The imaging system contains three lenses that together produce a magnified image of the sample on either a fluorescent screen, on photographic film, or the monitor screen of an electronic camera system. The three lenses present are the objective lens, intermediate lens, and projector lens.<sup>[172,173]</sup> The objective lens is the most important in TEM because it is the closest to the sample which is used primarily to focus and magnify the image. The intermediate lens magnifies the image coming from the objective lens. The projector lens further magnifies the image and projects it to produce an image. The design of all the imaging lenses determines the spatial resolution that can be obtained using TEM.<sup>[172,173]</sup> The electron image is then converted to a visible form and saved using a charge-coupled diode (CCD) camera.<sup>[173,174]</sup> **Figure 13** shows a schematic illustration of the TEM components.

There are two types of acquiring TEM images including bright-field and dark-field. In bright-field TEM, the transmitted unscattered electrons are selected with the aperture, and the scattered electrons are blocked.<sup>[175]</sup> Therefore, the areas that are crystalline or have high mass materials will appear dark since the unscattered beam is selected. In dark-field TEM, the unscattered electrons are excluded from the aperture, and the scattered electrons are selected instead.<sup>[175]</sup> Hence, the sample will appear bright white, while the area around the sample will appear black. Both types can be used to characterize the size and morphology of the sample, however, bright-field TEM is commonly used.<sup>[175]</sup> TEM can not only be used for determining the size and shape of specimens, but it can also be used to characterize samples at an atomic level. This is referred to as high-resolution TEM

(HR-TEM) where the objective lens aperture is changed to allow for the selection of more than two beams.<sup>[176]</sup> The HR-TEM or phase contrast image results from the multiple beam interference between the forward-scattered and diffracted electrons from the specimen.<sup>[177,178]</sup>

The inelastic electrons obtained as a result of the incident beam interacting with the sample can also be analyzed using TEM to provide information on the electronic structure of the specimen atom, their bonding, the nearest neighbor distribution, and their dielectric response.<sup>[179]</sup> This method is referred to as EELS, where the inelastic interactions measured could be a result of phonon excitations, inter- and intra-band transitions, inner-shell ionization, or plasmon excitations.<sup>[179]</sup> The EELS spectrum obtained contains several regions including zero-loss peak, low-loss region, and high-loss region.<sup>[170,180]</sup> The EELS spectrum is dominated by the zero loss peak, which contains electrons that have been transmitted through the sample without any detectable energy loss. This can include unscattered, elastically scattered, or inelastically scattered electrons which have lost minimal energy that cannot be distinguished from unscattered electrons due to limited spectral resolution of the instrument.<sup>[173]</sup> The low-loss region is mostly dominated by bulk plasmon excitation, however other outer shell electron excitation peaks including electron-hole pair, bandgap excitations, valence electron transitions into the conduction band, and phonon or surface plasmon excitation can be detected.<sup>[173,181]</sup> The high-loss region is the core-loss region where primary beam electrons have lost energy to excite core-shell electrons in the sample, this provides characteristic binding energy of the excited electron.<sup>[173]</sup> EELS can also be measured using scanning electron transmission spectroscopy (STEM) which is similar to TEM, except the beam is focused at a large angle

and is converged into a focal point and the transmitted signal is collected as a function of beam location as it is rastered across the sample.<sup>[173]</sup>

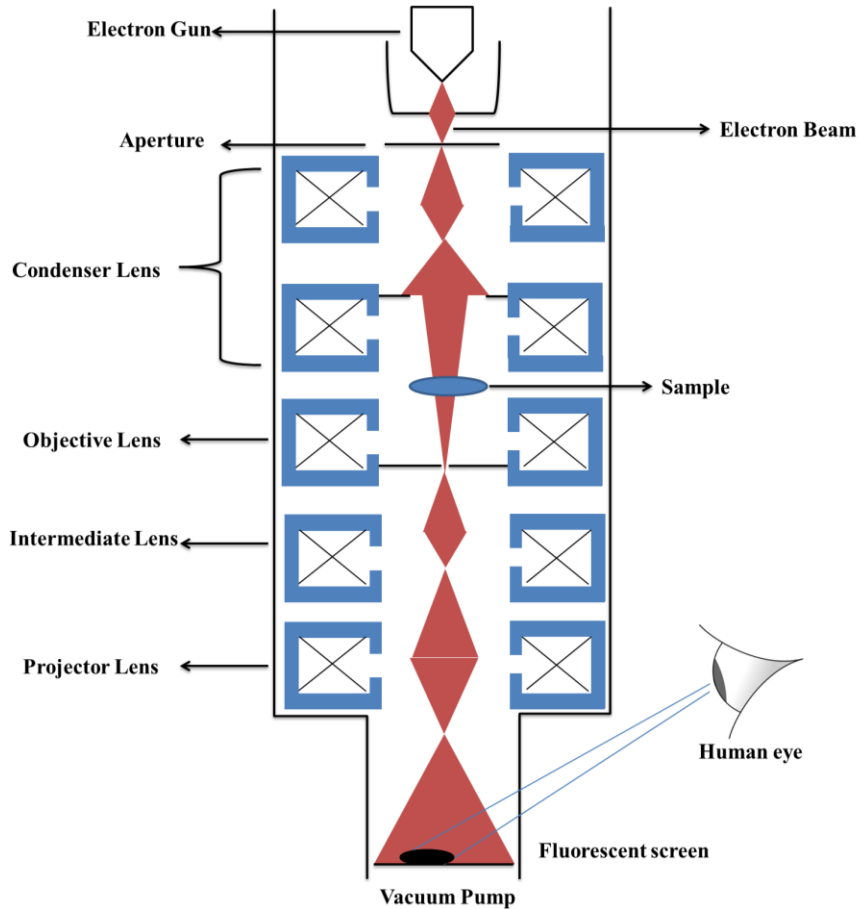


**Figure 13:** Schematic diagram of transmission electron microscopy system. Adapted from reference <sup>[172]</sup>.

In this thesis, bright-field TEM was used to determine the shape and sizes of the TMN NPs, and HRTEM was used to determine their crystallinity. Image J was used to analyze the sample size and the reported errors represent standard deviation within the same sample. In Chapter 6, STEM-EELS was used to analyze the composition and plasmonic responses of Cr<sub>2</sub>N by investigating the low-loss regions.

## 2.3 Scanning Electron Microscopy

SEM is another microscopic method that is used to characterize various materials on the micrometer to nanometer scale. One of the main advances made was the development of different types of electron sources such as high-brightness and field emission sources. SEM is one of the most versatile instruments due to its capability in obtaining three-dimensional images that helps analyze the topography and morphology of a sample. One of the main advantages of SEM includes fast data acquisition, ease of operation, high resolution, minimal sample preparation, small sample requirement and large depth of field.<sup>[182,183]</sup> **Figure 14** shows a schematic illustration of a typical SEM instrument. The basic theory of SEM involves scanning a high-energy focused beam of electrons over the sample to produce an image. The SEM column consists of the following main components: an electron gun, two condenser lenses, an objective lens, beam scanning coils, a large sample chamber with a stage, and an electron detection system, all operating in vacuum ( $10^{-3}$  to  $10^{-4}$  Pa).<sup>[183]</sup>

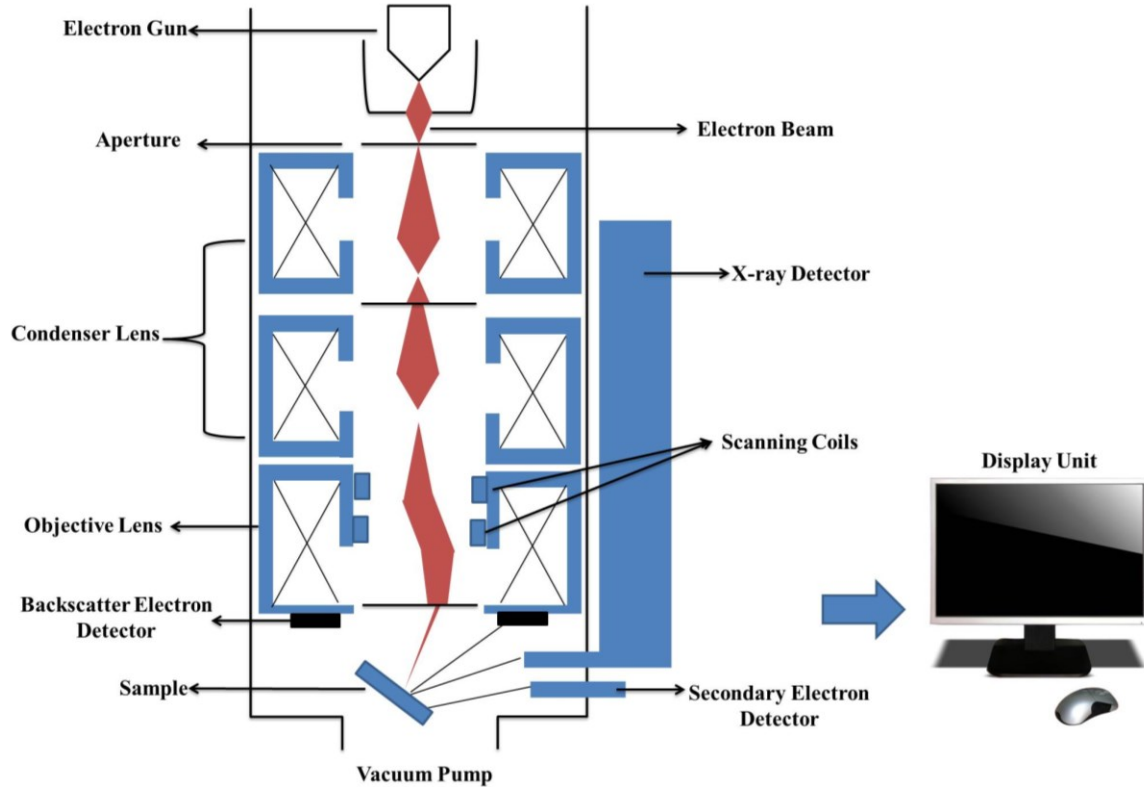


**Figure 14:** Schematic diagram of scanning electron microscopy system. Adapted from reference [183].

Most of the SEM components are very similar to the TEM components discussed above. The sample analyzed using SEM must be electrically conductive, or an ultrathin coating of metal can be applied onto non-conducting samples. Upon interacting with the sample, various types of scattered signals are generated and detected using electron detectors. The electron detectors can be secondary electrons (SEs) or back-scattered electrons (BSEs) detectors which are used to detect SEs or BSEs, respectively, as shown in **Figure 12**. SEs are obtained from the inelastic scattering of the incident electron beam as it interacted with the sample. SEs are lower energy (<50 eV) electrons that originate from the surface of the sample, and therefore can be used to provide surface topography,

shape, and size distribution of the sample.<sup>[173,183]</sup> BSEs are higher energy (>50 eV) electrons that are obtained from elastic scattering occurring as the incident beam interact with deeper volumes of the sample, and therefore providing information of the chemical composition of the sample.<sup>[184]</sup> The number of BSEs reaching the detector are proportional to the atomic number of the sample, therefore elements with high atomic numbers will appear brighter due to higher BSEs generated.<sup>[184]</sup> In this thesis, the TMN NPs were characterized using SEM to determine morphological information.

## 2.4 X-ray Powder Diffraction

XRD is one of the powerful and non-destructive techniques used to identify crystalline phases and structural properties such as grain size, phase composition, and lattice strains. X-ray diffractometer consists of three components: an X-ray source, sample stage, and a detector as shown in **Figure 15**. Generally, the X-rays are directed toward the sample stage where they interact with the sample at an angle  $\theta$  and diffract towards the detector at an angle  $2\theta$ . More specifically, the X-rays are generated through thermionic emission, where a tungsten filament is heated to produce electrons that are then accelerated toward a target by applying a voltage.<sup>[185,186]</sup>



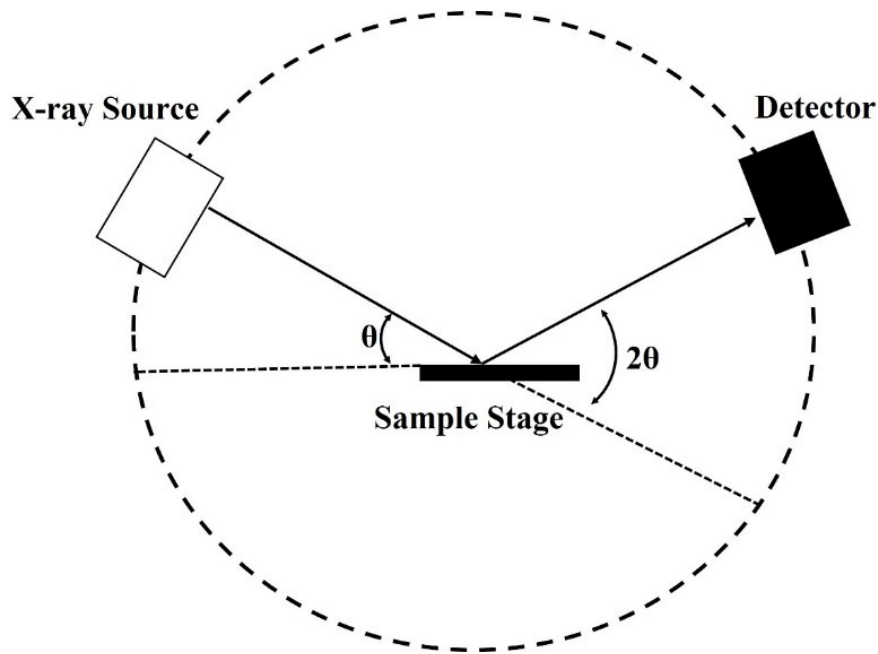


**Figure 15:** Schematic configuration of an X-ray diffractometer. Adapted from reference [185].

Different target materials such as Cu, Fe, Mo, or Cr are used, however, Cu is most commonly used as the target.<sup>[185,186]</sup> A series of monochromators are used to control the wavelength of the X-ray and the width of the beam is controlled using slits of varying sizes. The detector records and processes the signal and converts the signal to count rate and a diffractogram is obtained. To observe all the different orientations of the crystalline powder, both the sample stage and the detector are rotated at different angles. The X-rays are directed toward the sample stage where they interact with the sample and diffract.<sup>[185,186]</sup> The diffracted waves can interact with one another through either destructive or constructive interference. Destructive interference occurs when the X-ray waves are out of phase which results in canceling one another and the amplitude of the resultant wave will be reduced. At a fixed wavelength, the constructive interference of the scattered X-rays by

atoms in a periodic arrangement will result in characteristic diffraction peak. **Figure 16** illustrates a crystalline material with crystal planes that are separated by a distance  $d$ , where X-rays that are diffracted from different lattice planes must travel an extra distance which is indicated by  $AB + BC$ .

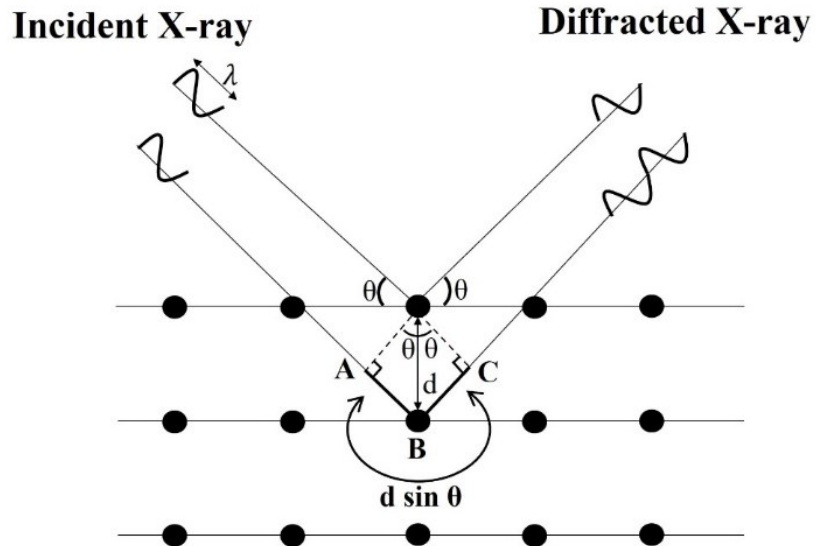


**Figure 16:** Schematic depicting the interaction of X-ray with the sample to satisfy Bragg's equation. Adapted from reference <sup>[186]</sup>.

These two distances are equal and therefore, they can be represented mathematically as **equation (11)**:

$$AB + BC = 2d \sin \theta \quad (11)$$

The travel path length difference between the diffracted beams must be equal to some integer multiple of the wavelength to remain in phase and for constructive

interference to occur. This can be seen by **equation (12)** which is referred to as Bragg's Law,

$$n \lambda = 2 d \sin \theta \quad (12)$$

where  $n$  is an integer,  $\lambda$  is the wavelength of the X-rays, and  $\theta$  is the angle of the X-ray beam with respect to these planes. Depending on the arrangement of atoms in a sample and the crystallite size, the broadness of the peaks can be influenced. For a crystalline material that has a long-range of periodic atom arrangement, intense sharp XRD peaks are obtained. However, for an amorphous material that lacks periodic atom arrangement, broader peaks are observed. The average size of the crystallites can be calculated using the Scherrer analysis as shown in **equation (13)**:

$$L = \frac{K\lambda}{\beta \cos \theta} \quad (13)$$

where,  $L$  is crystallite size,  $K$  is the shape factor (usually has a value of 0.9 for spherical crystals with cubic unit cells),<sup>[187]</sup>  $\lambda$  is the wavelength of the X-ray source,  $\beta$  is the FWHM, and  $\theta$  is the Bragg angle. In this thesis, XRD was used to analyze all the metal oxides and the TMN NPs synthesized to determine the crystal lattice structure, purity, and crystallinity.

## 2.5 X-ray Photoelectron Spectroscopy

XPS technique is a surface-sensitive technique used to analyze the top 1-10 nm of a material where the electrons can escape without significant energy loss.<sup>[188]</sup> XPS can provide information regarding the elemental composition of the material and oxidation state of an element (except H and He).<sup>[189]</sup> XPS consist of a monochromatic X-ray source

(Al or Mg), a sample chamber, an electron analyzer, and a detector as shown in **Figure 17**. Typically, XPS measurements are conducted under ultrahigh vacuum conditions ( $10^{-9}$  mbar) to avoid contamination of samples by air or water vapors and help photoelectron transport to the analyzer.

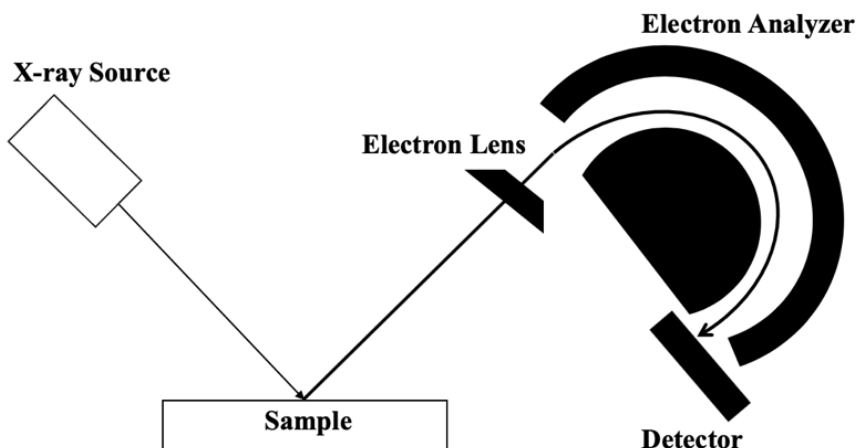


**Figure 17:** Schematic illustration of X-ray photoelectron spectroscopy set-up. Adapted from reference <sup>[188]</sup>.

The X-ray source consists of heated tungsten or LaB<sub>6</sub> filament from which electrons are accelerated towards a metal anode to generate soft X-rays (energies lower than ~6 KeV).<sup>[189]</sup> The produced X-rays should have sufficient energy to eject core electrons from atoms near the surface as illustrated in **Figure 18**. A photoelectron that overcomes its binding energy and the material work function, becomes a free electron as it reaches the vacuum level. The photoelectrons are focused on the analyzer by an electrostatic lens system whilst simultaneously adjusting their kinetic energy to match the pass energy of the analyzer.<sup>[190,191]</sup> The kinetic energy of the emitted photoelectrons is then analyzed by the

concentric hemispherical analyzer which consists of two concentric hemispheres that act as a band pass filter for the electrons' kinetic energy.<sup>[190,191]</sup> A potential difference is applied between the inner and outer hemispheres to guide the trajectory of the incoming electrons. Only electrons having specific pass energy will be able to pass through the center of the analyzer and reach the detector. Electrons with kinetic energy slightly above or below the pass energy will deflect the electron's path to the outer or the inner hemisphere, respectively.<sup>[190]</sup> A larger deviation from the pass energy will result in the electron not reaching the detector. Therefore, pass energy is an important parameter set by the user, and it is kept throughout the measurement to ensure the energy resolution is constant. The resolution of the analyzer can be significantly increased by reducing the pass energy of the analyzed electrons.<sup>[190,191]</sup>

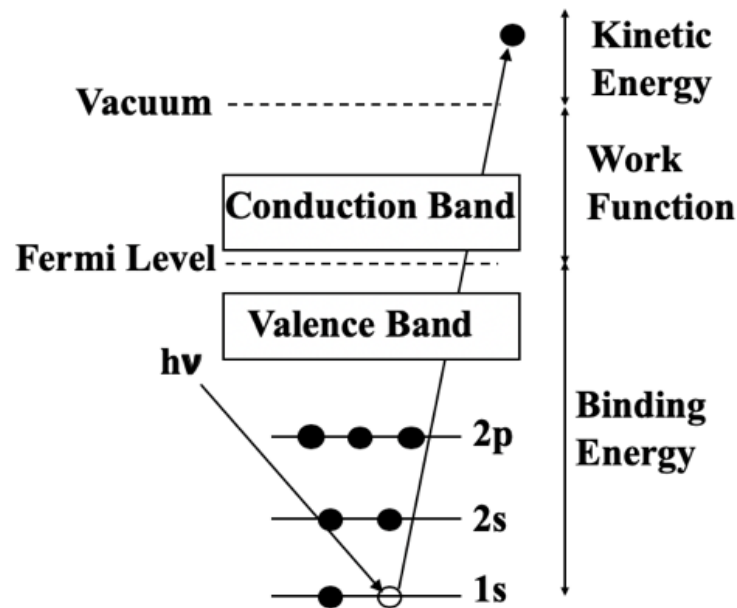


**Figure 18:** Emission of a core electron in XPS technique. Adapted from reference <sup>[192]</sup>.

Only photoelectrons of certain energy will be detected and counted using a channel-type electron multiplier detector, and an energy spectrum of intensity versus binding energy is obtained.<sup>[190]</sup> The binding energy is characteristic of the core electrons and therefore elements with different oxidation states would have specific binding energy. The binding energy for a solid sample is determined based on **equation (14)**:

$$\mathbf{BE = h\nu - KE_{\text{spectrometer}} - \phi_{\text{spectrometer}}} \quad (14)$$

where KE is the kinetic energy of the electron measured by the spectrometer,  $h\nu$  is the energy of the incident photon, BE is the binding energy, and  $\phi$  is the spectrometer work function. For a solid sample, the photoelectrons must overcome the potential barrier at the surface known as the work function, which corresponds to the energy difference between the Fermi level and the vacuum level, as shown in **Figure 19**.<sup>[189–191]</sup> Accordingly, for a conductive sample, the Fermi level of the sample and the spectrometer are aligned, and therefore, it is used as a reference level. The KE of the sample can be written as **equation (15)**:

$$\mathbf{KE_{\text{sample}} = h\nu - BE - \phi_{\text{sample}}} \quad (15)$$

However, the KE of the sample is different from the KE measured at the detector due to the differences in the work function that arises as a result of the negative charge transfer between the sample and the spectrometer.<sup>[191]</sup> This results in a contact potential difference that needs to be accounted for while the photoelectrons are traveling towards the entrance slit of the energy analyzer. Therefore, by substituting **equation 14** into

**equation 15**, the binding energy can be obtained which is independent of the sample work function as shown in **equation (16)**:

$$KE_{\text{sample}} + \phi_{\text{sample}} = KE_{\text{spectrometer}} + \phi_{\text{spectrometer}} \quad (16)$$

The spectrometer work function is an experimental constant, which is established during the calibration procedure. Thus, the photoelectrons originating from the core level will reach the detector with the same kinetic energy, regardless of the sample work function.<sup>[191,192]</sup>

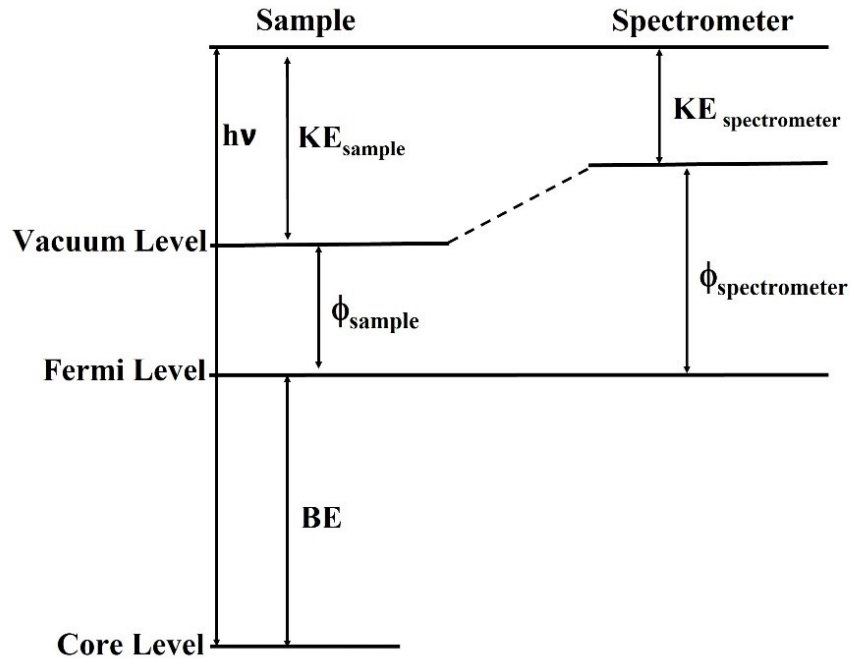


**Figure 19:** Energy level diagram of the sample and the spectrometer in a core-level photoemission experiment of a metallic sample. Adapted from reference <sup>[192]</sup>.

The XPS data obtained displays the number of electrons detected at a specific binding energy. Each element produces characteristic XPS peaks that correspond to the electron configuration of the electrons within the atoms (e.g., 2p, 3d, 4f, etc.). The number of electrons detected in each peak is directly related to the quantity of elements present. Core levels in XPS use the nomenclature  $nlj$  where  $n$  is the principal quantum number,  $l$  is the angular momentum quantum number, and  $j = l + s$  (where  $s$  is the spin angular quantum number which can be  $\pm 1/2$ ).<sup>[190]</sup> All orbitals except for  $s$  orbitals ( $l=0$ ) result in the formation of the doublets with the two possible states having different binding energies which are known as spin-orbit splitting.<sup>[193]</sup> These peaks have specific area ratios based on the degeneracy of each spin state which will be needed when fitting XPS data and constraining the peak area ratio. In this thesis, XPS was used to analyze the TMN NP surface composition.

## 2.6 Absorbance Spectroscopy

UV-vis absorption spectroscopy is one of the most widely used analytical tool for the quantitative determination of different analytes concentrations. UV-vis spectroscopy is related to the interaction of electromagnetic radiation (i.e. light) with matter which results in the excitation of electrons from lower to higher energy levels.<sup>[194]</sup> Since the energy levels are quantized, according to the Bohr-Einstein frequency relationship, only light with precise frequency can cause electronic transitions to occur, as shown in **equation (17)**:

$$\Delta E = E_2 - E_1 = h\nu \quad (17)$$



where  $\Delta E$  is the energy difference between two transition states,  $h$  is Planck's constant ( $6.626 \times 10^{-34}$  J), and  $\nu$  is the frequency of the electromagnetic radiation. As light interacts with matter, several processes can occur such as reflection, scattering, and absorbance. Typically, a UV-vis spectrometer measures the intensity of the transmitted light and compares it to the intensity of incident light.<sup>[195]</sup> The transmitted light that passes through the sample will be used to determine the absorbance which is usually plotted against the wavelength (nm).<sup>[194]</sup> The concentration of an absorbing analyte is linearly related to the absorbance according to Beer-Lambert law, as shown in **equation (18)**:

$$\mathbf{A = -\log T = \log \frac{P_0}{P} = \epsilon l c} \quad (18)$$

where  $A$  is absorbance,  $T$  is transmittance,  $P_0$  is the incident radiant power,  $P$  is the transmitted radiant power,  $\epsilon$  is the molar absorptivity,  $l$  is the path length of the sample, and  $c$  is the concentration of absorber. The basic components of a UV-vis spectrophotometer are a light source, monochromator or filter, cuvette compartment, detector, and amplifier, as shown in **Figure 20**. Various light sources can be used such as deuterium or hydrogen lamps, tungsten filament lamps, and xenon arc lamps.<sup>[194]</sup> A monochromator is a device that contains entrance and exit slits, collimating and focusing lenses, and a dispersing device that is used to isolate a single wavelength band. The cuvettes must be made of a material that is transparent to the radiation in the spectral region of interest. For example, quartz or fused silica is used to analyze samples in the UV region, silicate glasses can be used in the region between 350 and 2000 nm, plastic cuvettes can be used in the visible region, and sodium chloride cuvette is mostly used in the IR region.<sup>[194]</sup>

A detector that can convert light into an electrical signal while having high sensitivity, high signal-to-noise ratio, and a constant response over a range of wavelength is used (e.g. phototube, photomultiplier tube, diode array detector, and charge-coupled devices). In this thesis, UV-vis spectroscopy is used to analyze the shape and position of the LSPR peaks of plasmonic TMN NPs.

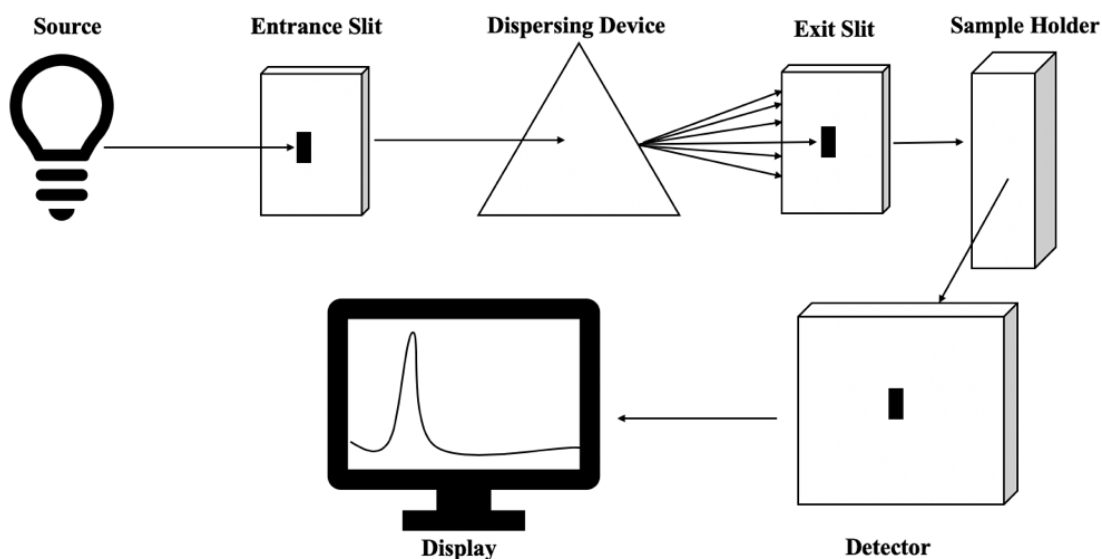


**Figure 20:** Schematic diagram of Ultraviolet-visible spectroscopy. Adapted from reference [194].

## 2.7 Dynamic Light Scattering and Zeta Potential

DLS has been used to analyze the size of emulsions, proteins, polymers, colloids, and NPs based on their Brownian motion in the dispersed medium.<sup>[196]</sup> The Brownian motion states that the NPs are in constant collision with the solvent molecules and these collisions have a certain energy that can be transferred to induce particle movement. As the

particle increase in size, the motion speed decreases because the NPs are not affected by the amount of energy.<sup>[196]</sup> The relationship between the speed of the particles and the particles size can be explained by the Stokes-Einstein equation (**equation 19**):<sup>[197]</sup>

$$\mathbf{D} = \frac{\mathbf{k_B T}}{6\pi\eta\mathbf{R_H}} \quad (19)$$

where D is the speed of the particles,  $k_B$  is Boltzmann Constant ( $1.38 * 10^{-23} \text{ m}^2\text{kgK}^{-1}\text{s}^{-2}$ ), T is temperature,  $\eta$  is the viscosity of the surrounding medium, and  $R_H$  is the hydrodynamic radius. The DLS determines the size of the NPs by monitoring their motion which can be obtained by focusing a monochromatic laser on a cuvette containing the solution. The scattered light collected can be measured at different angles ( $15^\circ$ ,  $90^\circ$ , and  $175^\circ$ ) with respect to the light source.<sup>[198]</sup> The forward angle at  $15^\circ$  is used to monitor aggregation or the presence of larger particles that tend to scatter more light in the forward direction. Side scattering at  $90^\circ$  is used for weakly scattering samples of small particles. Backscattering at  $175^\circ$  is used for a highly concentrated solution to minimize the effect of multiple scattering. Based on the sample solution, the instrument calibrates which scattering angle to be collected.<sup>[198]</sup>

The DLS instrument can be used to determine the zeta potential which is the charge on a particle at the slipping plane as shown in **Figure 21**. In an ionic solution, NPs with a net charge will have a layer of ions of opposite charge that will be strongly bound to the surface, this is referred to as the Stern layer.<sup>[197,198]</sup> A second diffuse outer layer will consist of loosely associated ions. These two layers will create an electrical double layer.

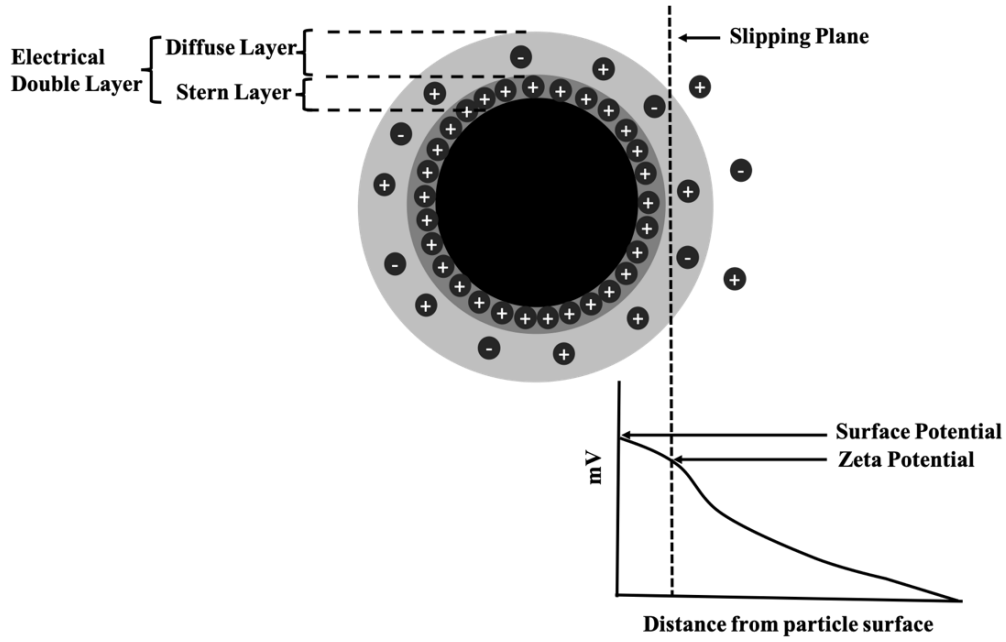


**Figure 21:** Schematic illustration of the electric double layer around the NPs. Adapted from reference <sup>[198]</sup>.

Determining the zeta potential can be useful in predicting the interaction between particles in a suspension to stabilize the NP solution. To measure the zeta potential, an electrical field is applied, and the movement of the NPs is measured by laser doppler velocimetry. The zeta potential can then be determined using Henry's equation, **(equation 20)**:<sup>[197]</sup>

$$U_e = \frac{2\varepsilon z f(ka)}{3\eta} \quad (20)$$

where  $U_e$  is the electrophoretic mobility,  $\varepsilon$  is the dielectric constant,  $z$  is the zeta potential,  $\eta$  is the absolute zero-shear viscosity of the medium, and  $f(ka)$  is the Henry function.<sup>[197]</sup>

A positive zeta potential indicates that the NPs are positively charged, and a negative zeta

potential indicates that the NPs are negatively charged. Typically, a zeta potential with a magnitude higher or lower than  $\pm 30$  mV indicates that the NP suspension is stable. In this thesis, hydrodynamic radius and zeta potential measurements were conducted on the TMN NPs to determine their size and surface charge.

## 2.8 Synthesis of Transition Metal Nitride Nanoparticles

The NPs in this thesis were synthesized using high temperature solid-state reactions and the general set-up for the process is shown in **Figure 22**. The detailed synthesis procedure for making water dispersible NPs is outlined in this section.

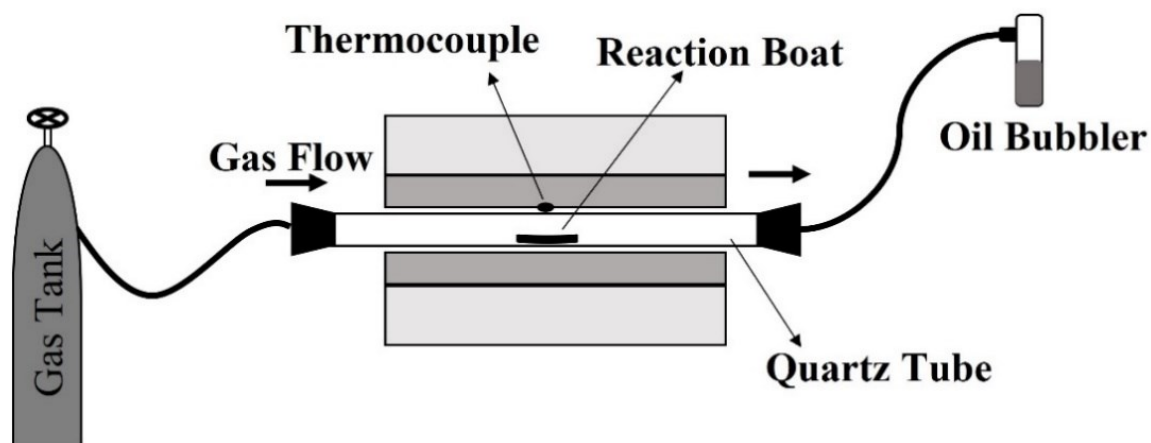


**Figure 22:** Representation of solid-state synthesis set-up.

### ***2.8.1 Preparation of Transition Metal Nitride Nanoparticles***

Chapter 3 and 4: 0.10 g of the oxide ( $\text{TiO}_2$ ,  $\text{ZrO}_2$  or  $\text{HfO}_2$ ) nanopowder was mixed thoroughly with 3 molar excess of magnesium nitride ( $\text{Mg}_3\text{N}_2$ ) powder with a spatula for ~40 seconds. The mixture was transferred to a Coors™ high alumina combustion boat and was immediately placed in a quartz tube. If the relative humidity was high (>40%), these steps were carried out in a  $\text{N}_2$  filled glovebox. The reaction mixture was heated to 1000 °C for 12 h at a ramp rate of 10 °C/min under Ar flow in a Lindberg Blue M™ furnace. The reaction was allowed to cool to room temperature and the resulting product was transferred to a 100 mL beaker and the reaction boat was rinsed with 20 mL deionized water (DI-water). 25 mL of 1.0 M HCl solution was added to the beaker slowly and the mixture was stirred for 1 h to remove magnesium oxide (MgO) and any unreacted  $\text{Mg}_3\text{N}_2$ . The solution was centrifuged for 15 min at 3300 rpm and the supernatant containing acid and soluble by-products was discarded (after the first centrifugation step, the supernatant is colorless). The solid was resuspended in 5.0 mL DI-water by sonication and centrifuged for 15 min at 3300 rpm. The colored supernatant was collected, and the precipitate was resuspended in 5 mL DI-water by sonication and centrifuged again for 15 min at 3300 rpm. The colored supernatant was collected and mixed with the supernatant from the previous step. The resulting powders and supernatants were then characterized using various spectroscopic/microscopic techniques.

Chapter 6:  $\text{Cr}_2\text{O}_3$  (0.152 g, 1.0 mmol) nanopowder was mixed with  $\text{Mg}_3\text{N}_2$  (0.403 g, 4.0 mmol) using a spatula. This step was performed in a  $\text{N}_2$  filled glovebox if the relative humidity was >40 % to avoid  $\text{Mg}_3\text{N}_2$  decomposition in the presence of moisture. The

powder mixture was transferred to a Coors™ high alumina combustion boat and the boat was immediately placed in a quartz tube. The reaction mixture was heated to 1000 °C at a ramp rate of 10 °C/min and held at that temperature for 3 hours under Ar flow in a Lindberg Blue M™ furnace. The washing and purification procedures are the same as highlighted above.

Chapter 7: 0.10 g of the oxide (TiO<sub>2</sub>, ZrO<sub>2</sub> or HfO<sub>2</sub>) nanopowder was mixed thoroughly with 6 molar excess of Mg powder using a mortar and pestle. The mixture was transferred to a Coors™ high alumina combustion boat and was immediately placed in a quartz tube. The reaction mixture was heated to 1000 °C for 12 h at a ramp rate of 10 °C/min under N<sub>2</sub> flow in a Lindberg Blue M™ furnace. The washing and purification procedures are the same as highlighted above.

## **2.9 Photothermal Measurements**

Plasmonic nanostructures can convert absorbed light into heat through non-radiative relaxation of excited free electrons.<sup>[58]</sup> As such, plasmonic nanomaterials have been used for photothermal applications such as photothermal therapy<sup>[58–60,199]</sup>, seawater desalination and evaporation<sup>[200–205]</sup>, and photothermal imaging.<sup>[206,207]</sup> The performance of plasmonic materials in photothermal applications can be evaluated by determining the transduction efficiencies which is the ability of the material to convert the absorbed light into heat and transfer it to the surroundings. To determine the photothermal transduction efficiency, the NP solution is illuminated using a light source, and the temperature is measured as a function of time. After the solution has reached the maximum

temperature, the light source is turned off and the cooling component is measured, as shown in the **Figure 23**.

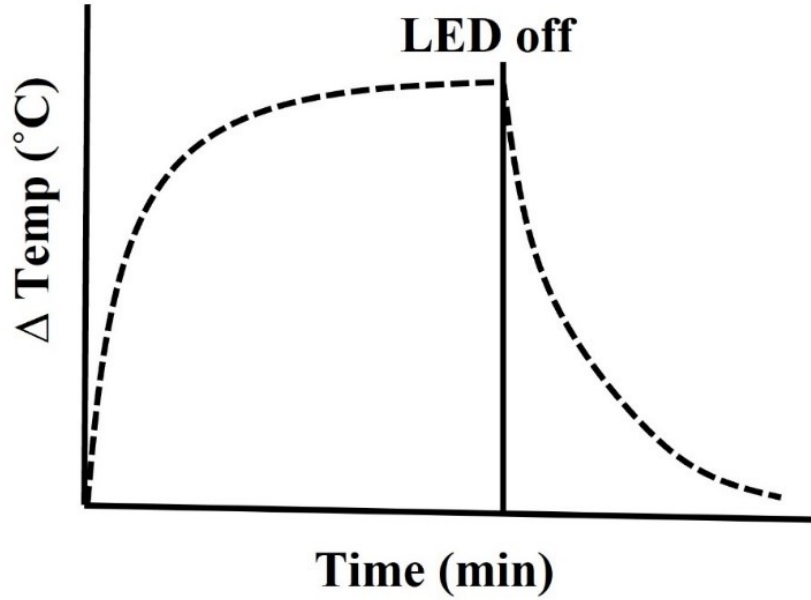


**Figure 23:** Representation of data obtained from photothermic experiment.

Few different methods have been reported in the literature to calculate the photothermal transduction efficiency however, many of these methods did not provide enough details on how the values were obtained. Therefore, an extensive literature search was done to find an accurate way to calculate the transduction photothermal efficiency. A paper published by Roper *et al.* demonstrated a straightforward method to calculate the photothermal transduction efficiency.<sup>[208,209]</sup> The energy balance of the system consisting of the plasmonic NP solution within a quartz container irradiated by a light source can be given using **equation 21**:

$$\sum_i m_i C_{p,i} \frac{dT}{dt} = Q_I + Q_0 - Q_{\text{ext}} \quad (21)$$



where  $m$  and  $C_p$  are the mass and heat capacity of each component of the sample cell, respectively.  $T$  is the sample cell temperature,  $Q_I$  is the photothermal energy input by the NPs,  $Q_0$  is the baseline energy input by the sample cell, and  $Q_{ext}$  is the heat transferred to the surroundings. When the light source is off,  $Q_{ext}$  is represented by **equation (22)**:

$$Q_{ext} = hS (T - T_{amb}) \quad (22)$$

where  $T_{amb}$  is the ambient temperature,  $h$  is the heat transfer coefficient, and  $S$  is the surface area of the illumination. The thermal and cooling cycle has an exponential time dependence and therefore a thermal time constant  $\tau$  can be expressed by **equation (23)**:

$$\tau = \frac{\sum_i m_i C_{p,i}}{hS} \quad (23)$$

The heat transfer coefficient,  $h$ , can be determined by **equation (22)** using either the heating or the cooling data. Once  $h$  is determined, the amount of heat energy accumulated or lost from the sample cell can be calculated. When the sample cell reaches an equilibrium temperature, the power flowing into the sample cell ( $Q_I$  and  $Q_0$ ) is equivalent to the power outflow as shown in **equation (24)**:

$$Q_I + Q_0 = hS (T_{max} - T_{amb}) \quad (24)$$

The  $Q_I$  can be represented as the heat dissipated by electron-phonon relaxation when the NPs are induced by irradiation, as expressed in **equation (25)**:

$$Q_I = I (1 - 10^{-A_\lambda}) \eta_T \quad (25)$$

where  $I$  is the incident light intensity,  $\eta_T$  is the photothermal transduction efficiency,  $A_\lambda$  is the optical density of the sample solution at the excitation wavelength. By substituting **equation 25** into **equation 24**, the photothermal transduction efficiency can be expressed as **equation (26)**:

$$\eta_T = \frac{hS(T_{\max} - T_{\text{amb}}) - Q_0}{I(1 - 10^{-A_\lambda})} \quad (26)$$

To determine the temperature changes in the TMN NP solutions, a continuous Solis LED source (850 or 365 nm) was used as the light source (ThorLabs). The illumination power density was calibrated using a silicon photodiode (ThorLabs). The temperature change was monitored using a K-type thermocouple device (EL-USB-TC-LCD, MicroDAQ) with data logger. A 1.0 cm path length quartz cuvette was used as the container and 3.00 mL of the NP solution was added to it, while constantly stirring using a small Teflon-coated magnetic stirring bar. The cuvette containing the NP solution was illuminated from the side, and the surface area of the illumination was 3.0 cm<sup>2</sup>. The thermocouple was placed in the cuvette such that the tip was halfway through the solution (**Figure 24**). The temperature data was collected at 15 second interval where the solution was illuminated for the first 30 minutes and then allowed to cool for another 30 minutes. Each measurement was repeated a minimum of five times to account for differences resulting from slight changes in stirring rates and ambient conditions, and the error bars represent the standard deviation from different replicates.

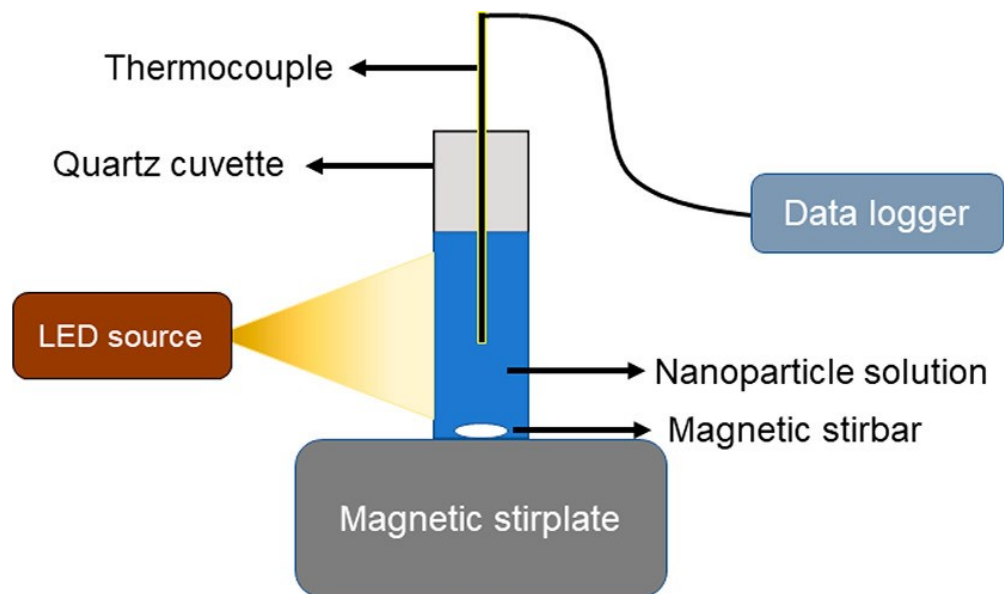


**Figure 24:** Illustration of the photothermal experimental set-up.

## 2.10 Computational Studies

All the calculations in this thesis were performed by Dr. Yashar Monfared.

*Chapter 3:* The optical spectra of group IVB TMN NPs were generated using a finite element method (FEM) solver for Maxwell's equations in Comsol MultiPhysics. To simulate the material optical properties, the real and imaginary parts of TiN, ZrN, and HfN dielectric constants as a function of excitation wavelength were used from Kumar *et al.*<sup>[68]</sup> To account for surface oxidation, our particles were modeled as spheres having a 14-15 nm overall diameter in a nitride core–oxide shell structure. The locations of absorption maxima in simulations and experiments are matched by considering a nitride core size plus oxide shell thickness of 12.5 + 2.5, 12 + 2, and 11.5 + 2.5 nm for TiN, ZrN, and HfN, respectively. Chosen dimensions are equal to the average size of the NPs in the

experiments. TiO<sub>2</sub>, ZrO<sub>2</sub>, and HfO<sub>2</sub> dielectric constants were obtained from DeVore and Wood *et al.*<sup>[210–212]</sup> Au NRs were modeled as cylindrical rods with 50 nm length and 12.3 nm width. To ensure the accuracy of the results, rigorous convergence analysis and perfectly matched layers (PML) boundary conditions as well as ultrafine mesh size were utilized in the simulations.

Chapter 8: The absorption spectra of Cr<sub>2</sub>N nanoparticles were computed using a FEM solver for Maxwell's equations in COMSOL MultiPhysics. To simulate the optical characteristics of the materials, Lorentz oscillator parameters of Cr<sub>2</sub>N were obtained from Aouadi *et al.*<sup>[213]</sup> to determine real and imaginary part of dielectric function of the material. In simulations, particles were modelled as three dimensional nanospheres suspended in water. To ensure the accuracy of the results, rigorous convergence analysis and PML boundary conditions as well as ultra-fine mesh size were utilized in the simulations.

### Chapter 3: Synthesis of Group IVB Plasmonic Metal Nitrides

*This author wishes to clarify her contribution to the research described in Chapter 3 of this thesis document.* This chapter discusses the synthesis of plasmonic group IVB TMN NPs using the solid-state metathesis reaction. The synthesized NPs were characterized using various techniques as described in experimental section of this thesis (Chapter 2).

My contribution to this study includes synthesizing the NPs and optimizing the reaction conditions (time, reaction temperature, etching time, acid concentration, etc.), characterizing the NPs using XRD, UV-vis spectroscopy, TEM, SEM, and DLS, and writing most of the manuscript. Initial synthetic screening experiments on this project were conducted by Govinda H. Humagain, and Benjamin R. A. Fleishchman. High magnification TEM images were obtained by Dr. Regina Sinelnikov and Hoayang Yu. XPS measurements were performed by Andrew George. Computational work was conducted by Dr. Yashar Monfared. This work has been published in *Angewandte Chemie Journal*.

**Reference:** R. A. Karaballi, G. Humagain, B. R. A. Fleischman, M. Dasog, Synthesis of Plasmonic Group IVB Nitride Nanocrystals via Solid-State Metathesis. *Angewandte Chemie International Edition*, **2019**, 58, 3147-3150. Reprinted by permission of John Wiley& Sons, Inc.

### 3.1 Introduction

There has been a growing interest in the development of plasmonic nanomaterials that are low-cost and have high chemical and thermal stability.<sup>[214]</sup> Transition metal nitrides (TMNs) have gained significant attention because such materials can exhibit plasmonic responses in the visible and NIR wavelength regimes and their properties can be tuned by varying the material composition.<sup>[135]</sup> Additionally, they can sustain high temperatures without succumbing to sintering and exhibit exceptional chemical stability.<sup>[69,134-136]</sup> However, many of the optoelectronic characteristics reported for TMNs are based on computational studies<sup>[68,69]</sup> and experimental evidence of their plasmonic properties remain scarce. Thin films of TiN, ZrN, and HfN have previously been investigated which were very similar to Au in terms of plasmonic behavior.<sup>[63,80,215]</sup>

To date, experimental investigations of the plasmonic properties of TMN NPs have mostly been limited to TiN and ZrN. These NPs have been prepared using laser ablation,<sup>[147]</sup> non-thermal plasma route,<sup>[154-156]</sup> and lithography,<sup>[141]</sup> each of which can be cost- and infrastructure-intensive. Chemical methods, such as the nitridation of transition metals, metal oxides, or halides, can offer straightforward routes toward the synthesis of metal nitride NPs. These methods have been used to prepare TMN nanostructures;<sup>[157-161]</sup> however, their plasmonic properties have not been investigated.

This chapter outlines the synthesis of plasmonic group IVB TMNs - TiN, ZrN, and HfN NPs using the solid-state metathesis reaction. Metal nitride NPs prepared in this manner were found to be crystalline and can be dispersed in water to yield brightly colored

solutions that showed LSPR in visible and NIR light. To the best of our knowledge, these studies show for, the first time, the synthesis of free-standing plasmonic HfN NPs.

### **3.1 Experimental**

#### ***3.1.1 Materials***

Titanium dioxide (TiO<sub>2</sub>, 99.9%, 18 nm), zirconium dioxide (ZrO<sub>2</sub>, 99.95%, 20 nm), hafnium dioxide (HfO<sub>2</sub>, 99.99%, 61-80 nm), and magnesium nitride (Mg<sub>3</sub>N<sub>2</sub>, 99%, -325 mesh) were purchased from U.S. Research Nanomaterials Inc. Sucrose (>99.5%) was purchased from Sigma Aldrich. All glassware was cleaned thoroughly with deionized water then acetone and placed in the oven to dry prior to use.

#### ***3.1.2 Preparation of Transition Metal Nitride Nanoparticles***

The group IVB TMN NP solutions were synthesized as discussed in section 2.8.1. For the refractive index measurements, sucrose solutions were prepared by dissolving sucrose in DI-water to obtain various concentrations (0, 20, 40, 60, 80%). The TMN NPs were dispersed in the aqueous sucrose solutions.

#### ***3.1.3 Characterization Techniques***

Powder XRD patterns were collected using a Rigaku Ultima IV X-ray diffractometer with CuK $\alpha$  radiation ( $\lambda = 1.54 \text{ \AA}$ ). The powder samples were placed on to a zero-background silicon (Si) wafer and the spectra were collected at angles between 20°-80° at a rate of 3 counts/s for an hour. Scherrer analysis were performed on the peaks resulting from (111), (200), and (220) crystal planes using **equation 13** and the average of

those three values were used to assign a crystallite size. The obtained XRD spectra were imported into Match program to confirm the composition of the analyzed sample. TEM images were obtained using either a Hitachi-9500 electron microscope with an accelerating voltage of 300 kV or a FEI Techani™ 12 electron microscope operating with an accelerating voltage of 120 kV. TEM samples were prepared by drop-casting NP suspensions onto a copper grid with a holey carbon film, and Image J software was used to analyze the samples. SEM images were obtained on a Hitachi S-4700 electron microscope. SEM samples were prepared by drop-casting thin film of NP suspensions onto a Si wafer. The images were processed using Gatan Micrograph Software (GMS 3).

XPS analyses were performed on the TMN NP powders using a Kratos Axis Ultra instrument operating in energy spectrum mode at 210 W. The base pressure and operating chamber pressure were maintained at  $10^{-7}$  Pa. A monochromatic Al K $\alpha$  source ( $\lambda = 8.34$  Å) was used to irradiate samples, and spectra were obtained with an electron takeoff angle of 90°. To minimize sample charging the charge neutralizer filament was used as appropriate. Survey spectra were collected using an elliptical spot with major and minor axis lengths of 2 and 1 mm, respectively, and 160 eV pass energy with a step of 0.33 eV. CasaXPS software (VAMAS) was used to interpret high-resolution (HR) XP spectra. All spectra were internally calibrated to the C 1s emission (284.8 eV). After calibration, the background was subtracted using a Shirley-type background to remove most of the extrinsic loss structure.

UV-vis spectra were collected using an Agilent CARY 5000 spectrometer. Diluted solutions were placed in a quartz cuvette and DI-water was used as the blank. The UV-vis



spectra were scanned at a medium rate between 1200 and 200 nm. DLS measurements were conducted using Zetasizer Nano Series Nano-ZS (Malvern Panalytical) with a built-in 623 laser. For the size measurements, dilute NP solutions were placed in a plastic cuvette, whereas for the zeta potential measurements, a DTS1070 folded capillary cell was used. Triplicate measurements for each sample were conducted and an average measurement was obtained. Zetasizer software was used for data analysis.

### ***3.1.4 Computational Studies***

Computational studies were performed as discussed in section 2.10.

## **3.2 Results and Discussion**

Commercially available metal oxide nanopowders,  $\text{MO}_2$  ( $\text{M} = \text{Ti}, \text{Zr}, \text{and Hf}$ ) were mixed with  $\text{Mg}_3\text{N}_2$  and the reaction was conducted at 1000 °C for 12 hrs. The precursor oxides were characterized using XRD and TEM. Anatase-phase  $\text{TiO}_2$  with an average particle size of  $25 \pm 2$  nm (**Figure 25**), monoclinic phase  $\text{ZrO}_2$  with an average particle size of  $24 \pm 5$  nm (**Figure 26**), and monoclinic phase  $\text{HfO}_2$  with an average particle size of  $39 \pm 10$  nm (**Figure 27**) were commercially purchased.

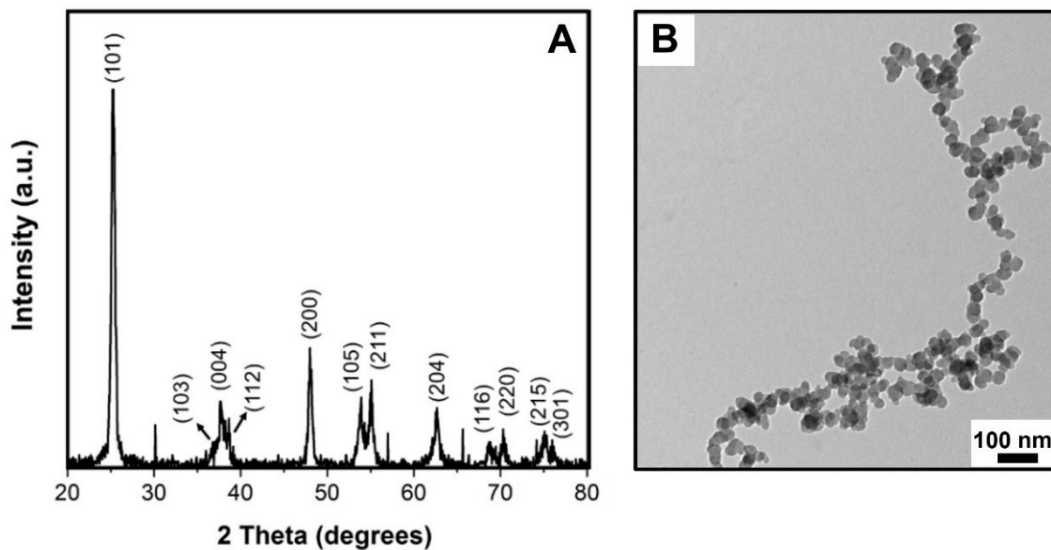


Figure 25: (A) Powder XRD pattern and (B) TEM image of anatase phase TiO<sub>2</sub> NPs.

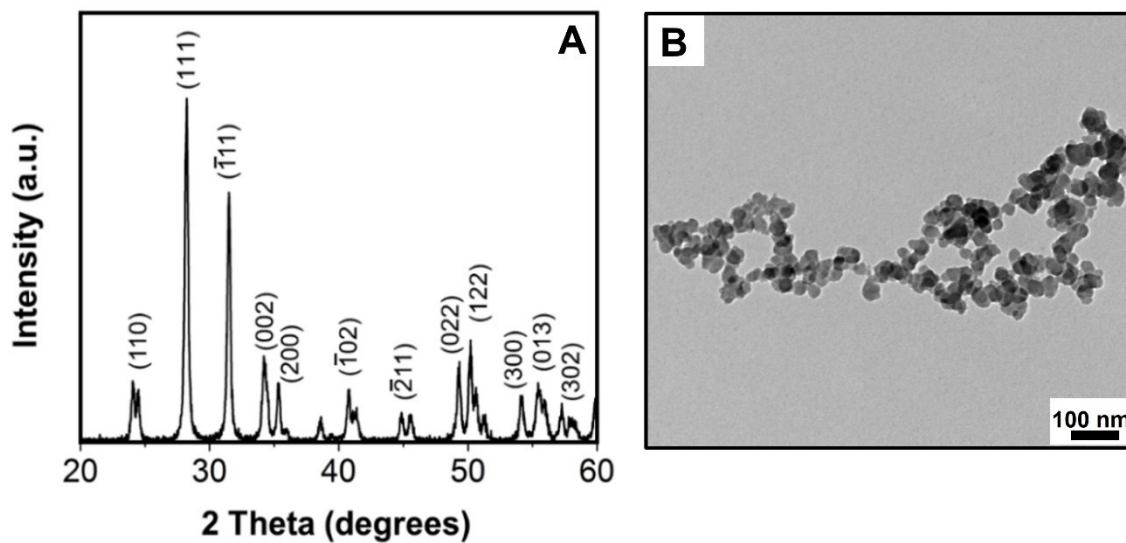
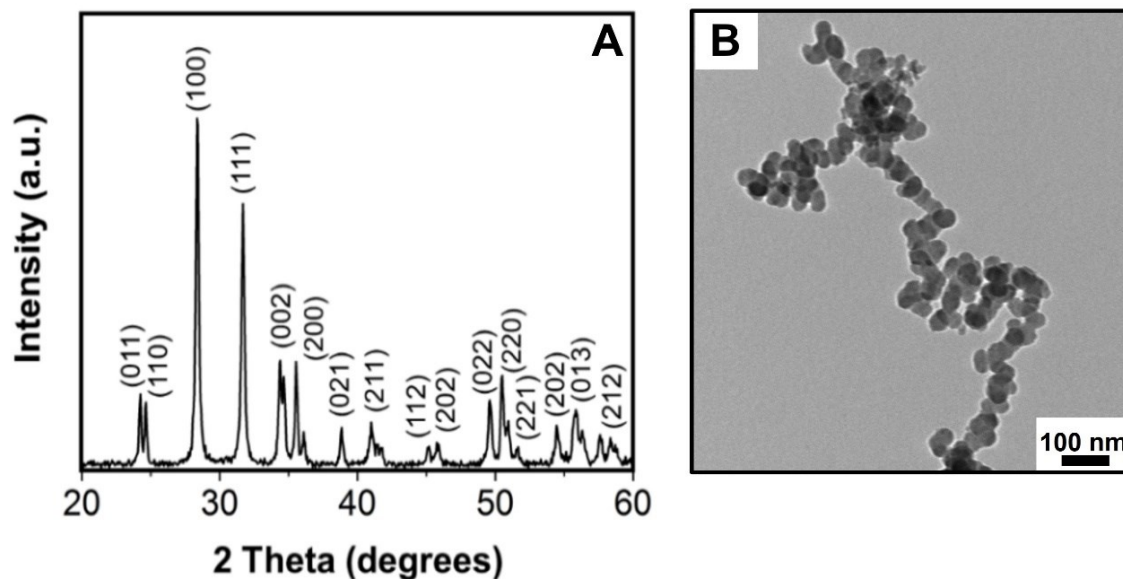
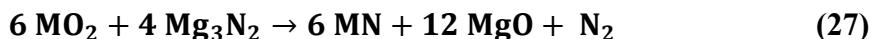


Figure 26: (A) Powder XRD pattern and (B) TEM image of monoclinic phase ZrO<sub>2</sub> NPs.



**Figure 27:** (A) Powder XRD pattern and (B) TEM image of monoclinic phase HfO<sub>2</sub> NPs.

The metal oxides were converted to the metal nitrides, MN as shown in **equation (27)**:



Mg<sub>3</sub>N<sub>2</sub> has previously been used as a nitriding reagent, but the metal precursors used were chloride salts that required storage and handling under an inert atmosphere due to their susceptibility to hydrolysis.<sup>[216–218]</sup> The air and moisture stable metal oxides used in this work allow for the reagents to be handled under ambient conditions. After the acid workup of the reaction, two fractions of nitrides were obtained. There is water dispersible nitride NPs (~60%) and the other component corresponds to non-dispersible nitride powders (**Figure 28**).

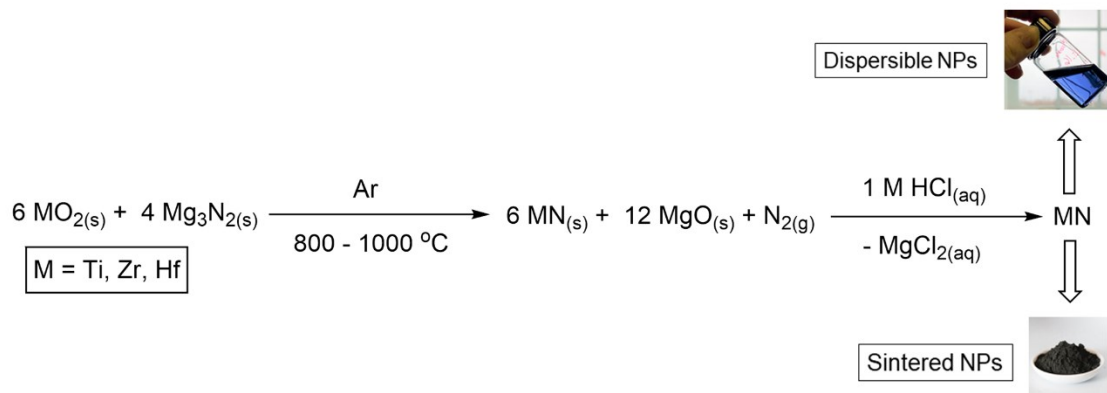


**Figure 28:** Schematic illustration of solid-state metathesis route and the resulting dispersible and sintered NPs.

Powder XRD analysis of the solid-state metathesis reaction powder products showed diffraction patterns (**Figure 29A**) characteristic of cubic phase TiN, ZrN, and HfN.<sup>[154,156,219]</sup> Both ZrN and HfN XRD patterns also have low intensity peaks between 28 and 32° corresponding to residual oxide. The XRD pattern of the dispersible product (**Figure 29B**) also showed the cubic phase mononitride as the major product for all the group IVB nitrides. The intensity of the oxide peaks in ZrN and HfN NPs was slightly higher in the suspended product compared to the non-dispersible powders.

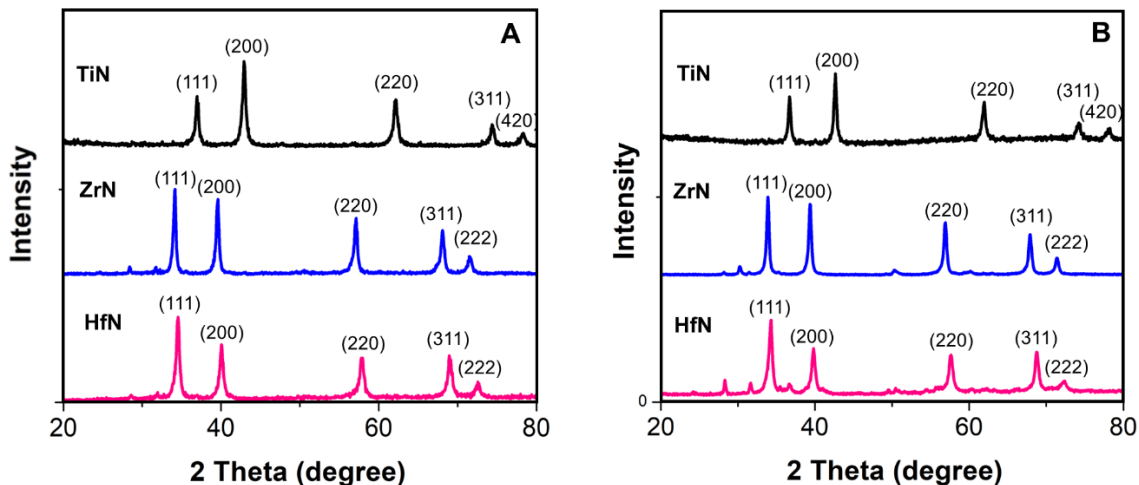


**Figure 29:** Powder XRD patterns of (A) TiN, ZrN, and HfN powder, and (B) dispersed TiN, ZrN, and HfN prepared via solid-state metathesis reaction.

TEM analysis of the metal nitride NPs dispersed in water (**Figure 30**) showed the presence of NPs with average particle sizes of  $12 \pm 3$ ,  $15 \pm 2$ , and  $11 \pm 4$  nm for TiN, ZrN, and HfN, respectively. Low-magnification TEM images (**Figure 30A, C, and E**) suggested that the particles were interconnected but high-magnification images showed the NPs to be overlapping without inter-particle connections (**Figure 30B, D, and F**). It is possible that the NPs aggregate on the TEM grid as they are being deposited on the grid. The average size of nitride NPs was found to be smaller than the parent oxide particles. The decrease in NP size is likely due to the smaller unit cell volume of the nitrides ( $0.0764 \text{ nm}^3$ ,  $0.0967 \text{ nm}^3$ , and  $0.0923 \text{ nm}^3$  for TiN, ZrN, and HfN, respectively)<sup>[220]</sup> compared to the oxides ( $0.136 \text{ nm}^3$ ,  $0.140 \text{ nm}^3$ , and  $0.137 \text{ nm}^3$  for  $\text{TiO}_2$ ,  $\text{ZrO}_2$ , and  $\text{HfO}_2$ , respectively).<sup>[221,222]</sup> This

will more likely lead to shrinking of the parent NP or formation of multiple nitride NPs from individual oxide NPs.

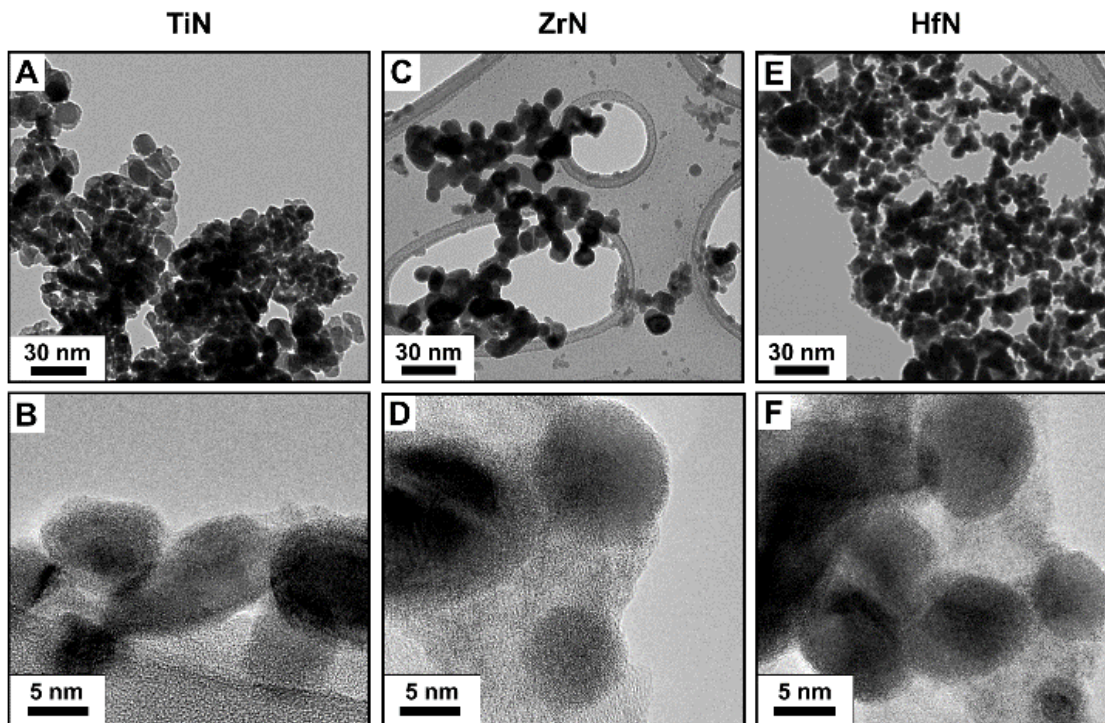


**Figure 30:** TEM images of water dispersed (A, B) TiN, (C, D) ZrN, and (E, F) HfN NPs.

TEM analysis was used to characterize the non-dispersible metal nitride powders as shown in **Figure 31**. The TEM images clearly show that the resulting NPs obtained from the powder samples are polydisperse in size and shape which results in the inability to determine their sizes accurately. The high degree of aggregation and sintering observed for the powder samples can be occurring due to the exothermic nature of the reaction. These NPs can be temporarily re-dispersed in water by sonication; however, the solution is unstable and over time the NPs precipitate from the solution.

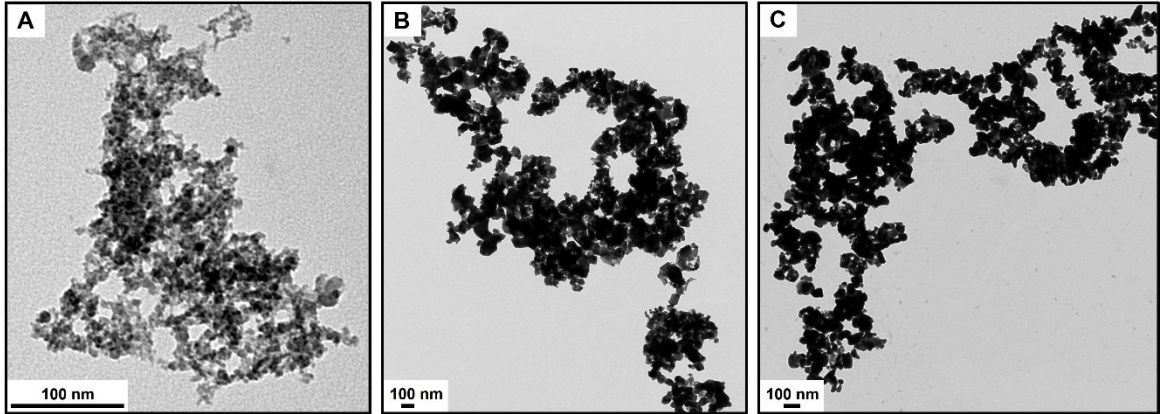


**Figure 31:** TEM images of non-dispersible (A) TiN, (B) ZrN, and (C) HfN powders.

The elemental composition of the dispersible TMN NPs were analyzed using XPS. The high-resolution XP spectrum of the Ti 2p region showed the presence of TiN with a  $2p_{3/2}$  peak at 454.9 eV, oxynitride ( $TiN_xO_y$ ) with a  $2p_{3/2}$  peak at 456.6 eV, and oxides ( $TiO_2$ ) with a  $2p_{3/2}$  at 458.4 eV (**Figure 32**).<sup>[223]</sup> Correspondingly, the high-resolution XP spectrum of the N 1s region showed the presence of TiN and  $TiN_xO_y$  with 1s peaks at 396.8 and 399.0 eV, respectively (**Figure 32**).<sup>[223]</sup> A high-resolution XP spectrum of the Zr 3d region showed the presence of Zr  $3d_{5/2}$  peaks at 179.3, 181.7, and 182.5 eV, corresponding to ZrN,  $ZrN_xO_y$ , and  $ZrO_2$ , respectively (**Figure 33**).<sup>[156]</sup> Similarly, the high-resolution XP spectrum of Hf 4f region showed the presence of HfN,  $HfN_xO_y$ , and  $HfO_2$ , with Hf  $4f_{7/2}$  peaks at 14.4, 16.1, and 18.1 eV, respectively (**Figure 34**).<sup>[224,225]</sup> N 1s spectra showed the presence of nitride (ZrN: 396.7 eV and HfN: 397.3 eV) and oxynitride ( $ZrN_xO_y$ : 400.2 eV and  $HfN_xO_y$ : 400.0 eV) for both ZrN and HfN NPs (**Figure 33** and **Figure 34**).<sup>[156,224,225]</sup> Previous reports have shown the formation of up to a nm thick layer of oxide and oxynitride phases on TiN and ZrN NPs, which agrees with the results obtained in this study.<sup>[154,156]</sup>



It has been determined that the presence of oxide and oxynitride layers could provide an additional degree of freedom for surface chemistry studies. The inertness of TMNs could limit their applications and therefore having an oxide layer can be useful for surface functionalization.<sup>[226]</sup> However, if the oxide layer is not desired, it can be removed by nitridation under  $\text{NH}_3$  flow at elevated temperatures.<sup>[227]</sup>

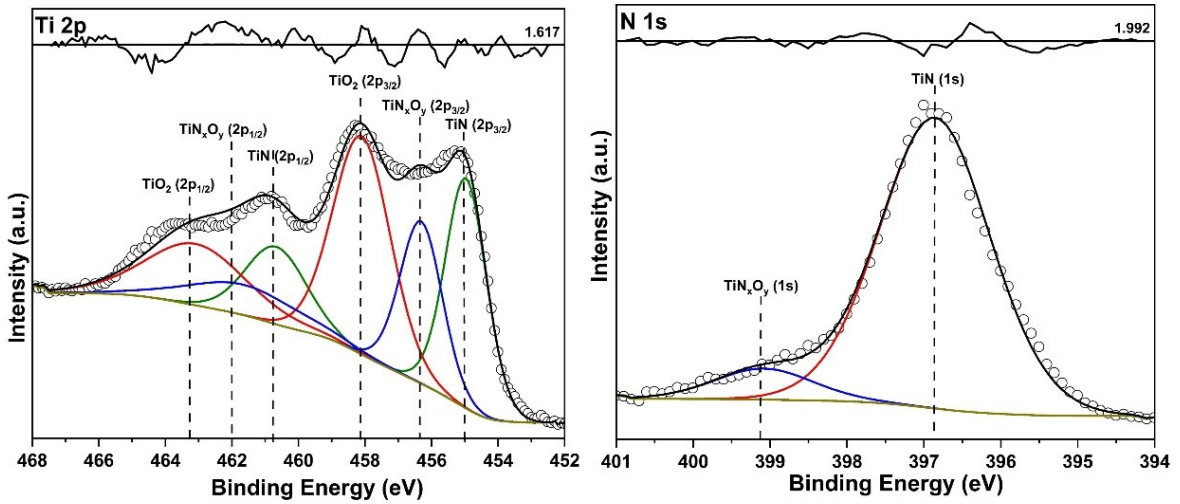


**Figure 32:** High-resolution X-ray photoelectron spectra of Ti 2p and N 1s region of TiN NPs. Experimental data represented as open circles, and the overall fitted data represented as a black line.



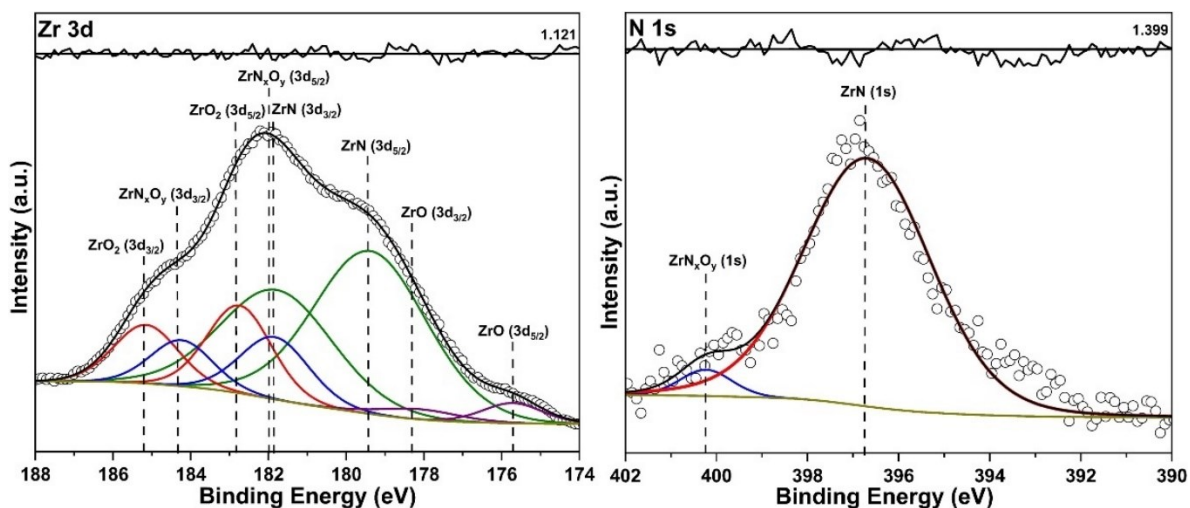


**Figure 33:** High-resolution X-ray photoelectron spectra of Zr 3d and N 1s region of ZrN NPs. Experimental data represented as open circles, and the overall fitted data represented as a black line.

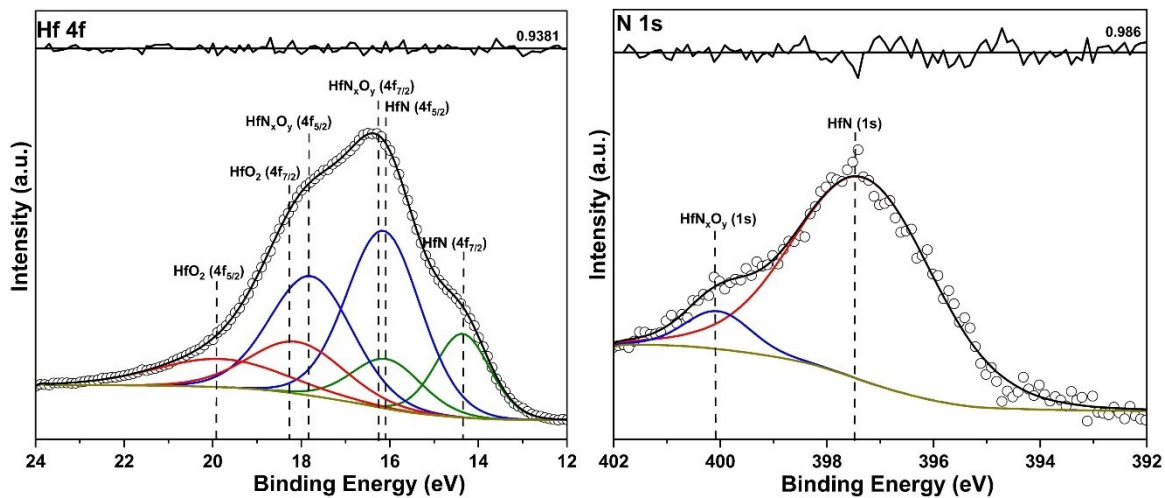


**Figure 34:** High-resolution X-ray photoelectron spectra of Hf 4f and N 1s region of HfN NPs. Experimental data represented as open circles, and the overall fitted data represented as a black line.

Based on the analysis conducted on the NPs, the absorption spectra were computed to represent NPs consisting of a nitride core, and an oxide layer as shown in **Figure 35A**. The data showed that the LSPR maxima of ZrN and HfN NPs should be in the visible region and that of TiN to be in the NIR region of the electromagnetic spectrum. It also showed that the LSPR linewidth of the HfN would be narrower compared to ZrN and TiN. The absorption spectra of the nitride NPs dispersed in water showed LSPRs with maxima at  $\sim 720$ ,  $650$ , and  $560$  nm for TiN, ZrN, and HfN, respectively (**Figure 35B**). The LSPR maxima observed matched very well with the computed data, however the experimental data showed a broader LSPR maxima for all the TMN NPs. This is likely due to the polydispersity of the NPs and particle-particle interactions which were not considered in the computational analysis.

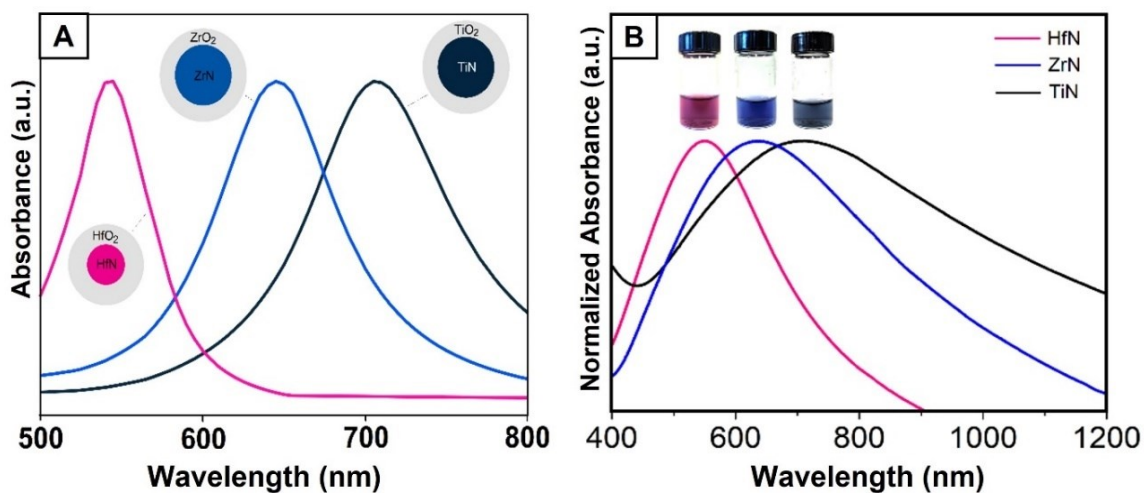


**Figure 35:** (A) Calculated absorption spectra of TiN, ZrN, and HfN NPs. (B) Absorption spectra of aqueous dispersions of TiN, ZrN, and HfN NPs. (Inset: photograph of NPs dispersed in water under white light).

A broad NIR LSPR band has previously been reported for TiN NPs with maxima between 700-1000 nm, and the current results are in agreement with these previous reports.<sup>[154,155]</sup> A recent report on ZrN NPs with an average particle size of 8 nm were reported to exhibit a LSPR at 585 nm.<sup>[156]</sup> The LSPR frequency reported here is comparatively red-shifted which is likely due to the larger NP size (~15 nm). While thin films of HfN have been experimentally examined,<sup>[80]</sup> the optical properties of the NPs remain unexplored to the best of our knowledge.

Calculations have predicted TiN to exhibit major optical losses that arises from transitions occurring from N p  $\rightarrow$  Ti d or Ti p  $\rightarrow$  Ti d bands.<sup>[136]</sup> The degree of optical losses is determined by the position of the p band with respect to the  $E_F$ , the farther the p band, the more energy is required for the transition to occur. Therefore, having a far p band results in minimal optical losses in the visible region. It has been reported that the interband transition for TiN, ZrN, and HfN occur at 1.95, 2.60, and 3.11 eV, respectively.<sup>[68]</sup> This indicates that HfN has the lowest losses, whereas TiN has the highest losses in the region examined. The higher losses would result in broader plasmon bandwidth which could explain the broadness of TiN LSPR compared to ZrN and HfN.<sup>[68]</sup> In these studies, the interband transitions were found to start at 440 nm (2.81 eV), 390 nm (3.18 eV), and 380 nm (3.27 eV) for TiN, ZrN, and HfN, respectively. The experimental values obtained deviate from the calculated ones likely due to the presence of surface oxides.

The colloidal stability of NPs can be determined by measuring their surface zeta potentials. Particles with a zeta potential value between -10 and +10 mV are considered to be charge neutral, and values greater than 10 mV and below -10 mV are considered to possess positively and negatively charged surfaces, respectively.<sup>[197]</sup> NPs with a zeta potential greater than +30 mV or below -30 mV yield long term colloidal stable suspensions.<sup>[197]</sup> The zeta potentials of aqueous suspensions of TiN, ZrN, and HfN NPs were determined to be  $33 \pm 2$ ,  $50 \pm 3$ , and  $43 \pm 1$  mV, respectively, indicating that the particles are positively charged and form stable colloidal suspensions. The hydrodynamic radius of the TMN NPs in Millipore water was determined using the DLS technique and was found to be  $53.4 \pm 0.5$  nm,  $59.4 \pm 0.2$  nm, and  $55 \pm 1$  nm, for TiN, ZrN, and HfN, respectively. The DLS size measurements provide the hydrodynamic radius of the TMNs NPs, whereas TEM provides the actual particle size. Hence, the hydrodynamic radius measured using the DLS is much larger than the particle size determined by TEM ( $12 \pm 3$ ,  $15 \pm 2$ , and  $11 \pm 4$  nm for TiN, ZrN, and HfN, respectively).

The position of the LSPR is dependent on the refractive index of the surrounding medium, as discussed in Chapter 1 (section 1.3.4). To further verify the plasmonic nature of the TMN NPs synthesized in this thesis, their optical properties were investigated in media of varying refractive indices. The NPs could not be effectively dispersed in non-polar solvents and therefore were dispersed in 0, 20, 40, 60, and 84% aqueous sucrose solutions with refractive indices of 1.33, 1.36, 1.40, 1.44, and 1.50, respectively.<sup>[228]</sup> In all the cases a red-shift in LSPR peak was observed with increasing refractive index (**Figure 36A, B, and C**). For TiN NPs, the absorption peak shifted from 721 to 732 nm as

the refractive index was increased from 1.33 to 1.50, respectively (**Figure 36A**). While only a net shift of 11 nm was observed for the TiN NPs, ZrN and HfN NPs were found to be more susceptible to change in local refractive index. A red shift from 650 to 675 nm and 561 nm to 612 nm was observed for ZrN and HfN, respectively (**Figure 36B and C**).

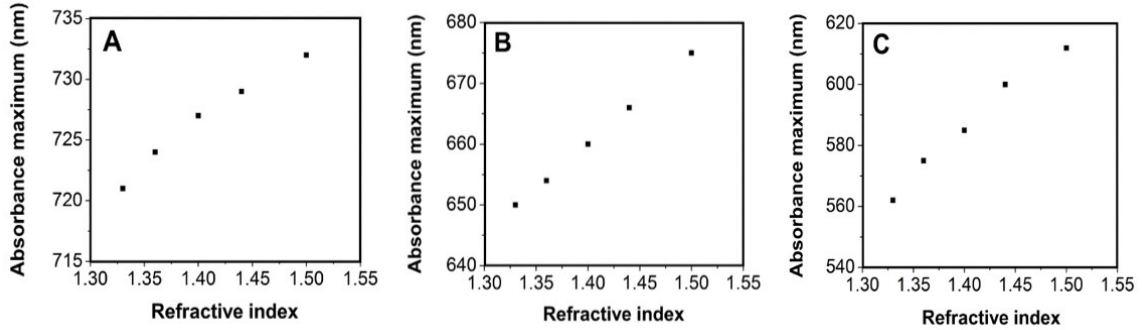


**Figure 36:** Refractive index dependent absorption maxima for (A) TiN, (B) ZrN, and (C) HfN NPs.

These observations are consistent with previous sensitivity studies of Au, Ag, and TiN surface plasmons to the changes in the refractive index of the surrounding medium.<sup>[154,229–231]</sup> The results observed could be due to the significant broadness of the LSPR of TiN compared to ZrN and HfN where shifts in the wavelength is more evident in narrower plasmon peaks compared to broader plasmon peaks.<sup>[85]</sup> Therefore, in this case HfN would be ideal for sensing applications as the plasmon bandwidth is narrow which resulted in a net shift of 51 nm. Recently, Monfared *et al.* have computationally examined the change of the LSPR frequency of TiN, ZrN, and HfN NPs as the refractive index of the surrounding medium was varied between 1.30 and 1.45.<sup>[232]</sup> The results obtained were consistent with the experimental observation indicating that HfN had the largest

wavelength net shift, whereas TiN had the lowest wavelength net shift.<sup>[232]</sup> A figure of merit (**equation 28**) has been introduced in literature<sup>[233]</sup> to compare sensing capabilities of different plasmonic nanostructures:

$$\mathbf{FOM} = \frac{\mathbf{slope (eV RIU^{-1})}}{\mathbf{FWHM (eV)}} \quad (28)$$

where slope is the linear regression slope for the dependence of the plasmon resonance energy on the refractive index, and the FWHM is the plasmon linewidth. However, one of the major issues that still exist is the synthesis of monodisperse NPs because that can play a role in the LSPR broadness. Therefore, future efforts need to focus on improving the particle size distribution.

The thermal stability of the TMN NPs was investigated in solid-state. Thin films of the NPs were drop cast onto a Si wafer and annealed for 1 h at 1000 °C. Some particle damage was observed for the ZrN NPs after the heat treatment, but no significant melting was observed in SEM images (**Figure 37D, E, and F**) compared to **Figure 37A, B, and C**. This result shows that TMN NPs could be promising toward high temperature application, as it is pivotal for NPs to retain their nano-character to maintain their optical properties. It has been reported that the melting temperature of free-standing metal NPs is linearly dependent on the inverse particle diameter.<sup>[234]</sup> Many studies have shown that Ag and Au start to sinter and lose their nano-characters between 120-300 °C depending on their size, shape, and surface coating.<sup>[235–239]</sup> One of the major issues with using NPs for photothermal applications is the presence of surface surfactants which desorb, collapse, or decompose upon heating to temperatures as low as 60 °C.<sup>[235]</sup> Recently, Krekeler *et al.* have

investigated the thermal stability of TiN films and the results revealed exceptional structural stability at elevated temperatures of 1400 °C under medium and high vacuum conditions.<sup>[240]</sup> Additionally, Setoura *et al.* have demonstrated that the threshold temperatures of the laser-induced photothermal reshaping of ZrN nanocubes ranged from 1127-1827 °C.<sup>[239]</sup> These findings demonstrate the capability of incorporating TMN nanostructures towards fabricating thermally stable photonic and plasmonic devices for harsh environments.

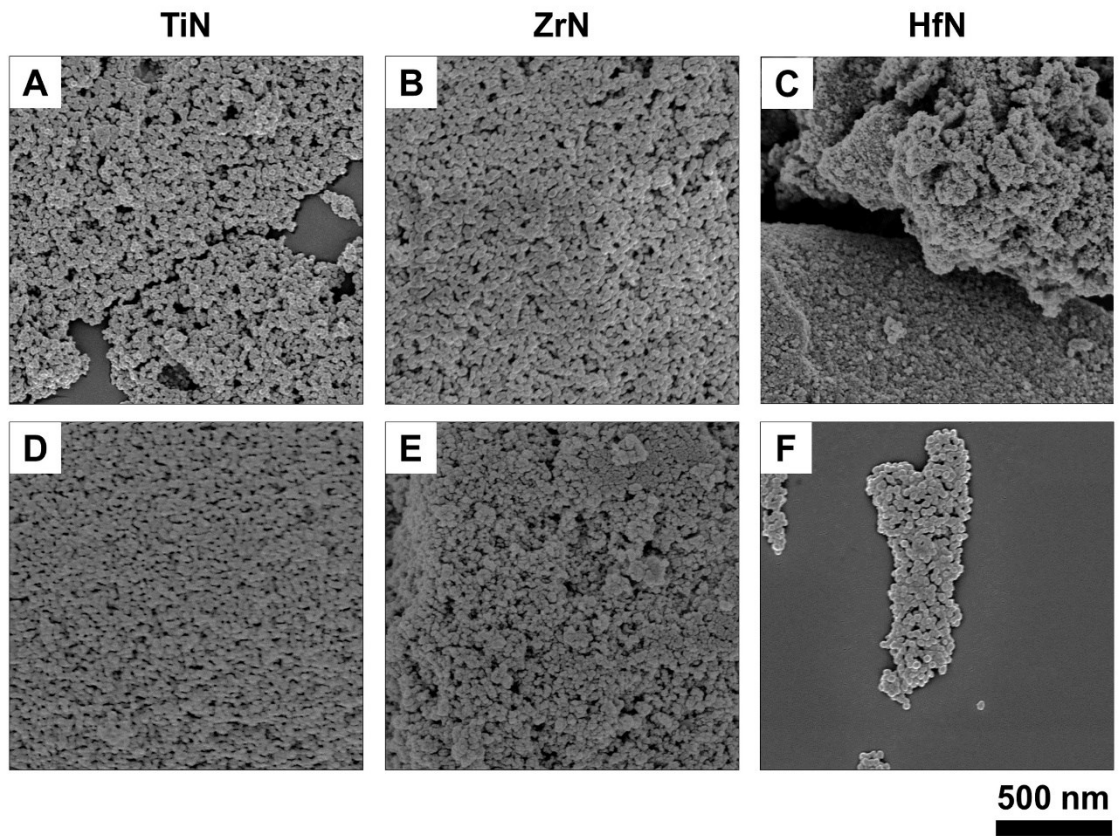


**Figure 37:** SEM images of TiN, ZrN, and HfN NPs before (A, B, and C) and after annealing at 1000 °C (D, E, and F).

### 3.3 Conclusion

In conclusion, a solid-state metathesis route was developed to prepare group IVB TMN plasmonic NPs using metal oxide precursors. The resulting TMN NPs were crystalline with a cubic structure. An average particle size of  $12 \pm 3$ ,  $15 \pm 2$ , and  $11 \pm 4$  nm was observed for TiN, ZrN, and HfN NPs, respectively. All the TMN NPs showed some degree of surface oxidation, and they were all dispersible in water. The absorbance measurements showed TiN to have a LSPR in the NIR region, whereas ZrN and HfN displayed LSPRs in the visible region. It was determined that the TMN NPs exhibit a positive zeta charge of  $33 \pm 2$ ,  $50 \pm 3$ , and  $43 \pm 1$  mV for TiN, ZrN, and HfN, respectively. The ease of synthesis, high thermal stability, and the effective plasmonic behavior exhibited by these nanomaterials make them ideal for various applications ranging from photothermal therapy to plasmon enhanced sensing.



## Chapter 4: Photothermal Properties of Group IVB Nitrides in NIR Region

*This author wishes to clarify her contribution to the research described in Chapter 4 of this thesis document.* This chapter discusses the photothermal properties of group IVB TMN NPs in NIR region. The photothermal results of the group IVB TMN NPs were compared to Au NRs which are the benchmark material for photothermal applications. The preparation of the group IVB TMN NPs and the photothermal measurements are discussed in Chapter 2.

My contribution to this study includes synthesizing the NPs and investigating the photothermal properties, characterizing the NPs using XRD, UV-vis spectroscopy, TEM, and writing the majority of the manuscript. HR-TEM images were obtained by Dr. Regina Sinelnikov and Hoayang Yu. Computational work was conducted by Dr. Yashar Monfared. This work has been published in Langmuir Journal.

**Reference:** R. A. Karaballi, Y. E. Monfared, M. Dasog, Photothermal Transduction Efficiencies of Plasmonic Group IVB Metal Nitride Nanocrystals. *Langmuir*, **2020**, 36, 5058-5064. Reprinted by permission of American Chemical Society.

## 4.1 Introduction

Plasmonic nanostructures can efficiently convert incident light into heat, a phenomenon known as photothermal effect. This occurs via three sequential processes: field enhancement, hot electron generation, and photothermal conversion, as shown in **Figure 38**.<sup>[241]</sup> Briefly, upon light absorption, the electrons are excited from occupied states to unoccupied states, forming hot electrons (illustrated as the red area in the **Figure 38**).<sup>[241]</sup> The non-thermally distributed electrons undergo non-radiative emission through electron-electron scattering to achieve a thermal distribution which increases the localized surface temperature of the NP. The rapid heating is followed by cooling to equilibrium through energy exchange between the electrons and lattice phonons via electron-phonon interactions which results in heat dissipation to the surrounding medium.<sup>[242]</sup>

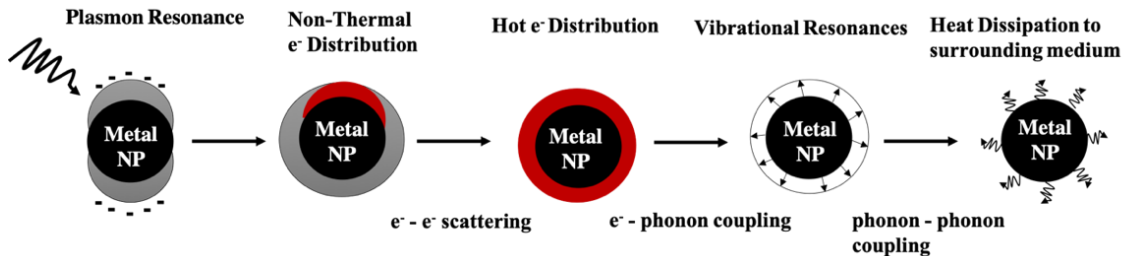


**Figure 38:** Illustration of the photothermal light to heat conversion of plasmonic NPs. Adapted from reference <sup>[242]</sup>.

This property of plasmonic nanostructures has been exploited for photothermal ablation of cancer cells and bioimaging,<sup>[88,243,244]</sup> catalysis,<sup>[245–248]</sup> and desalination and water treatment.<sup>[201,249]</sup> For biological photothermal therapy, plasmonic nanostructures that can absorb in the NIR region are important as biological tissues are transparent between

wavelengths of ~650–1350 nm.<sup>[250]</sup> Currently, Au NRs are the benchmark material studied for photothermal applications as the plasmon frequency of this material lies within the biological transparency window.<sup>[251–253]</sup> Photothermal transduction efficiencies between 20 and 65% have been reported for Au NRs.<sup>[254–257]</sup> Other plasmonic photothermal materials with higher efficiencies such as spiky Au NPs (78.8%),<sup>[258]</sup> Au-Ag nanourchins (80.4%),<sup>[259]</sup> Au-ZnS core/shell nanostructures (86%),<sup>[260]</sup> Fe<sub>3</sub>O<sub>4</sub>-Au core/shell nanostars (88.9%),<sup>[199]</sup> and Au nanobipyramids (97%)<sup>[261]</sup> have emerged, as shown in **Table 1**, however, such complex structures are often challenging to synthesize. To improve the blood-assisted circulation in the body, it is preferable to utilize nanostructures with sizes ranging from 5–50 nm,<sup>[262,263]</sup> however, many of the complex shapes and hybrid plasmonic materials tend to be larger (>50 nm) and Au NRs typically fall on the upper end of this size limitation.

Plasmonic TMNs have been theoretically predicted to have plasmonic responses in the visible and NIR region of the electromagnetic spectrum making them well-suited for photothermal therapy.<sup>[68,69,143]</sup> Furthermore, these nitrides have been shown to be biocompatible and can be used for biological implants.<sup>[264,265]</sup> Initial photothermic studies have focused on TiN NPs and efficiencies of 48% and 58.8% have been reported under NIR excitation.<sup>[166,266]</sup> TiN NPs have been added as a co-catalyst to Pt NPs to serve as a platform for the plasmon mediated photothermal catalysis.<sup>[267]</sup> He *et al.* have investigated the photothermal performance of PEGlated-TiN for photothermal cancer therapy and their utilization as photoacoustic tomography imaging agents for *in vivo* tumor detection.<sup>[268]</sup> For the photothermal measurements, the TiN NPs were irradiated with 808 nm laser at 2 W cm<sup>-2</sup> for 10 minutes and the change in temperature was monitored every

10 seconds.<sup>[268]</sup> The results revealed that the temperature of the solution containing TiN increased by 29.5 °C in 10 minutes, which suggest that TiN can rapidly and efficiently convert the NIR light into thermal energy. The photothermal transduction efficiency of the TiN NPs were determined to be 48%.<sup>[268]</sup> TiN NPs have also been used for solar water evaporation application and thermal conversion efficiencies upwards of 80% were observed.<sup>[269]</sup> While, thermal applications of TiN NPs have been reported, ZrN and HfN remain unexplored. If group IVB TMNs are to be used for photothermal applications, their transduction efficiencies need to be established.

Herein, the photothermal properties of unmodified and free-standing TiN, ZrN, and HfN NPs at 850 nm are reported. The photothermal transduction efficiencies were determined for 10.0 nM TMN solutions under 1 W cm<sup>-2</sup> illumination and compared to commercially purchased citrate stabilized Au NRs. The temperature change as a function of NP concentration and illumination power density were also investigated. The cycling stability of the TMNs were studied at 1 W cm<sup>-2</sup> irradiation. Computational analysis was conducted to understand the efficiency trends observed in the experimental data.

**Table 1:** Photothermal efficiencies of plasmonic nanostructures reported in the literature.

Material	Laser (nm)	Incident power	Photothermal efficiency (%)	Ref
Au@Cu <sub>2</sub> O + NaHS	808	1 W cm <sup>-2</sup>	34.2	[270]
AgI-Ag <sub>2</sub> S	808	420 mW	52	[271]
Au nanobipyramids	785	190 mW	97	[261]
Au nanobipyramids	808	265 mW	74	[261]
Ag-Au nanoplates	808	1 W cm <sup>-2</sup>	67	[272]
Au zein nanoshells	808	500 mW	22.85	[273]
Au nanostars	785	390 mW cm <sup>-2</sup>	34.5	[274]
Au nanostars	1064	390 mW cm <sup>-2</sup>	13.0	[274]
Au nanobranched shells	808	1.5 W cm <sup>-2</sup>	55.7	[275]
Au nanorods/MoS <sub>2</sub>	808	0.2 W cm <sup>-2</sup>	68.8	[276]

Material	Laser (nm)	Incident power	Photothermal efficiency (%)	Ref
Au@SiO <sub>2</sub> dots	808	2 W cm <sup>-2</sup>	22.7	[277]
Au nanorods	808	0.8 W cm <sup>-2</sup>	52.8	[254]
Au nanorods/graphene oxide	808	300 mW	72.59	[278]
Au@MOFs	808	1.8 W cm <sup>-2</sup>	30.2	[279]
Au@MOFs	1064	1.8 W cm <sup>-2</sup>	48.5	[279]
Au nanoplates@TiO <sub>2</sub>	1064	1 W cm <sup>-2</sup>	42.05	[280]
Au nanoparticles	514	2.4 W cm <sup>-2</sup>	9.9	[208]
Spiky Au nanostructures	980	0.5 W cm <sup>-2</sup>	78.8	[258]
Si-Au nanoparticles	808	1 W cm <sup>-2</sup>	24.1	[281]
Au nanorods	808	20 W cm <sup>-2</sup>	58	[282]
Au nanorods	815	0.151 W	55	[209]
Au-SiO <sub>2</sub> hybrid	815	0.151 W	30	[209]
Au-Au <sub>2</sub> S hybrid	815	0.151 W	59	[209]
Au nanorods	808	2 W cm <sup>-2</sup>	50	[283]
Au nanoshells	808	2 W cm <sup>-2</sup>	25	[283]
Au nanorods	808	1 W cm <sup>-2</sup>	22	[257]
Au nanoshells	808	1 W cm <sup>-2</sup>	13	[257]
Au nanovesicles	808	1 W cm <sup>-2</sup>	37	[257]
Core-shell Au nanorod @ layered double hydroxide	808	2 W cm <sup>-2</sup>	60	[284]
Au nanopolyhedrons	808	1.72 W	18	[260]
Au-Ag <sub>2</sub> S hybrid nanostructures	808	1.72 W	64	[260]
Au-ZnS hybrid	808	1.72 W	86	[260]
Hollow Au-Ag nanourchins	808	1 W	80.4	[259]
Fe <sub>3</sub> O <sub>4</sub> @Au nanostructures	808	0.3 W	88.9	[199]
Au-Cu <sub>7</sub> S <sub>4</sub> hybrid	980	0.3 W	63	[285]
Au-Cu <sub>2-x</sub> Se hybrid	808	1.34 W cm <sup>-2</sup>	32	[286]
Ag@Ag <sub>2</sub> S	635	420 mW	63.7	[287]
Ag@Ag <sub>2</sub> S	808	420 mW	64.7	[287]
Ag@Ag <sub>2</sub> S	1064	420 mW	79.3	[287]
Coral shaped Au nanostructures	808	0.5 W cm <sup>-2</sup>	32	[288]
FePt nanoparticles	800	1 μJ per pulse	30	[289]
TiN nanoparticles	808	2 W cm <sup>-2</sup>	48	[268]
PDDA/PSSA coated TiN	808	0.8 W cm <sup>-2</sup>	44.6	[266]
TiN nanoparticles	1064	1 W cm <sup>-2</sup>	22.8	[290]
SiO <sub>2</sub> coated TiN	785	2 W cm <sup>-2</sup>	58.5	[166]

## **4.2 Experimental**

### ***4.2.1 Materials***

Titanium dioxide (TiO<sub>2</sub>, 99.9%, 18 nm), zirconium dioxide (ZrO<sub>2</sub>, 99.95%, 20 nm), hafnium dioxide (HfO<sub>2</sub>, 99.99%, 61–80 nm), and magnesium nitride (Mg<sub>3</sub>N<sub>2</sub>, 99%, –325 mesh) were purchased from U.S. Research Nanomaterials Inc. Citrate-stabilized Au nanorods (55 nm x 15 nm, aspect ratio:4.1, hydrodynamic radius: 5 to 25 nm, zeta potential: -20 to -80 mV) were purchased from Nanocomposix. Hydrochloric acid was purchased from Anachemica. All glassware was cleaned thoroughly with deionized (DI) water and then acetone and placed in the oven to dry prior to use.

### ***4.2.2 Preparation of Transition Metal Nitride Nanoparticles***

The group IVB TMN NP solutions were synthesized as discussed in section 2.8.1.

### ***4.2.3 Characterization Techniques***

Powder XRD, TEM, and UV-vis were performed as discussed in section 3.1.3.

### ***4.2.4 Photothermal Measurements***

Photothermal studies were performed as discussed in section 2.9.

### ***4.2.5 Computational Studies***

Computational studies were performed as discussed in section 2.10.

### 4.3 Results and Discussion

TMN NPs with an average size of 15 nm was used for this study and their performance was compared to commercially purchased Au NRs with length and width of  $50 \pm 5$  and  $12.3 \pm 0.7$  nm, respectively (**Figure 39**).

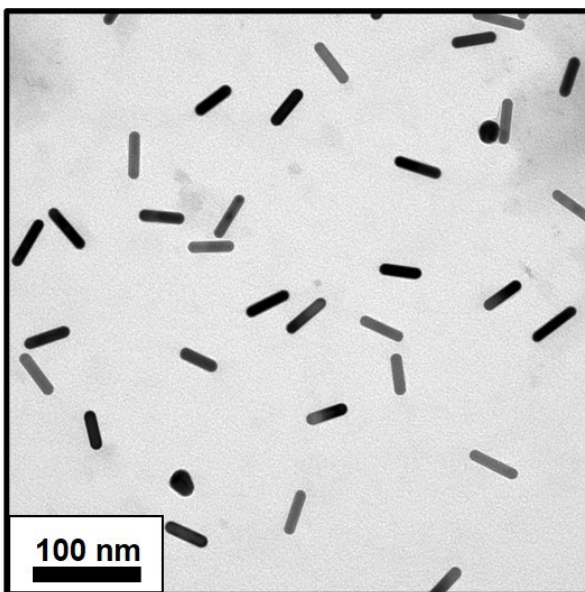


**Figure 39:** TEM image commercially purchased citrate stabilized Au NRs.

As seen in Chapter 3, XPS results have shown the presence of a shell consisting of oxides and oxynitrides around the TMN NPs prepared using the current method.<sup>[291]</sup> The exact thickness of the oxide shell is difficult to estimate given the nonuniform thickness of the oxide shell around each particle and the varying degree of oxidation observed on different particles in a sample set as shown in the TEM images of the HfN NPs (**Figure 40**). Based on multiple particle analyses, the oxide shell thickness typically varied between 1 and 4 nm for all TMN NPs.

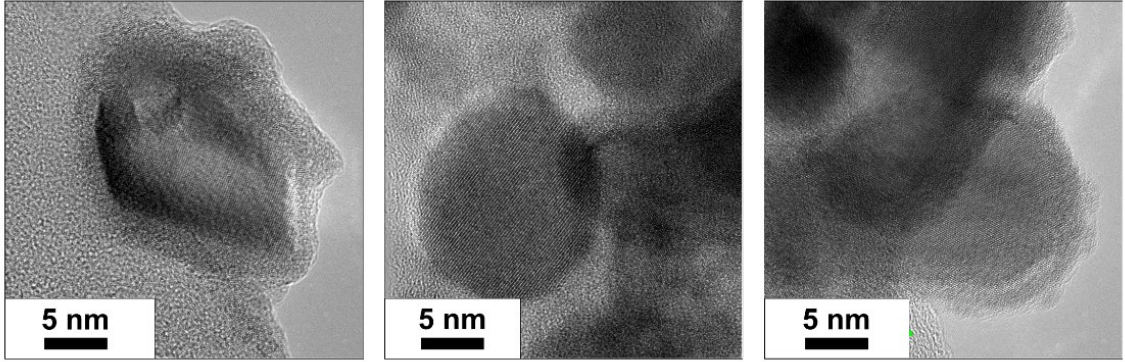


**Figure 40:** TEM images of HfN NPs showing varying thickness of oxide shell around the particles.

The molar concentrations of the TMN NP solutions were determined using **equation (29)**:<sup>[292]</sup>

$$\mathbf{C} = \frac{\mathbf{N}}{\mathbf{V}N_{\mathbf{A}}} \quad (29)$$

where,  $\mathbf{N}$  is the number of NPs in the solution,  $\mathbf{V}$  is the volume of the solution, and  $N_{\mathbf{A}}$  is Avogadro's constant. The number of NPs ( $\mathbf{N}$ ) can be calculated using **equation (30)**:

$$\mathbf{N} = \frac{\mathbf{m}_{\text{total}}}{\mathbf{m}_{\text{particle}}} \quad (30)$$

where,  $m_{\text{total}}$  and  $m_{\text{particle}}$  are the weights of all the NPs and individual NP, respectively. The weight of an individual spherical NP ( $m_{\text{particle}}$ ) can be calculated using **equation (31)**:

$$\mathbf{m}_{\text{particle}} = \frac{\pi d^3}{6} \rho \quad (31)$$



where,  $d$  is the diameter of the NP and  $\rho$  is the bulk density of the TMN. The molar extinction coefficients of 10.0 nM TMN and Au NR solutions as a function of wavelength is shown in **Figure 41A**. The Au NRs exhibited two LSPR peaks at 512 and 810 nm resulting from the transverse and longitudinal resonances, respectively. TiN LSPR peak is relatively broad compared to the other materials which has been reported previously in literature to be due to larger plasmon losses in the visible region.<sup>[68]</sup> Au NRs experiences losses due to interband transitions that occurs below 500 nm which results in broader transverse plasmon absorption.<sup>[66]</sup> Whereas, ZrN, and HfN experience interband transition below 300 nm which makes them the best materials with low losses in the visible region.<sup>[68]</sup> The mass extinction coefficient of TiN, ZrN, and HfN at the LSPR maximum was 19, 22, and 8 L g<sup>-1</sup> cm<sup>-1</sup>, respectively (**Figure 41B**). Similar values have been observed for TiN NPs previously and addition of a protective SiO<sub>2</sub> layer can further enhance the extinction coefficients.<sup>[166]</sup>

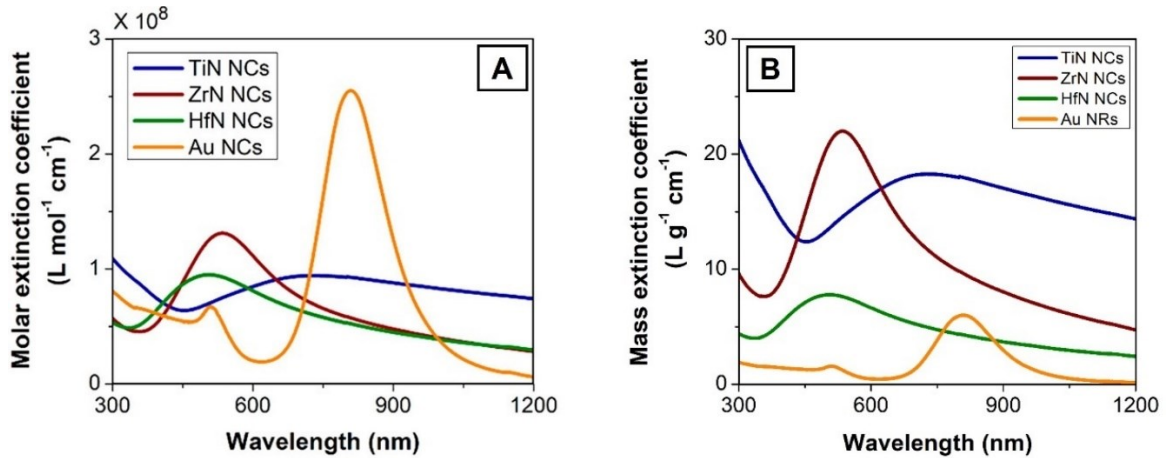


**Figure 41:** (A) Extinction spectra of TMN NPs and citrate functionalized Au NRs in water. (B) Mass extinction coefficients of TiN, ZrN, HfN NPs and Au NRs dispersed in water.

NIR illumination is commonly used for photothermal therapy applications as it provides a desirable tissue-penetration depth. For this study, an 850 nm LED source with 40 nm linewidth at FWHM was used as the excitation source. The temperature change of 10.0 nM aqueous solutions of TMNs and Au NRs was recorded as a function of time under continuous irradiation at power density of  $1.0 \text{ W cm}^{-2}$  (**Figure 42**). After 30 minutes, a steady-state temperature was reached and an average change in temperature of  $42 \pm 2$ ,  $40 \pm 1$ , and  $38 \pm 2$  °C was achieved for HfN, ZrN, and TiN, respectively. The Au NRs reached a maximum temperature of  $31 \pm 3$  °C and the water blank had a temperature increase of  $4 \pm 1$  °C. After the samples were irradiated for 30 minutes, the light source was subsequently turned off, and the temperature decay was monitored over the next 30 minutes to determine the rate of heat transfer from the nanostructures to the surroundings (**Figure 42**). The time constant ( $\tau$ ) for the heat dissipation from the system to the surroundings can be determined from the slope of the plot of time from the cooling period versus negative logarithm of the temperature change during the cooling period (**Figure 43**).

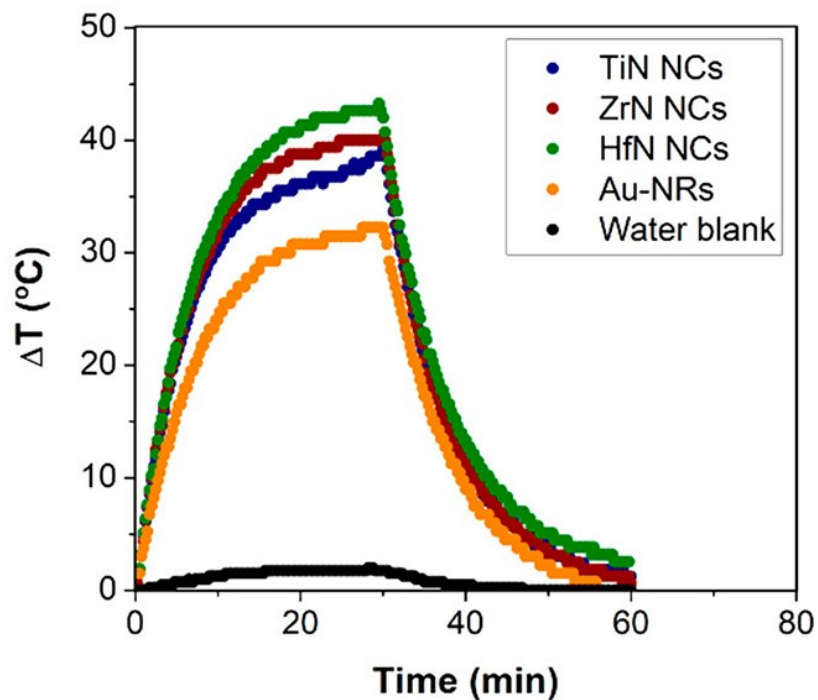


**Figure 42:** Representative temperature change plots as a function of time during heating (first 30 minutes) and cooling (last 30 minutes) for 10.0 nM TMN and Au NR solutions.

The value of the time constant ( $\tau$ ) from the slope (listed in **Table 2**) can be used in **equation (23)**, to calculate the product of heat transfer coefficient ( $h$ ) and the surface area ( $S$ ).  $Q_0$  represents the rate of heat production from the quartz cuvette and the water after light absorption and was measured to be 0.024 W. In order to accurately determine the photothermal transduction efficiencies, the average absorbance between 830–870 nm which corresponds to the linewidth of the LED source was used for the effective optical density  $A_\lambda$ , and the values are listed in **Table 2**.

**Table 2:** Summary of photothermal parameters for TMNs and Au NRs.

Sample	$\Delta T$ (°C)	$\tau$ (s)	A ( $\lambda = 850$ nm)	$\eta_T$ (%)
TiN NPs	$38 \pm 2$	$597 \pm 32$	0.906	$49 \pm 3$
ZrN NPs	$40 \pm 1$	$514 \pm 28$	0.527	$58 \pm 2$
HfN NPs	$42 \pm 2$	$555 \pm 20$	0.488	$65 \pm 4$
Au NRs	$31 \pm 3$	$428 \pm 52$	2.549	$43 \pm 3$

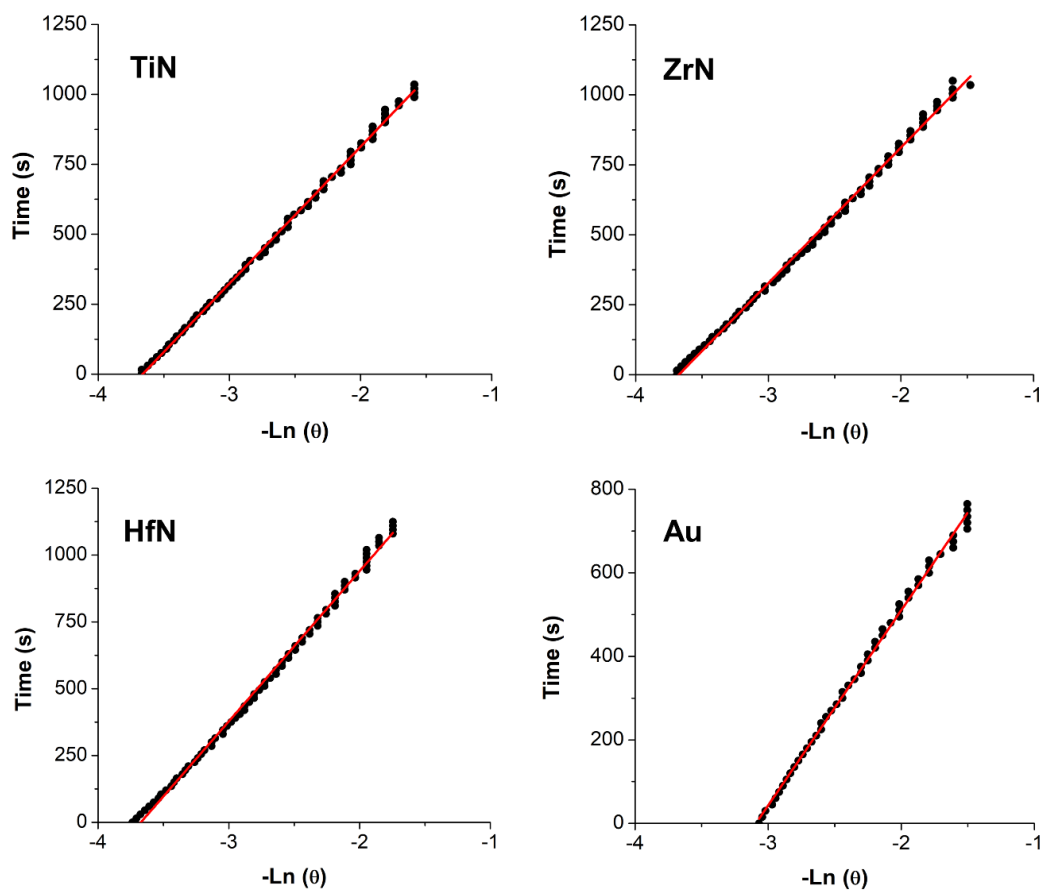


**Figure 43:** Plots of cooling time vs. negative natural log of the temperature change during the cooling stage for TMN NPs and Au NRs.

Thus, the photothermal transduction efficiencies were calculated using **equation (26)**, and were found to be  $65 \pm 4$ ,  $58 \pm 2$ ,  $49 \pm 3$ , and  $43 \pm 2\%$  for HfN, ZrN, TiN, and Au NRs, respectively (**Figure 44A**). Recent studies on solar-driven water evaporation using plasmonic TMN NP films deposited onto a nanoporous aluminium oxide substrate showed similar efficiency trends, where HfN performed better than ZrN and TiN.<sup>[293]</sup> Plasmonic nanomaterials with LSPR bands closer to the excitation wavelength (such as Au NRs and TiN NPs in this study) would be expected to have higher efficiency; however, the empirical data revealed the opposite trend. To further understand this trend, computational studies were performed to calculate absorption and scattering behaviour of the NPs.

The scattering cross-section of the TMN NPs and Au NRs were studied numerically. Considering 40 nm FWHM bandwidth of the LED source around 850 nm, the average (effective) scattering cross-section of TMN NPs and Au NRs between 830 nm and 870 nm were calculated. As shown in **Figure 44B**, the Au NRs had significantly higher effective scattering cross-section than the TMN NPs which is due to their larger size and asymmetric geometry. The results also indicate that the effective scattering cross-sections of TiN NPs are larger than that of the HfN and ZrN at 850 nm. The larger scattering cross-section causes a lower absorption efficiency for TiN NPs which can in turn be responsible for the lower photothermal conversion efficiency of these NPs. The simulations results are consistent with the trends observed experimentally, as HfN exhibit the smallest scattering cross-section and therefore the highest photothermal conversion efficiency. Recently, O'Neill *et al.* investigated, for the first time, the light induced relaxation process in water dispersed HfN NPs that were synthesized using our solid-state metathesis method,

and the results were compared to Au NPs.<sup>[294]</sup> These studies demonstrated that HfN NPs converts absorbed photons into heat within <100 femtoseconds (fs) which is much higher than Au NPs which occurs at 4.6 picoseconds (ps). This is due to stronger electron-phonon coupling in HfN compared to Au.<sup>[294]</sup> Compared to the other TMN NPs, HfN demonstrated the highest heating rate followed by ZrN and then TiN which is consistent with the trend observed in our studies. Due to lower light scattering and stronger electron-phonon coupling, we hypothesize that HfN undergoes rapid and efficient thermalization of excited electrons leading to higher photothermal efficiency.

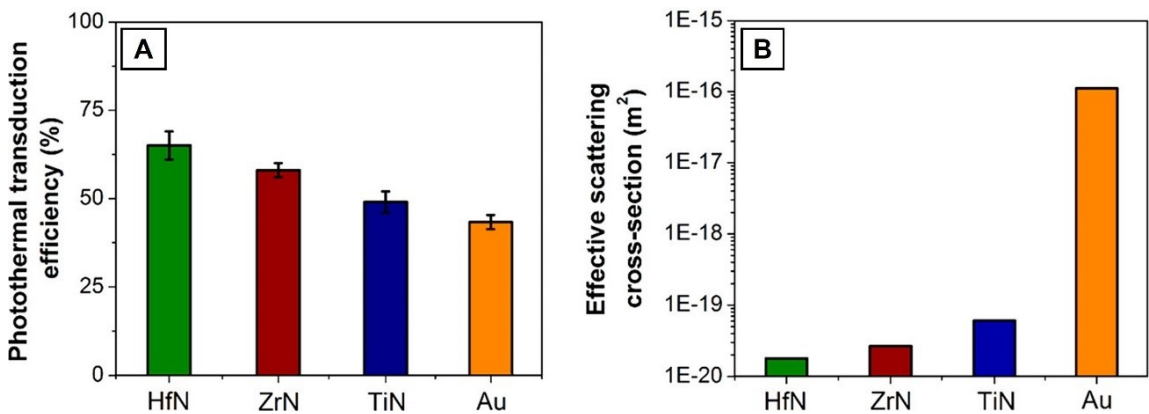


**Figure 44:** (A) Photothermal transduction efficiencies of TMN NPs and Au NRs under  $1.0 \text{ W cm}^{-2}$  illumination at 850 nm. (B) FEM simulations of effective scattering cross-sections of TMN NPs and Au NRs on a log scale at 850 nm.

The cycling stability of the TMNs were evaluated by switching the illumination on/off, for 30 minutes each, over 5 cycles (**Figure 45A, B, and C**). No significant degradation was observed for the change in temperature for any of the TMN solutions. The change in temperature of 10.0 nM TMN solutions at different illumination power densities (1.0, 0.75, 0.50, and 0.25 W cm<sup>-2</sup>) was recorded as shown in **Figure 46**. The temperature changed linearly with the illumination density which is consistent with the previous reports on Au NRs.<sup>[295]</sup> There was no significant change in the photothermal transduction efficiencies observed at different illumination intensities.

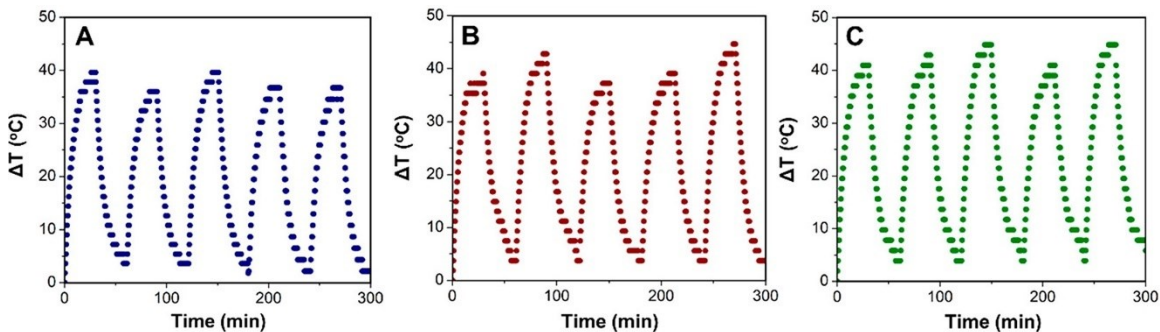


**Figure 45:** Photothermal stability of 10.0 nM (A) TiN, (B) ZrN, and (C) HfN NP solutions over 5 cycles at 850 nm under 1 W cm<sup>-2</sup> illumination.

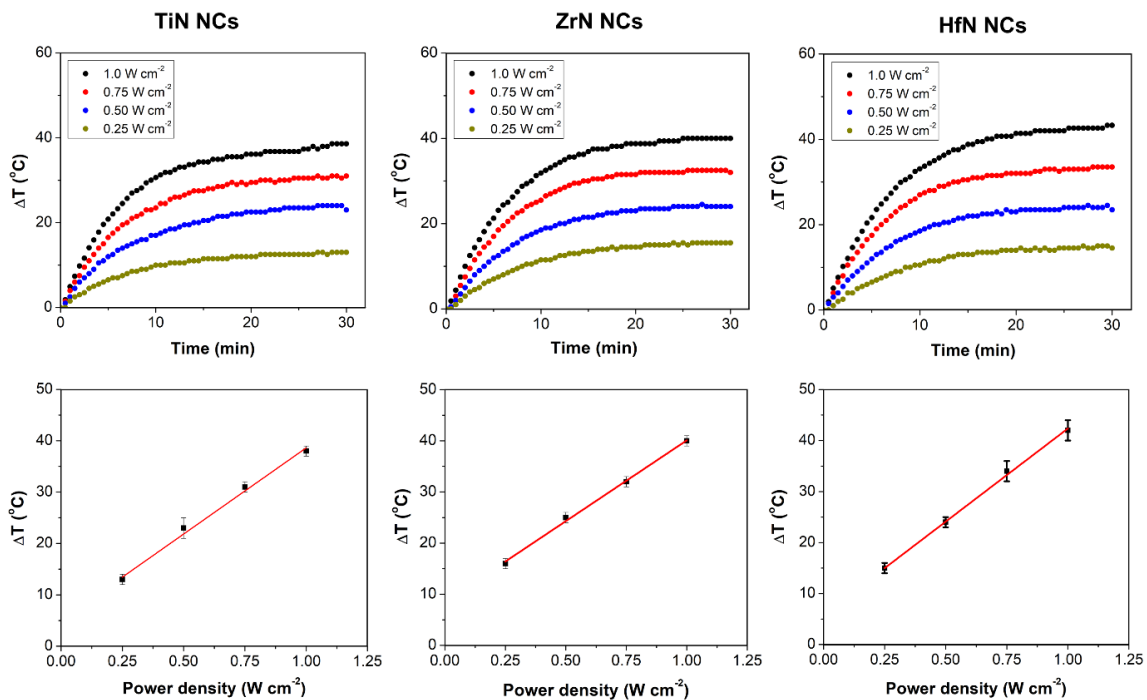


**Figure 46:** Representative temperature change plots as a function of time of TMN NPs at 1.0, 0.75, 0.50, and 0.25  $\text{W cm}^{-2}$  illumination intensities at 850 nm.



#### 4.4 Conclusion

In summary, photothermal transduction efficiencies of group IVB TMN NPs dispersed in water were determined at  $\lambda = 850$  nm. HfN displayed the highest efficiency of 65% despite having a LSPR maximum (510 nm) furthest from the excitation wavelength. This was followed by ZrN (58%), TiN (49%), and Au NRs (43%). Based on the FEM model, it was determined that the HfN had the lowest scattering cross-section which maximized the light-to-heat conversion, whereas Au NRs were determined to have a large scattering cross-section that resulted in lower photothermal transduction efficiencies. The TMN NPs were stable over five cycles of continuous excitation. The high photothermal efficiencies combined with their established biocompatibility, group IVB TMN NPs have a promising future as plasmonic cancer therapy agents. Future investigations will focus on establishing the surface chemistry of these NPs for *in vivo* studies.

## **Chapter 5: Oxidative and Colloidal Stability of Plasmonic Group IVB Nitrides**

*This author wishes to clarify her contribution to the research described in Chapter 5 of this thesis document.* This chapter discusses the oxidative and colloidal stability of plasmonic group IVB TMN NPs using the solid-state metathesis reaction. The synthesized NPs were characterized using various techniques as described in experimental section of this thesis (Chapter 2).

My contribution to this study includes synthesizing group IVB TMN NPs and testing their colloidal and oxidative stability. The colloidal stability was tested using UV-vis spectroscopy where the LSPR position and intensity were monitored over time. The oxidative stability was monitored by adjusting the pH of the solutions and performing the zeta potential measurements. My colleague Dreenan Shea assisted me with adjusting the pH of these colloidal solutions. The XPS measurements were performed by Andrew George.

## 5.1 Introduction

The recent studies of plasmonic group IVB TMNs have either focused on their synthesis or their application. However, one of the major challenges that many researchers have not been focusing on is investigating the stability of these nanostructures. As mentioned in Chapter 1, many of the plasmonic nanomaterials explored suffer from rapid oxidation which decreases their stability and alters their plasmonic responses. It has been shown that the long-term colloidal stability is dependent on the dispersion medium.<sup>[230]</sup> The liquid medium influences the interparticle forces and chemical reactivity, therefore, affects aggregation, size, and shape of the NPs and thus impacts the LSPR energy and intensity. For example, Ag NPs are prone to aggregation which decreases the active surface area and, as a result, a significant decrease in their unique antimicrobial or catalytic activities has been observed.<sup>[236,296,297]</sup> The dispersion stability of NPs is also influenced by the temperature, pH, oxygen concentration, and salt concentration.<sup>[298]</sup> Depending on the targeted applications, these parameters can be detrimental to the stability of the NPs. For example, when biological applications are considered, the NP stability against salts in physiological conditions is a requirement.<sup>[299]</sup> The increase in the ionic strength of the medium through the addition of salt has been shown to cause NP aggregation due to charge screening, thus proper surface modification of NPs is essential to avoid aggregation.<sup>[300]</sup>

Efforts have been made to explore effective ways to improve the stability and re-dispersibility of NPs. The use of capping agents (e.g., citrate, CTAB, etc.) to avoid agglomeration and aggregation of NPs has been commonly used for Au and Ag NPs.<sup>[83,84]</sup> The stabilization of NPs by a polymer has been extensively explored for many years,

especially towards biological applications because it inhibits aggregation *in vitro* and *in vivo* and protects the NPs from being detected by the immune system.<sup>[23]</sup> Recently, Andrade *et al.* investigated the long-term stability of Au NPs coated with cetuximab and reported solution stability up to 24 months.<sup>[301]</sup> Additionally, Sharaf *et al.* investigated the thermal stability of citrate-capped Au NPs solution and compared it with polymer-protected Au NPs, and found that the polymer-protected Au NPs exhibit much higher long-term stability after aging for over 3 years.<sup>[235]</sup> These studies have shown that the impact of prolonged and cyclic heating on the stability of the Au NPs suspension is highly dependent on the surface coating used.<sup>[235]</sup> Thus, researchers need to investigate the long-term stability of the NP colloidal suspension to maximize their application potential.

Bulk TMNs are known to exhibit high chemical and oxidative stability, hence their common use in decorative coatings, protective and anti-corrosive coatings, cutting tools and machining equipment.<sup>[143]</sup> However, at the nanoscale, the properties may be different than their bulk counterparts due to high surface to volume ratios. Rapid surface oxidation to form oxides or oxynitrides on group IVB TMN NPs has been demonstrated by our group (Chapter 3) and other researchers.<sup>[154–156]</sup> Currently there is no systematic study to determine if this surface oxide is passivating or if oxidation continues over time. Furthermore, the colloidal stability of group IVB TMN NPs prepared using the method discussed here is due to the positively charged NP surface. It remains unclear how this surface charge and colloidal stability changes as a function of solution pH. Recently, He *et al.* have shown that coating TiN NPs with PEG polymer resulted in narrower size distribution, better dispersibility, and longer colloidal stability up to one week without

aggregation.<sup>[268]</sup> The TiN-PEG NPs colloidal suspension was tested between the pH values of 6.8-7.4 and excellent stability and long blood retention for *in vivo* experiments was observed. PEGylation of NPs is a commonly used technique to prevent aggregation through increasing steric repulsion between the NPs and trapping smaller seed NPs to avoid uncontrolled growth via ripening.<sup>[302]</sup> These studies showed that TiN-PEG NPs have good biocompatibility and can be used as photothermal agents for cancer treatment.<sup>[268]</sup> Additionally, Gschwend *et al.* demonstrated that the plasmonic performance of TiN is much improved when coated with SiO<sub>2</sub> which prevents reoxidation, dissolution, and agglomeration.<sup>[166]</sup> The SiO<sub>2</sub>-coated TiN showed photothermal efficiency of 58.5%, outperforming bare TiN and Au nanoshells.<sup>[166]</sup> Similarly, Exarhos *et al.* have studied the effect of oxidation on uncoated ZrN NPs in comparison to SiO<sub>x</sub>N<sub>y</sub> coated ZrN NPs.<sup>[156]</sup> These studies demonstrated that coating the ZrN NPs with SiO<sub>x</sub>N<sub>y</sub> shell prevents oxidation and the plasmonic behavior is sustained even after annealing in air at 300 °C which is largely improved compared to unprotected NPs that oxidize and lose their plasmonic activity.<sup>[156]</sup>

To better understand the stability of plasmonic TMN NPs made using the solid-state metathesis method their oxidative and chemical stability was explored. The TMN NP suspensions were monitored using UV-vis spectroscopy, zeta potential measurements, and XPS at various solution pH and extended time under ambient conditions.

## **5.2 Experimental**

### ***5.2.1 Materials***

Hydrochloric acid (HCl) was purchased from Anachemica (12 M, 37%). Sodium hydroxide (NaOH) was purchased from Alfa Aesar (98%). Hydrogen peroxide (H<sub>2</sub>O<sub>2</sub>) was purchased from Walmart (3% USP).

### ***5.2.2 Preparation of Transition Metal Nitride Nanoparticles***

The group IVB TMN NP solutions were synthesized as discussed in section 2.8.1.

### ***5.2.3 Characterization Techniques***

The UV-vis and DLS measurements are the same as discussed in Chapter 3.

### ***5.2.4 Stability Measurements***

For the long-term oxidative stability measurements, the supernatants were stored at room temperature and measured over time using UV-vis spectroscopy. Water was used as a blank, and a quartz cuvette was used. For the stability measurements, the pH was varied from 0 to 10 by adding either HCl or NaOH. The pH of the solutions was measured by immersing an SX610 pH pen tester (Apera Instruments) into the solution while constantly stirring the solution using a magnetic stir bar. Once the pH has stabilized, a reading was recorded. The solution was stored at 4 °C overnight and used for DLS and UV-vis measurements. For the hydrogen peroxide test, few drops of H<sub>2</sub>O<sub>2</sub> were added to group IVB TMN NP solutions that were adjusted to pH 0.

### 5.3 Results and Discussion

The zeta potentials of aqueous suspensions of TiN, ZrN, and HfN NPs after the synthesis were determined to be  $35.0 \pm 0.8$ ,  $42 \pm 2$ ,  $41 \pm 5$  mV, respectively, which indicated that the NPs are positively charged and form stable colloidal suspensions. These results were consistent with the zeta potentials obtained for group IVB TMN NPs presented in Chapter 3.<sup>[303]</sup> The solution pH is typically between 2 and 3 after the HCl workup and product isolation. The positive charge on the NP surface likely originates from protonated hydroxyl groups (**Figure 47**).

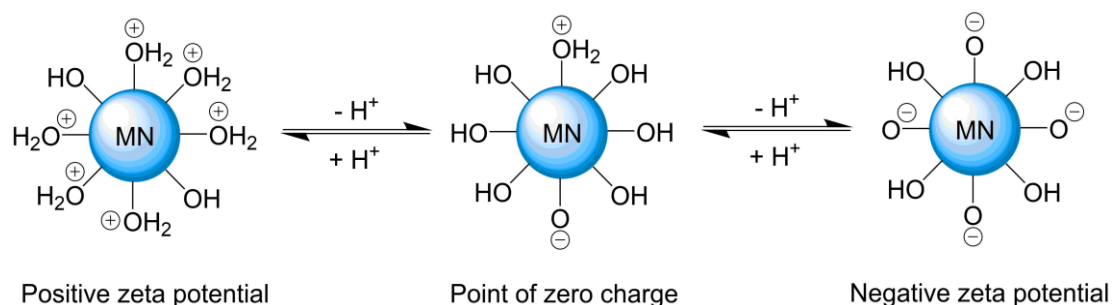


**Figure 47:** Schematic Illustration of surface charge of TMN NPs at different pH.

To test the colloidal stability of the TMN NP suspensions, the pH was varied between 0 and 10, and zeta potential was measured. Images of the colloidal suspensions of TiN, ZrN, and HfN at various pH are shown in **Figure 48A**. It is clear that at pH 2 and 3, all the TMN NPs are dispersible in water. By increasing the pH above 3, aggregation of the TMN NPs is observed (**Figure 48A**) and the values of the zeta potential decrease (**Figure 48B**). With increasing pH, the surface groups are deprotonated and point of zero charge (PZC) is reached between pH 4 and 5 (**Figure 48**). At PZC, the net surface charge

is zero and the zeta potential value is between 10 and  $-10$  mV. As the surface charge decreases the repulsive forces between NPs also decreases, allowing them to come close to each other, aggregate and precipitate out of the solution. At  $\text{pH} > 5$ , negative zeta potential values are observed due to a net negative charge on the NP surface. The negative charge likely results from the deprotonation of the surface hydroxyl groups. However, the values do not reach beyond  $-30$  mV and the NPs remain aggregated for ZrN and HfN samples. The aggregation observed at  $\text{pH} > 3$  is reversible and NPs can be redispersed in water after adjusting the pH back to 2–3 (Figure 49).

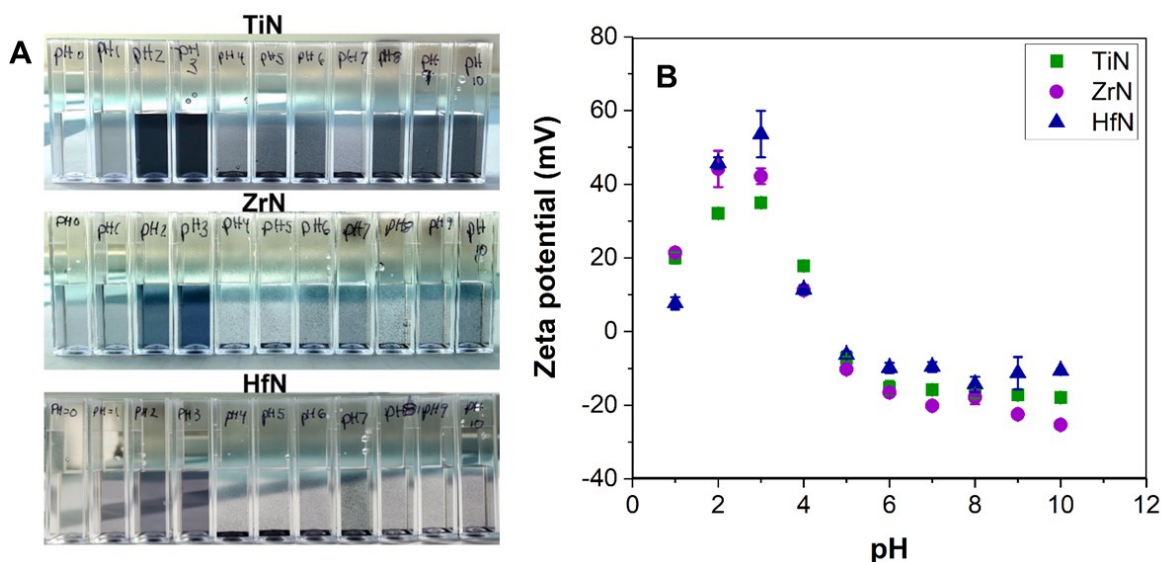


**Figure 48:** (A) Images of TiN, ZrN, and HfN NP dispersions in water at different pH. (B) Zeta potential of TiN, ZrN, and HfN NPs at different pH ranging between 1 and 10.



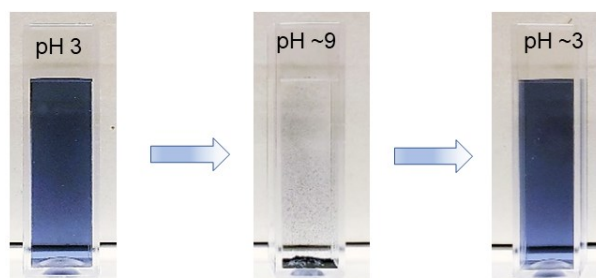


**Figure 49:** Demonstration of reversible colloidal stability of ZrN NPs.

At pH below 2, the solution color gets lighter but there is no significant precipitation of the NPs as observed at higher pH. Furthermore, the value of the zeta potential decreased below pH 2 (**Figure 48B**). This could indicate that the TMN NPs are undergoing degradation at very low pH. The dissolution of NPs has been observed previously in Ag NPs, where upon exposure to oxygen or low pH,  $\text{Ag}^+$  can be released which influences the size and morphology of Ag NPs.<sup>[304,305]</sup> Avasarala *et al.* have investigated the dissolution of surface oxides of TiN NPs in acidic media which results in forming colorless titanium (+4) oxysalts that readily decompose in water.<sup>[306,307]</sup> As discussed in earlier chapters, TiN NPs form a native oxide/oxy-nitride layer on their surfaces due to oxidation.<sup>[291]</sup> To validate the formation of titanium (+4) oxysalts in our studies, few drops of diluted  $\text{H}_2\text{O}_2$  solution was added to TiN colloidal suspension at pH 0 which immediately resulted in the formation of an orange colloidal suspension as shown in **Figure 50**. This is because the colorless hydrated  $\text{Ti}(+4)$  ions in the solution are converted to an orange hydrated  $(\text{Ti}(\text{O}_2)\text{OH})^+$  ions according to **equation (32)**:



This suggests that the nanoscale TMNs are not resistant towards acid corrosion as their bulk counterparts. Moreover, the TMN NPs prepared using the solid-state metathesis method have a very narrow window of colloidal stability. In the future, surface chemistry needs to be explored to allow dispersibility in wide range of pH.

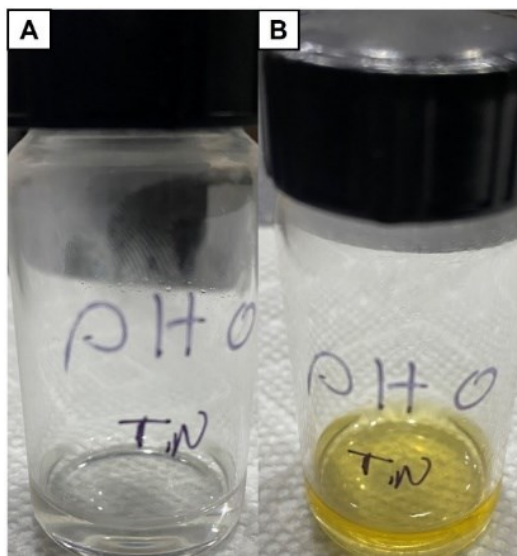


**Figure 50:** Colloidal suspension of TiN at pH 0 (A) before and (B) after the addition of H<sub>2</sub>O<sub>2</sub>.

To determine the long-term stability of the TMN colloidal suspensions, the NPs were stored under ambient conditions and their LSPR was monitored over 64 days, as shown in **Figure 51A**. The LSPR of TiN varied drastically over time and the absorbance maxima red shifted by 165 nm. Surface oxidation leads to red-shift in LSPR maximum and these results suggest that TiN oxidizes rapidly over time, and proper storage is required to prolong their stability.<sup>[232]</sup> The LSPR maxima of ZrN and HfN showed a gradual redshift over time by 47 and 40 nm, respectively. This indicates that ZrN and HfN exhibit better

oxidative stability than TiN. The LSPR intensity was also measured over time as shown in **Figure 51B**. These studies showed that the intensity of TiN significantly decreased after one week likely due to surface oxidation. The oxidation of TiN can be visibly seen where the color changed from dark grayish blue to light blue within the first couple of days, and eventually, a cloudy white solution was obtained after 60 days which is indicative of TiO<sub>2</sub> (as shown in the photographs in **Figure 51B** inset). The LSPR intensity of ZrN and HfN also decreased over time but not to the same extent as TiN. This shows that the oxide shell formed after the synthesis is not passivating and the NPs succumb to continued oxidation over time, however, the rate of oxidation is faster for TiN compared to ZrN and HfN.

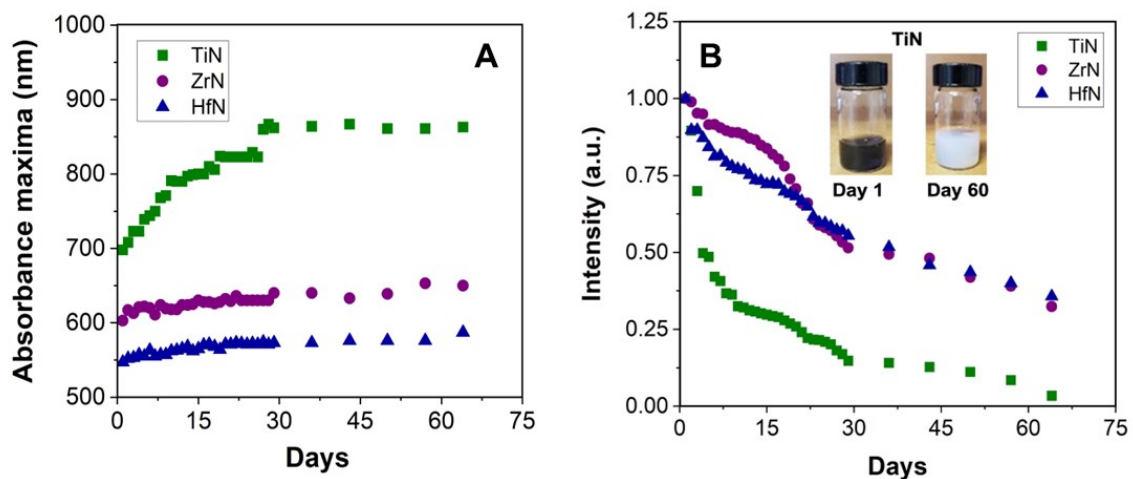


**Figure 51:** The change in LSPR (A) maxima and (intensity) over time for TiN, ZrN, and HfN. (Inset: photograph of TiN NPs dispersed in water under white light on day 1 vs. day 60).

It is possible that the rate of oxidation is enhanced during the measurements performed for this study. If the suspensions are stored in a vial at room temperature without being constantly analyzed, then very minimal changes in the intensity and position of the LSPR peak is observed. **Figure 52** shows a comparison of LSPR spectra of ZrN and HfN taken after four years after synthesis. The slight decrease in intensity and shift in the LSPR peak suggest that some degree of oxidation of the NPs occur but its rate can be minimized by limiting its exposure to fresh air constantly. These studies show that ZrN and HfN colloidal suspensions are stable for a long period of time if stored properly and as seen by the images, the colour of the colloidal suspension is still visible after four years (**Figure 52**).

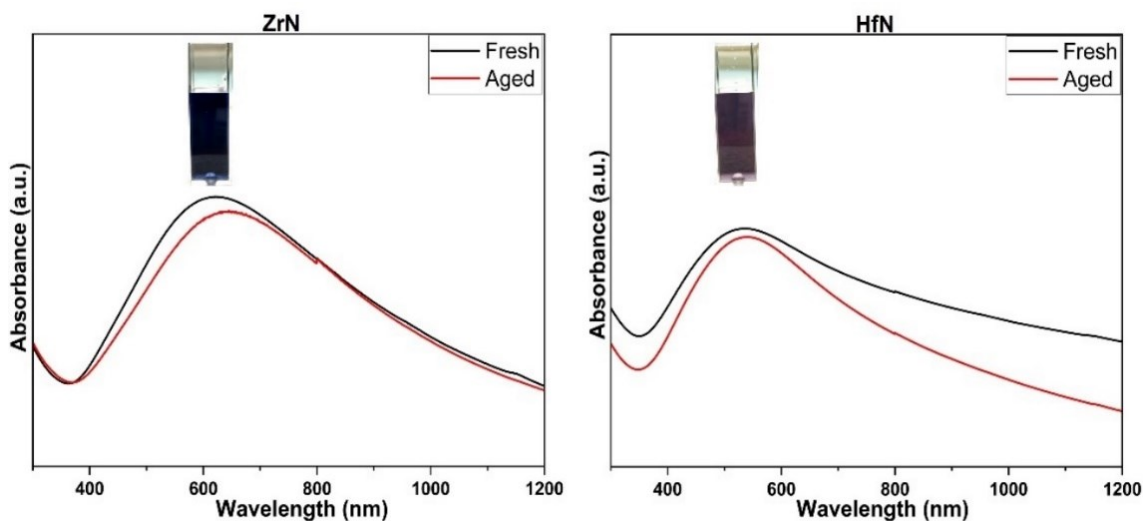


**Figure 52:** Comparison of absorption spectra of ZrN and HfN after four years. (Inset: photograph of NPs dispersed in water under white light).

It was further discovered that when the NPs were stored in a solid form rather than as a suspension, the oxidation was found to be minimal under ambient conditions. XPS was used to probe the oxidation process of the TMN NP over time when stored as a solid. For these experiments, the pH of the TMN NP colloidal suspensions was adjusted to ~5 in order for the NPs to precipitate out and be collected for XPS measurements. The high-resolution XP spectrum of the Ti 2p region showed the presence of TiN with a  $2p_{3/2}$  peak at 455.0 eV, oxynitride ( $TiN_xO_y$ ) with a  $2p_{3/2}$  peak at 456.4 eV, and oxides ( $TiO_2$ ) with a  $2p_{3/2}$  at 458.5 eV (**Figure 53**).<sup>[223]</sup> Correspondingly, the high-resolution XP spectrum of the N 1s region showed the presence of TiN and  $TiN_xO_y$  with 1s peaks at 396.7 and 399.1 eV, respectively (**Figure 53**).<sup>[223]</sup> After 30 days, the XPS measurements were re-measured. By looking at **Figure 53** it is clear that there was no significant changes detected over time. A high-resolution XP spectrum of the Zr 3d region showed the presence of Zr 3d<sub>5/2</sub> peaks at 179.8, 181.4, and 182.8 eV, corresponding to ZrN,  $ZrN_xO_y$ , and  $ZrO_2$ , respectively (**Figure 54**).<sup>[156]</sup> Correspondingly, the high-resolution XP spectrum of the N 1s region showed the presence of ZrN and  $ZrN_xO_y$  with 1s peaks at 396.4 and 399.5 eV, respectively (**Figure 54**).<sup>[156]</sup> After 30 days, there were minimal changes detected with a slight decrease in the ZrN peak intensity which could indicate that oxidation had occurred. Similarly, the high-resolution XP spectrum of Hf 4f region showed the presence of HfN,  $HfN_xO_y$ , and  $HfO_2$ , with Hf 4f<sub>7/2</sub> peaks at 16.7, 18.2, and 19.1 eV, respectively (**Figure 55**).<sup>[224]</sup> N 1s spectra showed the presence of nitride HfN at 396.7 eV and oxynitride  $HfN_xO_y$  at 400.6 eV for HfN NPs (**Figure 55**).<sup>[156,224,225]</sup> There were no significant changes observed other than the N 1s region being noisy.

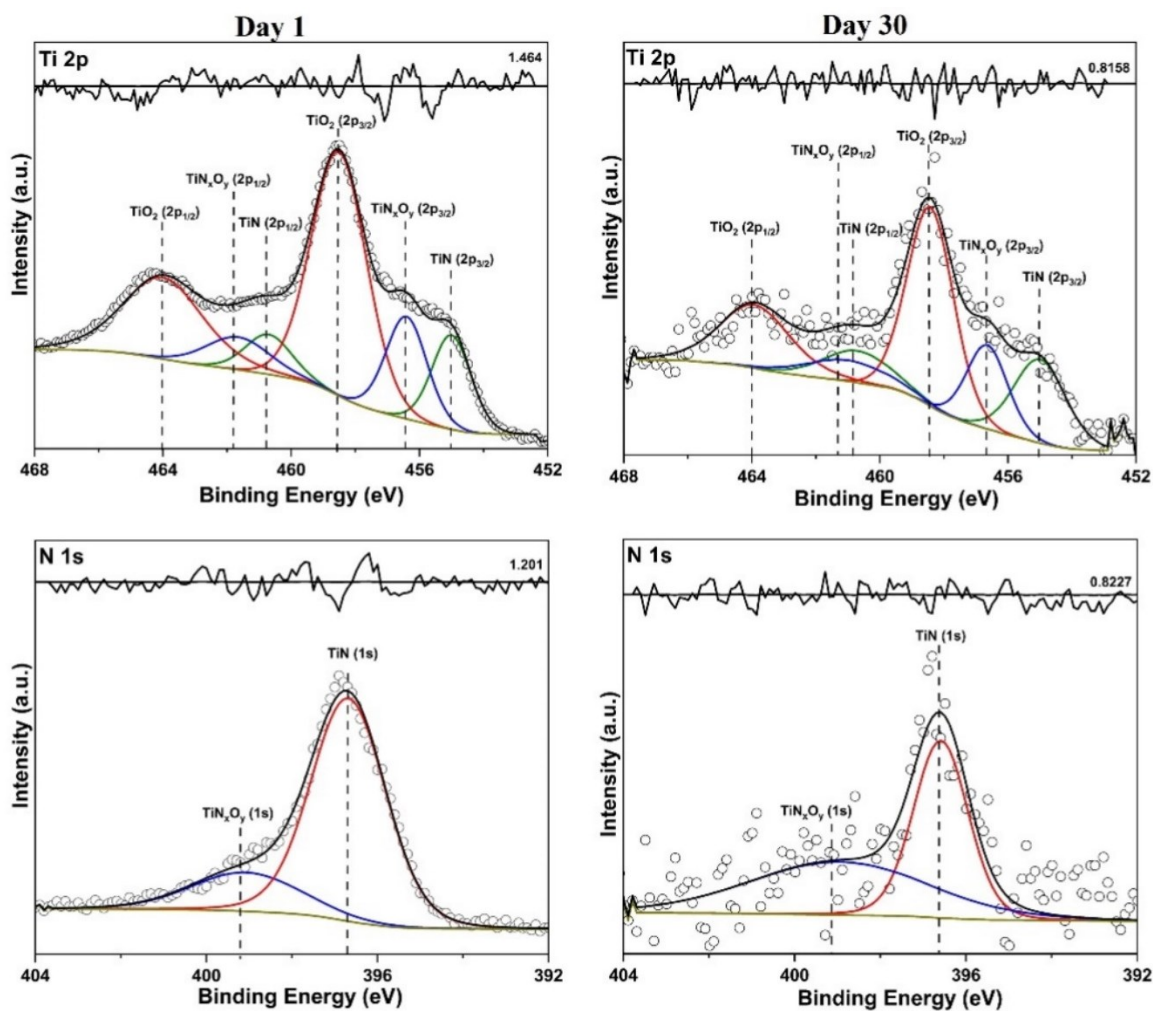


**Figure 53:** High-resolution X-ray photoelectron spectra of Ti 2p and N 1s region of TiN NPs on day 1 and day 30. Experimental data represented as open circles, and the overall fitted data represented as a black line.

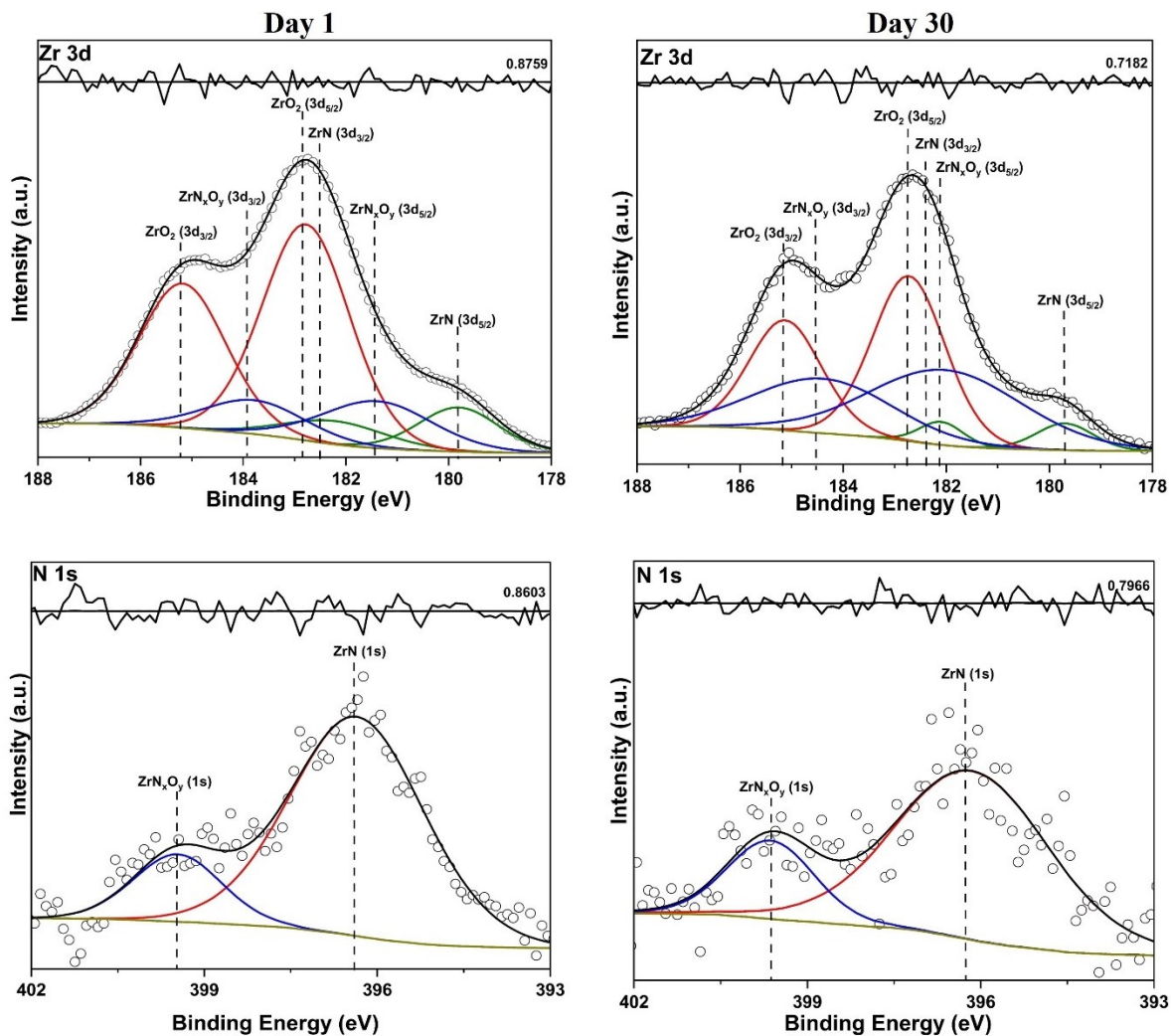


**Figure 54:** High-resolution X-ray photoelectron spectra of Zr 3d and N 1s region of ZrN NPs on day 1 and day 30. Experimental data represented as open circles, and the overall fitted data represented as a black line.

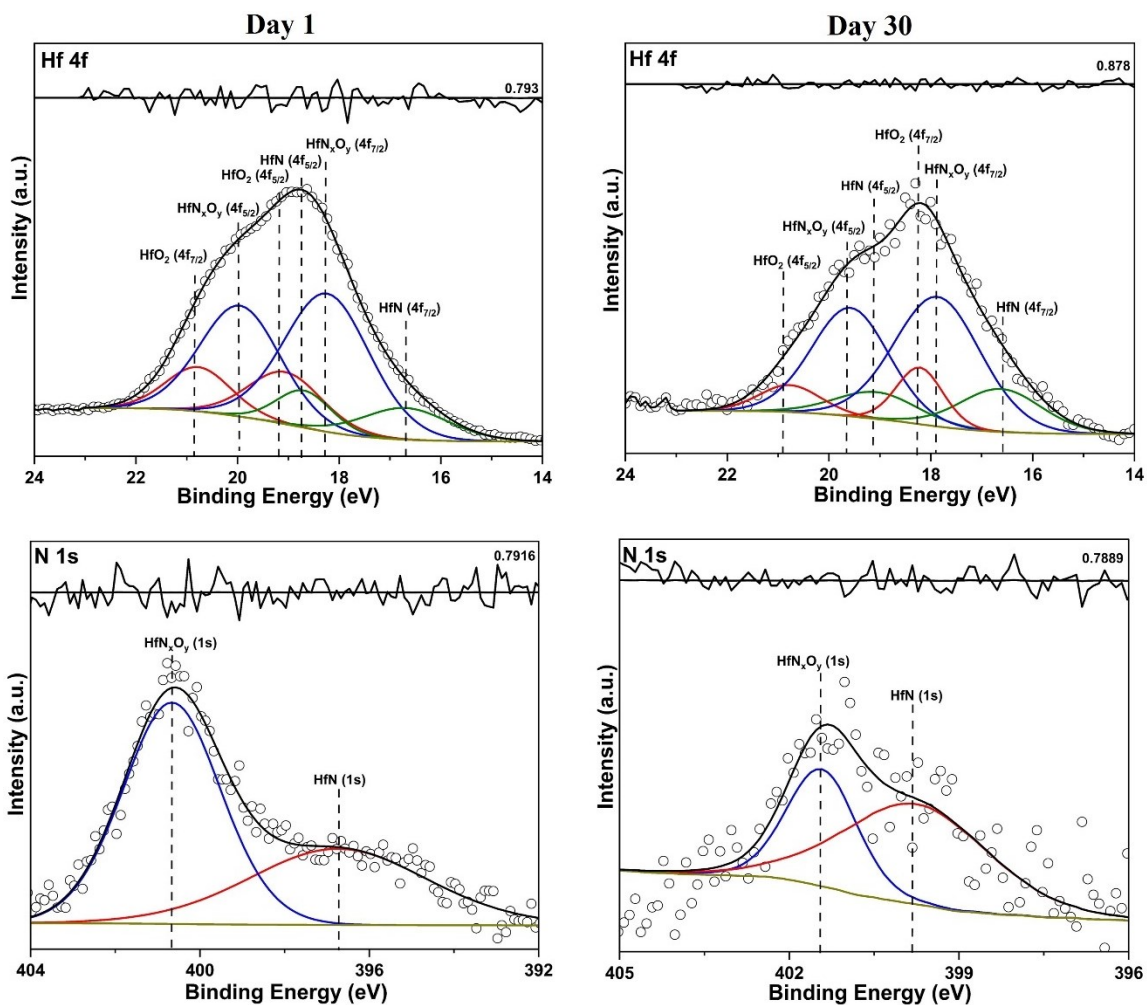


**Figure 55:** High-resolution X-ray photoelectron spectra of Hf 4f and N 1s region of HfN NPs on day 1 and day 30. Experimental data represented as open circles, and the overall fitted data represented as a black line.



## 5.4 Conclusions

The long-term chemical stability of TMN NP colloidal suspensions was investigated and the changes in the LSPR peaks were monitored using UV-vis spectroscopy. The TMN NPs have been shown to exhibit surface oxidation over time with TiN NPs being the least stable. Within ~60 days, TiN NPs lose their plasmonic properties and a cloudy white solution was obtained indicating the formation of TiO<sub>2</sub>. ZrN and HfN colloidal suspension are comparatively more stable especially if they are stored without air exposure. All the TMNs were found to be fairly oxidatively stable if stored as a solid compared to the suspensions. The presence of acidic water likely enhances the rate of oxidation. The colloidal stability of these solutions at various pH was also studied, and the results showed that lower pH led to dissolution whereas higher pH led to aggregation. Therefore, the TMN NP colloidal suspensions are only stable in a narrow pH range between 2–3. These studies have shed the light on the importance of investigating the stability of TMN NPs suspension to gain better perspective of potential applications. Future work will focus on improving the colloidal stability through surface modification and functionalization which could prevent grain growth and particle agglomeration.

## Chapter 6: Solid-State Synthesis of UV-Plasmonic Cr<sub>2</sub>N Nanoparticles

*This author wishes to clarify her contribution to the research described in Chapter 6 of this thesis document.* This chapter discusses the solid-state metathesis synthesis and photothermal properties of UV-plasmonic Cr<sub>2</sub>N NPs. The plasmonic properties of Cr<sub>2</sub>N NPs were probed in detail using EELS measurements and EELS loss probability maps. The experimental studies obtained were compared to computational studies. The preparation of the group Cr<sub>2</sub>N NPs and the photothermal measurements are discussed in Chapter 2.

My contribution to this study includes synthesizing and optimizing the solid-state metathesis reaction to synthesize pure Cr<sub>2</sub>N NPs. The resulting NPs were characterized using XRD, UV-vis spectroscopy, DLS, and TEM. The photothermal properties were investigated at various power densities and the cyclability of these NPs was examined. Computational work was conducted by Dr. Yashar Monfared. HR-TEM and EELS elemental mapping experiments were performed by Dr. Carmen Andrei. The XPS measurements were performed by Dr. Robert H. Coridan. The low-loss EELS, STEM-HAADF images, and EELS loss probability maps were performed and analyzed by Dr. Isobel C. Bicket.

## 6.1 Introduction

The chapters so far have explored TMNs with plasmonic responses in the visible and near-IR regions. In the recent years, materials with plasmonic responses in the UV region (100–400 nm) have garnered interest for disinfection, biological imaging, sensing, and developing metamaterials.<sup>[308]</sup> As mentioned earlier, many metals such as Al, Mg, In, Ga, Pd, Pt, etc. have shown to have bulk plasma frequency below 400 nm and have been explored for UV applications.<sup>[102,107,110,117,124]</sup> However, these metals can be either expensive, oxidatively unstable under ambient conditions, or have low melting points making them incompatible with high-temperature fabrication techniques.<sup>[117,124]</sup> Computational studies have predicted that chromium metal nitrides (CrN and Cr<sub>2</sub>N) can possess LSPR in the blue to UV region of the electromagnetic spectrum.<sup>[143,218]</sup>

Recently, plasmonic Cr<sub>2</sub>N NPs with size ranging between 0.8–30 nm were synthesized using a single step pulse laser irradiation.<sup>[218]</sup> The absorption spectra of these particles showed multiple LSPR between 320–420 nm with maximum at 372 nm. This broad absorption was hypothesized to be due to hot spot formation from particle-particle interaction. However, it currently remains unclear what the optical properties of Cr<sub>2</sub>N NPs without the interparticle interactions look like. This study focuses on exploring plasmonic properties of Cr<sub>2</sub>N NPs using UV-vis absorbance spectroscopy, low loss EELS, EELS loss probability maps, and numerical methods. The NPs were prepared using a solid-state reaction between Cr<sub>2</sub>O<sub>3</sub> and Mg<sub>3</sub>N<sub>2</sub> which resulted in water dispersible NPs and were characterized using different analytical and microscopy techniques. The NPs had bulk and surface plasmon resonances below 200 nm which corroborated with the calculations

performed using finite element method. The photothermal transduction efficiency of 10 nM Cr<sub>2</sub>N solution was investigated at 1 W cm<sup>-2</sup> illumination using a 365 nm LED source. The temperature change as a function of power density illumination was also investigated. Additionally, the stability of Cr<sub>2</sub>N colloidal suspension was investigated at different pH. The data presented herein highlights potential applications of Cr<sub>2</sub>N in water disinfection, photocatalysis, and sensing.

## **6.2 Experimental**

### ***6.2.1 Materials***

Chromium oxide (Cr<sub>2</sub>O<sub>3</sub>, 99.9%, 18 nm), and magnesium nitride (Mg<sub>3</sub>N<sub>2</sub>, 99%, -325 mesh) were purchased from U.S. Research Nanomaterials Inc., and HCl was purchased from Anachemica (37%). NaOH was purchased from Alfa Aesar (98%). Deionized water (DI-water) was obtained from Sartorius Arium water purification system. All glassware was cleaned thoroughly with DI-water then acetone and placed in oven to dry prior to use.

### ***6.2.2 Synthesis of Cr<sub>2</sub>N Nanoparticles***

The Cr<sub>2</sub>N NPs were synthesized as discussed in section 2.8.1.

### ***6.2.3 Photothermal Measurements***

Photothermal studies were performed as discussed in section 2.9.

#### ***6.2.4 Computational Studies***

Computational studies were performed as discussed in section 2.10.

#### ***6.2.5 Characterization techniques***

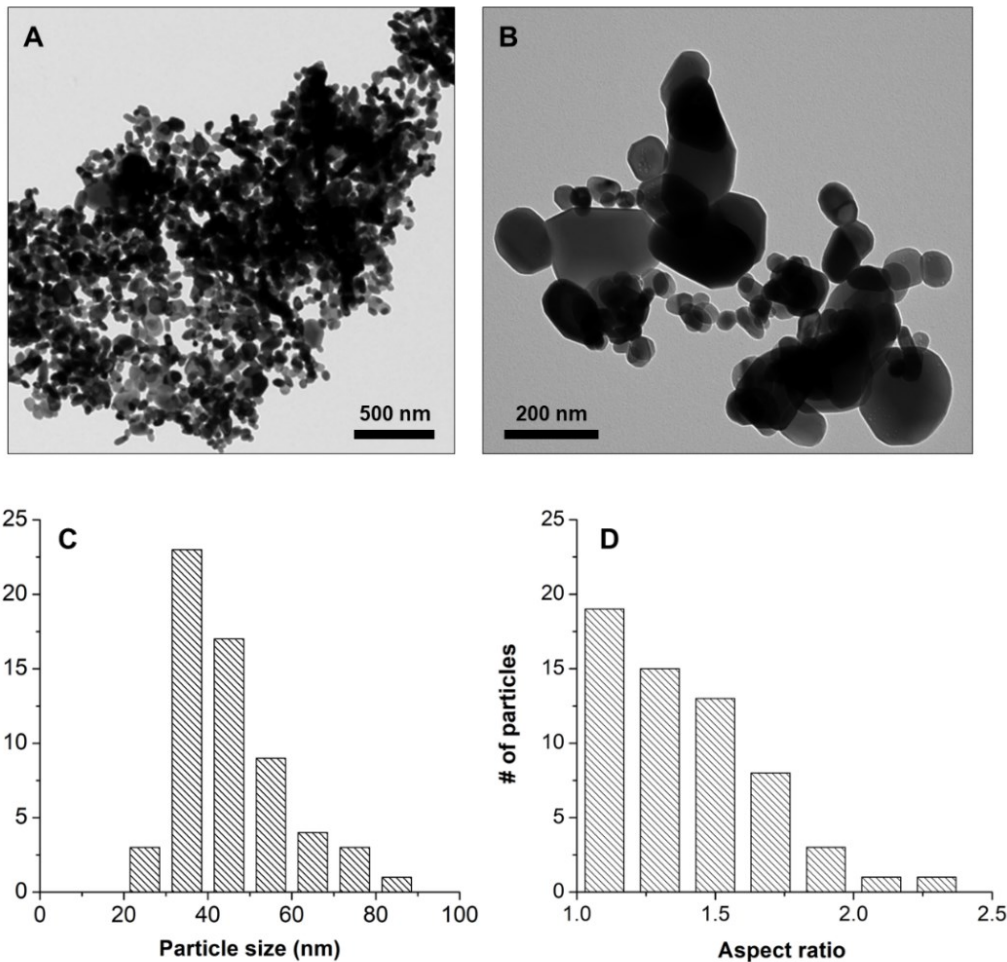
The powder XRD, UV-vis, and DLS are the same as discussed in Chapter 3. XPS measurements were performed on a PHI Versaprobe instrument with an Al K $\alpha$  source (1486.6 eV). Powders of each sample were dispersed in water, then dried as a near-coverage layer onto a diced Si wafer at 70 °C. CasaXPS software (VAMAS) was used to interpret high-resolution (HR) XP spectra. The background was subtracted using a Shirley-type background to remove most of the extrinsic loss structure. The TEM images were collected on either a Thermo Scientific Talos 200 X microscope or a Hitachi-9500 electron microscope at an operating voltage of 200 kV. High-angle annular dark-field scanning transmission electron microscopy (HAADF-STEM) images were collected on a Thermo Scientific Talos 200 X microscope. TEM samples were prepared by drop-casting NP suspensions onto a copper grid coated with a holey carbon film. Image J software was used to measure particle size and aspect ratios, and the error bars shown represent standard deviation.

EELS data was acquired on a FEI Titan scanning transmission electron microscope operated at 80 kV and equipped with a monochromator and Gatan Quantum GIF spectrometer. Briefly, a focused electron probe is scanned over the region of interest, and a spectrum acquired at each pixel, resulting in a 3D dataset with high spatial resolution across a wide spectral range. A K2 Summit® direct electron detector was used to collect

core-loss EELS data for elemental mapping, with a dispersion of 100 meV/channel, an electron beam convergence angle of 16.8 mrad, and a spectrometer collection angle of 26.4 mrad. For low-loss EELS data, the beam was monochromated to achieve an energy resolution of approximately 100 meV, using a dispersion of 10 meV/channel on a CCD camera with a convergence angle of 14.2 mrad and a collection angle of 25.4 mrad. Data processing on the low-loss EELS was done using custom Python software.

### 6.3 Results and Discussion

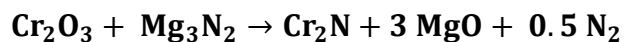
The solid-state nitridation of metal oxide nanopowders with  $\text{Mg}_3\text{N}_2$  has been previously used by our group to successfully synthesize free-standing group IVB plasmonic TMN nanostructures.<sup>[291]</sup> The  $\text{Cr}_2\text{O}_3$  precursor with an average particle size of  $45 \pm 10$  nm and ellipsoidal shape (**Figure 56A**) was commercially purchased. While most particles (~90%) were below 100 nm in size, a few larger (>100 nm) particles were also present in the oxide sample (**Figure 56B**). The powder XRD pattern of the oxide precursor showed reflections characteristic of cubic phase  $\text{Cr}_2\text{O}_3$  (**Figure 58A**).<sup>[309]</sup>



**Figure 56:** (A) and (B) transmission electron microscopy images, (C) particle size distribution, and (D) aspect ratio distribution of  $\text{Cr}_2\text{O}_3$  NPs.

Similar to the synthesis of group IVB TMN NPs, the reaction was performed at 1000 °C. The XRD pattern shown in **Figure 57A**, indicate that conducting the reaction at 1000 °C for 12 hours resulted in the formation of  $\text{Cr}_2\text{N}$  and elemental Cr. The presence of elemental Cr signal indicates the decomposition of  $\text{Cr}_2\text{N}$ .<sup>[310]</sup> Therefore, various reaction temperatures ranging from 1000 °C to 650 °C were investigated to eliminate the

decomposition of Cr<sub>2</sub>N. Conducting the reaction at 800 °C as shown in **Figure 57B** resulted in the decomposition of Cr<sub>2</sub>N to Cr metal, and incomplete reactivity as evidenced by the presence of Cr<sub>2</sub>O<sub>3</sub> peaks. Below 750 °C (**Figure 57C - E**), formation of two nitride phases, i.e., CrN/Cr<sub>2</sub>N along with unreacted Cr<sub>2</sub>O<sub>3</sub> was observed. Conducting the reaction at 650 °C resulted in the formation of CrN only which is consistent with previous studies.<sup>[311–313]</sup> Based on this analysis, the solid-state metathesis of Cr<sub>2</sub>N is assumed to be occurring in two steps where CrN is first formed (**equation 33**), and then decomposes to Cr<sub>2</sub>N at high temperatures (**equation 34**):<sup>[314]</sup>





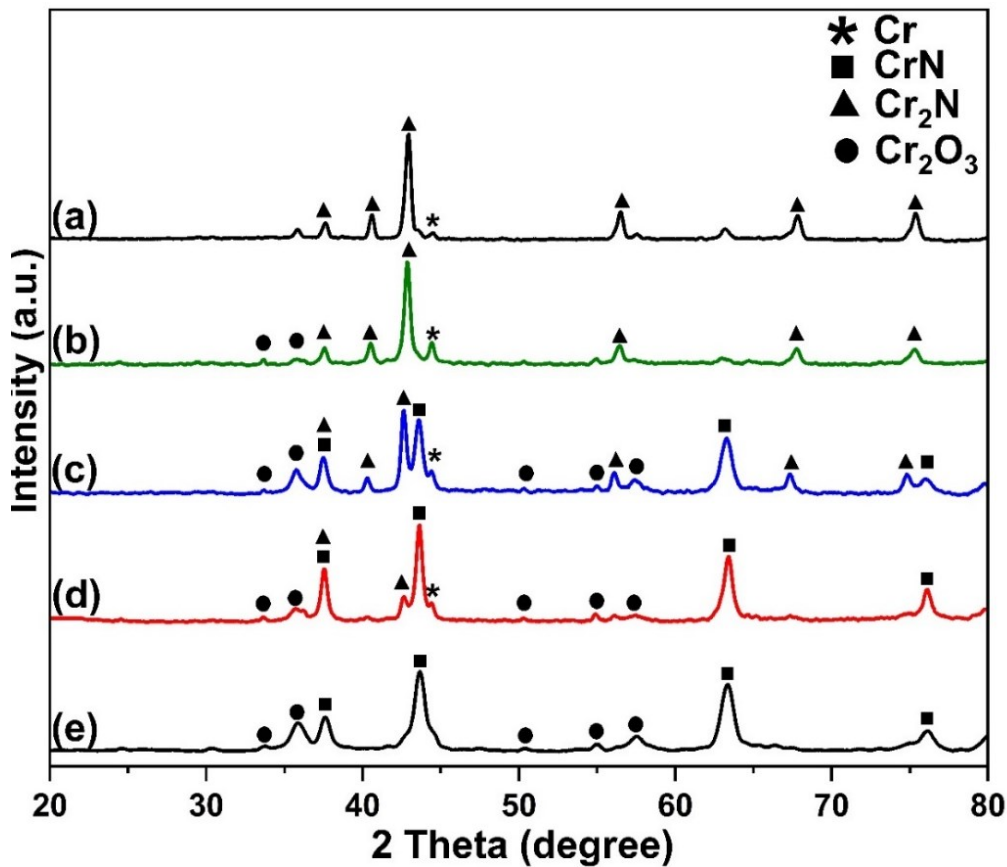


**Figure 57:** Powder XRD pattern of chromium nitride synthesized using the solid-state metathesis reaction at (A) 1000 °C, (B) 800 °C, (C) 750 °C, (D) 700 °C, and (E) 650 °C for 12 hours.

These studies highlighted the importance of controlling the solid-state metathesis reaction parameters to achieve the desired product. Further studies showed that lowering the reaction time to 3 hours while holding the reaction at 1000 °C resulted in the formation of pure  $\text{Cr}_2\text{N}$  without Cr metal or unreacted  $\text{Cr}_2\text{O}_3$ . As shown in **Figure 58A**, the powder XRD pattern of the dried NP dispersion showed reflections characteristic of  $\text{Cr}_2\text{N}$  with a hexagonal crystal structure<sup>[315]</sup> and no peaks corresponding to the starting materials or

reaction byproducts were observed. The TEM analysis showed most of the NPs to be pseudospherical with an average diameter of  $9 \pm 5$  nm (**Figure 58B** and C). While most particles were between 5–15 nm, a small portion of larger NPs ranging between 15–25 nm were also formed (**Figure 59**). Additionally, the chemical composition of the  $\text{Cr}_2\text{N}$  was investigated using EELS elemental mapping. The EELS analysis showed good overlap between Cr (**Figure 58E**) and N (**Figure 58F**) confirming the presence of a chromium nitride phase, whereas O (**Figure 58G**) was found to be predominantly in N deficient regions. The nitride NPs prepared using this method have been shown to oxidize after the HCl workup to form surface oxynitride and oxide species which is likely the origin of O species in the EELS map. Zeta potential measurements were conducted on the  $\text{Cr}_2\text{N}$  NP colloidal suspensions to determine surface charge and colloidal stability. The  $\text{Cr}_2\text{N}$  NPs dispersed in water exhibited a zeta potential of  $45 \pm 1$  mV, indicating that the NP surface is positively charged, and they form a stable colloidal suspension. The positive charge most likely originates from the protonated hydroxyl functional groups ( $-\text{OH}_2^+$ ) groups on the surface that result from the acid workup. The NP suspension had a hydrodynamic radius of  $47 \pm 0.5$  nm as determined by the DLS.

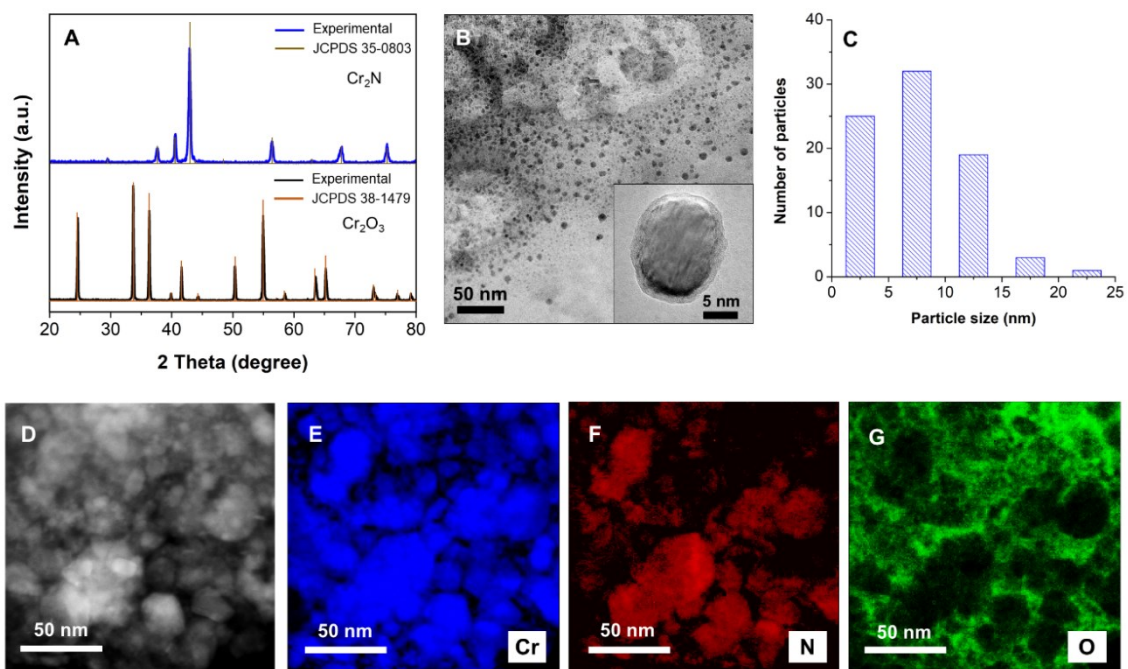


**Figure 58:** (A) Powder X-ray diffraction pattern of Cr<sub>2</sub>O<sub>3</sub> and Cr<sub>2</sub>N NPs. (B) TEM image of Cr<sub>2</sub>N NPs. Inset: Higher magnification TEM image of a single Cr<sub>2</sub>N NP showing the oxide shell. (C) Cr<sub>2</sub>N particle size distribution. (D) HAADF-STEM image and EELS map of (E) chromium (F) nitrogen and (G) oxygen content of Cr<sub>2</sub>N NPs.

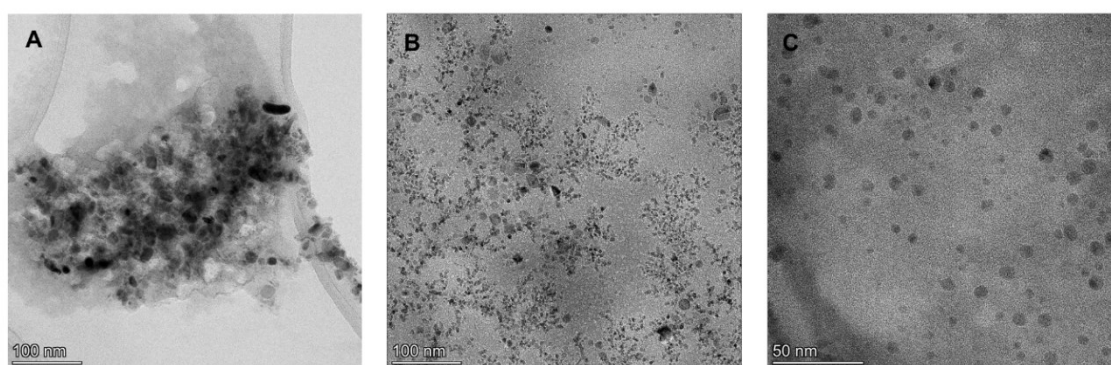


**Figure 59:** TEM images of Cr<sub>2</sub>N NPs from multiple synthesis.

To further probe the surface chemical state of the Cr<sub>2</sub>N, the NPs were analyzed using XPS technique. The high-resolution XP spectrum of the Cr 2p region (**Figure 60A**) for the precursor had 2p<sub>3/2</sub> peak fits at binding energies of 576.5, 578.9, and 580.6 eV corresponding to Cr<sub>2</sub>O<sub>3</sub>, Cr(OH)<sub>3</sub>, and CrO<sub>3</sub>, respectively.<sup>[316,317]</sup> The combined 2p<sub>1/2</sub> fit, and the satellite peak maxima were at 586.7 and 597.5 eV, respectively.<sup>[318]</sup> No distinctive peak was observed in the N 1s region in the precursor material (**Figure 60B**). The Cr 2p spectrum of Cr<sub>2</sub>N NPs had 2p<sub>3/2</sub> peak fits at binding energies of 573.8, 575.7, and 576.8 eV corresponding to Cr<sub>2</sub>N, CrO<sub>x</sub>N<sub>y</sub>, and Cr<sub>2</sub>O<sub>3</sub>, respectively (**Figure 60C**).<sup>[319,320]</sup> The chemical identity of the small peak located at 579.7 eV is currently unclear but could be due to Cr(V) species.<sup>[321]</sup> The data indicates presence of an oxide and oxynitride shell around the Cr<sub>2</sub>N NP core similar to previous reports.<sup>[154,291]</sup> This is further confirmed using TEM analysis which showed the presence of an oxide shell around the NPs (**Figure 61**). The thickness of this shell varied between 1–10 nm between various NPs and even within the same particle. The N 1s spectrum of Cr<sub>2</sub>N NPs showed a weak signal ca. 395.5 eV corresponding to the nitride (**Figure 60D**).<sup>[319]</sup> Given the oxide shell thickness, it is likely that not many electrons from the Cr<sub>2</sub>N core are detected.

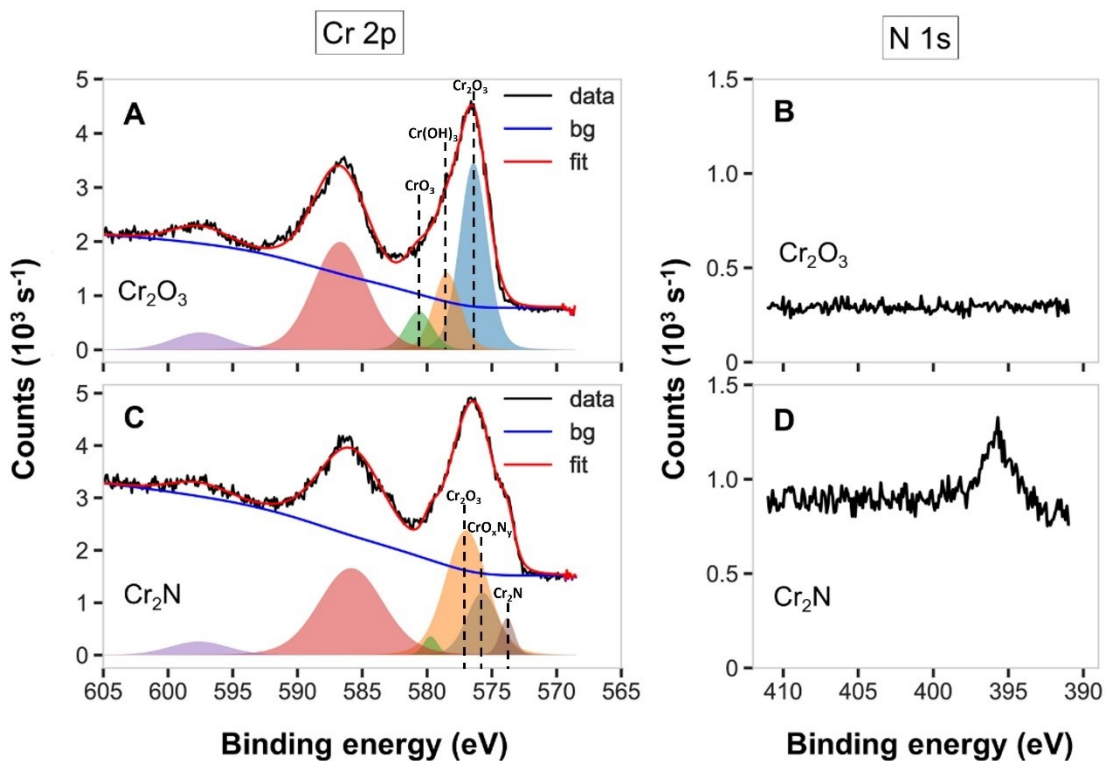


**Figure 60:** High resolution XP spectra of Cr 2p and N 1s regions of  $\text{Cr}_2\text{O}_3$  nanopowder and  $\text{Cr}_2\text{N}$  NPs.

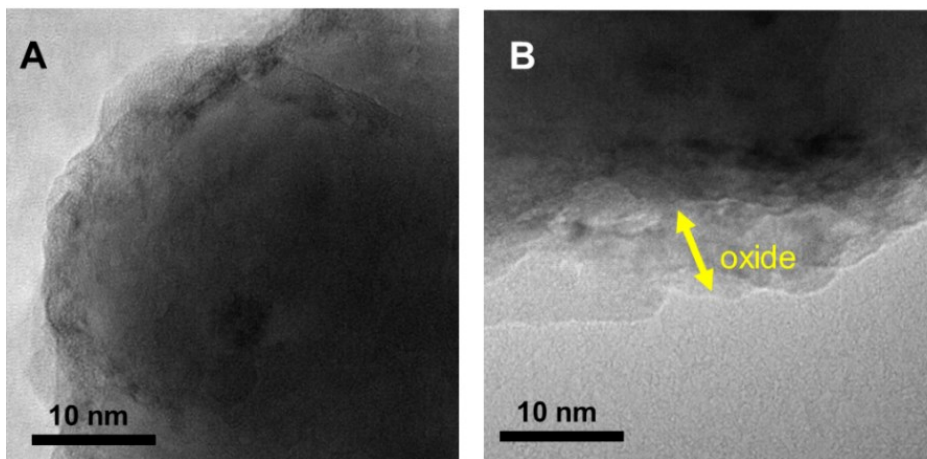


**Figure 61:** High magnification TEM images of  $\text{Cr}_2\text{N}$  NPs showing the oxide shell around the particles.

The  $\epsilon_r$  and  $\epsilon_i$  components of the dielectric function of Cr<sub>2</sub>N between 100 and 700 nm is shown in **Figure 62A**. A negative real permittivity is observed in this wavelength range indicating free electron behaviour.<sup>[322]</sup> The magnitude of imaginary component of the dielectric function increases with decreasing frequency indicating higher optical losses at longer wavelengths.<sup>[62]</sup> The absorption spectrum of Cr<sub>2</sub>N NPs with diameter of 9 and 25 nm was calculated using a finite element method (**Figure 62B**). The NP size chosen for the calculations are equal to the average and large particle size in the sample. The data suggest that the LSPR maximum of Cr<sub>2</sub>N NPs is in the deep UV region (around 60 nm for 9 nm NPs and at 145 nm for 25 nm particle size) and the LSPR peak of the experimental sample should be relatively broad covering all of the UV and parts of the visible spectrum. The Cr<sub>2</sub>N NP solution has a brown color (**Figure 62B inset**) and showed a broad absorbance (**Figure 62B**, solid line) when suspended in DI-water. The characteristic LSPR peak was not observed in the measured spectrum, however the calculations show this to be present below the spectrometer's wavelength cutoff (190 nm). The absorbance spectrum showed a shoulder peak at ~310 nm which could be due to plasmon coupling between NPs as observed by Gubert *et al.*<sup>[323]</sup>

The computational analysis on the absorption and scattering of Cr<sub>2</sub>N NPs was performed to evaluate the extinction behaviors of the NPs with different sizes. The normalized absorption and scattering coefficients ( $Q_{\text{abs}}$  and  $Q_{\text{sca}}$ ) are defined by the calculated absorption or scattering cross sections of NPs ( $C_{\text{abs}}$  and  $C_{\text{sca}}$ ) using FEM normalized to the geometrical cross section of NPs. Extinction coefficient of NPs can be then defined as:  $Q_{\text{ext}} = Q_{\text{abs}} + Q_{\text{sca}}$ . As shown in **Figure 62C**, for smaller NPs ( $\leq 50$  nm) the

absorbance is higher in the UV-C region (~100-280 nm) whereas for the larger NPs (70-100 nm), the absorbance is higher in the UV-B and UV-A regions (280-400 nm). It is also clear that the absorption and scattering maxima of particles redshifts and become broader with an increase in NP size (Figure 62C and D).

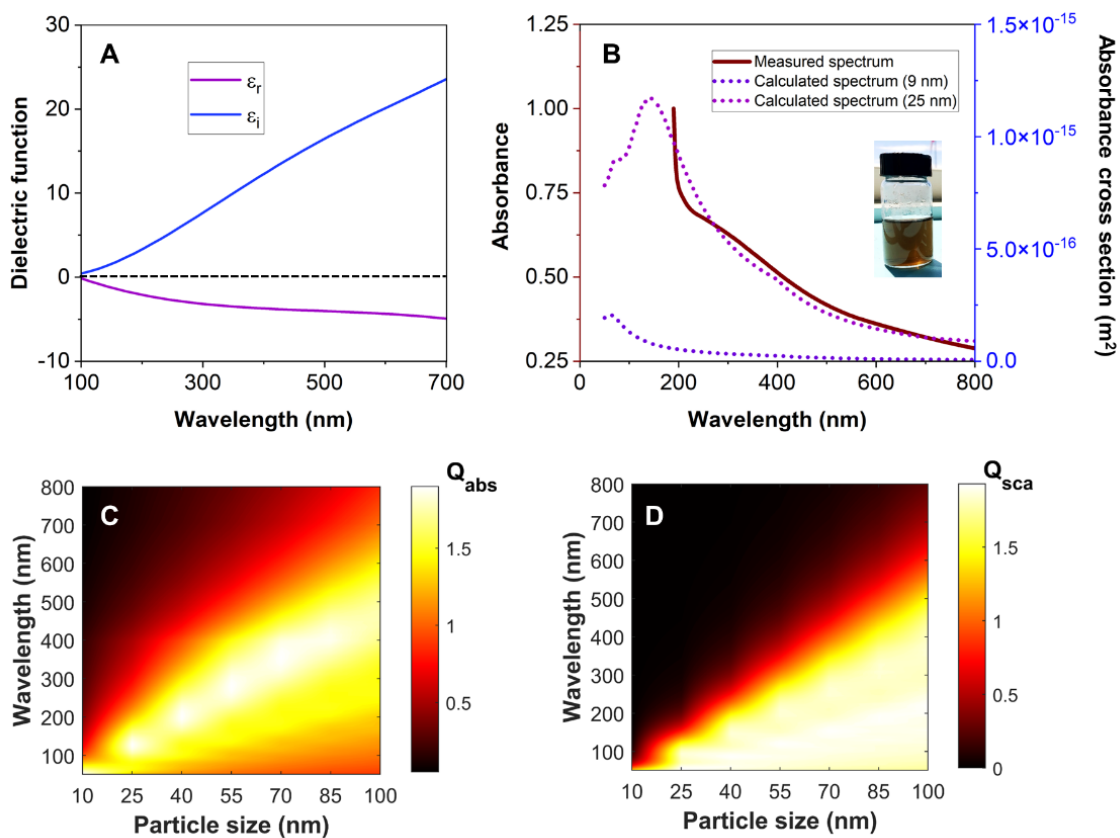


**Figure 62:** (A) Real and imaginary components of the dielectric function of Cr<sub>2</sub>N. (B) Calculated absorption cross-section and measured absorbance of Cr<sub>2</sub>N NPs. Inset: Photograph of Cr<sub>2</sub>N NP suspension in water. Calculated (C) absorption and (D) scattering coefficients of Cr<sub>2</sub>N NPs between 10-100 nm.

While a distinctive LSPR could not be observed in the absorbance spectrum limited by the instrument wavelength cutoff, EELS was used as an alternative technique to map both bulk and surface plasmon intensity and energy with high spatial resolution. Since the EELS experiments are conducted under high vacuum, some variations can be expected compared to the NPs suspended in a solvent.<sup>[324]</sup> The **Figure 63A** inset shows regions from which the EELS spectra that were acquired. All the spectra obtained in these studies were normalized to the zero-loss peak. The large signal observed below 100 nm is indicative of bulk plasmon (**Figure 63A**) which was only observed for spots 1–3 but not 4 and 5. This could be due to the latter regions being closer to vacuum or too small and thin to obtain a strong bulk plasmon signal. The peaks between 100–200 nm are indicative of surface plasmons, however, these are difficult to differentiate from the bulk plasmon signal.

To further confirm the presence of surface plasmons, aloof EELS experiments were conducted where the electron beam does not interact with the sample directly but does so through long-range Coulomb interactions with the evanescent field of the surface plasmon resonances.<sup>[325]</sup> As shown in **Figure 63B** inset, five different areas were chosen that are close to the NPs but not directly on the sample. The bulk plasmon peaks that appear at higher energies are no longer present in the aloof mode (except for spot 2) which is expected since the electron beam is not directly interacting with the particles (**Figure 63B**). It is possible the beam is still too close to the NPs in spot 2 and can excite bulk plasmons, whereas in spot 1 the interaction might be too weak to observe a significant peak. In the spots 3–5, the aloof EELS spectra indicate the presence of a surface plasmon signal



between 100 and 200 nm, which aligns with the calculations that indicate LSPR to be present in this wavelength region for NPs below 50 nm.

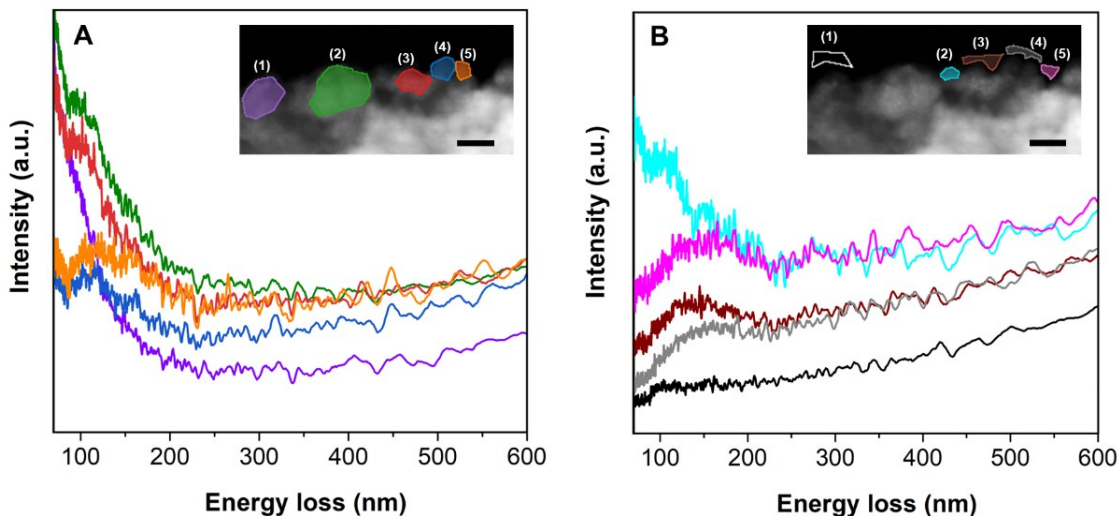


**Figure 63:** (A) Low-loss EELS spectra and (B) aloof EELS spectra of  $\text{Cr}_2\text{N}$  NPs. Inset: STEM-HAADF images indicating spots where the spectra were collected (scale bar = 20 nm).

**Figure 64** shows EELS loss probability maps with the energy ranges that were chosen based on the peak positions in the low-loss EELS spectra (**Figure 63A**). The intensity map at low energies (0.9 - 2.13 eV) shows a strong signal in the vacuum which can be attributed to the evanescent waves resulting from surface plasmons. Between the energies of 3.06 and 4.9 eV, signal is mostly arising on the top of the NPs where higher Cr and N signals were detected using the elemental mapping indicative of surface plasmons. Additionally, a region between two particles shows an intense signal that is potentially due to plasmon coupling (spot 5). Similar profiles are observed at energies between 6.96 and 8.60 eV where the map shows higher intensities around the NPs likely originating from

surface plasmons and coupling between the particles. At higher energies ( $> 9$  eV), most of the sample appears bright which can be attributed to both the surface and bulk plasmons.

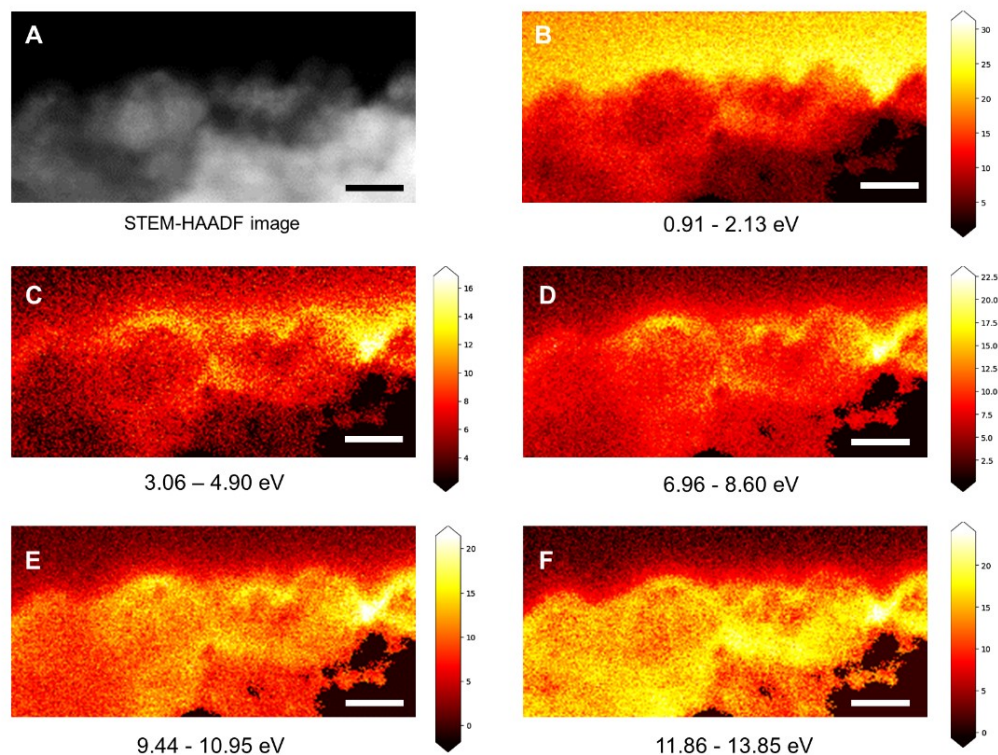


**Figure 64:** (A) STEM-HAADF image and EELS loss probability maps images in the energy range of (B) 0.91–2.13 eV, (C) 3.06–4.90 eV, (D) 6.96–8.6 eV, (E) 9.44–10.95 eV, and (F) 11.86–13.85 eV of  $\text{Cr}_2\text{N}$  NPs.

Once the plasmonic properties were established using the techniques described above, the stability of  $\text{Cr}_2\text{N}$  NPs was investigated at different pH as shown in **Figure 65**. The  $\text{Cr}_2\text{N}$  NPs colloidal suspension exhibited a brown color and the pH ranged between 2-3, as the pH decreases the  $\text{Cr}_2\text{N}$  NPs solution becomes colorless without any aggregation formation indicating that the  $\text{Cr}_2\text{N}$  NPs are dissolving. This results in having lower positive

zeta potential values suggesting that the Cr<sub>2</sub>N NPs are not stable at lower pH as shown in **Figure 65**. When the pH was adjusted between 4-7, the Cr<sub>2</sub>N NPs suspension exhibited a light brown color, and some aggregation began to occur which resulted in lower positive zeta potential values indicating the instability of the Cr<sub>2</sub>N NPs suspension. At basic pH, the Cr<sub>2</sub>N NPs aggregated and precipitated out of the solution while exhibiting a negative zeta potential indicating that the surface hydroxyl groups have likely been deprotonated. This shows that the Cr<sub>2</sub>N NPs suspension is only stable in a narrow pH range between 2-4, this trend was consistent with group IVB TMN NPs. However, the PZC was found to be between pH 7 and 8 for Cr<sub>2</sub>N NPs.

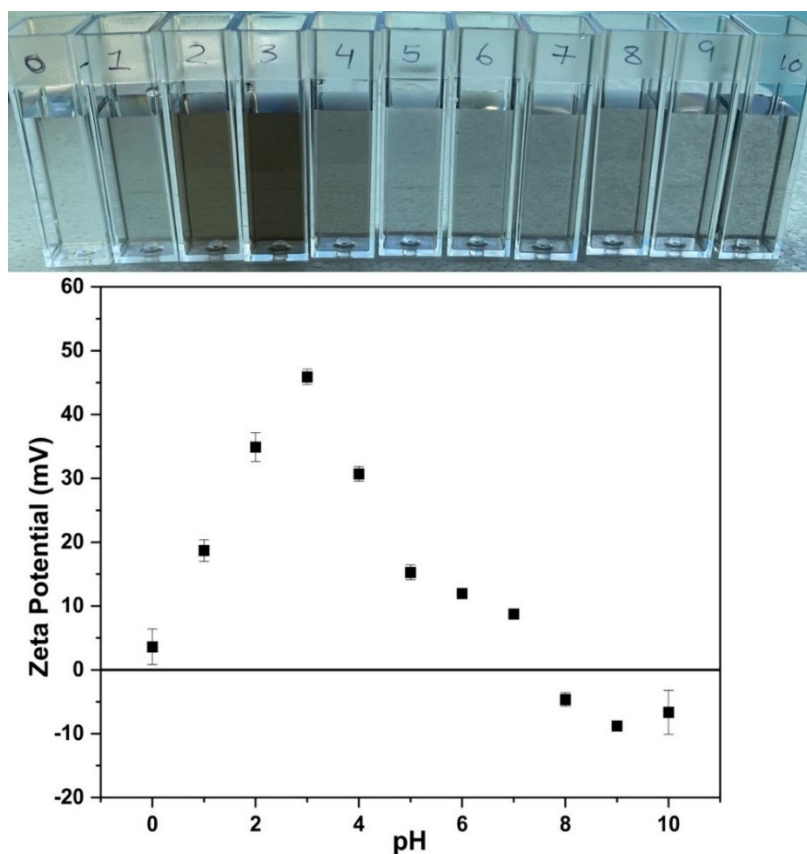


**Figure 65:** Images of Cr<sub>2</sub>N NPs suspension at different pH and the corresponding zeta potential.

After successfully synthesizing Cr<sub>2</sub>N NPs and investigating their plasmonic properties, the photothermal properties were investigated. In this study, 365 nm LED with 30 nm linewidth at FWHM was used as the excitation source. This light source was chosen as the excitation wavelength is closer to the LSPR. The temperature change of 10.0 nM aqueous solution of Cr<sub>2</sub>N NPs was recorded at 1 W cm<sup>-2</sup> illumination intensity. After 30 minutes, the steady-state temperature was reached, and an average change in temperature of 10 ± 0.3 °C was observed as shown in **Figure 66A**. A control study was conducted using water in the absence of Cr<sub>2</sub>N NPs and an increase of 1.6 ± 0.3 °C was observed. After irradiating the sample for 30 minutes, the LED source was turned off and the cooling temperature was recorded for another 30 minutes to determine the heat transfer from the NPs to the surroundings. Thus, the photothermal transduction efficiency of Cr<sub>2</sub>N NPs was determined to be 60 ± 2 %. The change in temperature of the 10.0 nM Cr<sub>2</sub>N NPs solution at different illumination power densities (1.0, 0.75, 0.50, and 0.25 W cm<sup>-2</sup>) was recorded as shown in **Figure 66A**. The temperature changes linearly with the illumination density as shown in **Figure 66B**, which is consistent with the previous data obtained for the group IVB TMN NPs.<sup>[303]</sup> The cycling stability of the Cr<sub>2</sub>N NPs was evaluated by switching the LED source on and off, for 30 minutes intervals, over 5 cycles as shown in **Figure 66C** and there was no significant degradation observed between cycles.

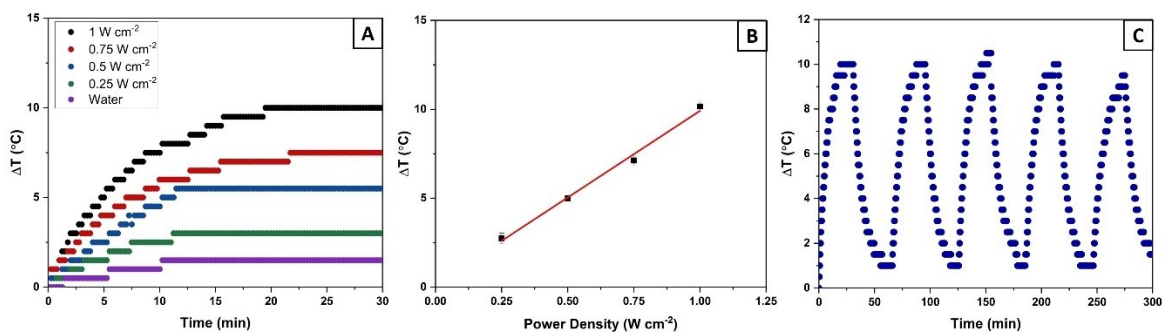


**Figure 66:** (A) Representative temperature change plots as a function of time of Cr<sub>2</sub>N NPs at 1.0, 0.75, 0.50, and 0.25 W cm<sup>-2</sup> illumination intensities at 365 nm. (B) Representative plot of temperature change at different illumination density. (C) Photothermal stability of 10.0 nM Cr<sub>2</sub>N NP solutions over 5 cycles at 365 nm under 1 W cm<sup>-2</sup> illumination.

## 6.4 Conclusion

Plasmonic Cr<sub>2</sub>N NPs were successfully synthesized using solid-state metathesis of Cr<sub>2</sub>O<sub>3</sub> with Mg<sub>3</sub>N<sub>2</sub>. This resulted in the formation of water dispersible Cr<sub>2</sub>N NPs with an average diameter size of  $9 \pm 5$  nm and positively charged surface. The particles had a varying thickness of oxide and oxynitride layer around the nitride core as determined from XPS and TEM analysis. The calculations predicted these NPs to have LSPR below 200 nm which aligned with the experimental observations. While a strong LSPR was not observed in the absorbance spectrum limited by the wavelength cutoff, low-loss EELS spectra showed the presence of surface and bulk plasmon resonances below 200 nm. The stability of the colloidal suspension of Cr<sub>2</sub>N NPs were investigated by measuring the zeta potential at different pH. These studies showed that the Cr<sub>2</sub>N NP suspensions are only stable at a narrow pH range between 2-3 which is consisted with group IVB TMNs studies. For the first time, the photothermal property of plasmonic Cr<sub>2</sub>N NPs were investigated at  $1 \text{ W cm}^{-2}$  illumination using a 365 nm LED source. It was observed that Cr<sub>2</sub>N NPs showed no degradability over time and the photothermal transduction efficiency was ~60 % which can be very promising for photothermal applications. The work presented here showed that the ease of synthesis, good photothermal performances, and stability of Cr<sub>2</sub>N NPs can represent a first step toward implementing Cr<sub>2</sub>N in deep ultraviolet plasmonic applications. Future work would focus on using these plasmonic Cr<sub>2</sub>N NPs for disinfection applications.

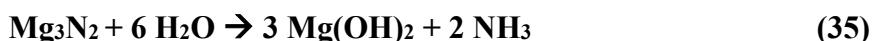
## **Chapter 7: Synthesis of Plasmonic Group IVB Nitrides using Solid-Gas Method**

*This author wishes to clarify her contribution to the research described in Chapter 7 of this thesis document.* This chapter discusses the synthesis of plasmonic group IVB TMN NPs using the solid-gas reaction. The synthesized NPs were characterized using various techniques as described in experimental section of this thesis (Chapter 2).

My contribution to this study includes synthesizing and optimizing the solid-gas reaction to obtain pure group IVB TMN NPs. The resulting NPs were characterized using XRD, UV-vis spectroscopy, DLS, and TEM. The XPS measurements were performed by Andrew George.

## 7.1 Introduction

As discussed in the previous chapters, plasmonic TMN NPs can be successfully synthesized using the solid-state metathesis reaction by reacting  $\text{Mg}_3\text{N}_2$  and the metal oxide precursors.<sup>[291]</sup> While  $\text{Mg}_3\text{N}_2$  is an attractive nitriding agent as it forms MgO as the reaction byproduct that can be easily removed with HCl, it does succumb to decomposition in humid conditions. Upon exposure to moisture,  $\text{Mg}_3\text{N}_2$  oxidizes to form  $\text{Mg}(\text{OH})_2$  and  $\text{NH}_3$  as shown in the **equation (35)**:



The varying humid conditions in Halifax, led to reaction reproducibility issues. We have since moved to handling the reactants in  $\text{N}_2$  filled glovebox but transferring the reaction boats and tubes in and out of the glovebox has made the synthesis method cumbersome. Recently, Wu *et al.* have successfully synthesized ZrN and HfN by magnesiothermic reduction process which involved reacting the metal oxide with  $\text{NaN}_3$  and Mg metal at 1273 K.<sup>[326]</sup> While Mg metal is easier to handle under humid conditions compared to  $\text{Mg}_3\text{N}_2$ ,  $\text{NaN}_3$  should be avoided as it can violently react with water.<sup>[327]</sup> Building on this method, this chapter focuses on synthesizing the group IVB TMN NPs using a simpler pathway which involves reacting the metal oxides with Mg metal under  $\text{N}_2$  flow at 1000 °C for 12 hours. Previous studies have shown that  $\text{Mg}_3\text{N}_2$  can be formed between 650 and 800 °C by reacting Mg metal with  $\text{N}_2$  gas.<sup>[328,329]</sup> It is possible to form  $\text{Mg}_3\text{N}_2$  in-situ during this reaction which would then nitridize the metal oxides to form TMNs.



## **7.2 Experimental**

### ***7.2.1 Material***

Titanium dioxide (TiO<sub>2</sub>, 99.9%, 18 nm), zirconium dioxide (ZrO<sub>2</sub>, 99.95%, 20 nm), and hafnium dioxide (HfO<sub>2</sub>, 99.99%, 61-80 nm) were purchased from U.S. Research Nanomaterials Inc. Magnesium powder was purchased from Oakwood Chemical (Mg, 99%, -325 mesh). All glassware was cleaned thoroughly with deionized water then acetone and placed in the oven to dry prior to use.

### ***7.2.2 Synthesis of Transition Metal Nitride Nanoparticles***

The group IVB TMN NPs solutions were synthesized as discussed in section 2.8.1.

### ***7.2.3 Characterization Techniques***

The powder XRD, XPS, UV-vis spectroscopy, and DLS are the same as discussed in Chapter 3.

## **7.3 Results and Discussion**

Mg metal powder was mixed with metal oxide nanopowders using a mortar and pestle. This allowed for better mixing of the precursors without the rapid decomposition of Mg<sub>3</sub>N<sub>2</sub> upon exposure to air/moisture. The mixed powders were heated under N<sub>2</sub> atmosphere for 12 hours at 1000 °C. The TMN NPs were isolated using the procedure similar to the solid-state reactions where ~79% of the product was dispersible in water whereas only ~60% of the NPs were dispersible when Mg<sub>3</sub>N<sub>2</sub> was used.

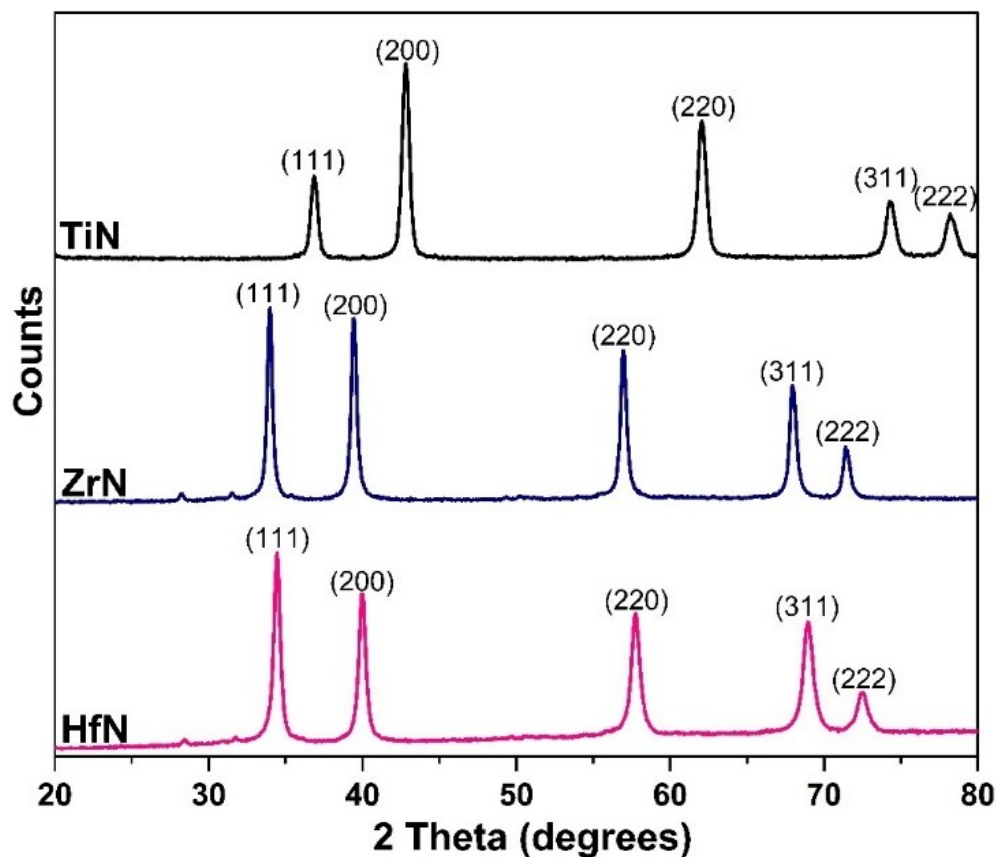


**Figure 67:** Powder XRD patterns of TiN, ZrN, and HfN NPs prepared by reacting metal oxides with Mg metal under N<sub>2</sub> flow.

Based on the powder XRD patterns shown in **Figure 67**, cubic phase TMN NPs were formed. The XRD patterns of ZrN and HfN show low amounts of oxide peaks which is consistent with studies shown in Chapter 3.<sup>[291]</sup> Scherrer analysis of the observed reflections yielded crystallite sizes of  $19 \pm 1$ ,  $23 \pm 1$ , and  $18 \pm 2$  nm, for TiN, ZrN and HfN, respectively. The results obtained using this route provides slightly bigger crystallite sizes which could be due the difference in reaction mechanisms between the solid-state and

solid-gas methods. The TEM analysis of the TMNs (**Figure 68**) showed the presence of NPs with average particle sizes of  $23 \pm 7$ ,  $27 \pm 6$ , and  $16 \pm 5$  nm for TiN, ZrN, and HfN, respectively. The zeta potential of TiN, ZrN, and HfN NP dispersions were determined to be  $29 \pm 2$ ,  $44.2 \pm 0.4$ ,  $45 \pm 2$  mV, respectively. These measurements were consistent with the zeta potential values obtained when synthesizing the TMN NPs using commercially purchased  $\text{Mg}_3\text{N}_2$ .<sup>[303]</sup> The hydrodynamic radius of TiN, ZrN, and HfN were determined to be  $59.0 \pm 0.4$ ,  $47.4 \pm 0.6$ , and  $45 \pm 1$  nm, respectively.

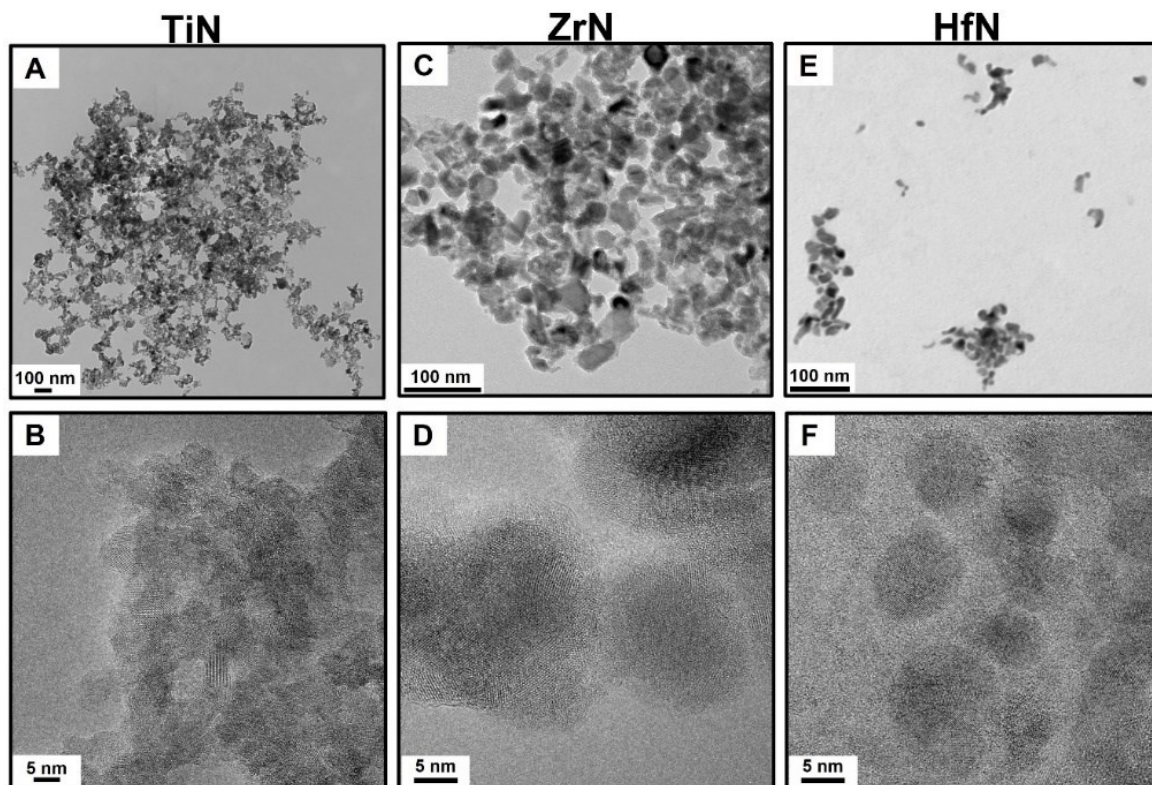


**Figure 68:** TEM images of (A, B) TiN, (C, D) ZrN, and (E, F) HfN NPs.

The formation of TMN can occur in one of two pathways where  $\text{Mg}_3\text{N}_2$  can form in-situ as shown in **equation (36)** and then can subsequently react with the metal oxide to form the nitride as shown in **equation (37)**.



Alternatively, Mg metal can reduce the  $\text{MO}_2$  powder to respective metals ( $\text{M} = \text{Ti}, \text{Zr}, \text{Hf}$ ) which can undergo nitridation with  $\text{N}_2$  gas as shown in **equations (38) and (39)**.



In-situ powder XRD studies or quenching the reactions at high temperatures can reveal the reaction intermediates and pathways. Depending on the reaction mechanism, variations in particle and crystallite sizes can be expected. The elemental composition of the nitride NPs was analyzed using XPS. The high-resolution XP spectrum of the Ti 2p region showed the presence of TiN with a  $2p_{3/2}$  peak at 454.5 eV, oxynitride ( $\text{TiN}_x\text{O}_y$ ) with a  $2p_{3/2}$  peak at 456.0 eV, and oxides ( $\text{TiO}_2$ ) with a  $2p_{3/2}$  at 460.8 eV (**Figure 69**).<sup>[223]</sup> Correspondingly, the high-resolution XP spectrum of the N 1s region showed the presence of TiN and  $\text{TiN}_x\text{O}_y$  with 1s peaks at 396.4 and 399.0 eV, respectively (**Figure 69**).<sup>[223]</sup> A high-resolution XP spectrum of the Zr 3d region showed the presence of Zr  $3d_{5/2}$  peaks at 179.9, 181.0, and 182.6 eV, corresponding to  $\text{ZrN}$ ,  $\text{ZrN}_x\text{O}_y$ , and  $\text{ZrO}_2$ , respectively (**Figure 70**).<sup>[156]</sup> Similarly, the high-resolution XP spectrum of Hf 4f region showed the

presence of HfN, HfN<sub>x</sub>O<sub>y</sub>, and HfO<sub>2</sub>, with Hf 4f<sub>7/2</sub> peaks at 15.2, 16.1, and 17.5 eV, respectively (**Figure 71**).<sup>[224,225]</sup> N 1s spectra showed the presence of nitride (ZrN: 396.5 eV and HfN: 396.7 eV) and oxynitride (ZrN<sub>x</sub>O<sub>y</sub>: 399.5 eV and HfN<sub>x</sub>O<sub>y</sub>: 400.0 eV) for both ZrN and HfN NPs (**Figure 70** and **Figure 71**).<sup>[156,224,225]</sup> Compared to the Mg<sub>3</sub>N<sub>2</sub> method (Chapter 3), higher amounts of surface oxide were observed for TiN and HfN using this method. It is currently unclear why that is the case, but a more detailed mechanistic study can help decipher this difference.

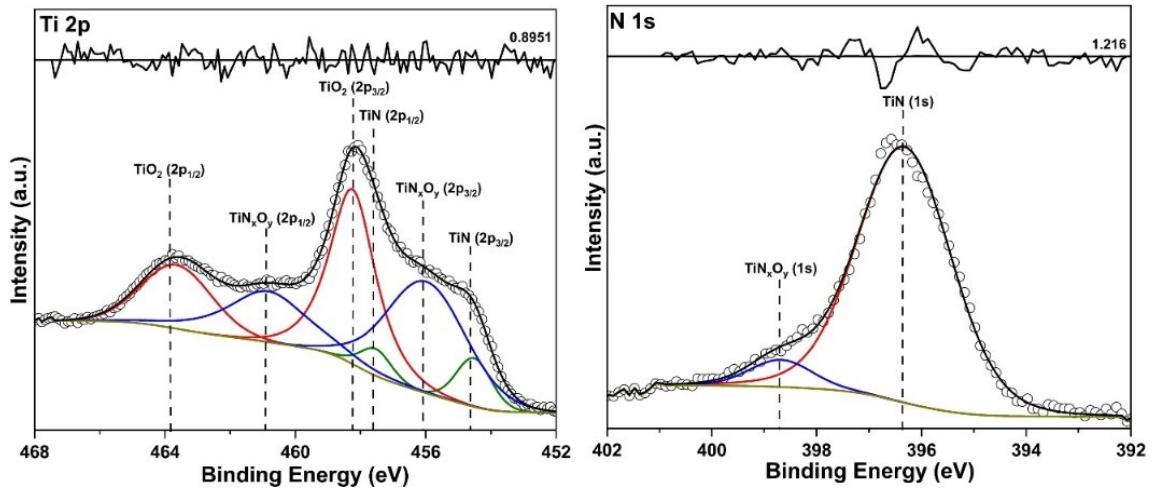


**Figure 69:** High-resolution X-ray photoelectron spectra of Ti 2p and N 1s region of TiN NPs. Experimental data represented as open circles, and the overall fitted data represented as a black line.

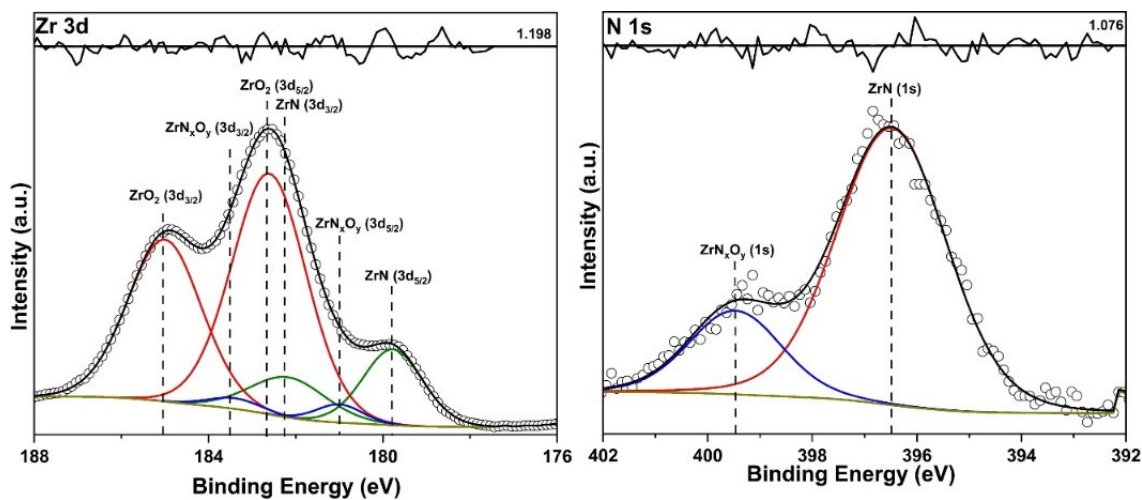


**Figure 70:** High-resolution X-ray photoelectron spectra of Zr 3d and N 1s region of ZrN NPs. Experimental data represented as open circles, and the overall fitted data represented as a black line.

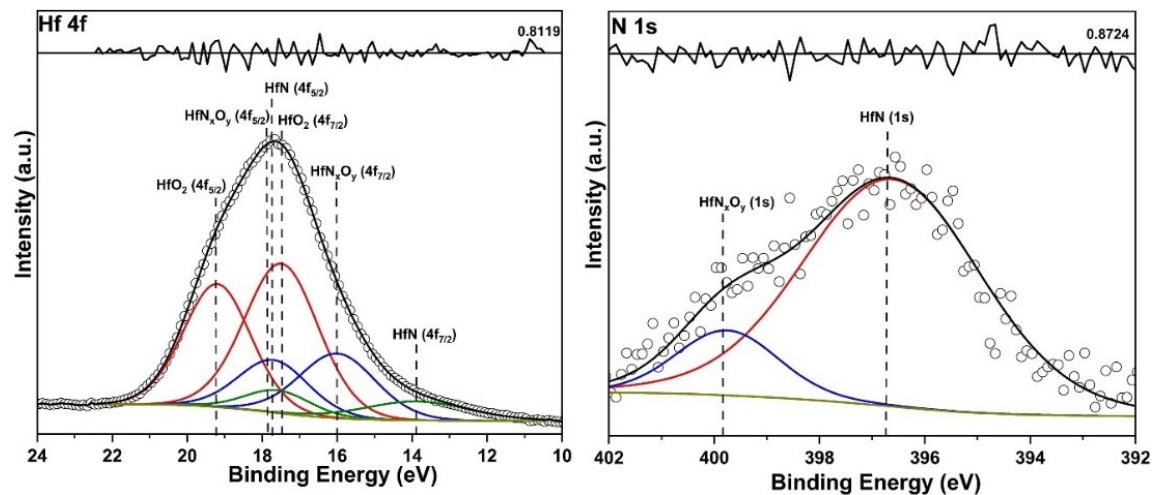


**Figure 71:** High-resolution X-ray photoelectron spectra of Hf 4f and N 1s region of HfN NPs. Experimental data represented as open circles, and the overall fitted data represented as a black line.

The UV-vis absorbance spectra showed an LSPR peak maxima at 840 nm, 630 nm, and 610 nm corresponding to TiN, ZrN, and HfN, respectively (**Figure 72**). The TiN and HfN peak positions were redshifted compared to the solid-state method discussed in Chapter 3 (**Table 3**). This can be either due to larger particle size or higher amounts of surface oxide as indicated in the XPS analysis. Since the ZrN LSPR is slightly blue-shifted despite the larger particle size indicates that the red-shift observed in TiN and HfN NPs prepared here is due to higher surface oxide content. It is currently unclear why higher amount of surface oxide is obtained using Mg metal and will need to be investigated in the future.

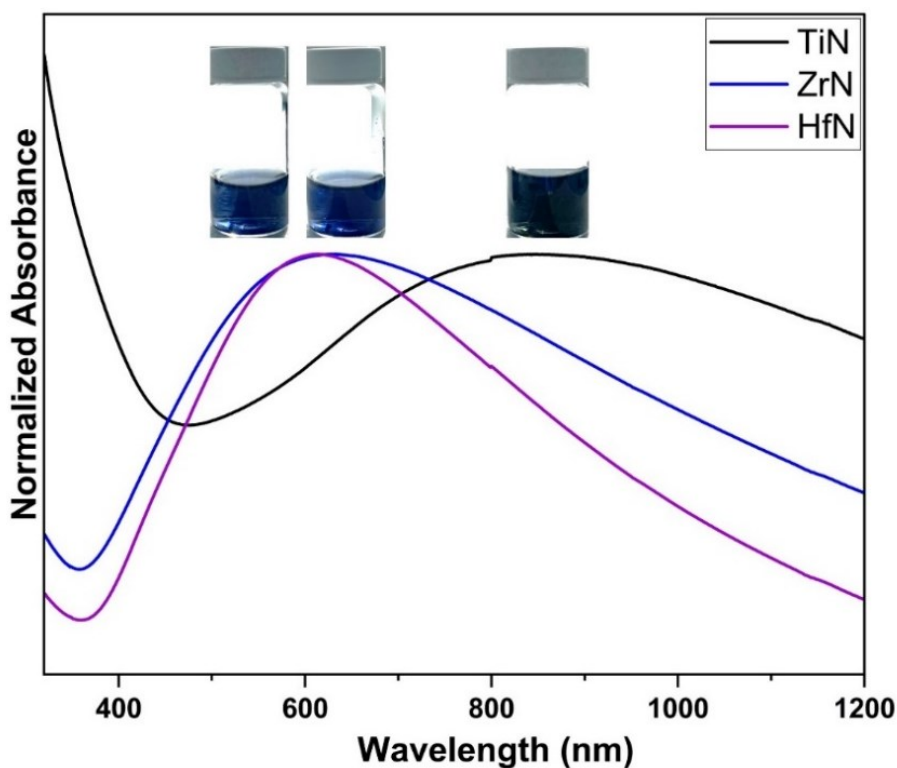


**Figure 72:** Normalized absorbance spectra of water dispersed TiN, ZrN, and HfN NPs. (Inset: photograph of NPs dispersed in water under white light).

**Table 3:** Comparison of TMN NPs prepared using solid-state metathesis ( $\text{MO}_2 + \text{Mg}_3\text{N}_2$ ), and solid-gas route ( $\text{Mg} + \text{N}_2$ ).

<b>Solid-State Metathesis</b>			
	<b>TiN</b>	<b>ZrN</b>	<b>HfN</b>
Crystallite size (nm)	15	17	15
TEM (nm)	$12 \pm 3$	$15 \pm 2$	$11 \pm 4$
Absorbance (nm)	720	650	560
Zeta Potential (mV)	$33 \pm 2$	$50 \pm 3$	$43 \pm 1$
Hydrodynamic Radius (nm)	$53.4 \pm 0.5$	$59.4 \pm 0.2$	$55 \pm 1$
<b>Solid-Gas Route</b>			
	<b>TiN</b>	<b>ZrN</b>	<b>HfN</b>
Crystallite size (nm)	$19.4 \pm 0.9$	$23.0 \pm 1.1$	$17.5 \pm 1.8$
TEM (nm)	$23 \pm 7$	$27 \pm 6$	$16 \pm 4$
Absorbance (nm)	840	630	610
Zeta Potential (mV)	$29 \pm 2$	$44.2 \pm 0.4$	$45 \pm 2$
Hydrodynamic Radius (nm)	$59.0 \pm 0.4$	$47.4 \pm 0.6$	$45 \pm 1$

#### 7.4 Conclusion

Herein, a solid-gas method was explored to prepare group IVB TMN NPs by reacting  $\text{MO}_2$  precursors with Mg metal and  $\text{N}_2$  gas. Compared to the  $\text{Mg}_3\text{N}_2$  synthesis, larger crystallite and particle size was obtained with this method. Interestingly, higher amount of surface oxide was observed in TiN and HfN NPs which resulted in broader and red-shifted LSPRs. Similar to the  $\text{Mg}_3\text{N}_2$  method, the NPs had positively charged surface with zeta potential ranging between 30–45 mV. This method offers an alternative method to prepare plasmonic group IVB TMN NPs which is less cumbersome than  $\text{Mg}_3\text{N}_2$  method.



## Chapter 8: Conclusions

This thesis highlighted various projects focusing on the synthesis, stability, and photothermal properties of plasmonic transition metal nitride nanostructures. During my doctoral program, I developed a solid-state metathesis method to prepare TiN, ZrN, HfN (Chapter 3) and Cr<sub>2</sub>N NPs (Chapter 6) and a solid-gas method to make TiN, ZrN, and HfN NPs (Chapter 7). To the best of our knowledge, we report the first synthetic method to prepare free-standing plasmonic HfN NPs. The plasmonic NPs were extensively characterized using various techniques including, powder XRD, TEM, SEM, XPS, DLS, and UV-vis spectroscopy. The photothermal properties (Chapters 4 and 6), and stability (Chapters 5 and 6) of these NPs were investigated in detail. This thesis outlines some of the first in-depth experimental analysis of plasmonic TMN NPs which is important to determine their applicability in future uses.

The solid-state synthetic method explored the reaction of metal oxide nanopowders with Mg<sub>3</sub>N<sub>2</sub> at 1000 °C under Ar atmosphere. The reaction byproducts were removed with an HCl workup. This method yielded NPs between 9 and 17 nm for group IVB nitrides and between 5 and 15 nm for Cr<sub>2</sub>N. While this synthesis method is easy to adapt compared to the laser ablation and non-thermal plasma methods, it results in polydisperse particles. All the nitride products were crystalline and phase pure as evidenced by the powder XRD patterns. ZrN and HfN did have trace amounts of unreacted oxide precursors. The XPS analysis and TEM analysis showed presence of an oxide/oxy-nitride shell around the nitride core for all the materials. The zeta potential of all the NPs suspensions were  $\geq 30$  mV and the surface was positively charged. The positive charge is hypothesized to result from the

protonation of surface hydroxyl groups after the HCl workup. This positive surface charge allows the NPs to be colloidally stable in water (**Figure 73**).

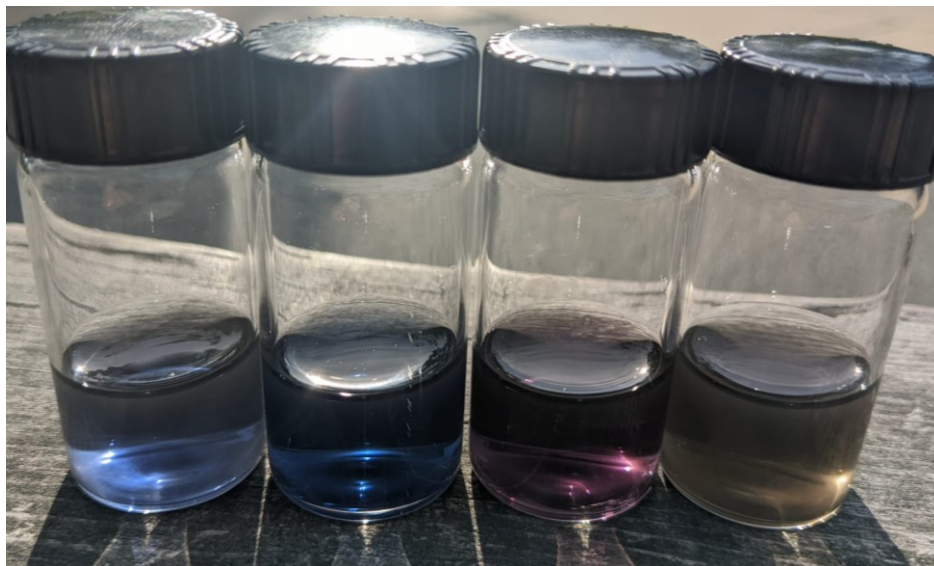


**Figure 73:** A photograph of TiN, ZrN, HfN, and Cr<sub>2</sub>N solution lined up from left to right.

The LSPR of these NPs was measured using absorbance spectroscopy and calculated using finite element method (calculations were performed by Dr. Yashar Monfared). Both the analysis showed the LSPR for TiN to be in the near-IR region and for ZrN and HfN to be in the visible region (**Figure 74**). A distinctive LSPR peak could not be observed in the absorbance spectrum for Cr<sub>2</sub>N since it is in the deep-UV which is below the wavelength cut-off of the spectrometer. However, low-loss EELS and EELS loss probability map studies showed the plasmon resonances for the Cr<sub>2</sub>N below 200 nm where it was predicted to be present via calculations. The absorbance exhibited by all the nitrides were broad due to polydispersity of the NPs and presence of oxide shell.

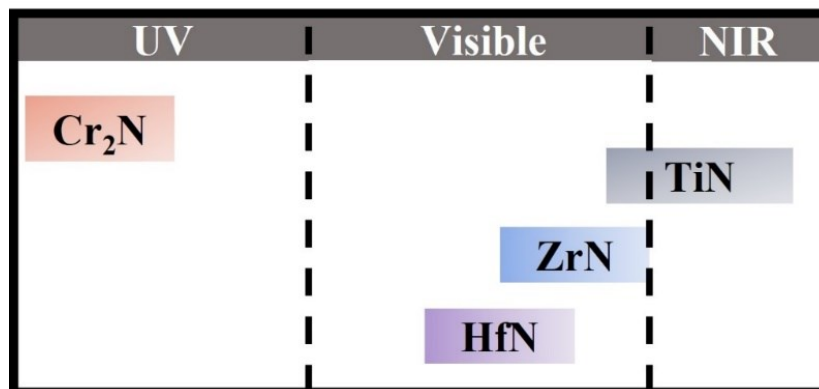


**Figure 74:** Spectral regions of LSPR for TiN, ZrN, HfN, and Cr<sub>2</sub>N NPs.

The chemical and oxidative stability of the TMN NPs was also explored. All NPs were found to be colloidally stable in a narrow pH window of 2-3. At pH higher than 3, the NPs aggregated owing to the loss of surface charge, however, this was reversible, and the NPs can be resuspended if the pH is adjusted to 2-3. At pH below 2, all the TMNs undergo dissolution to form metal oxysalts. The oxidative stability of group IVB nitrides was monitored by measuring the absorbance spectra of the TMN colloidal suspension over a period of 64 days. The results showed that TiN NPs were the least stable, since the absorbance peak was significantly broadened and red-shifted. The color of the TiN colloidal suspension has changed from dark blue to white indicating the formation of TiO<sub>2</sub>. On the other hand, ZrN and HfN showed slight reduction in the LSPR peak intensity over time. However, if the solutions are stored without constantly being analyzed, then the solutions are stable for a much longer time. XPS was used to monitor oxidation of the TMN NPs powder over time, and the results showed that all the TMNs were found to be fairly oxidatively stable if stored as a solid compared to the suspensions.

The photothermal transduction efficiencies of group IVB nitrides and Cr<sub>2</sub>N was determined under the illumination of 850 and 365 nm light, respectively. It was observed that the group IVB TMN NPs yielded higher photothermal transduction efficiency than Au NRs, and more specifically HfN NPs obtained the highest efficiency of  $65 \pm 4\%$  among the TMN NPs. The high photothermal transduction efficiency of HfN NPs could be attributed to the low scattering cross-section that were determined using FEM studies and efficient electron-phonon coupling as determined by Askes *et al.*<sup>[330]</sup> Cyclability studies were performed at  $1 \text{ W cm}^{-2}$  illumination indicated no thermal degradation for the TMN NPs after 5 cycles. The change in temperature was linear for different illumination power densities but non-linear for varying NP concentrations. This behaviour is consistent with the literature reports of Au and Ag based nanostructures and these studies have shown that TMN NPs can replace noble metals in future applications. The photothermal effect of plasmonic Cr<sub>2</sub>N NPs were investigated at  $1 \text{ W cm}^{-2}$  illumination using a 365 nm LED source. Cyclability studies were performed  $1 \text{ W cm}^{-2}$  indicated no change in performance for the TMN NPs after 5 cycles. The photothermal transduction efficiency at 365 nm was determined to be  $\sim 60\%$  which is very promising for photothermal applications in the UV region.

The final chapter discussed a solid-gas method to prepare group IVB nitrides by reacting metal oxide nanopowders with Mg metal and N<sub>2</sub> gas. This study showed the possibility of synthesizing plasmonic TMN NPs by using a different route. Based on the powder XRD analysis, crystalline TMN NPs with a cubic lattice structure were obtained. The average particle size varied between 10-30 nm which was larger than the solid-state

method. This difference in size is likely due to different nitridation mechanism. However, similar to the solid-state methods, the particles were dispersible in water, had a positively charged surface, and the zeta potential of the suspensions were  $\geq 28$  mV. Furthermore, the XPS showed that the TMN NPs have a layer of oxide and oxynitride on their surface similar to all the nitrides made using solid-state method. This suggests that the surface oxidation likely occurs during the HCl work-up step and is independent of the synthetic method used. The LSPR peak of TiN, ZrN, and HfN were at 840 nm, 630 nm, and 610 nm, respectively.

This thesis highlighted novel research toward synthesizing and characterizing plasmonic TMN NPs (TiN, ZrN, HfN, and Cr<sub>2</sub>N) using the solid-state metathesis route and paved the way to utilizing them in real-world application. However, there are many aspects that need to be addressed and more TMN NPs need to be synthesized. The long-term stability of Group IVB must be explored in more detail by investigating surface modification and functionalization strategies. Ongoing research is currently being conducted in our research laboratory to focus on surface-functionalization to prevent aggregation and enable dispersion of the NPs in different organic solvents. Monitoring the colloidal suspension using TEM, DLS, and UV-vis spectroscopy will determine the stability and observe changes in the NP sizes. There are many parameters that can be controlled such as the composition of the capping agent, and the storage parameters (temperature, solution, pH, etc.). Another approach is through alloying which can enable the formation of stable NPs without the need for additional functionalization/capping. For example, since TiN NPs exhibit higher surface oxidation, alloying it with ZrN or HfN can improve its stability.

Future work will involve exploring other plasmonic TMN nanostructures. Synthesis of Group VB and VIB metal nitrides using the solid-state metathesis reaction will be attempted. Various TMNs such as tantalum nitride, molybdenum nitride, and tungsten nitride have been predicted to be plasmonic, therefore exploring these TMNs will be worthwhile. Preliminary studies involved synthesizing plasmonic vanadium nitride (VN) NPs using the solid-state metathesis route were successful. The LSPR of VN NPs lies within the UV region which can be promising for water disinfection applications. The photothermal properties of plasmonic VN NPs were determined to be 57%. However, more studies need to be completed to investigate their long-term chemical and oxidative stability to assess their potential use in applications. Other materials such as niobium nitride (NbN) were also investigated using the solid-state metathesis however, a pure phase of NbN has not been obtained yet. Therefore, more optimization studies need to be conducted.

The solid-state metathesis reaction has been shown to be a promising route for synthesizing plasmonic TMN NPs. This route offers many advantages over other methods such as ease of preparation, minimal purification steps, good atomic economy, and simple infrastructure. However, one of the major disadvantages is the inability to probe the reaction in-situ to determine the reaction mechanism. Therefore, future work will focus on performing in-situ synchrotron XRD studies or trapping reaction intermediates using liquid N<sub>2</sub> to gain a better understanding of the reaction mechanism. This will help in selectively choosing the reaction parameters such as reaction temperature, reaction time, and ramp rate instead of attempting different conditions. Future work will also focus on investigating the possibility of synthesizing the TMN NPs at a large scale without compromising their

properties and ensuring the reaction is completed. The high temperatures of the solid-state metathesis and long reaction time can be problematic for large-scale applications. Preliminary work has investigated the use of an inert heat sink such as calcium chloride to increase the path length for diffusion of reacting components, thereby reducing the overall reaction temperature. Perhaps if these studies are optimized, then plasmonic TMN NPs can be synthesized at lower temperatures and/or reaction time.

The TMN NPs colloidal suspension obtained by mixing the transition metal oxides with Mg metal under N<sub>2</sub> flow provided very concentrated colloidal suspension compared to TMN NPs colloidal suspensions obtained using commercially purchased Mg<sub>3</sub>N<sub>2</sub>. The yield of the powder component was very minimal using the Mg metal route, which could indicate that NPs formed have better dispersibility. This could be potentially used as a better route for large-scale synthesis, therefore more experiments need to be conducted. Since, the melting point of Mg metal is 650 °C lower reaction temperatures might be enough for the nitridation, and perhaps better size dispersity can be obtained. The chemical and oxidative stability of these solutions needs to be studied. Photothermal studies on these colloidal suspensions can be conducted to determine if better photothermal transduction efficiencies can be achieved.

The performance of the TMNs materials can be improved by changing their composition which can allow tuning the electronic band structure to achieve desirable properties. Changing the material composition can shift the unwanted interband transitions to other regions of the spectrum or dampen them. An extensive theoretical study by Kumar *et al.* have shown that Ti<sub>1-x</sub>Zr<sub>x</sub>N alloy system can broaden the choices of alternative

plasmonic materials because they possess a great tunability of their plasmonic properties.<sup>[135]</sup> Therefore, alloyed Ti, Zr, and Hf nitride nanostructures will be explored experimentally in more detail. Atomic mixing is crucial to allow the band engineering in a favorable manner. Therefore, uniformly distributed mixed-metal oxides can be synthesized using sol-gel or hydrothermal techniques. Upon successful synthesis of the precursors, similar nitridation reactions will be performed to prepare respective alloyed TMNs. Preliminary studies have been conducted to prepare mixed metal oxides of Zr and Ti using sol-gel reactions which shown to be promising. However, more optimization is required to ensure atomic mixing is obtained.

Since the photothermic effect of TMNs been fully investigated, the next step would be implementing these materials into photothermic applications. For example, these TMNs can be investigated for cancer treatment therapy where they can be imbedded into a cancerous cell and the efficiency in destroying cancer cells can be monitored. However, this is complicated because there are various issues that need to be overcome such as cytotoxicity, biocompatibility, surface modification, size and shape modification of NPs. Currently, Au NRs have been investigated for photothermal therapy applications however, they exhibit high toxicity due to the adsorbed CTAB layer present on the surface of the particles which helps prevent aggregation. Therefore, extensive tuning of the surface of the Au NRs is needed to allow them to be used in biological applications which is not ideal. Therefore, TMN NPs can be investigated however, toxicity assays and appropriate surface modification need to be conducted prior to biological studies. These TMN NPs can also be used for solar-driven water evaporation or desalination processes.



The demand for clean water has been increasing and it is estimated that 70% of the world population will face water scarcity by 2050.<sup>[331]</sup> Consequently, large-scale, efficient technologies for seawater desalination are urgently needed. Traditional desalination technologies include membrane-based designs such as reverse osmosis which are economically unfeasible. Alternatively, solar vapor generation using sunlight as the only energy source is a desirable alternative and environmentally benign. However, due to the poor optical absorption of water and acute heat losses, the natural light-to-vapor conversion efficiency is too low to generate a reliable fresh water supply. Incorporating plasmonic NPs can help enhance the water evaporation rates to efficiently desalinate sea water.<sup>[241]</sup> In our group, TMN NPs were loaded onto an anodic aluminum oxide (AAO) substrate to generate interfaces for solar-driven water evaporation.<sup>[293]</sup> The studies have shown that the TMN-AAO substrates were successful in generating high vapor efficiencies and can be used toward water desalination. However, the AAO substrates are very brittle and expensive, therefore better substrates that are cost-effective, durable, robust, and stable are needed.

Lastly, plasmonic nanomaterials have been explored for field enhancement applications, specifically for SERS. Au and Ag are the commonly used material for field enhancement, but TMN NPs remain unexplored. Recently, computational studies have shown that ZrN exhibit electric field intensity amplification similar to Au, and although TiN produces significant amplification as well however, it is lower than ZrN and Au.<sup>[332]</sup> However, until now there are no experimental exploration of using group IVB TMNs toward SERS application. Recently, tungsten nitride and tantalum nitride were used as

SERS substrate for the first time.<sup>[333]</sup> These substrates were prepared by sputtering deposition techniques to ensure the substrates are uniform. In order to use our TMN NPs as SERS substrate, monodispersed NPs needs to be prepared and therefore this might be a challenge to obtain using the solid-state metathesis reaction and hence other methods can be explored. Nonetheless, investigating the field enhancement properties of plasmonic TMN NPs experimentally could provide a promising strategy for using them as SERS substrates.

Overall, the field of plasmonic TMNs will continue to expand, and their utilization will increase as researchers learn more about the properties of these materials. When thinking about choosing the appropriate plasmonic nanomaterial for an application, it is crucial to think about all the factors to ensure the right choice is made. Some factors to consider include the onset of interband transition ( $\omega_{\text{int}}$ ), the Q factor, plasma frequency ( $\omega_{\text{p}}$ ), cross-over frequency ( $\omega_{\text{c}}$ ), momentum scattering rate ( $\gamma$ ), cost, and melting point. Additionally, the chemical and oxidative stability, biocompatibility, synthetic parameters, experimental reproducibility, and material abundance needs to be considered.

## References:

- [1] X. Huang, M. A. El-Sayed, *J. Adv. Res.* **2010**, *1*, 13–28.
- [2] M. A. El-Sayed, *Acc. Chem. Res.* **2004**, *37*, 326–333.
- [3] J. Kim, H. Y. Son, Y. S. Nam, *Sci. Rep.* **2018**, *8*, 10464.
- [4] K.-T. Lin, H. Lin, B. Jia, *Nanophotonics* **2020**, *9*, 3135–3163.
- [5] H. J. Huang, J. C.-S. Wu, H.-P. Chiang, Y.-F. Chou Chau, Y.-S. Lin, Y. H. Wang, P.-J. Chen, *Catalysts* **2020**, *10*, 46.
- [6] N. Zhou, V. López-Puente, Q. Wang, L. Polavarapu, I. Pastoriza-Santos, Q.-H. Xu, *RSC Adv.* **2015**, *5*, 29076–29097.
- [7] Q. Duan, Y. Liu, S. Chang, H. Chen, J. Chen, *Sensors* **2021**, *21*, 5262.
- [8] M.-Q. He, Y.-L. Yu, J.-H. Wang, *Nano Today* **2020**, *35*, 101005.
- [9] W. Q. Lim, Z. Gao, *Nano Today* **2016**, *11*, 168–188.
- [10] M. You, Z. Li, S. Feng, B. Gao, C. Yao, J. Hu, F. Xu, *Trends Biotechnol.* **2020**, *38*, 637–649.
- [11] S. Bayda, M. Adeel, T. Tuccinardi, M. Cordani, F. Rizzolio, *Molecules* **2020**, *25*, 112.
- [12] I. Muhammad, G. Saima, K. Murad Ali, K. M. I, *Am. Sci. Pub.* **2016**, *17*, 119-135.
- [13] R. P. Feynman, *Resonance* **2011**, *16*, 890.
- [14] N. Baig, I. Kammakakam, W. Falath, *Mater. Adv.* **2021**, *2*, 1821–1871.
- [15] G. Guisbiers, S. Mejía-Rosales, F. Leonard Deepak, *J. Nanomater.* **2012**, *2012*, e180976.

- [16] J. K. Patel, A. Patel, D. Bhatia, in *Emerg. Technol. Nanoparticle Manuf.*, Springer International Publishing, Cham, **2021**, pp. 3–23.
- [17] A. Moores, F. Goettmann, *New J. Chem.* **2006**, *30*, 1121–1132.
- [18] N. Dasgupta, S. Ranjan, E. Lichtfouse, Eds. , *Environmental Nanotechnology*, Springer International Publishing, Cham, **2018**.
- [19] T. Pradell, J. Molera, A. D. Smith, A. Climent-Font, M. S. Tite, *J. Cult. Herit.* **2008**, *9*, 123–128.
- [20] P. Sciau, *Nanoparticles in Ancient Materials: The Metallic Lustre Decorations of Medieval Ceramics*, IntechOpen, **2012**.
- [21] S. M. Morton, D. W. Silverstein, L. Jensen, *Chem. Rev.* **2011**, *111*, 3962–3994.
- [22] N. Zhang, C. Han, X. Fu, Y.-J. Xu, *Chem* **2018**, *4*, 1832–1861.
- [23] E. Boisselier, D. Astruc, *Chem. Soc. Rev.* **2009**, *38*, 1759–1782.
- [24] S. Link, M. A. El-Sayed, *Int. Rev. Phys. Chem.* **2000**, *19*, 409–453.
- [25] K. C. Majhi, M. Yadav, in *Green Sustain. Process Chem. Environ. Eng. Sci.* (Eds.: Inamuddin, R. Boddula, M.I. Ahamed, A.M. Asiri), Elsevier, **2021**, pp. 109–135.
- [26] Z. Wang, T. Hu, R. Liang, M. Wei, *Front. Chem.* **2020**, *8*.
- [27] Q. Zhang, Y. N. Tan, J. Xie, J. Y. Lee, *Plasmonics* **2009**, *4*, 9–22.
- [28] M. A. Kebede, T. Imae, in *Adv. Supramol. Nanoarchitectonics*, William Andrew Publishing, **2019**, pp. 3–16.
- [29] R. Baby, B. Saifullah, M. Z. Hussein, *Nanoscale Res. Lett.* **2019**, *14*, 341.
- [30] J. Lue. *Physical Properties of Nanomaterials.* **2007**.
- [31] S. Eustis, M. A. el-Sayed, *Chem. Soc. Rev.* **2006**, *35*, 209–217.

- [32] M. E. Stewart, C. R. Anderton, L. B. Thompson, J. Maria, S. K. Gray, J. A. Rogers, R. G. Nuzzo, *Chem. Rev.* **2008**, *108*, 494–521.
- [33] N. Elahi, M. Kamali, M. H. Baghersad, *Talanta* **2018**, *184*, 537–556.
- [34] L. S. B. Upadhyay, N. Verma, *Anal. Lett.* **2015**, *48*, 2676–2692.
- [35] A. Cunningham, S. Mühlig, C. Rockstuhl, T. Bürgi, *J. Phys. Chem. C* **2012**, *116*, 17746–17752.
- [36] R. W. Wood, *Lond. Edinb. Dublin Philos. Mag. J. Sci.* **1902**, *4*, 396–402.
- [37] G. Kumar, P. K. Sarswat, in *Rev. Plasmon. 2015*, Springer International Publishing, Cham, **2016**, pp. 103–129.
- [38] Lord Rayleigh, *Lond. Edinb. Dublin Philos. Mag. J. Sci.* **1907**, *14*, 60–65.
- [39] D. Bohm, D. Pines, *Phys. Rev.* **1953**, *92*, 609–625.
- [40] E. A. Stern, R. A. Ferrell, *Phys. Rev.* **1960**, *120*, 130–136.
- [41] J. A. Dionne, H. A. Atwater, *MRS Bull.* **2012**, *37*, 717–724.
- [42] E. C. Le Ru, P. G. Etchegoin, in *Princ. Surf.-Enhanc. Raman Spectrosc.* (Eds.: E.C. Le Ru, P.G. Etchegoin), Elsevier, Amsterdam, **2009**, pp. 121–183.
- [43] R. B. M. Schasfoort, A. J. Tudos, *Handbook of Surface Plasmon Resonance*, Royal Society Of Chemistry, **2008**.
- [44] T. Maurer, P.-M. Adam, G. Lévêque, *Nanophotonics* **2015**, *4*, 363–382.
- [45] J. Liu, H. He, D. Xiao, S. Yin, W. Ji, S. Jiang, D. Luo, B. Wang, Y. Liu, *Materials* **2018**, *11*, 1833.
- [46] J. Jana, M. Ganguly, T. Pal, *RSC Adv.* **2016**, *6*, 86174–86211.
- [47] E. B. Guidez, C. M. Aikens, *Nanoscale* **2014**, *6*, 11512–11527.

- [48] V. Amendola, R. Pilot, M. Frasconi, O. M. Maragò, M. A. Iatì, *J. Phys. Condens. Matter* **2017**, *29*, 203002.
- [49] A. Gellé, A. Moores, *Curr. Opin. Green Sustain. Chem.* **2019**, *15*, 60–66.
- [50] R. Ahmed Karaballi, S. Merchant, S. R. Power, C. L. Brosseau, *Phys. Chem. Chem. Phys.* **2018**, *20*, 4513–4526.
- [51] B. L. Goodall, A. M. Robinson, C. L. Brosseau, *Phys. Chem. Chem. Phys.* **2013**, *15*, 1382–1388.
- [52] M. Mesch, B. Metzger, M. Hentschel, H. Giessen, *Nano Lett.* **2016**, *16*, 3155–3159.
- [53] P. D. Howes, S. Rana, M. M. Stevens, *Chem. Soc. Rev.* **2014**, *43*, 3835–3853.
- [54] M. Li, S. K. Cushing, N. Wu, *Analyst* **2014**, *140*, 386–406.
- [55] S. Carretero-Palacios, A. Jiménez-Solano, H. Míguez, *ACS Energy Lett.* **2016**, *1*, 323–331.
- [56] V. E. Ferry, L. A. Sweatlock, D. Pacifici, H. A. Atwater, *Nano Lett.* **2008**, *8*, 4391–4397.
- [57] Y. Zhang, Z. Sun, S. Cheng, F. Yan, *ChemSusChem* **2016**, *9*, 813–819.
- [58] D. Jaque, L. M. Maestro, B. del Rosal, P. Haro-Gonzalez, A. Benayas, J. L. Plaza, E. M. Rodríguez, J. G. Solé, *Nanoscale* **2014**, *6*, 9494–9530.
- [59] H. Norouzi, K. Khoshgard, F. Akbarzadeh, *Lasers Med. Sci.* **2018**, *33*, 917–926.
- [60] S. Wang, P. Huang, L. Nie, R. Xing, D. Liu, Z. Wang, J. Lin, S. Chen, G. Niu, G. Lu, X. Chen, *Adv. Mater.* **2013**, *25*, 3055–3061.
- [61] G. V. Hartland, *Chem. Rev.* **2011**, *111*, 3858–3887.
- [62] P. R. West, S. Ishii, G. V. Naik, N. K. Emani, V. M. Shalaev, A. Boltasseva, *Laser Photonics Rev.* **2010**, *4*, 795–808.

- [63] G. V. Naik, V. M. Shalaev, A. Boltasseva, *Adv. Mater. Deerfield Beach Fla* **2013**, *25*, 3264–3294.
- [64] M. Hu, J. Chen, Z.-Y. Li, L. Au, G. V. Hartland, X. Li, M. Marquez, Y. Xia, *Chem. Soc. Rev.* **2006**, *35*, 1084–1094.
- [65] M. I. Stockman, K. Kneipp, S. I. Bozhevolnyi, S. Saha, A. Dutta, J. Ndukaife, N. Kinsey, H. Reddy, U. Guler, V. M. Shalaev, A. Boltasseva, B. Gholipour, H. N. S. Krishnamoorthy, K. F. MacDonald, C. Soci, N. I. Zheludev, V. Savinov, R. Singh, P. G. s, C. Lienau, M. Vadai, M. L. Solomon, D. R. Barton, M. Lawrence, J. A. Dionne, S. V. Boriskina, R. Esteban, J. Aizpurua, X. Zhang, S. Yang, D. Wang, W. Wang, T. W. Odom, N. Accanto, P. M. de Roque, I. M. Hancu, L. Piatkowski, N. F. van Hulst, M. F. Kling, *J. Opt.* **2018**, *20*, 043001.
- [66] M. Rycenga, C. M. Cobley, J. Zeng, W. Li, C. H. Moran, Q. Zhang, D. Qin, Y. Xia, *Chem. Rev.* **2011**, *111*, 3669–3712.
- [67] F. Wang, Y. R. Shen, *Phys. Rev. Lett.* **2006**, *97*, 206806.
- [68] M. Kumar, N. Umezawa, S. Ishii, T. Nagao, *ACS Photonics* **2016**, *3*, 43–50.
- [69] A. Lalisse, G. Tessier, J. Plain, G. Baffou, *Sci. Rep.* **2016**, *6*, 38647.
- [70] M. B. Cortie, A. M. McDonagh, *Chem. Rev.* **2011**, *111*, 3713–3735.
- [71] R. Ferrando, J. Jellinek, R. L. Johnston, *Chem. Rev.* **2008**, *108*, 845–910.
- [72] K. M. Mayer, J. H. Hafner, *Chem. Rev.* **2011**, *111*, 3828–3857.
- [73] P. K. Jain, K. S. Lee, I. H. El-Sayed, M. A. El-Sayed, *J. Phys. Chem. B* **2006**, *110*, 7238–7248.
- [74] M. A. Garcia, *J. Phys. Appl. Phys.* **2011**, *44*, 283001.
- [75] H. B. Jeon, P. V. Tsalu, J. W. Ha, *Sci. Rep.* **2019**, *9*, 13635.

- [76] J. Cao, T. Sun, K. T. V. Grattan, *Sens. Actuators B Chem.* **2014**, *195*, 332–351.
- [77] X. Huang, P. K. Jain, I. H. El-Sayed, M. A. El-Sayed, *Lasers Med. Sci.* **2008**, *23*, 217–228.
- [78] D. T. Hue, T. T. Thu Huong, P. T. Thu Ha, T. T. Trang, N. T. Ha Lien, V. Xuan Hoa, *AIP Adv.* **2021**, *11*, 055319.
- [79] N. Jiang, X. Zhuo, J. Wang, *Chem. Rev.* **2018**, *118*, 3054–3099.
- [80] G. V. Naik, J. Kim, A. Boltasseva, *Opt. Mater. Express* **2011**, *1*, 1090–1099.
- [81] P. Wulandari, T. Nagahiro, N. Fukada, Y. Kimura, M. Niwano, K. Tamada, *J. Colloid Interface Sci.* **2015**, *438*, 244–248.
- [82] P. K. Jain, X. Huang, I. H. El-Sayed, M. A. El-Sayed, *Acc. Chem. Res.* **2008**, *41*, 1578–1586.
- [83] K. Alaqad, T. A. Saleh, *J. Environ. Anal. Toxicol.* **2016**, *6*, DOI 10.4172/2161-0525.1000384.
- [84] H. Kang, J. T. Buchman, R. S. Rodriguez, H. L. Ring, J. He, K. C. Bantz, C. L. Haynes, *Chem. Rev.* **2019**, *119*, 664–699.
- [85] “Refractive Index Sensitivity Analysis of Ag, Au, and Cu Nanoparticles | SpringerLink,” can be found under <https://link.springer.com/article/10.1007/s11468-011-9206-7>, **n.d.**
- [86] H. Wang, F. Tam, N. K. Grady, N. J. Halas, *J. Phys. Chem. B* **2005**, *109*, 18218–18222.
- [87] J. B. Vines, J.-H. Yoon, N.-E. Ryu, D.-J. Lim, H. Park, *Front. Chem.* **2019**, *7*.



- [88] A. B. Bucharskaya, G. N. Maslyakova, M. L. Chekhonatskaya, G. S. Terentyuk, N. A. Navolokin, B. N. Khlebtsov, N. G. Khlebtsov, A. N. Bashkatov, E. A. Genina, V. V. Tuchin, *Lasers Surg. Med.* **2018**, *50*, 1025–1033.
- [89] A. Pramanik, Y. Gao, S. Patibandla, D. Mitra, M. G. McCandless, L. A. Fassero, K. Gates, R. Tandon, P. C. Ray, *Nanoscale Adv.* **2021**, *3*, 1588–1596.
- [90] T. T. S. Lew, K. M. M. Aung, S. Y. Ow, S. N. Amrun, L. Sutarlie, L. F. P. Ng, X. Su, *ACS Nano* **2021**, *15*, 12286–12297.
- [91] K. S. Siddiqi, A. Husen, R. A. K. Rao, *J. Nanobiotechnology* **2018**, *16*, 1–28.
- [92] A. Comin, L. Manna, *Chem. Soc. Rev.* **2014**, *43*, 3957–3975.
- [93] G. V. Naik, B. Saha, J. Liu, S. M. Saber, E. A. Stach, J. M. K. Irudayaraj, T. D. Sands, V. M. Shalaev, A. Boltasseva, *Proc. Natl. Acad. Sci.* **2014**, *111*, 7546–7551.
- [94] Y. V. Stebunov, D. I. Yakubovsky, D. Yu. Fedyanin, A. V. Arsenin, V. S. Volkov, *Langmuir* **2018**, *34*, 4681–4687.
- [95] G. H. Chan, J. Zhao, E. M. Hicks, G. C. Schatz, R. P. Van Duyne, *Nano Lett.* **2007**, *7*, 1947–1952.
- [96] W.-J. Chen, Y.-C. Lin, G. Kumar, S.-Y. Xie, F.-C. Chen, *Synth. Met.* **2021**, *273*, 116675.
- [97] C.-L. Huang, G. Kumar, G. D. Sharma, F.-C. Chen, *Appl. Phys. Lett.* **2020**, *116*, 253302.
- [98] D. Gérard, S. K. Gray, *J. Phys. Appl. Phys.* **2014**, *48*, 184001.
- [99] M.-N. Su, P. D. Dongare, D. Chakraborty, Y. Zhang, C. Yi, F. Wen, W.-S. Chang, P. Nordlander, J. E. Sader, N. J. Halas, S. Link, *Nano Lett.* **2017**, *17*, 2575–2583.

- [100] B. Ostovar, M.-N. Su, D. Renard, B. D. Clark, P. D. Dongare, C. Dutta, N. Gross, J. E. Sader, C. F. Landes, W.-S. Chang, N. J. Halas, S. Link, *J. Phys. Chem. A* **2020**, *124*, 3924–3934.
- [101] M. W. Knight, L. Liu, Y. Wang, L. Brown, S. Mukherjee, N. S. King, H. O. Everitt, P. Nordlander, N. J. Halas, *Nano Lett.* **2012**, *12*, 6000–6004.
- [102] M. W. Knight, N. S. King, L. Liu, H. O. Everitt, P. Nordlander, N. J. Halas, *ACS Nano* **2014**, *8*, 834–840.
- [103] G. Maidecchi, G. Gonella, R. Proietti Zaccaria, R. Moroni, L. Anghinolfi, A. Giglia, S. Nannarone, L. Mattera, H.-L. Dai, M. Canepa, F. Bisio, *ACS Nano* **2013**, *7*, 5834–5841.
- [104] M. J. Meziani, C. E. Bunker, F. Lu, H. Li, W. Wang, E. A. Guliants, R. A. Quinn, Y.-P. Sun, *ACS Appl. Mater. Interfaces* **2009**, *1*, 703–709.
- [105] Yang Shuang, Lu Shaoyong, Li Yang, Yu Hua, He Linxia, Sun Tianmeng, Yang Bai, Liu Kun, *CCS Chem.* **n.d.**, *0*.
- [106] A. Pujari, T. Thomas, *Mater. Chem. Phys.* **2020**, 123419.
- [107] J. S. Biggins, S. Yazdi, E. Ringe, *Nano Lett.* **2018**, *18*, 3752–3758.
- [108] H.-H. Jeong, A. G. Mark, P. Fischer, *Chem. Commun.* **2016**, *52*, 12179–12182.
- [109] L. Zhang, J. Xing, X. Wen, J. Chai, S. Wang, Q. Xiong, *Nanoscale* **2017**, *9*, 12843–12849.
- [110] J. M. Sanz, D. Ortiz, R. Alcaraz de la Osa, J. M. Saiz, F. González, A. S. Brown, M. Losurdo, H. O. Everitt, F. Moreno, *J. Phys. Chem. C* **2013**, *117*, 19606–19615.
- [111] A. García Marín, T. García-Mendiola, C. Navio Bernabeu, M. Jesús Hernández, J. Piqueras, J. Luis Pau, F. Pariente, E. Lorenzo, *Nanoscale* **2016**, *8*, 9842–9851.

- [112] S. Catalán-Gómez, C. Bran, M. Vázquez, L. Vázquez, J. L. Pau, A. Redondo-Cubero, *Sci. Rep.* **2020**, *10*, 4187.
- [113] A. Samadi, H. Klingberg, L. Jauffred, A. Kjær, P. Martin Bendix, L. B. Oddershede, *Nanoscale* **2018**, *10*, 9097–9107.
- [114] L. Qin, G. Wang, Y. Tan, *Sci. Rep.* **2018**, *8*, 16198.
- [115] I. Sarhid, I. Abdellah, C. Martini, V. Huc, D. Dragoe, P. Beaunier, I. Lampre, H. Remita, *New J. Chem.* **2019**, *43*, 4349–4355.
- [116] A. Pathak, B. D. Gupta, *Sens. Actuators B Chem.* **2021**, *326*, 128717.
- [117] J. M. McMahon, G. C. Schatz, S. K. Gray, *Phys. Chem. Chem. Phys.* **2013**, *15*, 5415–5423.
- [118] A. G. Bezerra, T. N. Machado, T. D. Woiski, D. A. Turchetti, J. A. Lenz, L. Akcelrud, W. H. Schreiner, *J. Nanoparticle Res.* **2018**, *20*, 142.
- [119] J. Toudert, R. Serna, *Opt. Mater. Express* **2016**, *6*, 2434–2447.
- [120] A. Cuadrado, J. Toudert, R. Serna, *IEEE Photonics J.* **2016**, *8*, 1–11.
- [121] X. Zhang, P. Li, Á. Barreda, Y. Gutiérrez, F. González, F. Moreno, H. O. Everitt, J. Liu, *Nanoscale Horiz.* **2016**, *1*, 75–80.
- [122] Y. Gutiérrez, R. Alcaraz de la Osa, D. Ortiz, J. M. Saiz, F. González, F. Moreno, *Appl. Sci.* **2018**, *8*, 64.
- [123] M. G. Blaber, M. D. Arnold, M. J. Ford, *J. Phys. Condens. Matter* **2010**, *22*, 143201.
- [124] S. Kim, J.-M. Kim, J.-E. Park, J.-M. Nam, *Adv. Mater. Deerfield Beach Fla* **2018**, *30*, e1704528.

- [125] W. T. Hsieh, P. C. Wu, J. B. Khurgin, D. P. Tsai, N. Liu, G. Sun, *ACS Photonics* **2018**, *5*, 2541–2548.
- [126] Y. Wang, B. Liu, Y. Wang, H. Yuan, X. Wang, X. Peng, *Int. J. Hydrog. Energy* **2021**, *46*, 29858–29888.
- [127] J. Li, Z. Lou, B. Li, *J. Mater. Chem. A* **2021**, *9*, 18818–18835.
- [128] W. Xu, H. Liu, D. Zhou, X. Chen, N. Ding, H. Song, H. Ågren, *Nano Today* **2020**, *33*, 100892.
- [129] J. Sheng, L. Zhang, L. Deng, Y. Han, L. Wang, H. He, Y.-N. Liu, *Chem. Eng. J.* **2020**, *383*, 123071.
- [130] B. Doiron, M. Mota, M. P. Wells, R. Bower, A. Mihai, Y. Li, L. F. Cohen, N. McN. Alford, P. K. Petrov, R. F. Oulton, S. A. Maier, *ACS Photonics* **2019**, *6*, 240–259.
- [131] S. Ishii, S. L. Shinde, T. Nagao, *Adv. Opt. Mater.* **2019**, *7*, 1800603.
- [132] G. V. Naik, J. L. Schroeder, X. Ni, A. V. Kildishev, T. D. Sands, A. Boltasseva, *Opt. Mater. Express* **2012**, *2*, 478–489.
- [133] J. Pflüger, J. Fink, W. Weber, K. P. Bohnen, G. Crecelius, *Phys. Rev. B* **1984**, *30*, 1155–1163.
- [134] U. Guler, V. M. Shalaev, A. Boltasseva, *Mater. Today* **2015**, *18*, 227–237.
- [135] M. Kumar, S. Ishii, N. Umezawa, T. Nagao, *Opt. Mater. Express* **2016**, *6*, 29.
- [136] P. Patsalas, N. Kalfagiannis, S. Kassavetis, *Materials* **2015**, *8*, 3128–3154.
- [137] A. P. Hibbins, J. R. Sambles, C. R. Lawrence, *J. Mod. Opt.* **1998**, *45*, 2051–2062.
- [138] M. B. Cortie, J. Giddings, A. Dowd, *Nanotechnology* **2010**, *21*, 115201.
- [139] N. C. Chen, W. C. Lien, C. R. Liu, Y. L. Huang, Y. R. Lin, C. Chou, S. Y. Chang, C. W. Ho, *J. Appl. Phys.* **2011**, *109*, 043104-043104–7.

- [140] U. Guler, G. V. Naik, A. Boltasseva, V. M. Shalaev, A. V. Kildishev, *Appl. Phys. B* **2012**, *107*, 285–291.
- [141] U. Guler, J. C. Ndukaife, G. V. Naik, A. G. A. Nnanna, A. V. Kildishev, V. M. Shalaev, A. Boltasseva, *Nano Lett.* **2013**, *13*, 6078–6083.
- [142] J. Meng, Z. Fu, M. Du, X. Liu, L. Hao, *Mater. Lett.* **2016**, *164*, 291–293.
- [143] P. Patsalas, N. Kalfagiannis, S. Kassavetis, G. Abadias, D. V. Bellas, C. Lekka, E. Lidorikis, *Mater. Sci. Eng. R Rep.* **2018**, *123*, 1–55.
- [144] L. Yuan, G. Fang, C. Li, M. Wang, N. Liu, L. Ai, Y. Cheng, H. Gao, X. Zhao, *Appl. Surf. Sci.* **2007**, *253*, 8538–8542.
- [145] R. Nowak, S. Maruno, *Mater. Sci. Eng. A* **1995**, *202*, 226–237.
- [146] M. Quinten, *Appl. Phys. B* **2001**, *73*, 317–326.
- [147] A. Reinholdt, R. Pecenka, A. Pinchuk, S. Runte, A. L. Stepanov, Th. E. Weirich, U. Kreibig, *Eur. Phys. J. - At. Mol. Opt. Plasma Phys.* **2004**, *31*, 69–76.
- [148] A. Reinholdt, R. Detemple, A. L. Stepanov, T. E. Weirich, U. Kreibig, *Appl. Phys. B* **2003**, *77*, 681–686.
- [149] A. A. Popov, G. Tselikov, N. Dumas, C. Berard, K. Metwally, N. Jones, A. Al-Kattan, B. Larrat, D. Braguer, S. Mensah, A. Da Silva, M. A. Estève, A. V. Kabashin, *Sci. Rep.* **2019**, *9*, 1194.
- [150] P. R. Taylor, S. A. Pirzada, *Adv. Perform. Mater.* **1994**, *1*, 35–50.
- [151] V. N. Chuvil'deev, Yu. V. Blagoveshchenskiy, A. V. Nokhrin, M. S. Boldin, N. V. Sakharov, N. V. Isaeva, S. V. Shotin, O. A. Belkin, A. A. Popov, E. S. Smirnova, E. A. Lantsev, *J. Alloys Compd.* **2017**, *708*, 547–561.

- [152] S. Yick, A. T. Murdock, P. J. Martin, D. F. Kennedy, T. Maschmeyer, A. Bendavid, *Nanoscale* **2018**, *10*, 7566–7574.
- [153] U. R. Kortshagen, R. M. Sankaran, R. N. Pereira, S. L. Girshick, J. J. Wu, E. S. Aydil, *Chem. Rev.* **2016**, *116*, 11061–11127.
- [154] A. Alvarez Barragan, N. V. Ilawe, L. Zhong, B. M. Wong, L. Mangolini, *J. Phys. Chem. C* **2017**, *121*, 2316–2322.
- [155] K. S. Schramke, Y. Qin, J. T. Held, K. A. Mkhoyan, U. R. Kortshagen, *ACS Appl. Nano Mater.* **2018**, *1*, 2869–2876.
- [156] S. Exarhos, A. Alvarez-Barragan, E. Aytan, A. A. Balandin, L. Mangolini, *ACS Energy Lett.* **2018**, *3*, 2349–2356.
- [157] R. Xu, W. Pang, Q. Huo, Eds. , *Modern Inorganic Synthetic Chemistry*, Elsevier, Amsterdam, **2011**.
- [158] A. W. Weimer, *Carbide, Nitride and Boride Materials Synthesis and Processing*, Springer Science & Business Media, **2012**.
- [159] S. Kaskel, K. Schlichte, G. Chaplais, M. Khanna, *J. Mater. Chem.* **2003**, *13*, 1496–1499.
- [160] E. G. Gillan, R. B. Kaner, *Inorg. Chem.* **1994**, *33*, 5693–5700.
- [161] R. A. Janes, M. Aldissi, R. B. Kaner, *Chem. Mater.* **2003**, *15*, 4431–4435.
- [162] C. Giordano, M. Antonietti, *Nano Today* **2011**, *6*, 366–380.
- [163] X. Z. Chen, J. L. Dye, H. A. Eick, S. H. Elder, K.-L. Tsai, *Chem. Mater.* **1997**, *9*, 1172–1176.
- [164] L. Yu, S. Song, B. McElhenny, F. Ding, D. Luo, Y. Yu, S. Chen, Z. Ren, *J. Mater. Chem. A* **2019**, *7*, 19728–19732.

- [165] R. A. Janes, M. A. Low, R. B. Kaner, *Inorg. Chem.* **2003**, *42*, 2714–2719.
- [166] P. M. Gschwend, S. Conti, A. Kaech, C. Maake, S. E. Pratsinis, *ACS Appl. Mater. Interfaces* **2019**, *11*, 22550–22560.
- [167] P. M. Gschwend, F. Krumeich, S. E. Pratsinis, *Ind. Eng. Chem. Res.* **2019**, *58*, 16610–16619.
- [168] H.-J. Meyer, *Dalton Trans.* **2010**, *39*, 5973–5982.
- [169] D. B. Williams, C. B. Carter, *Transmission Electron Microscopy: A Textbook for Materials Science*, Springer US, **2009**.
- [170] F. Krumeich. Properties of Electrons, their Interactions with Matter and Applications in Electron Microscopy. **2015**.
- [171] P. Buseck, J. Cowley, L. Eyring, *High-Resolution Transmission Electron Microscopy: And Associated Techniques*, Oxford University Press, **1989**.
- [172] L. Reimer, H. Kohl, *Transmission Electron Microscopy: Physics of Image Formation*, Springer-Verlag, New York, **2008**.
- [173] R. F. Egerton, *Physical Principles of Electron Microscopy: An Introduction to TEM, SEM, and AEM*, Springer US, **2005**.
- [174] J. M. Zuo, J. C. H. Spence, in *Adv. Transm. Electron Microsc. Imaging Diffraction Nanosci.* (Eds.: J.M. Zuo, J.C.H. Spence), Springer, New York, NY, **2017**, pp. 1–18.
- [175] Q. D. Truong, M. K. Devaraju, T. Tomai, I. Honma, *ACS Appl. Mater. Interfaces* **2013**, *5*, 9926–9932.
- [176] L. A. Bendersky, F. W. Gayle, *J. Res. Natl. Inst. Stand. Technol.* **2001**, *106*, 997–1012.

- [177] B. Fultz, J. M. Howe, Eds. , in *Transm. Electron Microsc. Diffractometry Mater.*, Springer, Berlin, Heidelberg, **2008**, pp. 517–582.
- [178] J. Liu, in *Handb. Microsc. Nanotechnol.* (Eds.: N. Yao, Z.L. Wang), Springer US, Boston, MA, **2005**, pp. 325–359.
- [179] H. Hirai, in *Carbon Alloys*, Elsevier Science, Oxford, **2003**, pp. 239–256.
- [180] D. J. Smith, in *Handb. Microsc. Nanotechnol.*, Springer US, Boston, MA, **2005**, pp. 427–453.
- [181] F. J. García de Abajo, *Rev. Mod. Phys.* **2010**, 82, 209–275.
- [182] J. Goldstein, D. E. Newbury, P. Echlin, D. C. Joy, A. D. R. Jr, C. E. Lyman, C. Fiori, E. Lifshin, *Scanning Electron Microscopy and X-Ray Microanalysis: A Text for Biologists, Materials Scientists, and Geologists*, Springer US, **1992**.
- [183] J. Goldstein, D. E. Newbury, D. C. Joy, C. E. Lyman, P. Echlin, E. Lifshin, L. Sawyer, J. R. Michael, *Scanning Electron Microscopy and X-Ray Microanalysis: Third Edition*, Springer US, **2003**.
- [184] L. Reimer, *Scanning Electron Microscopy: Physics of Image Formation and Microanalysis*, Springer, **2013**.
- [185] C. Suryanarayana, M. G. Norton, *X-Ray Diffraction: A Practical Approach*, Springer Science & Business Media, **1998**.
- [186] B. D. Cullity, *Elements of X-Ray Diffraction*, Instituto Cubano Del Libro, **1971**.
- [187] A. Monshi, M. R. Foroughi, M. R. Monshi, *World J. Nano Sci. Eng.* **2012**, 2, 154–160.



- [188] C. R. Brundle, C. A. Evans, S. Wilson, *Encyclopedia of Materials Characterization: Surfaces, Interfaces, Thin Films*, Gulf Professional Publishing, **1992**.
- [189] F. A. Stevie, C. L. Donley, *J. Vac. Sci. Technol. A* **2020**, *38*, 063204.
- [190] P. van der Heide, *X-Ray Photoelectron Spectroscopy: An Introduction to Principles and Practices*, John Wiley & Sons, **2011**.
- [191] G. Greczynski, L. Hultman, *Prog. Mater. Sci.* **2020**, *107*, 100591.
- [192] W. H. Doh, V. Papaefthimiou, S. Zafeiratos, in *Surf. Sci. Tools Nanomater. Charact.* (Ed.: C.S.S.R. Kumar), Springer, Berlin, Heidelberg, **2015**, pp. 317–366.
- [193] I. S. Tilinin, A. Jablonski, W. S. M. Werner, *Prog. Surf. Sci.* **1996**, *52*, 193–335.
- [194] D. A. Skoog, F. J. Holler, S. R. Crouch, *Principles of Instrumental Analysis*, Nelson Education, **2017**.
- [195] L. D. S. Yadav, in *Org. Spectrosc.*, Springer Netherlands, Dordrecht, **2005**, pp. 7–51.
- [196] R. Xu, *Particuology* **2008**, *6*, 112–115.
- [197] J. D. Clogston, A. K. Patri, in *Charact. Nanoparticles Intend. Drug Deliv.* (Ed.: S.E. McNeil), Humana Press, Totowa, NJ, **2011**, pp. 63–70.
- [198] B. J. Berne, R. Pecora, *Dynamic Light Scattering: With Applications to Chemistry, Biology, and Physics*, Courier Corporation, **2000**.
- [199] Y. Hu, R. Wang, S. Wang, L. Ding, J. Li, Y. Luo, X. Wang, M. Shen, X. Shi, *Sci. Rep.* **2016**, *6*, 28325.
- [200] Y. H. Teow, A. W. Mohammad, *Desalination* **2019**, *451*, 2–17.

- [201] L. Zhu, L. Sun, H. Zhang, D. Yu, H. Aslan, J. Zhao, Z. Li, M. Yu, F. Besenbacher, Y. Sun, *Nano Energy* **2019**, *57*, 842–850.
- [202] L. Zhou, Y. Tan, J. Wang, W. Xu, Y. Yuan, W. Cai, S. Zhu, J. Zhu, *Nat. Photonics* **2016**, *10*, 393–398.
- [203] S. Yu, Y. Zhang, H. Duan, Y. Liu, X. Quan, P. Tao, W. Shang, J. Wu, C. Song, T. Deng, *Sci. Rep.* **2015**, *5*, 13600.
- [204] Y. Zeng, K. Wang, J. Yao, H. Wang, *Chem. Eng. Sci.* **2014**, *116*, 704–709.
- [205] P. Zhang, Q. Liao, H. Yao, Y. Huang, H. Cheng, L. Qu, *Energy Storage Mater.* **2019**, *18*, 429–446.
- [206] P. Manivasagan, N. Quang Bui, S. Bharathiraja, M. Santha Moorthy, Y.-O. Oh, K. Song, H. Seo, M. Yoon, J. Oh, *Sci. Rep.* **2017**, *7*, 43593.
- [207] S. Lee, R. G. Thomas, M. J. Moon, H. J. Park, I.-K. Park, B.-I. Lee, Y. Y. Jeong, *Sci. Rep.* **2017**, *7*, 2108.
- [208] D. K. Roper, W. Ahn, M. Hoepfner, *J. Phys. Chem. C* **2007**, *111*, 3636–3641.
- [209] J. R. Cole, N. A. Mirin, G. P. Goodrich, N. J. Halas, *J. Phys. Chem. C* **2009**, *113*, 12090–12094.
- [210] J. R. DeVore, *JOSA* **1951**, *41*, 416–419.
- [211] D. L. Wood, K. Nassau, *Appl. Opt.* **1982**, *21*, 2978–2981.
- [212] D. L. Wood, K. Nassau, T. Y. Kometani, D. L. Nash, *Appl. Opt.* **1990**, *29*, 604–607.
- [213] S. M. Aouadi, D. M. Mihut, M. L. Kuruppu, S. R. Kirkpatrick, S. L. Rohde, *J. Vac. Sci. Technol. A* **2001**, *19*, 2800–2804.
- [214] A. Boltasseva, H. A. Atwater, *Science* **2011**, *331*, 290–291.

- [215] Y. Wang, A. Capretti, L. D. Negro, *Opt. Mater. Express* **2015**, *5*, 2415–2430.
- [216] I. P. Parkin, A. M. Nartowski, *Polyhedron* **1998**, *17*, 2617–2622.
- [217] M. D. Aguas, A. M. Nartowski, I. P. Parkin, M. MacKenzie, A. J. Craven, *J. Mater. Chem.* **1998**, *8*, 1875–1880.
- [218] G. Gubert, R. C. Oliveira, D. S. Costa, G. K. Metzger, I. Mazzaro, G. Kellermann, E. Ribeiro, J. Varalda, D. H. Mosca, *J. Appl. Phys.* **2019**, *125*, 024301.
- [219] D. Ö. Thorsteinsson, J. T. Gudmundsson, *AIP Adv.* **2018**, *8*, 035124.
- [220] Z. T. Y. Liu, B. P. Burton, S. V. Khare, D. Gall, *J. Phys. Condens. Matter* **2016**, *29*, 035401.
- [221] L. Zeng, Z. Lu, M. Li, J. Yang, W. Song, D. Zeng, C. Xie, *Appl. Catal. B Environ.* **2016**, *183*, 308–316.
- [222] H. Jiang, R. I. Gomez-Abal, P. Rinke, M. Scheffler, *Phys. Rev. B* **2010**, *81*, 085119.
- [223] P. Yang, D. Chao, C. Zhu, X. Xia, Y. Zhang, X. Wang, P. Sun, B. K. Tay, Z. X. Shen, W. J. Mai, H. J. Fan, *Adv. Sci.* **2016**, *3*, 1500299.
- [224] Q. Zhou, J. Zhai, *AIP Adv.* **2013**, *3*, 032102.
- [225] F. Piallat, V. Beugin, R. Gassilloud, L. Dussault, B. Pelissier, C. Leroux, P. Caubet, C. Vallée, *Appl. Surf. Sci.* **2014**, *303*, 388–392.
- [226] U. Guler, S. Suslov, A. V. Kildishev, A. Boltasseva, V. M. Shalaev, *Nanophotonics* **2015**, *4*, 269–276.
- [227] J. Li, L. Gao, J. Sun, Q. Zhang, J. Guo, D. Yan, *J. Am. Ceram. Soc.* **2001**, *84*, 3045–3047.
- [228] D. Harris, *Quantitative Chemical Analysis*, **2007**.
- [229] J. J. Mock, D. R. Smith, S. Schultz, *Nano Lett.* **2003**, *3*, 485–491.

- [230] C. Novo, A. M. Funston, I. Pastoriza-Santos, L. M. Liz-Marzán, P. Mulvaney, *J. Phys. Chem. C* **2008**, *112*, 3–7.
- [231] K. L. Kelly, E. Coronado, L. L. Zhao, G. C. Schatz, *J. Phys. Chem. B* **2003**, *107*, 668–677.
- [232] Y. E. Monfared, M. Dasog, *Can. J. Chem.* **2021**, *99* (7), 576-584.
- [233] J. Olson, S. Dominguez-Medina, A. Hoggard, L.-Y. Wang, W.-S. Chang, S. Link, *Chem. Soc. Rev.* **2015**, *44*, 40–57.
- [234] P. Schlexer, A. B. Andersen, B. Sebok, I. Chorkendorff, J. Schiøtz, T. W. Hansen, *Part. Part. Syst. Charact.* **2019**, *36*, 1800480.
- [235] O. Z. Sharaf, N. Rizk, C. J. Munro, C. P. Joshi, W. Waheed, E. Abu-Nada, A. Alazzam, M. N. Martin, *Energy Convers. Manag.* **2021**, *244*, 114463.
- [236] W. Liu, R. An, C. Wang, Z. Zheng, Y. Tian, R. Xu, Z. Wang, *Micromachines* **2018**, *9*, 346.
- [237] S. K. Volkman, S. Yin, T. Bakhishev, K. Puntambekar, V. Subramanian, M. F. Toney, *Chem. Mater.* **2011**, *23*, 4634–4640.
- [238] M. J. Coutts, M. B. Cortie, M. J. Ford, A. M. McDonagh, *J. Phys. Chem. C* **2009**, *113*, 1325–1328.
- [239] K. Setoura, S. Ito, *AIP Adv.* **2021**, *11*, 115027.
- [240] T. Krekeler, S. S. Rout, G. V. Krishnamurthy, M. Störmer, M. Arya, A. Ganguly, D. S. Sutherland, S. I. Bozhevolnyi, M. Ritter, K. Pedersen, A. Y. Petrov, M. Eich, M. Chirumamilla, *Adv. Opt. Mater.* **2021**, *9*, 2100323.
- [241] L. Zhu, M. Gao, C. K. N. Peh, G. W. Ho, *Nano Energy* **2019**, *57*, 507–518.
- [242] J. A. Webb, R. Bardhan, *Nanoscale* **2014**, *6*, 2502–2530.

- [243] M. Kim, J. Lee, J. Nam, *Adv. Sci.* **2019**, *6*, 1900471.
- [244] X. Huang, M. A. El-Sayed, *Alex. J. Med.* **2011**, *47*, 1–9.
- [245] J. R. Adleman, D. A. Boyd, D. G. Goodwin, D. Psaltis, *Nano Lett.* **2009**, *9*, 4417–4423.
- [246] Q. Yang, Q. Xu, S. H. Yu, H. L. Jiang, *Angew. Chem. - Int. Ed.* **2016**, *55*, 3685–3689.
- [247] F. Wang, Y. Huang, Z. Chai, M. Zeng, Q. Li, Y. Wang, D. Xu, *Chem. Sci.* **2016**, *7*, 6887–6893.
- [248] R. Long, Y. Li, L. Song, Y. Xiong, *Small* **2015**, *11*, 3873–3889.
- [249] Z. Wang, T. Horseman, A. P. Straub, N. Y. Yip, D. Li, M. Elimelech, S. Lin, *Sci. Adv.* **2019**, *5*, eaax0763.
- [250] A. M. Smith, M. C. Mancini, S. Nie, *Nat. Nanotechnol.* **2009**, *4*, 710–711.
- [251] M. F. Tsai, S. H. G. Chang, F. Y. Cheng, V. Shanmugam, Y. S. Cheng, C. H. Su, C. S. Yeh, *ACS Nano* **2013**, *7*, 5330–5342.
- [252] Y. Wu, M. R. K. Ali, B. Dong, T. Han, K. Chen, J. Chen, Y. Tang, N. Fang, F. Wang, M. A. El-Sayed, *ACS Nano* **2018**, *12*, 9279–9290.
- [253] S. A. Selim, M. A. El-sayed, *Cancers* **2019**, *11*, 851.
- [254] Y. Wang, L. Wang, M. Yan, A. Cai, S. Dong, J. Hao, *J. Colloid Interface Sci.* **2019**, *536*, 728–736.
- [255] H. J. Moon, M. Ku, H. Lee, N. Yoon, J. Yang, K. W. Bong, *Sci. Rep.* **2018**, *8*, 1–12.
- [256] J. R. Cole, N. A. Mirin, M. W. Knight, G. P. Goodrich, N. J. Halas, *J. Phys. Chem. C* **2009**, *113*, 12090–12094.

- [257] P. Huang, J. Lin, W. Li, P. Rong, Z. Wang, S. Wang, X. Wang, X. Sun, M. Aronova, G. Niu, R. D. Leapman, Z. Nie, X. Chen, *Angew. Chem. - Int. Ed.* **2013**, *52*, 13958–13964.
- [258] C. Bi, J. Chen, Y. Chen, Y. Song, A. Li, S. Li, Z. Mao, C. Gao, D. Wang, H. Möhwald, H. Xia, *Chem. Mater.* **2018**, *30*, 2709–2718.
- [259] Z. Liu, L. Cheng, L. Zhang, Z. Yang, Z. Liu, J. Fang, *Biomaterials* **2014**, *35*, 4099–4107.
- [260] H. Chen, L. Shao, T. Ming, Z. Sun, C. Zhao, B. Yang, J. Wang, *Small* **2010**, *6*, 2272–2280.
- [261] A. Campu, A.-M. Craciun, M. Focsan, S. Astilean, *Nanotechnology* **2019**, *30*, 405701.
- [262] H. Soo Choi, W. Liu, P. Misra, E. Tanaka, J. P. Zimmer, B. Itty Ipe, M. G. Bawendi, J. V. Frangioni, *Nat. Biotechnol.* **2007**, *25*, 1165–1170.
- [263] W. Jiang, B. Y. S. Kim, J. T. Rutka, W. C. W. Chan, *Nat. Nanotechnol.* **2008**, *3*, 145–150.
- [264] C. S. Geetha, A. Sabareeswaran, P. V. Mohanan, *Toxicol. Mech. Methods* **2012**, *22*, 144–150.
- [265] G. Brunello, P. Brun, C. Gardin, L. Ferroni, E. Bressan, R. Meneghello, B. Zavan, S. Sivolella, *PLoS ONE* **2018**, *13*, 1–17.
- [266] W. Jiang, Q. Fu, H. Wei, A. Yao, *J. Mater. Sci.* **2019**, *54*, 5743–5756.
- [267] O. Anjaneyulu, S. Ishii, T. Imai, T. Tanabe, S. Ueda, T. Nagao, H. Abe, *RSC Adv.* **2016**, *6*, 110566–110570.
- [268] W. He, K. Ai, C. Jiang, Y. Li, X. Song, L. Lu, *Biomaterials* **2017**, *132*, 37–47.

- [269] M. Kaur, S. Ishii, S. L. Shinde, T. Nagao, *ACS Sustain. Chem. Eng.* **2017**, *5*, 8523–8528.
- [270] C. Tao, L. An, J. Lin, Q. Tian, S. Yang, *Small Weinh. Bergstr. Ger.* **2019**, e1903473–e1903473.
- [271] W. Zeng, L. Suo, C. Zhang, D. Wu, H. Zhu, *J. Taiwan Inst. Chem. Eng.* **2019**, *95*, 273–280.
- [272] J. Zhu, Y. Wang, D. Huo, Q. Ding, Z. Lu, Y. Hu, *Mater. Sci. Eng. C* **2019**, *105*, 110023.
- [273] D. S. Chauhan, P. Arunkumar, R. Prasad, S. K. Mishra, B. P. K. Reddy, A. De, R. Srivastava, *Mater. Sci. Eng. C* **2018**, *90*, 539–548.
- [274] C. Song, F. Li, X. Guo, W. Chen, C. Dong, J. Zhang, J. Zhang, L. Wang, *J. Mater. Chem. B* **2019**, *7*, 2001–2008.
- [275] Y. Liu, X. Zhang, L. Luo, L. Li, R. Y. Zhu, A. Li, Y. He, W. Cao, K. Niu, H. Liu, J. Yang, D. Gao, *Nanomedicine Nanotechnol. Biol. Med.* **2019**, *18*, 303–314.
- [276] M. R. Younis, C. Wang, R. An, S. Wang, M. A. Younis, Z.-Q. Li, Y. Wang, A. Ihsan, D. Ye, X.-H. Xia, *ACS Nano* **2019**, *13*, 2544–2557.
- [277] J. Hong, C. Park, Y. Kim, *Colloids Surf. Physicochem. Eng. Asp.* **2019**, *574*, 115–121.
- [278] M. R. Younis, R. B. An, Y.-C. Yin, S. Wang, D. Ye, X.-H. Xia, *ACS Appl. Bio Mater.* **2019**, *2*, 3942–3953.
- [279] X. Deng, S. Liang, X. Cai, S. Huang, Z. Cheng, Y. Shi, M. Pang, P. Ma, J. Lin, *Nano Lett.* **2019**, *19*, 6772–6780.

- [280] F. Gao, G. He, H. Yin, J. Chen, Y. Liu, C. Lan, S. Zhang, B. Yang, *Nanoscale* **2019**, *11*, 2374–2384.
- [281] L. Sun, Y. Chen, F. Gong, Q. Dang, G. Xiang, L. Cheng, F. Liao, M. Shao, *J. Mater. Chem. B* **2019**, *7*, 4393–4401.
- [282] H. J. Moon, M. Ku, H. Lee, N. Yoon, J. Yang, K. W. Bong, *Sci. Rep.* **2018**, *8*, 13683.
- [283] V. P. Pattani, J. W. Tunnell, *Lasers Surg. Med.* **2012**, *44*, 675–684.
- [284] K. Ma, Y. Li, Z. Wang, Y. Chen, X. Zhang, C. Chen, H. Yu, J. Huang, Z. Yang, X. Wang, Z. Wang, *ACS Appl. Mater. Interfaces* **2019**, DOI 10.1021/acsami.9b10373.
- [285] J. Zhang, G. Liu, F. He, L. Chen, Y. Huang, *RSC Adv.* **2015**, *5*, 87903–87907.
- [286] D. Zhu, M. Liu, X. Liu, Y. Liu, P. N. Prasad, M. T. Swihart, *J. Mater. Chem. B* **2017**, *5*, 4934–4942.
- [287] Q. Jiang, W. Zeng, C. Zhang, Z. Meng, J. Wu, Q. Zhu, D. Wu, H. Zhu, *Sci. Rep.* **2017**, *7*, 17782.
- [288] Y. Xing, T. Kang, X. Luo, J. Zhu, P. Wu, C. Cai, *J. Mater. Chem. B* **2019**, *7*, 6224–6231.
- [289] C.-L. Chen, L.-R. Kuo, S.-Y. Lee, Y.-K. Hwu, S.-W. Chou, C.-C. Chen, F.-H. Chang, K.-H. Lin, D.-H. Tsai, Y.-Y. Chen, *Biomaterials* **2013**, *34*, 1128–1134.
- [290] C. Wang, C. Dai, Z. Hu, H. Li, L. Yu, H. Lin, J. Bai, Y. Chen, *Nanoscale Horiz.* **2019**, *4*, 415–425.
- [291] R. A. Karaballi, G. Humagain, B. R. A. Fleischman, M. Dasog, *Angew. Chem. - Int. Ed.* **2019**, *58*, 3147–3150.
- [292] J. Shang, X. Gao, *Chem. Soc. Rev.* **2014**, *43*, 7267–7278.



- [293] E. Traver, R. A. Karaballi, Y. E. Monfared, H. Daurie, G. A. Gagnon, M. Dasog, *ACS Appl. Nano Mater.* **2020**, *3*, 2787–2794.
- [294] D. B. O’Neill, S. K. Frehan, K. Zhu, E. Zoethout, G. Mul, E. C. Garnett, A. Huijser, S. H. C. Askes, *Adv. Opt. Mater.* **2021**, *9*, 2100510.
- [295] S. Maity, W. C. Wu, J. B. Tracy, L. I. Clarke, J. R. Bochinski, *Nanoscale* **2017**, *9*, 11605–11618.
- [296] R. Zhao, M. Lv, Y. Li, M. Sun, W. Kong, L. Wang, S. Song, C. Fan, L. Jia, S. Qiu, Y. Sun, H. Song, R. Hao, *ACS Appl. Mater. Interfaces* **2017**, *9*, 15328–15341.
- [297] M. Sivera, L. Kvitek, J. Soukupova, A. Panacek, R. Pucek, R. Vecerova, R. Zboril, *PLOS ONE* **2014**, *9*, e103675.
- [298] P. Tabib Zadeh Adibi, T. Pingel, E. Olsson, H. Grönbeck, C. Langhammer, *ACS Nano* **2016**, *10*, 5063–5069.
- [299] Y. Wang, J. E. Q. Quinsaat, T. Ono, M. Maeki, M. Tokeshi, T. Isono, K. Tajima, T. Satoh, S. Sato, Y. Miura, T. Yamamoto, *Nat. Commun.* **2020**, *11*, 6089.
- [300] X. Zhang, M. R. Servos, J. Liu, *J. Am. Chem. Soc.* **2012**, *134*, 9910–9913.
- [301] L. M. Andrade, E. M. N. Martins, A. F. Versiani, D. S. Reis, F. G. da Fonseca, I. P. de Souza, R. M. Paniago, E. Pereira-Maia, L. O. Ladeira, *Mater. Sci. Eng. C* **2020**, *107*, 110203.
- [302] A. P. Stevenson, D. Blanco Bea, S. Civit, S. Antoranz Contera, A. Iglesias Cerveto, S. Trigueros, *Nanoscale Res. Lett.* **2012**, *7*, 151.
- [303] R. A. Karaballi, Y. Esfahani Monfared, M. Dasog, *Langmuir* **2020**, *36*, 5058–5064.
- [304] P. Korshed, L. Li, D.-T. Ngo, T. Wang, *Nanomaterials* **2018**, *8*, 218.
- [305] B. Molleman, T. Hiemstra, *Langmuir* **2015**, *31*, 13361–13372.

- [306] B. Avasarala, P. Haldar, *Int. J. Hydrog. Energy* **2011**, *36*, 3965–3974.
- [307] B. Avasarala, P. Haldar, *Electrochimica Acta* **2010**, *55*, 9024–9034.
- [308] D. Zhao, Z. Lin, W. Zhu, H. J. Lezec, T. Xu, A. Agrawal, C. Zhang, K. Huang, *Nanophotonics* **2021**, *10*, 2283–2308.
- [309] M. M. Abdullah, F. M. Rajab, S. M. Al-Abbas, *AIP Adv.* **2014**, *4*, 027121.
- [310] W. Ernst, J. Neidhardt, H. Willmann, B. Sartory, P. H. Mayrhofer, C. Mitterer, *Thin Solid Films* **2008**, *517*, 568–574.
- [311] K. Suzuki, T. Kaneko, H. Yoshida, Y. Obi, H. Fujimori, *J. Alloys Compd.* **1998**, *280*, 294–298.
- [312] X. Yang, C. Li, B. Yang, W. Wang, Y. Qian, *Mater. Res. Bull.* **2004**, *39*, 957–962.
- [313] P. Cai, J. Zhu, Z. Yang, Y. Qian, *Mater. Chem. Phys.* **2006**, *95*, 1–4.
- [314] C. Real, M. Roldan, M. D. Alcalá, A. Ortega, **2007**, DOI 10.1111/J.1551-2916.2007.01898.X.
- [315] L. Shen, N. Wang, *J. Nanomater.* **2011**, *2011*, e781935.
- [316] A. Kadari, T. Schemme, D. Kadri, J. Wollschläger, *Results Phys.* **2017**, *7*, 3124–3129.
- [317] D. Gazzoli, M. Occhiuzzi, A. Cimino, G. Minelli, M. Valigi, *Surf. Interface Anal.* **1992**, *18*, 315–322.
- [318] M. Aronniemi, J. Sainio, J. Lahtinen, *Surf. Sci.* **2005**, *578*, 108–123.
- [319] A. Lippitz, Th. Hübert, *Surf. Coat. Technol.* **2005**, *200*, 250–253.
- [320] W. Zhao, F. J. DiSalvo, *Chem. Commun. Camb. Engl.* **2015**, *51*, 4876–4879.
- [321] K. Jagannathan, A. Srinivasan, C. N. R. Rao, *J. Catal.* **1981**, *69*, 418–427.

- [322] P. Patsalas, N. Kalfagiannis, S. Kassavetis, G. Abadias, D. V. Bellas, Ch. Lekka, E. Lidorikis, *Mater. Sci. Eng. R Rep.* **2018**, *123*, 1–55.
- [323] G. Gubert, R. C. Oliveira, D. S. Costa, G. K. Metzger, I. Mazzaro, G. Kellermann, E. Ribeiro, J. Varalda, D. H. Mosca, *J. Appl. Phys.* **2019**, *125*, 024301.
- [324] Y. Wu, G. Li, J. P. Camden, *Chem. Rev.* **2018**, *118*, 2994–3031.
- [325] P. A. Crozier, *Ultramicroscopy* **2017**, *180*, 104–114.
- [326] Z.-Y. Wu, Z. Chen, L. Wang, L. Fang, T. Zhou, T. Mei, C. Zhang, Q. Li, *J. Ceram. Soc. Jpn.* **2021**, *129*, 200–203.
- [327] R. Verrelli, M. E. Arroyo-de-Dompablo, D. Tchitcheкова, A. P. Black, C. Frontera, A. Fuertes, M. R. Palacin, *Phys. Chem. Chem. Phys.* **2017**, *19*, 26435–26441.
- [328] F. Zong, C. Meng, Z. Guo, F. Ji, H. Xiao, X. Zhang, J. Ma, H. Ma, *J. Alloys Compd.* **2010**, *508*, 172–176.
- [329] S. Cui, S. Liao, Y. Zhang, Y. Xu, Y. Miao, M. Lu, Y. Fan, W. Guo, *J. Mater. Sci.* **1999**, *34*, 5601–5604.
- [330] S. H. C. Askes, N. J. Schilder, E. Zoethout, A. Polman, E. C. Garnett, *Nanoscale* **2019**, *11*, 20252–20260.
- [331] M. Kaur, S. Ishii, S. L. Shinde, T. Nagao, *Adv. Sustain. Syst.* **2019**, *3*, 1800112.
- [332] S. Juneja, M. S. Shishodia, *Opt. Commun.* **2019**, *433*, 89–96.
- [333] L. Lan, H. Yao, G. Li, X. Fan, M. Li, T. Qiu, *Nano Res.* **2022**, *15*, 3794–3803.

## Appendix

### Copyright permission for Figure 1.

CCC RightsLink

Carbon Nanomaterials for the Treatment of Heavy Metal-Contaminated Water and Environmental Remediation

Author: Nasser Babji et al.  
Publication: Nanoscale Research Letters  
Publisher: Springer Nature  
Date: Nov 11, 2019  
Copyright © 2019, The Author(s)

**SPRINGER NATURE**

**Creative Commons**  
This is an open access article distributed under the terms of the Creative Commons CC BY license, which permits unrestricted use, distribution, and reproduction in any medium, provided the original work is properly cited.  
You are not required to obtain permission to reuse this article.  
To request permission for a type of use not listed, please contact Springer Nature.

© 2022 Copyright - All Rights Reserved | Copyright Clearance Center, Inc. | Privacy statement | Terms and Conditions  
Comments? We would like to hear from you. E-mail us at [customerservice@copyright.com](mailto:customerservice@copyright.com)

### Copyright permission for Figure 4.

CCC RightsLink

Calculated Absorption and Scattering Properties of Gold Nanoparticles of Different Size, Shape, and Composition: Applications in Biological Imaging and Biomedicine

Author: Prashant K. Jain, Somying Suk Lee, In-Ho El-Sayed, et al.  
Publication: The Journal of Physical Chemistry B  
Publisher: American Chemical Society  
Date: April 1, 2006  
Copyright © 2006, American Chemical Society

**ACS Publications**

**PERMISSION/LICENSE IS GRANTED FOR YOUR ORDER AT NO CHARGE**  
This type of permission/license, instead of the standard Terms and Conditions, is sent to you because no fee is being charged for your order. Please note the following:  
- Permission is granted for your request in both print and electronic formats, and translations.  
- If figures and/or tables were requested, they may be adapted or used in part.  
- Please print this page for your records and send a copy of it to your publisher/graduate school.  
- Appropriate credit for the requested material should be given as follows: "Reprinted (adapted) with permission from (COMPLETE REFERENCE CITATION). Copyright (YEAR) American Chemical Society." Insert appropriate information in place of the capitalized words.  
- One-time permission is granted only for the use specified in your RightsLink request. No additional uses are granted (such as derivative works or other editions). For any uses, please submit a new request.  
- If credit is given to another source for the material you requested from RightsLink, permission must be obtained from that source.

BACK CLOSE WINDOW

© 2021 Copyright - All Rights Reserved | Copyright Clearance Center, Inc. | Privacy statement | Terms and Conditions  
Comments? We would like to hear from you. E-mail us at [customerservice@copyright.com](mailto:customerservice@copyright.com)

### Copyright permission for Figure 6.

Quick Reference Topics  
---Please Select---

Submit a Paper  
Manuscript Preparation  
Open Access

Open Access Overview  
Open Access License Options  
Article Processing Charges  
Reuse and Attribution  
Article Deposit Policies

Publication Fees  
Editorial Policies  
Copyright and Licensing

Copyright Transfer  
Open Access License Options  
Reuse and Attribution  
Permissions and Reports  
Other Resources

Reuse on such sites as ResearchGate, Academia.edu, etc., and/or for sales and marketing purposes

Contact: [copyright@optica.org](mailto:copyright@optica.org) OR [copyright@optica.org](mailto:copyright@optica.org)

In addition, we allow authors to post their manuscripts on the Cornell University Library's arXiv site prior to submission to Optica Publishing Group's journals.

**ATTRIBUTION**  
Non-open-access articles

If an author chooses to post a non-open access article published under the our Copyright Transfer Agreement on his or her own website, in a closed institutional repository or on the arXiv site, the following message must be displayed at some prominent place near the article and must include a working hyperlink to the online abstract in the journal:  
© XXXX (year) Optica Publishing Group. One print or electronic copy may be made for personal use only. Systematic reproduction and distribution, duplication of any material in this paper for a fee or for commercial purposes, or modifications of the content of this paper are prohibited.

Open access articles

If an author or third party chooses to post an open access article published under our OAFA on his or her own website, in a repository, on the arXiv site, or anywhere else, the following message should be displayed at some prominent place near the article and include a working hyperlink to the online abstract in the journal:  
© XXXX (year) Optica Publishing Group. Users may use, reuse, and build upon the article, or use the article for text or data mining, so long as such users are for non-commercial purposes and appropriate attribution is maintained. All other rights are reserved.

When adapting or otherwise creating a derivative version of an article published under our OAFA, users must maintain attribution to the author(s) and the published article's title, journal citation, and DOI. Users should also indicate if changes were made and avoid any implication that the author or Optica Publishing Group endorses the use.

If an author chooses to post an open access article published under the CSA Copyright Transfer Agreement (prior to September 2017) on his or her own website, in a closed institutional repository or on the arXiv site, the following message must be displayed at some prominent place near the article and must include a working hyperlink to the online abstract in the journal:  
© XXXX (year) Optical Society of America. One print or electronic copy may be made for personal use only. Systematic reproduction and distribution, duplication of any material in this paper for a fee or for commercial purposes, or modifications of the content of this paper are prohibited.

CC BY licensed articles

Any subsequent reuse or distribution of content licensed under CC BY must maintain attribution to the author(s) and the published article's title, journal citation, and DOI. Users should also indicate if changes were made and avoid any implication that the author or Optica Publishing Group endorses the use.

Top

## Copyright permission for Figure 7.

CCC RightsLink®

Examining the Performance of Refractory Conductive Ceramics as Plasmonic Materials: A Theoretical Approach

Author: Mukesh Kumar, Naoto Umezawa, Satoshi Ishii, et al  
 Publication: ACS Photonics  
 Publisher: American Chemical Society  
 Date: Jan 1, 2016  
 Copyright © 2016, American Chemical Society

PERMISSION/LICENSE IS GRANTED FOR YOUR ORDER AT NO CHARGE

This type of permission/license, instead of the standard Terms and Conditions, is sent to you because no fee is being charged for your order. Please note the following:

- Permission is granted for your request in both print and electronic formats, and translations.
- If figures and/or tables were requested, they may be adapted or used in part.
- Please print this page for your records and send a copy of it to your publisher/graduate school.
- Appropriate credit for the requested material should be given as follows: "Reprinted (adapted) with permission from (COMPLETE REFERENCE CITATION). Copyright (YEAR) American Chemical Society." Insert appropriate information in place of the capitalized words.
- One-time permission is granted only for the use specified in your RightsLink request. No additional uses are granted (such as derivative works or other editions). For any uses, please submit a new request.

If credit is given to another source for the material you requested from RightsLink, permission must be obtained from that source.

BACK CLOSE WINDOW

© 2021 Copyright. All Rights Reserved. | Copyright Clearance Center, Inc. | Privacy statement | Terms and Conditions  
 Comments? We would like to hear from you. E-mail us at customersaw@copyright.com

## Copyright permission for Figure 8 A.

1. Nanoscale  0.00 CAD

Article: Tuning the plasmonic response of TiN nanoparticles synthesised by the transferred arc plasma technique.

ISSN 2040-3372  
 Type of Use Republish in a thesisdissertation  
 Publisher Portion  
 RSC Pub Chart/graph/table/figure

[Hide Details](#)

LICENSED CONTENT

Publication Title	Nanoscale	Publication Type	e-Journal
Article Title	Tuning the plasmonic response of TiN nanoparticles synthesised by the transferred arc plasma technique.	Start Page	7566
		End Page	7574
Author/Editor	National Center for Nanoscience and Technology, Royal Society of Chemistry (Great Britain)	Issue	16
		Volume	10
Date	01/01/2009	URL	http://www.rsc.org/Publishing/journa...
Language	English		
Country	United Kingdom of Great Britain and Northern Ireland		
Rightsholder	Royal Society of Chemistry		

REQUEST DETAILS

Portion Type	Chart/graph/table/figure	Distribution	Canada
Number of charts / graphs / tables / figures requested	1	Translation	Original language of publication
Format (select all that apply)	Print, Electronic	Copies for the disabled?	No
Who will republish the content?	Academic institution	Minor editing privileges?	No
Duration of Use	Current edition and up to 5 years	Incidental promotional use?	No
Lifetime Unit Quantity	Up to 499	Currency	CAD
Rights Requested	Main product		

NEW WORK DETAILS

Title	Synthesis, Characterization, and Photothermal Properties of Plasmonic Metal Nitride Nanoparticles	Institution name	Dalhousie University
Instructor name	Reem Karabali	Expected presentation date	2022-04-01

ADDITIONAL DETAILS

Order reference number	N/A	The requesting person / organization to appear on the license	Reem Karabali
------------------------	-----	---	---------------

REUSE CONTENT DETAILS

Title, description or numeric reference of the portion(s)	Synthesis, Characterization, and Photothermal Properties of Plasmonic Metal Nitride Nanoparticles	Title of the article/chapter the portion is from	Tuning the plasmonic response of TiN nanoparticles synthesised by the transferred arc plasma technique.
Editor of portion(s)	Bendavid, A; Kennedy, D F; Martin, P J; Maschmeyer, T; Murock, A T; Yick, S	Author of portion(s)	Bendavid, A; Kennedy, D F; Martin, P J; Maschmeyer, T; Murock, A T; Yick, S
Volume of serial or monograph	10	Issue, if republishing an article from a serial	16
Page or page range of portion	7566-7574	Publication date of portion	2018-04-11

[Remove](#)

Total Items: 1 Cart Total: 0.00 CAD

## Copyright permission for Figure 8 B.

Your confirmation email will contain your order number for future reference.

License Number 5331470998215

[Printable Details](#)

License date Jun 17, 2022

### Licensed Content

**Licensed Content Publisher** Springer Nature  
**Licensed Content Publication** Applied Physics B: Lasers and Optics  
**Licensed Content Title** Novel nanoparticle matter: ZnN-nanoparticles  
**Licensed Content Author** A. Reinholdt et al  
**Licensed Content Date** Nov 1, 2003

### Order Details

**Type of Use** Thesis/Dissertation  
**Requestor type** academic/university or research institute  
**Format** electronic  
**Portion** figures/tables/illustrations  
**Number of figures/tables/illustrations** 1  
**Will you be translating?** no  
**Circulation/distribution** 1 - 29  
**Author of this Springer Nature content** no

### About Your Work

**Title** Synthesis of Plasmonic Nanomaterials  
**Institution name** Dalhousie University  
**Expected presentation date** Jul 2022

### Additional Data

**Portions** Figure 3

### Requestor Location

Dalhousie university  
6274 Coburg Rd

### Tax Details

### Requestor Location

halifax, NS B3H 4R2  
Canada  
Attn: Dalhousie university

## Copyright permission for Figure 8C.

 ? Help Email Support

---

**Laser-synthesized TiN nanoparticles as promising plasmonic alternative for biomedical applications**  
**Author:** Anton A. Popov et al  
**Publication:** Scientific Reports  
**Publisher:** Springer Nature  
**Date:** Feb 4, 2019  
Copyright © 2019. The Author(s)


**Creative Commons**  
This is an open access article distributed under the terms of the [Creative Commons CC BY](#) license, which permits unrestricted use, distribution, and reproduction in any medium, provided the original work is properly cited.  
You are not required to obtain permission to reuse this article.  
To request permission for a type of use not listed, please contact [Springer Nature](#)

© 2021 Copyright - All Rights Reserved | [Copyright Clearance Center, Inc.](#) | [Privacy statement](#) | [Terms and Conditions](#)  
Comments? We would like to hear from you. E-mail us at [customerscare@copyright.com](mailto:customerscare@copyright.com)

## Copyright permission for Figure 9 (A and B).

1. Nanoscale		0.00 CAD	
Article: Tuning the plasmonic response of TiN nanoparticles synthesised by the transferred arc plasma technique.			
Order License ID	Pending	Publisher Portion	RSC Pub Image/photo/illustration
ISSN	2040-3364		
Type of Use	Republish in a thesis/dissertation		
<a href="#">Hide Details</a>			
LICENSED CONTENT			
Publication Title	Nanoscale	Rightholder	Royal Society of Chemistry
Article Title	Tuning the plasmonic response of TiN nanoparticles synthesised by the transferred arc plasma technique.	Publication Type	Journal
Author/Editor	Guo jia na mi ke xue zhong xin (China), Royal Society of Chemistry (Great Britain)	Start Page	7566
Date	12/31/2008	End Page	7574
Language	English	Issue	16
Country	United Kingdom of Great Britain and Northern Ireland	Volume	10
REQUEST DETAILS			
Portion Type	Image/photo/illustration	Distribution	Canada
Number of images / photos / illustrations	2	Translation	Original language of publication
Format (select all that apply)	Electronic	Copies for the disabled?	No
Who will republish the content?	Academic institution	Minor editing privileges?	No
Duration of Use	Current edition and up to 5 years	Incidental promotional use?	No
Lifetime Unit Quantity	Up to 499	Currency	CAD
Rights Requested	Main product		
NEW WORK DETAILS			


## Copyright permission for Figure 10 (A and B).



[Home](#) | [Help](#) | [Email Support](#) | [Reem Karabali](#)

**A Non-Thermal Plasma Route to Plasmonic TiN Nanoparticles**

Author: Alejandro Alvarez Barragan, Niranjan V. Sawe, Lianlan Zhong, et al


 Publication: The Journal of Physical Chemistry C  
 Publisher: American Chemical Society  
 Date: Feb 1, 2017  
 Copyright © 2017, American Chemical Society

---

**PERMISSION/LICENSE IS GRANTED FOR YOUR ORDER AT NO CHARGE**

This type of permission/license, instead of the standard Terms and Conditions, is sent to you because no fee is being charged for your order. Please note the following:

- Permission is granted for your request in both print and electronic formats, and translations.
- If figures and/or tables were requested, they may be adapted or used in part.
- Please print this page for your records and send a copy of it to your post/undergraduate school.
- Appropriate credits for the requested material should be given as follows: "Reprinted (adapted) with permission from (COMPLETE REFERENCE CITATION), Copyright (YEAR) American Chemical Society." Insert appropriate information in place of the capitalized words.
- One-time permission is granted only for the use specified in your RightsLink request. No additional uses are granted (such as derivative works or other editions). For any other use, please submit a new request.

If credit is given to another source for the material you requested from RightsLink, permission must be obtained from that source.

[BACK](#)
[CLOSE WINDOW](#)

© 2021 Copyright - All Rights Reserved | [Copyright Clearance Center, Inc.](#) | [Privacy statement](#) | [Terms and Conditions](#)  
 Comment? We would like to hear from you. Email us at [customerservice@copyright.com](mailto:customerservice@copyright.com)

## Copyright permission for Figure 10 C.

CCC RightsLink<sup>®</sup> Home Help Email Support Reem Karabali

**Nonthermal Plasma Synthesis of Titanium Nitride Nanocrystals with Plasmon Resonances at Near-infrared Wavelengths Relevant to Photothermal Therapy**  
Author: Katelyn S. Schramke, Yunsiang Qin, Jacob T. Held, et al  
Publication: ACS Applied Nano Materials  
Publisher: American Chemical Society  
Date: Jun 1, 2018  
Copyright © 2018, American Chemical Society

**PERMISSION/LICENSE IS GRANTED FOR YOUR ORDER AT NO CHARGE**

This type of permission/license, instead of the standard Terms and Conditions, is sent to you because no fee is being charged for your order. Please note the following:

- Permission is granted for your request in both print and electronic formats, and translations.
- If figures and/or tables were requested, they may be adapted or used in part.
- Please print this page for your records and send a copy of it to your publisher/graduate school.
- Appropriate credit for the requested material should be given as follows: "Reprinted (adapted) with permission from (COMPLETE REFERENCE CITATION). Copyright (YEAR) American Chemical Society." Insert appropriate information in place of the capitalized words.
- One-time permission is granted only for the use specified in your RightsLink request. No additional uses are granted (such as derivative works or other editions). For any uses, please submit a new request.

If credit is given to another source for the material you requested from RightsLink, permission must be obtained from that source.

[BACK](#) [CLOSE WINDOW](#)

© 2021 Copyright - All Rights Reserved | Copyright Clearance Center, Inc. | Privacy statement | Terms and Conditions  
Comments? We would like to hear from you. Email us at [customerservice@copyright.com](mailto:customerservice@copyright.com)

## Copyright permission for Figure 10 (D-G).

CCC RightsLink<sup>®</sup> Home Help Email Support Reem Karabali

**Plasmonic Core-Shell Zirconium Nitride-Silicon Oxynitride Nanoparticles**  
Author: Stephen Exarhos, Alejandro Alvarez-Barragan, Ece Aytan, et al  
Publication: ACS Energy Letters  
Publisher: American Chemical Society  
Date: Oct 1, 2018  
Copyright © 2018, American Chemical Society

**PERMISSION/LICENSE IS GRANTED FOR YOUR ORDER AT NO CHARGE**

This type of permission/license, instead of the standard Terms and Conditions, is sent to you because no fee is being charged for your order. Please note the following:

- Permission is granted for your request in both print and electronic formats, and translations.
- If figures and/or tables were requested, they may be adapted or used in part.
- Please print this page for your records and send a copy of it to your publisher/graduate school.
- Appropriate credit for the requested material should be given as follows: "Reprinted (adapted) with permission from (COMPLETE REFERENCE CITATION). Copyright (YEAR) American Chemical Society." Insert appropriate information in place of the capitalized words.
- One-time permission is granted only for the use specified in your RightsLink request. No additional uses are granted (such as derivative works or other editions). For any uses, please submit a new request.

If credit is given to another source for the material you requested from RightsLink, permission must be obtained from that source.

[BACK](#) [CLOSE WINDOW](#)

© 2021 Copyright - All Rights Reserved | Copyright Clearance Center, Inc. | Privacy statement | Terms and Conditions  
Comments? We would like to hear from you. Email us at [customerservice@copyright.com](mailto:customerservice@copyright.com)

## Copyright permission for Figure 11.

CCC RightsLink<sup>®</sup> Home Help Email Support Reem Karabali

**Silica-Coated TiN Particles for Killing Cancer Cells**  
Author: Pascal M. Goehemid, Simona Cori, Andres Kech, et al  
Publication: Applied Materials  
Publisher: American Chemical Society  
Date: Jun 1, 2019  
Copyright © 2018, American Chemical Society

**PERMISSION/LICENSE IS GRANTED FOR YOUR ORDER AT NO CHARGE**

This type of permission/license, instead of the standard Terms and Conditions, is sent to you because no fee is being charged for your order. Please note the following:

- Permission is granted for your request in both print and electronic formats, and translations.
- If figures and/or tables were requested, they may be adapted or used in part.
- Please print this page for your records and send a copy of it to your publisher/graduate school.
- Appropriate credit for the requested material should be given as follows: "Reprinted (adapted) with permission from (COMPLETE REFERENCE CITATION). Copyright (YEAR) American Chemical Society." Insert appropriate information in place of the capitalized words.
- One-time permission is granted only for the use specified in your RightsLink request. No additional uses are granted (such as derivative works or other editions). For any uses, please submit a new request.

If credit is given to another source for the material you requested from RightsLink, permission must be obtained from that source.

[BACK](#) [CLOSE WINDOW](#)

© 2021 Copyright - All Rights Reserved | Copyright Clearance Center, Inc. | Privacy statement | Terms and Conditions  
Comments? We would like to hear from you. Email us at [customerservice@copyright.com](mailto:customerservice@copyright.com)